Brain inspired organic electronic devices and systems for adaptive signal processing, memory, and learning

A Dissertation Presented for the

Doctor of Philosophy

Degree

The University of Tennessee, Knoxville

Subhadeep Koner

August 2022

Copyright © 2022 by Subhadeep Koner

All rights reserved.

DEDICATION

This work is dedicated

to humanity

as my late grandfather would have wanted me to do.

ACKNOWLEDGEMENTS

Research in any capacity requires a will and support of many individuals. Without financial support scientific research is difficult to be carried out. I would like to thank National Science Foundation (NSF), AFOSR, DARPA, and Center for materials processing (UTK) for all the financial help they have provided me through my advisor to conduct scientific research. Scientific research also requires peer review to be accepted worldwide. I would like to thank all the anonymous reviewers and my committee members for reviewing my work from time to time.

Now, research for five years do take help from one's colleagues in the lab. I would like to thank them for putting up with me and offering physical and intellectual help through my graduate student years.

My advisor has been one of my closest friend and critic over the years providing me direction and opportunities to freely debate about research topics. That has brought out the best of me. It is a blessing which is priceless and never be repaid with a 'thank you'. All, I have to say we were strangers and moving forward maybe competitors or collaborators but will always remain close friends.

Although the direct inputs to my research productivity have been guidance and significant personal effort, the silent support of family and loved ones is the backbone for all of it. No words are enough to thank the support of my parents and my lovely wife. I love you all.

My maternal grandfather, who passed away at the very start to my Ph.D. journey had always wanted me to succeed in higher education and research. He has continued to be around in spirit. I miss him terribly and cannot describe how big a role he has played in keeping me motivated.

ABSTRACT

A new class of electronic device has emerged which bear the potential for low powered brain like adaptive signal processing, memory, and learning. It is a non-linear resistor with memory coined as memristor. A memristor is a two-terminal electrical device which simultaneously changes its resistance (processing information) and store the resistance state pertaining to the applied power (memory). Therefore, it can collocate memory and processing much like our brain synapse which can save time and energy for information processing. Leveraging stored memory, it can thereby help future engineered systems to learn autonomously from past experiences. There has been a growing interest in understanding the working dynamics of these devices, exploring materials and engineering material combinations to build them, developing methods to integrate them in electronic systems, and building software for its operation with other traditional electronic devices, therefore encompassing multiple disciplines of science and engineering.

In Chapter 1, I review literature on memristive devices from their varied properties to different functionalities, different materials used, and different applications. I discuss the progress in the development of these devices, the gaps that persist, specific research objectives and state my approach to address some of the research gaps. Across chapters 2 to 5, I describe my work on different types of memristive devices and systems to address these research gaps. I demonstrated electrical synapse inspired device synchronizing firing of two neurons in chapter 2, revealed effect of low molecular weight amphiphilic block copolymers on the equilibrium properties of lipid membranes in chapter 3.

Chapter 4 presents a hardware alone system combining materials for distributed sensing (dimpled flexible sheet) and non-volatile memory (PEDOT:PSS thin film memristor) for distributed sensing, memory, and learning. This prototype can be physically trained to learn different input patterns and generate responses accordingly very similar to our biological tactile sensing and reaction system. Chapter 5 reveals the previously unknown resistive switching mechanism of the Cu/PEDOT:PSS thin film memristors.

As a summary of the contribution of this dissertation is to understand the contribution of material architecture and composition on resistive switching and memory in emerging biomolecular and polymeric neuromorphic devices.

TABLE OF CONTENTS

CHAPTER I. Literature review……...1

Introduction…….....2

Memristor device overview……..……...……....4

Memristor device property…….....…...7

Memristive device functionality……7

Electrical model of a memristor……..9

Memristor classification based on different materials……...10

Structural change driven memristors…….…...10

Oxide materials……12

Spin torque transfer memristors……...15

Organic memristors…….....18

Organic-inorganic memristors…….…….....22

Bio-based materials for memristors…….23

Extracted biomaterials as active matrix……...……23

Biomolecular memory devices…….....24

Limitations of memristors…….25

Potential applications of memristors……..29

Non-volatile memories…….29

Aid digital computing…….....29

Building block for different analog devices……..29

Integration with sensors and transducers……..31

Motivation for future research…….……..32

Research gaps, objectives, and approaches…….....32

Electrical synaptic mimic ignored and never studied……33

Limited types of membranes for bio-molecular devices…….....33

Limited attention on integration of memristors with other electronic components……...34

Resistive switching mechanism of Cu/PEDOT:PSS device unknown……..35

Contributions and novelty……36

Summary……...37

References……39

CHAPTER II. Memristive plasticity in artificial electrical synapses via geometrically reconfigurable, gramicidin-doped biomembranes……..54

Abstract……55

Introduction…….....55

Materials and Methods……..57

Materials…….....57

Methods for DIB formation……..58

Electrical measurements…….....58

Simulating the model……59

Results and discussions…….....59

A gramicidin doped lipid membrane has similar structure and composition to biological ES……..……..59

Current-voltage relationships reveal memristive behavior……...59

Modeling gramicidin-doped membrane AES…….....62

Short-term facilitation and depression in AES……..70

AES enable variable synchronization of neurons……..73

Conclusion ……77

References…….78

Appendix……..…….84

CHAPTER III. Comprehensive assessment of homogeneous hybrid droplet interface bilayers assembled from binary mixtures of DPhPC phospholipids and PB-*b*-PEO di-block copolymers…….....101

Abstract ……..102

Introduction…….102

Materials and Methods……105

Materials…….105

Large Unilamellar vesicle (LUVs) preparation…….....105

DIB formation……106

Giant Unilamellar vesicles (GUVs) formation and confocal imaging…….106

Electrophysiology…….....106

Monolayer formation and interfacial tension measurement……107

Results and discussions …….....107

hDIB formation and electrical characterization……..107

Equilibrium energetics of hDIBs……111

Ion channel formation and hDIB stability under applied voltage……115

Conclusion ……..119

References…….....121

Appendix……128

CHAPTER IV. Neuromorphic metamaterials for mechanosensing and perceptual associative learning ……...133

Preface…...……134

Abstract…….....135

Introduction…….135

Materials and methods……137

Unit cell and metasheet fabrication……137

Unit cell resistance measurements…….138

Mechanical tests ……138

Finite element analysis……...138

Fabrication of memristors…….....139

Characterization of memristors…….....139

Programming of pulsatile input……...……...139

Results and discussion……139

Mechanosensing……139

Filtering and thresholding…….....140

Non-linear signal amplification……142

Spatiotemporal memory ……146

Spatially distributed input learning: physical Hopfield networks …….....150

Conclusion……..154

References…….....156

Appendix……160

CHAPTER V. Understanding the influence of electrode material on the bipolar resistive switching mechanism of a Cu/PEDOT:PSS memristor…….....180

Abstract…….....181

Introduction……181

Materials and methods……182

Fabrication of device……..182

Electrical characterization of vertical device……183

I-V mathematical analysis……..183

X-ray photoelectron spectroscopy (XPS)……..……183

Results and discussion…….……...183

Cu plays crucial role in the resistive switching……..183

Eliminating involvement of PEDOT:PSS bulk in the RS of the device…….……...185

Charge transport mechanism……..186

Resistive switching mechanism and hysteresis…….....189

Conclusion……..194

References…….....195

Appendix…….198

CHAPTER VI. Conclusion……..……199

VITA……206

LIST OF TABLES

Table 1.1. Table of different class of memristors built from different materials and their applications.....26

Table 2.1. Summary of electrowetting (EW), electro-compression (EC), and gramicidin channel density dependencies on voltage…….……...65

Table 2.2. EW, EC, and gramicidin channel density dependencies on voltage obtained when the membrane area was reduced through mechanical droplet manipulation……...99

Table 3.1. Summary of the measured hybrid droplet interface bilayer (hDIB) parameters at 0 mV……114

Table 3.2. Equilibrium interfacial tension (IFT) values obtained on DPhPC and PBPEO monolayers…….....132

Table 4.1. Dome inversion and memristance logic……..148

Table 4.2. Mechanosensor print settings…….…….161

Table 4.3. U_i experimental test values obtained from memristor data. Comparison with expected U vector……...…….177

Table 4.4. Hopfield network accuracy. Expected results with regular training and results with experimental tests……...……..178

Table 5.1. Resistance values of Cu/PEDOT:PSS/Cu and Au/PEDOT:PSS/Au devices…….…….188

Table 5.2. Table 2: Field emission work function of metals, metal-oxides, and polymer……193

LIST OF FIGURES

Figure 1.1. Relation between the fundamental circuit elements suggested a missing circuit element……..6

Figure 1.2. Different types of memristors originating from the diverse types of materials used to build them……..……11

Figure 1.3. I-V diagram typical of a phase change materials memory storage unit….……13

Figure 1.4. Different domains for memristor applications……30

Figure 2.1. Two terminal Artificial Electrical Synapse (AES) exhibiting nonlinear memristive behavior…….....59

Figure 2.2. Characterization of the state variables at steady-state EW and EC conditions based of EW and EC time constants respectively…….....64

Figure 2.3. Simulated dynamic responses of AES. Membrane area and channel density using EW and EC parameters for a DPhPC membrane…….....69

Figure 2.4. Short term plasticity in symmetric and asymmetric AES……...72

Figure 2.5. Hodgkin Huxley neuron synchronization through AES plasticity……..75

Figure 2.6. Experimental setup used to assemble and characterize DIBs…….....86

Figure 2.7. I-V relationship of an insulating DOPC membrane……87

Figure 2.8. I-V relationship of AES at varying gramicidin concentrations……..……88

Figure 2.9. Bilayer area growth and decay……89

Figure 2.10. Steady-state normalized area of a DOPC bilayer in C16, for different starting areas……...……90

Figure 2.11. Steady-state dielectric thickness versus applied voltage…….……..91

Figure 2.12. Transient current measurements following stepwise changes in applied voltage……..……..92

Figure 2.13. Nominal channel density versus voltage for different lipids…….93

Figure 2.14. Comparison of experimental data and simulated……..94

Figure 2.15. I-V response of an asymmetric AES……..……...95

Figure 2.16. Experimental characterization of voltage-dependent state variables for an asymmetric AES……96

Figure 2.17. Simulated bilayer area (top) and channel density (bottom) versus time……...97

Figure 2.18. Simulation of asymmetric AES interfacing two fully synchronized Hodgkin-Huxley neurons……...98

Figure 3.1. Hybrid droplet interface bilayers (hDIBs) and Giant Unilamellar vesicles (GUVs)…….....83

Figure 3.2. Electrical properties of hDIBs……..……...84

Figure 3.3. Energetic of hDIBs……..……87

Figure 3.4. Behavior of alamethicin in hDIBs…….....88

Figure 3.5: Side view images of connected droplets suspended in hexadecane oil……128

Figure 3.6. Chemical structures of DPhPC phospholipids and PBPEO diblock copolymers, with hydrophilic portions, highlighted…….128

Figure 3.7. Brightfield with phase contrast (A) and fluorescence (B) images of PBPEO-only GUVs…….....129

Figure 3.8. Brightfield with phase contrast (A) and fluorescence (B) images of GUVs containing 20 mol% DPhPC and 80 mol% PBPEO plus 0.1 mol% Nile Red…….....129

Figure 3.9. Brightfield with phase contrast (A) and fluorescence (B) images of GUVs containing 80 mol% DPhPC and 20 mol% PBPEO plus 0.1 mol% Nile Red……...130

Figure 3.10. Confocal fluorescence images of GUVs containing 80 mol% DPhPC and 20 mol % PBPEO (A) versus those with 80 mol% DPhPC and 20 mol % PBPEO (B)……..130

Figure 3.11. Representative confocal slices of unique GUVs…….……131

Figure 4.1 Neuromorphic metamaterial composed of mechanosensing unit cells with inherent filtering, transduction, mechano-electric signal amplification, and memory capabilities……...141

Figure 4.2. Mechanical and electrical properties of bi-stable domes……..143

Figure 4.3. Integration scheme for transducing dome inversions into electrical memories……149

Figure 4.4. Physical Hopfield network implementation and test for different input patterns…152

Figure 4.5. The key dimensions of the dome unit cell……160

Figure 4.6. Viscoelastic behavior of dome…….162

Figure 4.7. The resistance of the inverted state is maintained over time.....163

Figure 4.8. Instron testing setup for measuring snap-through load of domes……166

Figure 4.9. The filtering tunability of domes……...……...166

Figure 4.10. Curved sensors are more prone to cracking……167

Figure 4.11. Circuit diagram for amplification of input signal……...167

Figure 4.12. Selection of a resistor in series to achieve distinguishable change in V_m (~ resistance of memristor)……...……...168

Figure 4.13. (a) Schematic describing polymeric thin-film device architecture……168

Figure 4.14. Technique for calculating V_{th}, HRS ,and LRS of PEDOT:PSS devices and the corresponding nominal values of 12 devices……..173

Figure 4.15. Cycle to cycle behavior of Cu / PEDOT:PSS / ITO device studied here……...173

Figure 4.16. Response of PEDOT:PSS device to 50 mHz and 100 mHz sinusoidal voltage waveforms …….....174

Figure 4.17. Cumulative change in resistance of six memristors to different voltage…….174

Figure 4.18. Response of a Cu/PEDOT:PSS/PSS device to (a) step voltage input (b) pulsatile voltage input…….175

Figure 4.19. a) Associative memory energy landscape and stored memories b) Energy minimization path. Initial distorted pattern ζ to retrieved memory ξ……...……....175

Figure 4.20. Pairwise interaction of two domes……..176

Figure 4.21. Probability of occurrence of errors in final retrieved memories from physical Hopfield network…….....179

Figure 5.1 Responses of vertically stacked (sandwiched) devices with and without PEDOT:PSS for different electrode combinations……..…….....184

Figure 5.2. Response from Cu/PEDOT:PSS/Cu and Au/PEDOT:PSS/Au electrode combinations……186

Figure 5.3. Slopes of current traces in (A) positive and (B) negative polarity indicate different charge transport mechanisms of the device in different voltage regions…….……190

Figure 5.4. Schematic displaying the modulation in energy barrier to hole movement giving rise to bipolar resistive switching in Cu/PEDOT:PSS/Au device……..192

Figure 5.5. Schottky emission detected from fitting of current response in the HRS region in positive polarity……...198

CHAPTER I. Literature review.

1.1 Introduction

Present day computational systems leverage Von Newman architecture [1] and solid state electronic components to process information at exceptional speeds (10 billion basic operations/second) [2]. These machines are segmented into specialized units for control, memory, and arithmetic and other operations [3]. The whole machine follows a single program stored in memory, operating on data represented with binary states. Computation is performed symbolically on the foundation of Boolean logic, and sequentially following the globally stored program. Enhancement of computing capabilities of these components (and trying to make them denser) have been driven by reduction in device size. Now, these systems face two limitations: i) Moore's law restricts them to be scaled down any further; ii) Von Neumann bottleneck causes either the processor, or the memory to sit idle when the other one of them is active, which hinders throughput of the system and makes them energy inefficient. Its inability to parallelly process information [3, 4] also render them handicapped when faced with a wide variety of data. When armed with artificially intelligent software, these systems can learn from experience and adjust to new inputs to perform human like tasks too. But they are limited by energy inefficiency (100 watts) [5]. In contrast the human brain can perform adaptive computation for signal/information processing, provide memory, learning, classification, and decision-making abilities. This ability of the brain is derived from the massively parallel signal processing capabilities of its comparatively slow (<1000/sec), yet energy efficient (10 watts) complex network of neurons and collocation of memory and processing in the synapse.

A neuron can be thought to be a node with a variety of inputs and one output. Its goal is to receive a stimulus at the inputs and provide a response at the output. The inputs often in the form of electrical signals received via synapses affects the time-course of the neuron's membrane potential. If the membrane potential exceeds a threshold voltage at the cell body, it evokes a sharp voltage spike, called action potential, which is transmitted to other neurons un-attenuated along a fiber, called axon [6]. The transmission along the axon in form of spikes represents digital communication, while the local processing performed by the neuron is analog. At the end of axons, individual neurons connect to target neurons and excite or hinder their activity, establishing circuits that can keep processing incoming information and respond in a desired manner. The point of communication of two neurons happens at the synapse. At the synapse, the action potential fired

in the presynaptic (sending) neuron causes neurotransmission of the signal to the postsynaptic (receiving) neuron. Only if the received signal crosses a certain potential threshold at the postsynaptic neuron it fires its own action potential [6]. Thus, the brain's complex network of neurons, paired with high level autonomous interactions among them through synapses, provides it superior information processing and cognitive capabilities over modern-day computing systems.

The motivation to build brain-inspired hardware has been to mimic the brain's ability to do complex processing and learning with very little energy in artificial hardware[7] with neural circuits robust to imperfections of the essential devices. In biology, learning is achieved through activity dependent changes in the synaptic junction strength. Similarly, activity driven dynamic plasticity of resistance levels in artificial synaptic devices would enable these devices to learn over time [8]. Physical systems capable of sensing, and parallel processing (memory included) of information through memristors can emulate functionality of biological sensory nerves [9]. Realization of these neural circuits would therefore require devices that behave like synapses (for signal processing) and neurons (lossless signal propagation, data classification).

Memristors have gained the spotlight because of their analog switching [10, 11] of resistance states bearing resemblance with biological synapses modulating their synaptic connection strengths (or synaptic weights) depending on the applied action potential [12-16]. They promise on-chip memory and storage, biologically inspired computing and in-memory computing which attracts waves of research interests [5]. Memristors, alike biological synapses, can collocate memory (specific resistance levels or synaptic weights) and processing (naturally transmit signals onto post neurons) of signals. These devices can have high speed [17] and low energy consumption [18]. Therefore, these are two-terminal devices which undergo dynamic reconfiguration of their resistance states with application of external stimuli.

Since the first physical demonstration of a memristor[10], there has been a growing curiosity in search for novel materials to build different kinds of memristors. State of the art redox (reduction and oxidation) memristors [10, 19-23] and phase-change memristors [24-27] have displayed high switching speeds as well as degree of memory retention. They have also found integration in conventional CMOS circuits [28, 29]. Organic memristors [30] in contrast to traditional oxide-based memristive devices are inherently modular and offer the promise of spatially-uniform resistive switching, tunable molecular functionalities, choice of electrodes, and lower operating

energies for adaptable memory retention that are highly desirable but elusive with other material systems [31]. They additionally offer high endurance and mechanical flexibility, making them suitable for wearable compliant and flexible devices. But they are limited in reproducibility and understanding of their working mechanisms. Also, current organic devices are unable to capture the variety of mechanisms and dynamics [32], including the morphological growth and remodeling that are exhibited by biological synapses, therefore limiting their integration in functionally dense neural networks.

Bio-molecular memristors, uniquely mimic the structure, composition, and biophysical properties of synaptic membranes. These modular systems consist of a capacitive lipid membrane doped with one or more types of voltage-dependent ion channels that operate at biologically relevant voltages (<|200 mV|). These relatively inexpensive and significantly low powered devices (~0.1−10 nW) [32], are easily scalable via droplet-based printing [33] or microfluidic methods [34], thus proving valuable contributions towards achieving brain like cognitive capability at biologically relative voltages.

Therefore, diverse electrical responses of different materials due to complicated physical transformations in them motivates continued research to understand, model, and design the non-linear resistive switching dynamics in these devices. Continued outcome from these researches will expand the scope of the implementation of synaptic devices as volatile and non-volatile devices for embedded signal processing and computing of sensor outputs in autonomous smart systems through retention and reorganization of memory processes.

Memristor device overview and history

The known fundamental passive circuit elements were limited to the capacitor (discovered in 1745), a proportional factor relating charge and voltage ($dq = Cdv$), the resistor (1827) again a proportional factor relating voltage and current ($dv = Rdi$), and the inductor (1831) a constant between flux and current ($d\Phi = Ldi$)[35]. Leon Chua identified the missing relation between flux and charge and in 1971 proposed the fourth basic two-terminal circuit element, the *memristor* [36]. He demonstrated that this element behaves like a non-linear resistor with memory (contracted as memristor). *Memristor* can be described to be an electronic element that adjusts its resistance in accordance with the total amount of charge that flows through it. Its basic functionality is to remember the history of its resistance states. Later in 1976, he introduced a broader definition for

memristive devices and systems that included multiple input forces, multiple output variables, and multiple internal mechanisms capable of altering the memristance [37]. This broader definition allowed effects of threshold voltages [10, 38, 39], volatile relaxation [40], thermal [41], optical [42], and magnetic inputs [43, 44]. Even after the initial conceptualization of a memristor, no one managed to build it for the next 30 years. In 2008, a group from Hewlett-Packard labs, California, led by Stanley Williams surprised the electronics community with the physical realization of a memristor. This provided an alternate route to build denser connections in memory devices other than building tinier transistors. The size of conventional transistor has been dropping as forecasted by Moore's law, but now the size is approaching inter-atomic distances and quantum phenomena will degrade their performance and reliability [45].

Therefore, accelerated research for new beyond-CMOS devices and circuits and research interests for physical memristors and memristor models grew exponentially. In 2009, a non-linear drift memristor was modeled by Biolek et al [46]. A nano-scale memristive device mimicking the biological synapse was proposed by Wei Lu from University of Michigan in 2010 [12]. Till 2017, there has been approximately 30,000 papers [47] published in peer reviewed journals related to memristor fabrication or application.

Although there is significant footprint of emerging technologies like Phase change memory (PCM), Spin-Transfer Torque (STT), and REDOX, memristors stand out as the most promising one amongst them because they offer memory array that are denser than those of Flash memories and Hard Disk Drives (HDD), and interestingly are of a speed comparable to the DRAM and SRAM. Simple crossbar structure, with each memory cell occupying just a few nanometers makes memristive arrays dense. Thus, memristors are forecasted to as supplements or even replacements for CMOS-based memories [48-51]. Another encouraging application for memristors is bio-inspired computing [12]. Here, the goal is to enable collocation of memory and processing mimicking the parallel processing capability of our brain. Memristors being low powered devices also makes them lucrative devices for powerful and energy efficient computing systems. In addition to memory and bio-inspired computing, memristors offer design possibilities for building electronic oscillators [52], chaotic oscillators [53-55], hardware security [56-58] and sensors [59-61]. Therefore, memristors have the potential to revolutionize the way future computers and electronic systems will work.

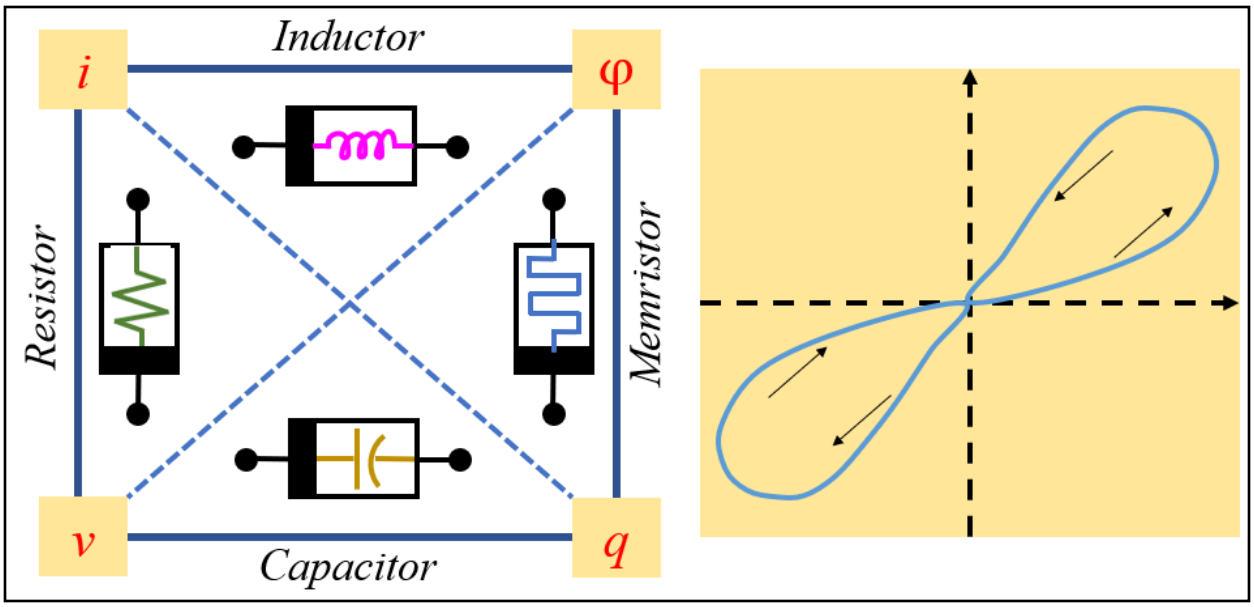


Figure 1.1. Relation between the fundamental circuit elements suggested a missing circuit element [10].

Memristor device property

Any two-terminal device can be called a memristor if it displays a *pinched hysteretic loop* for bipolar periodic excitation on a current-voltage (*i*-*v*) plane [36]. This is loosely similar to the working of a transistor where the output current can be controlled by controlling the gate voltage. But, unlike a transistor, a memristor does not have a third terminal to control the device state. The hysteretic response of a memristive device demonstrates its ability to remember the input stimuli and change its resistance state accordingly[37].

A second signature of a memristor is its response to different frequencies of stimuli, displaying its limiting linear characteristics[37]. Memristors display maximum current voltage (*I*-*V*) hysteresis at a certain frequency which indicates the speed of resistive switching due physical changes in the material of the device or in-short speed of the device. Its periodic operation degenerates into a linear invariant resistor with the input frequency increasing towards infinity. With the input frequency dropping towards zero, the memristor sinks into a non-linear resistor. Therefore, memristive device operation under *DC voltage* is similar to non-linear resistor.

Third property of memristor is its *volatility*, i.e its ability to hold on to a resistive state. A memristor can be volatile (cannot retain the newer resistance state with removal of power supply) contributing to short term memory or non-volatile (retains memory states even after removal of the stimuli/power supply) contributing to long time memory capability of the device.

Also, memristors act only as *passive* elements, in that they enable computing by modulating the connections between active units, but do not directly inject energy or amplify signals themselves [62]. Memristors being a passive device, the instantaneous *power is always non-negative*. Therefore, there is no need for discharge.

Chua et.al also pointed out that memristors can bear an odd symmetric *i*-*v* relationship with respect to origin whenever the memristive weight (resistance) is periodic of the same period as that of the input *v(t)* and is a quarter-wave symmetric [37].

Memristive device functionality

The function of a resistor is to obstruct the flow of charge. Its resistance for a given material can vary only with the dimension of the resistor and cannot change its resistance based on the input

stimuli. Unlike a resistor, the central function of a memristor is to change its resistance state with the amount and direction of the input stimuli. Memristors which are often compared to chemical synapses of the brain retain its initial resistance state even with power supply till a threshold, eclipsing which the resistance switches to a newer resistance state. When the direction of the supply changes and starts dropping, the new resistance state is retained till the power supply is taken off. Some memristors retain the newer resistance state even with power supply off (non-volatile) while others cannot (volatile).

Chua had initially theorized the relation between flux and charge to memristor very similar to the relation between current and voltage for a resistor [36]. But this did not explain the physical interaction between charge and voltage. Williams et.al explained the relation between the functioning of the physical memristor [10] and Chua's mathematical model. Their memristor used Titanium di-oxide bilayer of different oxygen vacancies as the resistive material. With a positive voltage sweep (power applied), the oxygen vacancies would get repelled and move towards the insulating part of the bilayer. This thinning of the insulative layer and increasing percentage of TiO_2-x increased conductivity of the device. Similarly, with a negative voltage would decrease the conductive layer and insulative layer would regain its thickness. Thus, with voltage the conductivity could be controlled. But unlike a resistor, the conductive front (vacancies) would not migrate to initial state when power supply was removed, thereby remembering the last resistive state. The current-voltage response of the device depicts: i) non-linearity from the current increasing at an accelerated rate with increase in voltage; and ii) descending current traces a different path though dropping to zero when voltage applied turns zero, thereby plotting a hysteretic response. This means memristors can have plastic change in memory states.

Synaptic memory devices like memristors can also exhibit potentiation and depression of synaptic weight, that is, synaptic plasticity. Primarily, there are two types of synaptic plasticity: short-term plasticity (STP) and long-term plasticity (LTP). STP is the temporal strengthening of synaptic connections [63], which exists for a few seconds to minutes and then diminishes to its initial value. LTP [64] represents an enduring change in synaptic connections, which exists for hours or years or even a lifetime. These motivated Hebbian learning mechanisms, where the synaptic weight is updated in accordance to neural activities in pre-neuron and post-neuron cells [65]. In this form, one of the most important learning rules is spiking-time-dependent plasticity (STDP) [66]. STDP

controls the plasticity of synapses based on temporal difference in spiking events of pre-synaptic and post-synaptic neurons, that is the synaptic weight is adjusted according to the timing of the fired spikes by connected neurons. According to this rule, the synapse potentiates if presynaptic spikes precede postsynaptic spikes repeatedly, and the synapse depresses if postsynaptic spike precedes presynaptic spike repeatedly. The precise pre- and post-spike timing window controls the sign and magnitude of synaptic weight modulation. Facilitation or inhibition of information transfer in human neural networks is related to the average firing rate of action potentials [67]. Therefore, spike-rate-dependent plasticity (SRDP) is an important synaptic learning mechanism in brain cognitive behaviors [64]. The synaptic weight between neurons can be modified by the firing frequency. In general, presynaptic spikes with high frequency will lead to potentiation, whereas presynaptic spikes with low frequency will result in depression. Moreover, there is a threshold frequency between potentiation and depression [68] which is a historical activity related function that can be modulated under different historical activities. Therefore, via emulating such synaptic behaviors (like plasticity) on neuromorphic devices we can build different types of temporal memories for neuromorphic systems.

Functionally the memristors can be divided into two-level (one-bit) and multilevel (multibit) ones [69]. One-bit device may be used as a cell of non-volatile memory with a large storage time and high resistance to radiation. Whereas the multibit memristors on the one hand can increase the density of integration of the non-volatile memory, and on the other hand can be used to form the basis of adaptive neuromorphic (cognitive) computational systems [69, 70]. Therefore, these devices can memorize the flow of charge in a set of time, providing resiliency and reliability to computing systems at power disruptions and being power efficient, makes them excellent candidate for a variety of computing and sensing applications.

Electrical model of a memristor

The memristor is envisioned to revolutionize signal processing and computing circuits in the future. But the complexity of ionic/electronic transport, tunneling mechanism, and nanoscale feature of the memristor introduces challenges in modeling and simulation of future circuits. Therefore, modeling the functioning of memristors can help their integration into circuits for simulation and accurate estimation of their performance. With application of an electric field across the terminals of a memristor, the current through the device results from the change in

conductivity of the device, which can be threshold dependent multi-states loosely mimicking a chemical synapse or non-threshold dependent like an electrical synapse simply given by

$$v(t) = R_{mem} * i(t) \quad (1)$$

R_{mem} depends on the material of the nano device.

Based on the material composition and mechanism of resistive switching, different models have surfaced over the years of which the *Linear Drift model[10, 71]* and *Non-linear drift model* [10, 46, 72, 73] are most commonly used models. Various memristor models stemming from the basic memristor model continue to surface with progress in research, which helps in facilitating integration of these devices in various electrical circuits. While mathematical models are imperative to building circuits for realizing smart signal processing and learning, understanding the underlying switching mechanisms of memristive devices made from wide variety of materials, and applications of those are essential.

Memristor classification based on different materials.

In the article titled "If it's pinched it's a memristor", Leon Chua referred to the fact that a device which satisfies the property of a hysteretic current-voltage response pinched at zero volts to a periodic input should be a memristor. But the hysteretic behavior can stem from a number of reasons. Conduction pathway creation and annihilation can be either abrupt (binary) or continuous (analogue), with different physical processes evolving at different timescales, leading to rich device behaviors in this seemingly simple device structure [5]. From Joule heating in macroscopic granular materials [74] to Kubo response theory [75] (dependent perturbation driven resistance correction) for nanoscale devices can display hysteretic response of a device. We can classify different types of memristors based on the materials that constitute the device and contribute to memristive behavior in device in three main types:

i) Solid state materials ii) Organic materials iii) Biomaterials.

Structural change driven memristors

Phase change driven memory storage devices are considered the most mature of the emerging memory technologies [76]. Phase change materials (PCM) are those which have diverse phases in

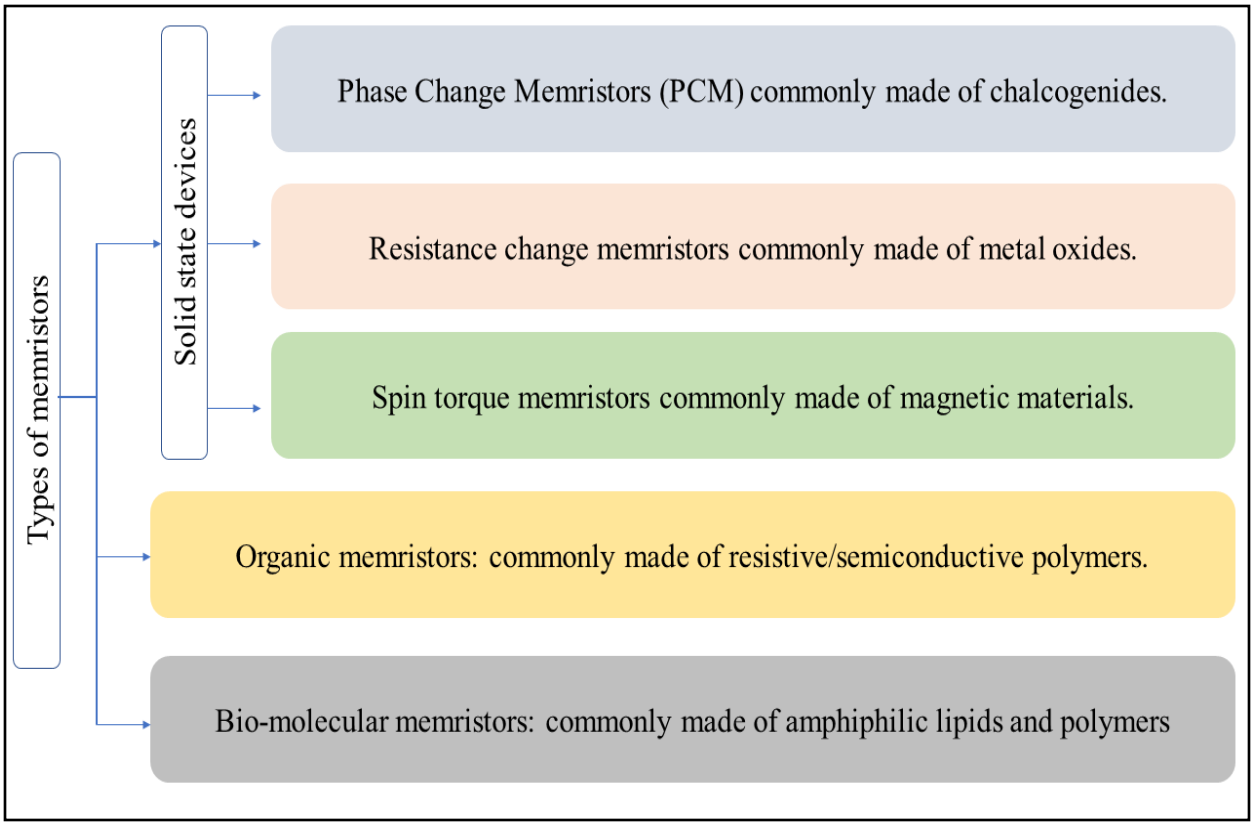


Figure 1.2. Different types of memristors originating from the diverse types of materials used to build them.

which the material can be either ordered (crystalline-like) or disordered (amorphous, as in a liquid), also commonly known as glassy materials[77]. These were discovered in late 1960s [78] in amorphous chalcogenides. These diverse phases have different resistances associated with them. If the structural changes can be stimulated by an applied voltage, then the phase transitions can drive swift switching between resistive states [78-80] due to electrical instability. For PCM memory devices, a certain change in stimuli from the electric field or change in environment initiates a phase transition these materials on a lower scale (∼20 nm). These materials were not commercial for years due to the rapid advancement of silicon-based technology. PCM devices are generically constructed with two types of materials squeezed between two electrodes. One of the two materials is usually an insulative material with tiny conducting channel, directly connected to the other material, i.e., the phase change material. With application of voltage, the channel heats up which causes local transformations in the phase change material, starting from point of contact at the conduction channel, continuing to the opposite electrode. Also, in some chalcogenides-based memristors ions are constrained to follow certain self-directed channels, and their operation is similar to both PCM-components and atomic switches [81].

Oxide materials

Resistive random-access memories (ReRAM/RRAM) have employed oxide based resistive materials for storage function [17] via a mechanism of resistive switching between a high resistance state and a low resistance state [82]under an external electrical input signal. These are constructed mostly of inorganic (grouped into binary oxides [83], ternary and multinary oxides, nitrides [84], chalcogenides [85], and others) and anionic materials i.e through merger of two different materials, one being a charge donor (one that has an excess of electrons) and the other being a charge acceptor (one with a deficiency of electrons), also commonly called doped and undoped materials.

Very similarly oxide based two terminal memristors employ diverse mechanisms for resistive switching most common being movement of oxygen vacancies [19, 86] which results in valence changes in the active layer material [87, 88] and also filament formation [89] by the charge carrier, i.e also oxygen in these cases. Usually there exists a junction where one side is doped, and the other is undoped. This results in two different resistances: one is a high resistance (undoped) and the other is a low resistance (doped). With the application of an external bias v(t) across the device,

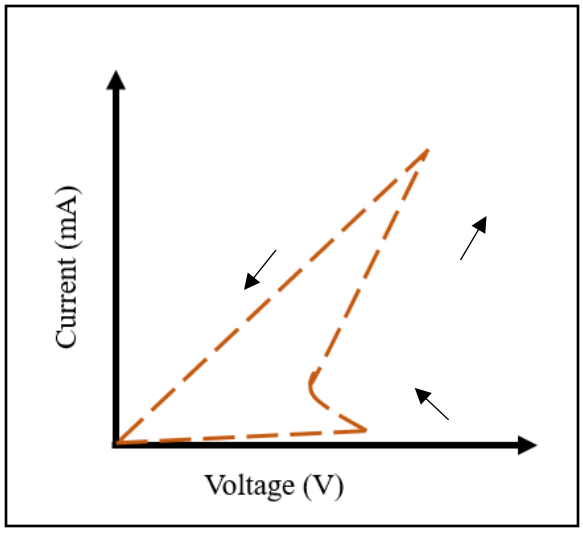


Figure 1.3. Current voltage (I-V) diagram typical of a phase change materials memory storage unit. [77].

the boundary between the two regions migrates by causing the charged dopants to drift. Irrespective of whether the RS is thermally or electrically driven, it is the chemical transition occurring in the material that causes it, and the hysteresis results due to vacancy movements in the materials. The change is a result of either direct application of the electric field, or as a consequence of the heating of the material (explained through models[90]) due to the current. The non-linear hysteretic change in the resistance states can be volatile and non-volatile. Non-linearities present in non-volatile materials means that the switching is dominated by the electrical switching.

This work by Strukov et al. [10] invigorated a lot of interest in construction of solid state memristors with different oxide materials [12]. While some research was directed towards demonstrating a faster switching speed device [17], major focus was also directed towards newer resistive switching (RS) mechanisms.

For memristors using transition metal oxides as the insulative materials in between two metal electrodes, it is critical to note the p and n type nature of the oxides. This is crucial because the RS mechanism is then affected by the interface between the metal electrode and the active oxide layer [91-93]. Electric field induced variation of Schottky barrier height near the metal–oxide interface is a critical role player in the charge transport of the devices [91]. RS response varies for similar metal oxides but with active and inactive metal contacts [92, 94]. Efforts were made to understand the contribution of Schottky barrier dependent interfacial reaction towards RS [95] of Metal-oxide-metal (MOM) devices, but significant gaps remain in the explanation without experimental evidence indicating the theory proposed and very little efforts to explain the hysteresis observed.

Wei Lu created amorphous silicon memristors [12] constructed of a layered device structure including a co-sputtered Ag and Si active layer. The device had Ag-rich (high conductivity) region and an Ag-poor (low conductivity) region. RS mechanism banked on the Ag conductive filament formation and dissolution. These devices displayed switching speed faster than 5ns, high endurance with a few mA on-currents making them promising candidate for high-speed application comparable to conventional flash memory devices. These amorphous silicon memristor also had the edge of being fabricated with a CMOS compatible simple fabrication process already present in the semiconductor industry. One disadvantage of conducting filament based solid state devices have been their requirement of a high forming voltage forming (typically $\geq$ 10 V) for repeatable switching behavior which reduces the performance of power efficiency of

devices [96]. Also, the retention time (how long the data is stored) was short (a few months) in comparison to other solid-state devices.

Wang et.al displayed a synaptic emulator where ion transport was by diffusion and not drift. The device explored how concentration difference of ions could promote diffusion of the same under influence of voltage. They used in situ high-resolution transmission electron microscopy (HRTEM) to study the nature of threshold switching and relaxation of the diffusive memristor. The Ag nano-particle dynamics of the diffusive memristors functionally resemble the synaptic Ca^{2+} behavior in chemical synapses and lead to a direct and natural emulation of multiple synaptic functions for both short-term and long-term plasticity, such as PPF, PPD, PPD following PPF, SRDP and STDP. Their diffusive memristor can also serve as a selector with a large transient nonlinearity that is critical for the operation of a large crossbar array as a neural network [97].

Pickett et.al fabricated and characterized niobium oxide current controlled-Negative Differential Resistance (CC-NDR) [98] devices. Joule-heating-induced [99-101] filamentary insulator-to-metallic phase transformation [98, 101][16, 3] in these devices drives switching of resistance states in the memristor. With application of current, when small part of the device is Joule heated above the transformation temperature more current flows through this region heating it further and expanding the region. This creates 'threshold switching' because of existence of bi-stable resistance states under voltage bias and a s-like shape of the current–voltage curve (S-NDR). Their device was volatile in nature because the formation and presence of the metallic phase is sustained by current flow but disappears upon the removal of bias [102].

Spin torque transfer

The key point in the definition of memristor [36] is its dependence on the historic behavior of current (or, for example, the integral of current profile over time). In a spintronic device, the current electron spin changes the magnetization state of the device. The magnetization state (magnetoresistance) of the device is thus dependent upon the cumulative effects of electron spin excitations. These are often categorized as second-order memory devices but a simplified model of spin-torque induced resistance is provided in [61]. The starting point is the Landau–Ginzburg–Gilbert (LGG) equation with a spin-torque interaction [103]. Two magnetic layers are considered to be perpendicular to the flow of the current, where one is fully polarized (i.e its magnetic orientation is fixed in a direction perpendicular to the current) while the second layer is free. Via

the LGG equation with rotational symmetry, the dynamics of the angle between the pinned and free layer is given by

$$\frac{d\Theta(t)}{dt} = \alpha\gamma H_k \sin(\Theta(t))(p - \cos(\Theta(t))) \tag{2}$$

where γ is called gyromagnetic ratio, α is the damping parameter, H_k is the perpendicular anysotropy in the free layer and p = f hI is current dependent which represents the effect of the current-polarization interaction. The presence of 'h' implies its quantum correction. Considering a simple case with full rotational symmetry, the induced magneto-resistance R(θ) depends on the angle θ in the case of full rotational symmetry as:

$$R(\Theta(t)) = \frac{1}{a + b\cos(\Theta(t))} \tag{3}$$

$$\frac{d\Theta(t)}{dt} = \alpha\gamma H_k \sin(\Theta(t))(p - \cos(\Theta(t))) \tag{4}$$

$$R(\Theta(t)) = \frac{1}{a + b\cos(\Theta(t))} \tag{5}$$

where a and b are constants which depend on the resistance in the free layer and on the ratio between the highest and lowest achievable resistances. We thus see that, in the case of full rotational symmetry, spin-torque materials are first order memristors.

The use of a fundamentally different degree of freedom allows for the realization of memristive behavior [43]. It is provided by the electron spin and memristive behavior is obtained from the broad class of semiconductor spintronic devices. This class encompasses systems whose transport properties depend on the level of electron spin polarization in a semiconductor which is influenced by an external stimulus (such as an applied voltage). The structure and material of these proposed spin torque memristors are based upon existing (and/or commercialized) magnetic devices and can be easily integrated on top of a CMOS [104]. The integration of the spin torque memristor on CMOS is similar to the integration of magnetic random-access memory cell on CMOS. The potential applications of spintronic memristor are in multibit data storage and logic, novel sensing scheme, low power consumption computing, and information security. However, the small resistance ON/OFF ratio remains a notable concern for spintronic memristor devices. Gao et.al displayed application in multi-bit cell switching of a spin-torque device. By controlling switching

current pulse width, the sub-cells of magnetic tunneling junction are designed to switch freely between different bits combinations thereby encoding multibit data storage and logic [105].

Spintronic memristor has remarkable characters to sense nano-scale temperature. This is because of following unique properties of ferromagnetic materials used for these devices. Ferromagnetic materials have stable coherent macroscopic ordered states, such as multi-stable magnetization states, domain wall structure etc. Understanding and manipulating these structures have led to rapid growth of magnetic information storage capacity. These devices can be scaled down to structures at nano-scale that explicitly interact with thermal fluctuations. The interactions between macroscopic coherent magnetic structures and thermal fluctuations in ferromagnetic material provide the opportunity for nano-scale temperature sensing. Memristor device is special for this application because it is an integration system. The positive feedback between memristor resistance and driving strength is the key for this application. The unique ferromagnetic spintronic memristor device characters can be used for other novel sensing scheme. Besides temperature sensing, spintronic memristor can be designed to sense current fluctuations, electromagnetic field fluctuations and even material defects. Like for active power control systems, when the circuit power increases, memristor domain wall is pushed toward a direction to increase the memristor resistance which reduces the current and power through circuit. These devices are also used in data security, where the administrator fully saturate high resistance state and partially saturate low resistance state. Now, by checking the resistance change reading, the administrator knows whether the device information has been accessed or not. The integration capabilities and positive feedback mechanism in spintronic memristor make it particularly suitable for sensing random and fluctuating events. Nano-scale feature size, low cost and the mature integration technology with CMOS are the main advantages for their practical applications.

Advantages of solid state memristor: Solid state memristors provide high repeatability across cycles of periodic excitation and also across multiple devices. They are also compatible with current CMOS fabrication procedures and easier integration to CMOS architecture. They can also withstand higher temperatures during fabrication, therefore can be developed in currently available semiconductor foundries. The notable advantage of solid-state devices is the speed at which they function. The fast switching [71] abilities of these devices make them favorable

candidates for current generation computing systems where high-speed processing is a vital requirement.

Organic memristors

The pursuit of high-performance data storage and smart data processing technique in most electronic devices has been growing fast for applications not restricted to traditional computers but also in flexible electronic systems. Flexible memristors can revolutionize flexible electronics for wearables, electronic-skin or bio-medical devices. Incorporation of light weight polymer as the switching matrix in memristors adds advantages like low-power flexible edge computing applications [106-109]. They also have advantages in terms of functionality, the deposition technique (like spin coating), costs and above all switching matrix tunability (i.e the material properties may be tailored by a chemical approach) [110]. These polymeric memristors employ different mechanisms like thermochemical changes in polymer, charge trapping and de-trapping, charge transfer (CT), electrochemical redox reaction, conformation reconfiguration, ion migration, and etc.[110] resulting in localized resistive switching in polymer memristor devices. With application of voltage, the conductive regions (or conductive filaments) are generated more preferentially under the locally intensified electric field in defects-rich areas.

The first resistive switching (RS) behavior noticed in polymeric materials displayed thermochemical reaction mechanism[111, 112]. Joule heating created pyrolysis of the polymers which created local formation of carbon-rich conducting filaments inside the insulating layer and switch the device resistance from an initial HRS to a LRS. With increase in voltage (periodic), intensified Joule heating effect rupture these conductive filaments and drive the device back to HRS. Carbon-rich filaments and their dissolution were directly viewed with a cross-sectional transmission electron microscope (TEM) in a Cu/pEGDMA/ITO device [113]. The thermochemical reaction is significantly independent of the polymer molecular structure therefore tuning it for varied purpose is difficult. In addition, the pyrolysis procedure also creates polymeric inter layer voids.

Conduction of charge through filaments formed by ion migration also contribute towards memristive switching devices. Under the influence of an electric field across the insulative matrix, mobile ions can migrate from the adjacent electrodes (oxidation of electrodes) or within the matrix through the RS layer, which are then reduced and aggregate into metal filaments (typical charge

carriers are either silver ions or some silver compounds) [113, 114]. Metal filaments grow and eventually connect the anode and cathode, creating a highly conductive pathway inside the insulator and switching the device to LRS. With polarity reversal, the conductive filaments get dissolved via electrochemical oxidization and turn the device back to HRS. Also called Electrochemical metallization (ECM) memories, these are often regarded as next generation memory devices having the room to be scaled down to atomic level, with fast read-write times and long-lasting memory[87, 88]. The most commonly used metal for these filaments has been silver (Ag). Works by Rajan et al, displayed that a polymeric (poly vinylidene fluoride-hexafluoropropylene-- PVDF) thin film doped with silver nano-particles (NP) and ionic liquid (dried thin film forms the solid electrolyte) had the ability to exhibit highly tunable and adaptable memory retention (i.e. from volatile to non-volatile) through simple changes to device composition, structure and applied stimulus[30]. They demonstrated that the polymer matrix viscosity and crystallinity is reduced, improving the ionic mobility in the matrix and thereby reducing the set voltage range and triggering non-volatile memory to the device, with the addition of room temperature ionic liquid to a polymer and nano-particle matrix. They also showed that the volatility of the device could be manipulated (volatile to non-volatile in this device) by enforcing a compliance current, which stabilizes the formed filament.

The Diffusion-Limited-Aggregation growth model comes closest in describing evolution of the filaments. The observed features of these filament based memristive devices are the collective behavior of memristive networks (multiple filaments) or Atomic Switch Networks, whose collective dynamics (intrinsic nonlinearity [115]) is crucial for resulting of seemingly critical states [116]. While the dynamics of a single filament is fundamental to understand the working of the device, the system exhibits collective power spectrum of a higher order (an exponent close to 2). This exponent can be explained via the superposition of wide range of relaxation timescales for each memristor [117]. Native anions such as carboxyl ($–COO^-$) moieties in graphene oxides [118] and I^- in organic–inorganic hybrid perovskites [119] can also induce resistive switching phenomena.

Some organic memristive devices exploit the differences in the molecular orbital energy levels of metal nanoparticles [120, 121] quantum dots [122, 123] and semiconducting small molecules [124, 125] distributed in an insulating polymer matrix which trap charge carriers injected from

electrodes. With enough charge carriers trapped inside an insulating bulk, local leakage networks (moieties) of the charged trapping centers provide a continuous carrier hopping pathway in the bandgap of the polymer material. Conducting pathways connecting electrodes switch the device from initial HRS to LRS. With reversal in polarity, the trapped carriers are pushed out of the trapping centers, which consequently leads to dissolution of existing conductive pathways, and this switches the device to HRS.

Some of the polymeric memristors depend on the charge transfer (CT) mechanism for voltage dependent RS. Under an external electric field, the electrons in donor (D) moieties are partially transferred into acceptor(A) moieties, generating holes in the donors [126-128]. This process creates partially filled molecular orbitals and fuels the concentration of free charge carriers with high mobility, thus switching the D–A systems into a more conductive state. Like most organic devices, a reverse polarity of the input pushes the electrons back to the donor group and force their recombination with holes. This decreases hole concentration and the D–A system returns to HRS. But this CT mechanism may not be uniform across the cross-section of the device and is dependent on the uniform distribution of the electric field inside the switching layer.

Devices with polymers containing carbazole groups such as PVK-PF [129] have randomly orientation carbazole groups that hinder the ordered p–p stacking and charge transport through the conjugated system. This creates high resistance for charge flow through the system keeping the device at a HRS. With the application of an electric field, the carbazole groups get rearranged to an almost face-to-face conformation, which smoothens carrier delocalization and transport thereby switching the device to LRS. Alike most organic memristors, a reversal in input polarity ruptures the ordered face-to-face conformation of carbazole groups and turns the device back to HRS.

Some memristive devices have the sandwiched switching matrix constructed from polymers or combination of polymers which themselves undergo voltage activated redox reactions. The mechanism is to remove unpaired or lone pair electrons from the electron rich molecules by an external electric field, which in turn introduces impurity energy levels into the bandgap of the insulating materials. The conductance of the device is majorly enhanced via intra- and inter-molecular hopping through these charged centers. Polymeric mixtures with electroactive molecules can be used as the active layer in resistive switching memories [110, 130] These polymer composites can provide advantages of both components and thus offer improved physical

properties of electronics, processability, and mechanical flexibility. Poly(3,4-ethylenedioxythiophene): poly(styrenesulfonate) (PEDOT: PSS) is one where the addition of PSS into PEDOT improves the conductivity of the conjugated PEDOT polymer by proton doping and also makes the PEDOT water-soluble. PEDOT: PSS for resistive switching memory applications [131, 132] have been in use. The first reported use was where PEDOT: PSS layered onto the surface of a thin-film Si p–i–n diode deposited onto a stainless-steel substrate. Here, $PEDOT^{+}$ was reduced to $PEDOT^{0}$ with application of electric field which resulted in Write Once Read Many time memory effect from LRS to HRS. In contrast, Alshareef et al. [132] displayed a flexible and transparent PEDOT: PSS resistive switching device on plastic PET substrate, which consists of a PEDOT: PSS thin film (conductivity: 1–3 S cm-1) as the active layer sandwiched between two highly conducting PEDOT: PSS (m-PEDOT, conductivity: 4900 S cm-1) electrodes. When the device eclipsed an input voltage threshold, it was irreversibly switched from the initial LRS to HRS with a large HRS/LRS ratio of 4103. The device could not be brought back to LRS even after applying high positive or negative voltage. This change resulted from a high current density driven accumulation of the insulating PSS chains near the electrode/polymer interface. The drop-in conduction was due to $PEDOT^{+}$ getting reduced to $PEDOT^{0}$ in the bulk film. After the film was reduced, the switchable diode behavior was displayed which was explained by the trapping of holes and proton transport in PEDOT: PSS film under redox reaction of adsorbed water in the film.

Lee et.al used a PEDOT PSS film to exhibit co-existence of two memory effects, namely the switchable diode effect and write once read many times memory. Li et al displayed synaptic plasticity and learning behaviors using a Ag/ (PEDOT: PSS)/Ta memristor. They demonstrated that the movement of the Ag interface upon the initiation of a redox reaction contributes to the resistive switching behavior. Their conclusion was the natural p–n junction in the PEDOT: PSS/Ta compound resulted in rectifying, high resistance, and low power consumption. PEDOT:PSS has been extensively used to build non-volatile memory devices which work in ambient conditions. Heonjun et.al theorized that for their ITO/PEDOT:PSS/Al device, via injection of holes or electrons into the film they could oxidize and reduce the PEDOT chain between the two electrodes driving formation and dissolution of current pathways to result in the resistive switching properties [133]. But due to lack of experimental evidence to support the proposed switching mechanism, function of the electrode materials in the charge transport mechanism keeps open gaps in the understanding the resistive switching mechanism of the device. Advanced efforts were made to

develop and explain the bipolar switching mechanism of Al/PEDOT:PSS/Al devices via known charge transport mechanisms in polymers like space charge limited current dynamics [134].

Organic-inorganic memristors

A hybrid approach to combine the properties of both organic and in-organic materials is gaining popularity [135-137]. Here composite of both materials can be used for device fabrication to build devices to gain flexibility with longer lifetime, and thermal stability [138, 139]. Some commonly used inorganic materials are ZnO [140], ZrO2 [141], TiO2 [2] and reactive metals like Al, Cu, Mg which rapidly forms metal oxides during the metal deposition process [134]. Some of the commonly used organic materials used have been PVP [141], pentacene [142], hyaluronic acid [143], PEDOT:PSS [134], rose Bengal [144]etc. Charge transport through these devices have been conveniently explained from the slopes of the traces of the current-voltage response of the device when plotted on a double-log scale [134, 145]. Resistive switching in these devices have been suggested to be driven by conduction channel (mostly oxygen ion bridge) formation and disruption with voltage/polarity [141]. The high resistance state of these devices is often attributed to the work-function difference between the work-function of the oxide layer and the highest occupied molecular orbital (HOMO) of the polymer matrix [141]. Some recent researches have also claimed negligible role of some the organic layers in these devices by comparing device responses with and without the polymeric layer [144]. Although multiple different mechanisms have been proposed for possible charge transport in these devices none bears strong experimental evidence to support them and also explain the resistive switching and hysteretic response seen in these devices.

Advantages of organic memristors: But molecular chemistry of organic materials provides a platform to fine-tune the geometry and electronic structures of functional monomers (thereby engineering polymer characteristics) through the molecular design and synthesis strategy [15, 146, 147]. For instance, by manipulating the coplanarity of macromolecules with two-dimensionally (2D) conjugated electron donor moieties in the polymer skeleton, the intermolecular π–π stacking and crystallinity of the polymeric thin films can be efficiently improved [148-151]. The resultant may encourage effective charge transport through the extended π-conjugation system and enhance the overall performance of polymer optoelectronic devices [152]. Another way is to focus on other established mechanisms like redox reactions, ion migration, etc. which can be optically imaged by

in situ fluorescence, XPS, and high-resolution TEM measurements [130, 153, 154]. With deeper understanding of these switching mechanisms, discovery of more novel functional materials via rational molecular design and with clearer understanding of the material relationships, rapid improvements can be made in organic RS memories.

Therefore, findings suggest that via application of bipolar voltage input, the doping and un-doping of polymers can be controlled. Thus, we can tune the resistive-switching effect and develop high performance organic nonvolatile memory devices.

Bio-based materials for memristors.

Recently, there is a growing need for the development of bio-based materials for resistive memory devices because unlike inorganic materials, bio-based materials usually exhibit superior biocompatibility, biodegradability, sustainability, and flexibility [155-161]. Most biomaterials can be easily extracted from naturally abundant resources and, hence, they are inexpensive. Bio-based materials are also less toxic and less polluting in comparison to existing traditional inorganic materials. These motivate interest for biocompatible and bio-degradable resistive switching devices for in-vivo applications as implantable devices.

Extracted biomaterials as active matrix: Yan et. al used egg albumen as the active element as a highly transparent and flexible memristor device [155] which displayed different neural bionic behaviors from application of pulse trains and proving natural low-cost materials applicable for intelligent artificial synaptic systems. Albumen-based, large-area paper substrates fabricated by Zhou et al via a simple thermal and chemical reaction process [157] displayed excellent memory behavior with good stability, satisfactory endurance, and device-to-device reproducibility. Jang et al displayed high-performance RS devices owing to the formation and dissolution of conductive Cu filaments in the protein layer (DnaJ) in a Cu/DnaJ/Pt memory cell [162].

Keratin from human hair as the solid electrolyte layer brought in multilevel RS devices good repeatability [161, 163]. Ag/keratin/FTO devices displayed Flash-type RS and afforded reliable nonvolatile multilevel memory behaviors. The RS behavior originated from the electrochemical formation and rupture of Ag conductive filaments in the keratin layer. The Ag/sericin/Au devices, with sericin protein extracted from silk presented a large ON/OFF current ratio above 106 and multilevel memory performance by setting different CCs [164]. The flexible Ag/pectin/ITO

sandwich device on the PET substrate exhibited a low switching voltage of ~1.1 V, a fast-switching speed (< 70 ns), and multilevel storage behaviors under the assistance of different CCs [159]. These research progresses facilitate the development of smart and wearable memory electronics based on bio-inspired materials. Although these devices were constructed from biological components, they bear very little resemblance to the structure, composition or switching mechanisms of biological synapses. There are unable to capture the mechanisms and dynamics like morphological growth and remodeling exhibited by biological synapses. Therefore, realistic synaptic model should target not only the integration density and computational power efficiency of current approaches but also the degree of biological realism on both structural and functional levels. This approach requires designing systems that are energy efficient, soft, stochastic, fault tolerant, capable of self- or external-healing, and preferably biological [32].

Bio-molecular memory devices: Najem, et. al reported the construction of a biomolecular memristor with composition, structure, switching mechanism, and ionic transport similar to bio-synapses. The two-terminal device consisted of a highly insulating planar lipid bilayer assembled at the interface of lipid-encased aqueous droplets held in an oil reservoir. Conductive and memristive ion channels were realized through reversible, voltage-driven insertion of alamethicin peptides (alm) into the insulating bilayer membrane. The device exhibited pinched hysteresis in the current voltage (I-V) plane. The functionalities of this biomolecular memristor are comparable to those of ion channels [165] in pre- and postsynaptic neurons that are partially responsible for short-term and long-term plasticity (STP and LTP) which was demonstrated through paired-pulse facilitation (PPF) and depression (PPD) [63], Previous works displaying STP and LTP required sophisticated materials and fabrication processes to be achieved in conventional solid-state memristors or other devices [14, 166]. Now, while memristors have been widely studied, efforts to explore other kinds of mem-elements have been lagging. Najem et.al were the first to report a volatile, voltage-controlled memcapacitor in which capacitive memory stems from reversible and hysteretic geometrical changes in a lipid bilayer that mimics the composition and structure of bio-membranes [167]. They further demonstrated that the nonlinear pinched hysteretic dynamics and memory were governed by two implicitly-coupled, voltage-dependent state variables—membrane radius and thickness.

Although these biomolecular systems are low-power, analog, less noisy, biocompatible, and capable of exhibiting multiple timescales of short-term synaptic plasticity. A limitation of lipid membranes is they lack structural stability and modularity necessary for a long-lasting adaptive material system. Basham et.al replaced phospholipids with amphiphilic polymers to create artificial membranes, which have been demonstrated to be more durable than phospholipids. Thereafter they demonstrated that polymeric bilayers could exhibit pinched hysteresis in the *Q-v* plane because of voltage-induced geometrical changes. This represents a significant enhancement in the field of soft-matter, geometrically reconfigurable memcapacitors. But these polymeric bilayer membranes are too thick to span any ionophore for ionic conduction [168]. A comparison related to material of different classes of the memristors is presented in table below.

Limitations of memristors

Solid state memristors: Some limitations of solid state memristive devices remain till date. i) Majority of these type of devices are functional at voltages much higher relative to biological synapses. ii) These devices are also very difficult to fabricate consistently due to the lack of complete control over fabrication conditions, i.e., to regulate the concentration of oxygen within a film. This yield devices with greatly different electrical characteristics. iii) Another difficulty is to restrict exposure of the active material to an atmosphere that is not a vacuum. Therefore, keeping oxygen out of the device post fabrication is challenging. Endurance in oxide materials is one of the key problems in the technological competitiveness of memristors [169]. These conditions contribute towards device-to-device variation in high switching voltages, erratic behavior within the same device, and poor state retention. iv) As these devices are solely dependent on migration of oxygen vacancies, they are limited in tunability (features of composite materials). Majority of these devices exhibit steep change from high resistance to low resistance at high speed, which limits ability to explore multiple resistance states in those devices. v) Device modelling is required to understand the switching mechanism beyond the resolutions of available characterization techniques. Existing approaches face the challenge of how to accurately model the ion migration through polycrystalline, amorphous, or complex stack structures in actual memristive devices because of complex structural and material components present. Complex computation methodology available till date just adds to the challenges to simulate long-term and multievent dynamic processes.

Table 1.1. Table of different class of memristors built from different materials and their applications.

Memristor	Advantage	Disadvantage	Application
Oxide	Small scale, fast switching, simple structure	Still non-reliable for commercial use	Memory, logic gates, neuromorphic
Spintronic	Magnetic memory	Small resistance ON/OFF ratio	Neuro-inspired systems
Organic	Low power, flexible, easy chemical tunability	Slow switching	Wearable neural and sensing devices
Bio-molecular	Ultra-low power, biologically similar structure, biologically similar mechanism	Non-durable	For study of biologically relevant neural systems.

Consequences: i) Higher working voltages accounts for higher power needs, making them energy inefficient. ii) Different electrical characteristics from device to device disrupt their prospective from being used commercially. iii) Difficulty to arrest any penetration of aerial oxygen into the active matrix limits the shelf life of these memristors. iv) Difficulty to model these devices creates challenges for device optimization and design device architecture to improve device uniformity and reliability.

Organic memristors: Major challenges of organic devices are relatively large variability in response to similar stimulus and poor cycling endurance, i.e., these devices struggle with repeatability, reproducibility and longevity. Structural anisotropy, uneven thickness of thin film and inhomogeneity of most polymer materials during fabrication creates uneven electric field distribution in the as-fabricated thin films [152]. Repeated electrical stressing also fatigues organic devices quickly. Hybridizing the organic and inorganic species may answer some of these problems, wherein metal–organic framework (MOF) materials have exhibited stable resistive switching characteristics under mechanical deformation [154, 170]. For filamentary materials, the spatial inhomogeneity of the defects and internal electric field contribute to the random distribution of conductive filaments inside the switching matrix. Now, downscaling of the devices into nanometer scale may result in the allocation of certain devices in regions that show different electrical behavior or do not exhibit any resistive switching characteristics at all (make a diagram to explain) [152]. Additionally, the molecular level imperfections of these polymeric devices stemming from polymer chain-ends folding, stacking faults, dislocations, as well as the macroscopic grain boundaries, voids and cracks, introduce unwanted charge trapping sites or scattering centers into the organic layers and congregate the internal electric field around these regions. They also lack direct evidence confirming long lasting effects of CT state (hours, days, and even years) for LTP. Similarly, uncertainties are growing over the previously observed resistive switching in organic Donor-acceptor (D–A) systems. The consequences being electrical behavior may be a result of supplementary effects such as the active presence of reactive metal electrodes. Also, an existing challenge with organic memristors is the high voltage thresholds required for switching. Knowledge about the mechanism resulting dynamic switching are necessary to thoroughly explain the phenomena observed through *in situ* characterization. Therefore, even with polymer memristor display ambitious scientific importance for low-power

computing applications, their poor fabrication yield and reliability keep hindering them from direct practical applications.

Consequence: Now, with non-uniform microstructural features for down-sampled fabrication of the device may result in devices with dissimilar electrical performance which will lead to low production yield and reliability that are unsuitable for practical applications. Random and highly localized resistive switching characteristic will make these devices to be reproduced across large batches for large-scale commercialization. Even for a laboratory / research purpose, lack of repeatability and reproducibility will provide hindrance to them being integrated in neural circuits.

Bio-molecular memristors: Most biomolecular systems are made from synthetic or naturally derived phospholipids which closely resemble the membranes with similar dimensions and physical properties as those in living cells, their use ex vivo is often curtailed by chemical degradation, higher permeability to water, and limited mechanical strength (i.e. bending rigidity, lysis strain). In addition, bio-molecular materials have not been used to build electronic devices for adaptive signal processing and memory like the brain.

Consequence: Bio-molecular systems and devices limited by chemical degradation and mechanical robustness prevents their use in integrated neural circuits and commercial applications. Lesser knowledge about bio-molecular synaptic device limits understanding of the working dynamics of such devices, potential of these devices for commercial or extended research utilization, even avenues for advanced materials processing/engineering.

Potential application of memristors

Memristors aim to be an alternative building blocks for neuromorphic chips. Unlike other projected components with neural behavior, these can accomplish computation without the need of complementary metal–oxide–semiconductor (CMOS). This is categorized as a sufficiently new and innovative technology, and therefore has the potential to evolve over time, which will further broaden the field of its application. Considering current advancement on memristor technology it offers a wide spectrum of usage from digital memory, logic circuits, biological and neuromorphic sensing devices, in neural networks as well as analog electronics, analogic filter applications signal processing etc. Figure 2.5 below enlists the potential applications based on the type of memristor.

Non-volatile memories: Memristor-based nonvolatile memory has been the most obvious application of memristors [171]. The non-volatile, memristor-based memory cell compared to SRAM and DRAM, can exhibit non-volatility, good scalability, compatible with conventional CMOS electronics, and no leakage power. Several types of memories are introduced using memristor nanodevice, like Resistive RAM (RRAM) [172], Phase change memory (PCM) [173], Conductive Bridge memory (CBRAM) [174], ferroelectric memory (FeRAM) [175] and the spintronic memristor that can be a promising replacement for Magnetic memory (MRAM) [176]. A memory array of Memristors what is called a resistive RAM or RRAM is another form of memristor memory. RRAM operates faster than phase-change memory (PCRAM), and it has simpler and smaller cell structure than magnetic memory (MRAM). These retain memory for years rather than less than seconds. Compared to SRAM, however, whose read-write time is less than a nanosecond, memristors with current technology are one order of magnitude slower. In addition, in terms of read–write cycles, the technology of memristors and PCM is between 3–5 orders of magnitude less, but still much more durable than hard disk drive (HDD).

Aid digital computing: Another possible application of memristor is digital design and computation. Memristors can be applied in hybrid CMOS-memristor circuits, or as a basic component to shape the logic gates [177]. One remarkable logic application is using memristor as a reconfigurable switch (FPGA) [178]. The implication logic synthesis [179] and crossbar array architecture [180] are two alternatives presented as new approaches to make efficient digital gate library.

Building block for different analog devices: Memristive devices have been heavily employed for research in analog domain application such as neuromorphic computing, amplifiers, memristor oscillators, filters, chaotic circuits and neuristors [41, 53, 181-184]. Simple circuits of memristors with a single capacitor or inductor are discussed in [185]. Circuits employing memristors aim to achieve cognitive computing by emulating highly parallel processing capability of neurons. As most memristors function similarly to the biological synapses, they form proper building blocks in neuromorphic systems, where neurons and synapses are modeled as electronic devices [12]. The brain-like computing capability of the memristor-based complex spike time dependent plasticity (STDP) learning networks was demonstrated by Afifi et al[186]. Wang et.al demonstrated an artificial neuron with stochastic dynamics based on a diffusive memristor to implement

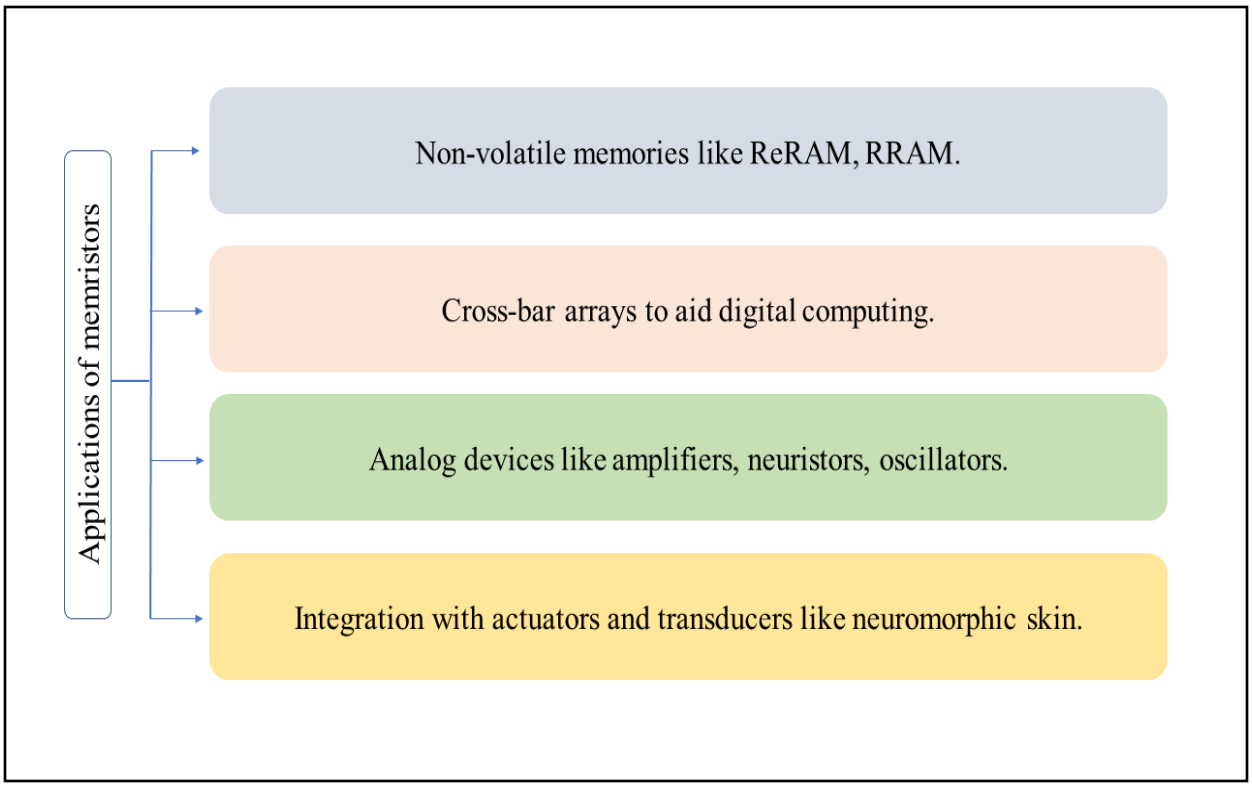


Figure 1.4. Displays various major domains for memristor applications.

convolution layers, rectified linear units (ReLUs) and fully connected layers of a functioning neural network in order to demonstrate pattern classification capability enabled by unsupervised synaptic weight update in fully memristive neural networks [7]. This representation was one of the simplest, yet faithful realization of electronic neuronal functionality to date, achieved without the requirement of tens to hundreds of CMOS devices.

Integration with sensors and transducers: The human brain can also classify tactile information and therefore development of neuromorphic system to emulate the sense of touch gained steam early on. These were mainly constructed using field effect transistor (FET)-based synaptic devices. Bao and co-workers displayed a mechanoreceptor combining a pressure sensor and a ring oscillator to transduce mechanical signals into action potentials in form of digital frequency output Tee, 2015 #481}. Lee and co-workers then integrated the mechanoreceptors with a synaptic transistor to convert the action potentials into postsynaptic currents. The synaptic transistor served as an interface with cockroach efferent nerves to form a hybrid reflex arc [187]. Recently, Lee et al. developed a groundbreaking organic optoelectronic sensorimotor by utilizing a stretchable synaptic transistor, which introduces optical signals to the sensory system to actuate artificial muscles [188].

Chen et.al exhibited that by connecting pressure sensors with a multi-gated transistor via a polyvinyl alcohol ionic cable, realization of the recognition of convex and flat patterns, enabling the perceptual learning of e-skin was possible [189]. Zhu and co-workers adopted dual transistors to acquire pressure data and process these data in a synapse-like manner [190]. Recently Zhang et.al demonstrated an artificial sensory neuron system by first integrating a piezoresistive pressure sensor with a Nafion based organic memristor [9]. The piezoresistive pressure sensor converts pressure stimuli into electrical signals with high sensitivity and durability. They wired the pressure sensor and memristor synapse. Now, external touch could activate the memristor-based synapse and this artificial sensory system was capable of processing and learning the pressure stimuli history with a series of amplitude, duration, frequency, and speed. As a proof-of-concept, implementation of supervised learning method in letter recognition could achieve 91.7% accuracy to illustrate perceptual learning process. These progresses promise energy efficient, biocompatible, and large-scale integration of memristor based systems towards next-generation neurorobotics and neuro-prosthetics.

Motivation for future research: Memristors display retention of memory without power supply and activity dependent adaptability (plasticity). The varied forms of plasticity of memristors stemming from their different volatilities motivates research on memristive networks for supervised and unsupervised learning [7] which can then revolutionize image processing, more specifically edge detection and face/object recognition [7]. Researchers are exploring the capability of memristors to perform quantum computation in addition to conventional neuromorphic and digital data processing [21], compute arithmetic operations in memristor-based structures (using both analog and digital approaches) [191] or be used in memristive Neuro-Fuzzy System [192]. Also in order to tackle the problem of miniaturization of transistor size, several specific transistors can be replaced with a crossbar of memristors and circuits could be shrunk by nearly a factor of 10 in area with improved speed relative to power consumption performance [10].

Till date different types of materials have been explored to build memristor to address speed of switching, introduce different mechanisms of RS, lower power needs, and find diverse applications. One common feature amongst significant majority of these devices is they change resistance states only after an input threshold. This loosely mimics the functioning of the chemical synapse in biology. It is believed that the chemical synapse via its threshold dependent communication and activity dependent plasticity helps in decision making and learning over time. Although Chua's theory of memristors was purely based on physics, realization of the similarity of these devices with brain synapse has encouraged researchers to be on the lookout for newer materials and find newer applications. Since 2008, there have been rapid development and ever-growing interest in realizing memristors ready for commercial use and extending the research beyond just devices but to integrated systems for supervised or unsupervised learning [7, 9, 187]. Therefore, research for device technology shall continue, motivated by materials displaying newer mechanisms for memristive switching, lower threshold voltages for switching, higher speeds of switching etc. Mathematical models explaining the device physics with newer mechanisms shall help easier integration of these devices.

Scientific Gaps, objectives, and research plan

My goal has been to fabricate and characterize electronic devices and systems capable of adaptive signal processing and memory. While reviewing the literature I identified several significant gaps in research including fewer examples of artificial electrical synaptic devices, less exploration of

biomolecular components like synthetic membranes as neuromorphic devices or lack in understanding of resistive switching mechanisms of metal/PEDOT:PSS thin film memristive devices. These motivated my research objectives and my research plan to address those gaps.

Electrical synaptic mimic ignored and never studied:

Efforts to create volatile or non-volatile memristors inherently mimic the discrete, threshold-dependent conductance switching used by chemical synapses. In contrast, electrical synapses (ES) have long been thought to form fixed-conductance connections (modeled as resistors) between neurons. However, it was recently reported that the magnitude of electrical coupling (*i.e.*, proportional to synapse conductance) between neurons connected *via* electrical synapses can vary significantly through activity-dependent plasticity [193-195] to control the level of synchronization in neural networks. Similar to their chemical counterparts, ES exhibit multiple forms of plasticity (*e.g.*, facilitation, depression) at timescales ranging from milliseconds to days [196]. Therefore, major research gap lies in the construction and characterization of artificial synaptic devices that emulate the synaptic plasticity and functionality of electrical synapses. In parallel, due to the recent introduction of biomaterials as components of memristor building, there are significant opportunities to advance our learning about the methods to build, characterize, use, and improve these devices.

The corresponding research objective is to construct synthetic bio-membranes doped with voltage-independent, pore-forming peptides, like gramicidin, which could then display continuous conductance with highly analog change in resistance states thereby exhibiting ion transport mechanisms of electrical synapses. This will provide faster signal processing and computational functionalities.

My approach here was to i) fabricate, characterize and model the gramicidin doped bio-molecular membranes to assess memristance, ii) understand the physical states that determine the response of the system and develop models to describe the dynamic responses to voltage, and iii) display synchronization of neurons brought in by synaptic plasticity of artificial electrical synapse device.

Limited types of membranes for bio-molecular devices:

Neuromorphic devices constructed from lipid membranes have low longevity because lipid membranes lack structural stability and modularity necessary for a long-lasting adaptive material

system. Amphiphilic copolymers as lipid substitutes represents one route to improve biomimetic membranes. However, the use of co-polymers to form bilayer membranes using the DIB method is quite limited, and the membranes formed were substantially thicker than a lipid bilayer, which limits the use of stimuli-responsive transmembrane proteins to control transport in various applications. More robust yet thin enough membranes facilitating gating of ion channels will be ideal for durable bio-molecular synaptic devices. Research gaps prevail in the understanding of the effect of block co-polymers in a lipid membrane. Can these block copolymers as lipid substitutes represent one route to improve biomimetic membranes? Can these hybrid droplet interface bilayers (hDIBs) be similar in thickness to a lipid bilayer, which will then allow the use of stimuli-responsive transmembrane proteins to control transport in various applications.

My research objective was to understand how doping lipid membranes with low molecular weight PBPEO (polybutadiene-co-polyethylene oxide, M_w=1000 g/mol) di-block species affect the bilayer, including its thickness, sensitivity to applied voltages, durability, and response to ion channel forming species.

My approach was to i) study composite monolayer assembly by measuring the interfacial tension of a pendant water drop in the oil solution. ii) Assess hDIBs properties at varying di-block: lipid ratios by monitoring the contact angle of the droplets and electrical capacitance (and resistance) in response to steady state and periodic voltages respectively. Analysis of images from confocal microscopy of di-block: lipid vesicles revealed arrangement of the di-block polymer with the lipids helping us determine a homogenous/heterogenous mixed presence in the hDIBs. Electrical characterization of the membrane revealed thicknesses similar to pure phospholipid membranes in hexadecane oil. Electrical characterization of membrane (with varying di-block: lipid ratios) doped with alamethicin ion channels in response to periodic voltage demonstrated effect of the di-block polymer towards any alteration in voltage dependent ion channel gating dynamics.

Limited attention on integration of memristors with traditional electronic components:

In animals, and especially humans, trained neural networks form associative learning patterns that allow rapid classification and decision making (e.g. object identification via tactile inputs). In contrast, engineered systems are unable to sense and classify information without significant instrumentation and software. But this might be possible in hardware alone if a system were constructed in a way that combines materials for distributed sensing, intrinsic computing (for

classification), and memory (for learning). But methodology and understanding to combine autonomous reconfigurable systems with distributed sensing and embedded memory—akin to a peripheral nervous system, and achieve onboard classification in engineered structures is yet to be demonstrated. Therefore, research gap prevails in understanding how tactile information received can be processed and memorized leading to learning. Research by Arrieta, et al recently showed that thin, flexible dimpled sheets, comprised of planar arrays of bi-stable domes, reconfigure their global shapes in emergent forms when specific domes are inverted.

The corresponding research objective is to reveal how mechanical signals from touch can be sensed via dome inversion events on the thin, flexible dimpled sheets (meta-sheet), and remembered by integrating resistive strain sensors connected electrically to memory storage elements to process and learn temporal shapes of the meta-sheet.

My approach was to i) fabricate and characterize PEDOT:PSS thin film memristors. ii) develop techniques for integration of the memory storage elements with sensors on domes (constructed at Purdue University) for effective operation. ii) Study the dynamic and steady state response of the device to determine threshold voltage for switching of resistance states, volatility of the device and ball-park the high and low resistance states (HRS & LRS) of the device respectively. Based on this we studied how polymeric thin film memristors connected in series and biased with voltage to a transient change in sensor resistance caused by deformation of the dome encode a permanent change in the resistance of the memristor.

Resistive switching mechanism of Cu/PEDOT:PSS device unknown:

The flexible polymeric thin film memristors used in combination with dome sheets for classification of spatial data, were constructed from PEDOT:PSS polymer. Significant gap lies in understanding the resistive switching mechanism and hysteretic current-voltage response of devices made with PEDOT:PSS and most semi-conductive polymers in general. While most research highlighted construction of a flexible memristive device with organic material, there is very little understanding about the working mechanism mainly limited due to lack of significant experimental evidence.

Therefore, my research objective is to reveal the physics behind the resistive switching mechanism and the hysteresis for a Cu/PEDOT:PSS device via electrical and elemental analysis of the device and device materials respectively.

My approach was to i) construct vertical sandwiched and planar PEDOT:PSS thin film devices and electrically characterize their response with different electrode materials (active metal/ inert metal), ii) perform HR-TEM and EDS at the interface of electrode-polymer interface and polymer bulk on a virgin device and the same device after multiple cycles of voltage cycling. Findings from the electrical response suggest the charge transport mechanism of the device. Elemental analysis reveal changes in the material because of voltage stimulation. Together, the procedures reveal contribution of all materials in the device towards the resistive switching mechanism and hysteresis. These findings will further contribute towards making the electrical behavior of the devices reproducible across multiple cycles and multiple devices which has been a lingering challenge with these devices [153, 197].

Contributions/novelty: The outcomes of this work include the following contributions:

i) This work on bio-molecular memristor displays ability of these devices to emulate synaptic behavior of electrical synapses. Therefore, it is a step forward towards broadening the potential of bio-molecular devices in displaying varied functionality beyond the threshold dependent change in resistance similar to a chemical synapse as shown by Najem.et.al [32]. It highlights the activity dependent plasticity of electrical synapses. This work displays that through short term potentiation it could regulate the resistance of the device (similar to gap junction in biology) from repeated excitation to synchronize two connecting neurons. Therefore, novelty lies in the fact that, this works displays importance of artificial electrical synaptic device in neural circuits, quashing aside the age-old understanding of electrical synapses as mere conducting pathways. This work also relies on a novel fabrication approach through highly modular design of the device. By changing the composition of the membrane, oil environment, the response of the device can be widely tuned, thereby delivering possibility to be integrated in systems aiming at achieving varied non linearities or a wide spectrum of resistance tuning (for example different neuron connections requiring different levels of resistance drops).

ii) This work contributes towards expanding the types of membranes needed for robust biomolecular devices. Phospholipid membranes and co-polymer membranes have limitation of

their own. These motivated research for hybrid membranes. Hybrid membranes comprising phospholipids and block co-polymers explored here reveal the bilayer membranes have decreasing levels of adhesive energy leading to smaller bilayer at formation, larger magnitudes of electrowetting, lower insertion thresholds for ion channel gating. Findings here contribute towards understanding the equilibrium and dynamic properties of DPhPC: $PB_{12}PEO_8$ hybrid membrane. Understanding here will help engineer modular hybrid membranes or pure low molecular weight polymeric membranes will expand the types of membranes required for bioelectronics or bio-medical purposes.

iii) Our prototype introduced a new class of flexible metamaterials which demonstrate spatiotemporal mechanosensing and neuromorphic functionalities. While much attention has been focused on building memristors, few efforts were directed towards making use of these hardware devices in electronic circuits[9, 187]. Our work uniquely contributed towards the understanding required for the integration of memristors with traditional electronic components. The cumulative resistance changes of our metamaterial's memristors allow for retrieving all the stored patterns from their final states. As a result, novelty also lies in the fact that our metamaterial encodes several input patterns without the need to store temporal information. We envision this unique capability as providing a route to continuously learning new spatiotemporal mechanical inputs which can be compared to known patterns of interest that may trigger specific control actions.

iv) Understanding of the resistive switching mechanism of Cu/PEDOT:PSS/Au device contributes towards a) further tunability of these devices for desired application, b) engineering materials processing techniques for metal-semiconductive polymeric devices for higher reproducibility in commercial applications. Novelty here lies in the incorporation of Cu as an electrode material on a p-type semiconductive polymer PEDOT:PSS. Also, with Cu electrodes these devices displayed significant enlargement of i-v hysteresis and RS at distinct voltage thresholds which makes it favorable for integration with other electronic transducers in a neuromorphic circuit.

Summary

The literature review in Chapter 1 motivated me to focus on research gaps like under-development of memristive devices and networks utilizing functionalities of electrical synapse from biology, under-exploration of biomaterials for electronic devices, very less effort on integration of memristive devices with traditional electronic components for networks, understanding of the

material physics driving resistive switching mechanism of most organic memristors. I believe the combination of different materials not only propose new research studies but also take the advantages of using more useful properties of each material in the device. Therefore, in chapter 2, I study an artificial electrical synaptic device and displayed in short term plastic properties and its application in neural networks. In chapter 3, I studied hybrid fluidic biomaterial-based membranes in order to better their robustness to stimuli over time. My interests to integrate memristors with traditional transducing components/systems took me to explore polymeric thin film memristors with soft strain sensors to build integrated networks processing spatial information received from tactile stimuli. Chapter 4 explains the integration process and learning from the integrated circuit. In chapter 5, I studied the conduction mechanism and resistive switching mechanism of polymeric thin film memristor I built and used in chapter 4. Chapter 6 concludes on my findings throughout these chapters and aims to establish the future research this dissertation motivates.

References

1. Neumann, J.V., *The Principles of Large-Scale Computing Machines.* Annals of the History of Computing, 1981. **3**(3): p. 263-273.
2. Neumann, J.v. The Computer and the Brain. 2012: Yale University Press.
3. Backus, J., *Can programming be liberated from the von Neumann style? a functional style and its algebra of programs*, in *ACM Turing award lectures*. 2007, Association for Computing Machinery. p. 1977.
4. McKee, S.A., *Reflections on the memory wall*, in *Proceedings of the 1st conference on Computing frontiers*. 2004, Association for Computing Machinery: Ischia, Italy. p. 162.
5. Zidan, M.A., J.P. Strachan, and W.D. Lu, *The future of electronics based on memristive systems.* Nature Electronics, 2018. **1**(1): p. 22-29.
6. Südhof, T.C. and R.C. Malenka, *Understanding synapses: past, present, and future.* Neuron, 2008. **60**(3): p. 469-476.
7. Wang, Z., et al., *Fully memristive neural networks for pattern classification with unsupervised learning.* Nature Electronics, 2018. **1**(2): p. 137-145.
8. Schemmel, J., K. Meier, and E. Mueller. *A new VLSI model of neural microcircuits including spike time dependent plasticity*. in *2004 IEEE International Joint Conference on Neural Networks (IEEE Cat. No.04CH37541)*. 2004.
9. Zhang, C., et al., *Bioinspired Artificial Sensory Nerve Based on Nafion Memristor.* Advanced Functional Materials, 2019. **29**(20): p. 1808783.
10. Strukov, D.B., et al., *The missing memristor found.* Nature, 2008. **453**(7191): p. 80-3.
11. Yakopcic, C., et al., *A Memristor Device Model.* IEEE Electron Device Letters, 2011. **32**(10): p. 1436-1438.
12. Jo, S.H., et al., *Nanoscale Memristor Device as Synapse in Neuromorphic Systems.* Nano Letters, 2010. **10**(4): p. 1297-1301.
13. Ohno, T., et al., *Short-term plasticity and long-term potentiation mimicked in single inorganic synapses.* Nature Materials, 2011. **10**(8): p. 591-595.
14. Wang, Z., et al., *Memristors with diffusive dynamics as synaptic emulators for neuromorphic computing.* Nature Materials, 2017. **16**(1): p. 101-108.
15. Choi, J.-H., et al., *Interregional synaptic maps among engram cells underlie memory formation.* Science, 2018. **360**(6387): p. 430.

16. Whitlock, J.R., et al., *Learning Induces Long-Term Potentiation in the Hippocampus.* Science, 2006. **313**(5790): p. 1093.
17. Torrezan, A.C., et al., *Sub-nanosecond switching of a tantalum oxide memristor.* Nanotechnology, 2011. **22**(48): p. 485203.
18. Zhou, J., et al., *Very Low-Programming-Current RRAM With Self-Rectifying Characteristics.* IEEE Electron Device Letters, 2016. **37**(4): p. 404-407.
19. Yang, J.J., et al., *Memristive switching mechanism for metal/oxide/metal nanodevices.* Nature Nanotechnology, 2008. **3**: p. 429.
20. La Barbera, S., D. Vuillaume, and F. Alibart, *Filamentary Switching: Synaptic Plasticity through Device Volatility.* ACS Nano, 2015. **9**(1): p. 941-949.
21. Pershin, Y.V. and M.D. Ventra, *Neuromorphic, Digital, and Quantum Computation With Memory Circuit Elements.* Proceedings of the IEEE, 2012. **100**(6): p. 2071-2080.
22. Prezioso, M., et al., *Training and operation of an integrated neuromorphic network based on metal-oxide memristors.* Nature, 2015. **521**(7550): p. 61-64.
23. Hu, S.G., et al., *Associative memory realized by a reconfigurable memristive Hopfield neural network.* Nature Communications, 2015. **6**(1): p. 7522.
24. Suri, M., et al. *Phase change memory as synapse for ultra-dense neuromorphic systems: Application to complex visual pattern extraction*. in *2011 International Electron Devices Meeting*. 2011.
25. Eryilmaz, S.B., et al., *Brain-like associative learning using a nanoscale non-volatile phase change synaptic device array.* Frontiers in Neuroscience, 2014. **8**(205).
26. Burr, G.W., et al., *Experimental Demonstration and Tolerancing of a Large-Scale Neural Network (165 000 Synapses) Using Phase-Change Memory as the Synaptic Weight Element.* IEEE Transactions on Electron Devices, 2015. **62**(11): p. 3498-3507.
27. Ambrogio, S., et al., *Unsupervised Learning by Spike Timing Dependent Plasticity in Phase Change Memory (PCM) Synapses.* Frontiers in Neuroscience, 2016. **10**(56).
28. Indiveri, G., et al., *Neuromorphic Silicon Neuron Circuits.* Frontiers in Neuroscience, 2011. **5**(73).
29. Merolla, P.A., et al., *A million spiking-neuron integrated circuit with a scalable communication network and interface.* Science, 2014. **345**(6197): p. 668.

30. Rajan, K., et al., *Ionic liquid-enhanced soft resistive switching devices.* RSC Advances, 2016. **6**(96): p. 94128-94138.
31. Goswami, S., S. Goswami, and T. Venkatesan, *An organic approach to low energy memory and brain inspired electronics.* Applied Physics Reviews, 2020. **7**(2): p. 021303.
32. Najem, J.S., et al., *Memristive Ion Channel-Doped Biomembranes as Synaptic Mimics.* ACS Nano, 2018. **12**(5): p. 4702-4711.
33. Villar, G., A.D. Graham, and H. Bayley, *A Tissue-Like Printed Material.* Science, 2013. **340**(6128): p. 48.
34. Nguyen, M.-A., et al., *Hydrodynamic trapping for rapid assembly and in situ electrical characterization of droplet interface bilayer arrays.* Lab on a Chip, 2016. **16**(18): p. 3576-3588.
35. Shahsavari., M., *Unconventional Computing Using Memristive Nanodevices: From Digital Computing to Brain-like Neuromorphic Accelerator*, in *Neural and Evolutionary Computing*. 2016, Université de Lille.
36. Chua, L., *Memristor-The missing circuit element.* IEEE Transactions on Circuit Theory, 1971. **18**(5): p. 507-519.
37. Chua, L.O. and K. Sung Mo, *Memristive devices and systems.* Proceedings of the IEEE, 1976. **64**(2): p. 209-223.
38. Jo, S.H., K.-H. Kim, and W. Lu, *Programmable Resistance Switching in Nanoscale Two-Terminal Devices.* Nano Letters, 2009. **9**(1): p. 496-500.
39. Chen, C., et al., *Bipolar resistive switching with self-rectifying effects in Al/ZnO/Si structure.* Journal of Applied Physics, 2012. **111**(1): p. 013702.
40. Nian, Y.B., et al., *Evidence for an Oxygen Diffusion Model for the Electric Pulse Induced Resistance Change Effect in Transition-Metal Oxides.* Physical Review Letters, 2007. **98**(14): p. 146403.
41. Pickett, M.D., G. Medeiros-Ribeiro, and R.S. Williams, *A scalable neuristor built with Mott memristors.* Nature Materials, 2013. **12**(2): p. 114-117.
42. Shank, J.C., M.B. Tellekamp, and W.A. Doolittle, *Evidence of ion intercalation mediated band structure modification and opto-ionic coupling in lithium niobite.* Journal of Applied Physics, 2015. **117**(3): p. 035704.

43. Pershin, Y.V. and M. Di Ventra, *Spin memristive systems: Spin memory effects in semiconductor spintronics.* Physical Review B, 2008. **78**(11): p. 113309.
44. Wang, X., et al., *Spintronic Memristor Through Spin-Torque-Induced Magnetization Motion.* IEEE Electron Device Letters, 2009. **30**(3): p. 294-297.
45. Lanza, M., *Redefining microelectronics.* Microelectronic Engineering, 2022. **258**: p. 111767.
46. Z.Biolek, D.B., and V.Biolkova, *Spice model of memristor with nonlinear dopant drift.* Radioengineering, 2009. **18**: p. 210-214.
47. Chua, L., *Memristor: Remembrance of Things Past.* IEEE Micro, 2018. **38**(5): p. 7-12.
48. Kim, K.-H., et al., *A Functional Hybrid Memristor Crossbar-Array/CMOS System for Data Storage and Neuromorphic Applications.* Nano Letters, 2012. **12**(1): p. 389-395.
49. Ho, Y., G.M. Huang, and P. Li, *Dynamical Properties and Design Analysis for Nonvolatile Memristor Memories.* IEEE Transactions on Circuits and Systems I: Regular Papers, 2011. **58**(4): p. 724-736.
50. Cheng, K.-T.T. and D.B. Strukov, *3D CMOS-memristor hybrid circuits: devices, integration, architecture, and applications*, in *Proceedings of the 2012 ACM international symposium on International Symposium on Physical Design*. 2012, Association for Computing Machinery: Napa, California, USA. p. 33–40.
51. Lastras-Montaño, M.A., A. Ghofrani, and K. Cheng. *HReRAM: A hybrid reconfigurable resistive random-access memory*. in *2015 Design, Automation & Test in Europe Conference & Exhibition (DATE)*. 2015.
52. Zidan, M.A., et al., *A family of memristor-based reactance-less oscillators.* Int. J. Circuit Theory Appl., 2014. **42**(11): p. 1103–1122.
53. ITOH, M. and L.O. CHUA, *MEMRISTOR OSCILLATORS.* International Journal of Bifurcation and Chaos, 2008. **18**(11): p. 3183-3206.
54. Sun, J., et al., *Compound synchronization of four memristor chaotic oscillator systems and secure communication.* Chaos: An Interdisciplinary Journal of Nonlinear Science, 2013. **23**(1): p. 013140.
55. Sabarathinam, S., C.K. Volos, and K. Thamilmaran, *Implementation and study of the nonlinear dynamics of a memristor-based Duffing oscillator.* Nonlinear Dynamics, 2017. **87**(1): p. 37-49.

56. Mathew, J., et al., *A Novel Memristor-Based Hardware Security Primitive.* ACM Trans. Embed. Comput. Syst., 2015. **14**(3): p. Article 60.
57. Rose, G.S., et al. *Hardware security strategies exploiting nanoelectronic circuits*. in *2013 18th Asia and South Pacific Design Automation Conference (ASP-DAC)*. 2013.
58. Rose, G.S., et al. *Foundations of memristor based PUF architectures*. in *2013 IEEE/ACM International Symposium on Nanoscale Architectures (NANOARCH)*. 2013.
59. Sacchetto, D., et al., *New Insight on Bio-sensing by Nano-fabricated Memristors.* BioNanoScience, 2011. **1**(1): p. 1-3.
60. Puppo, F., et al., *Memristive Biosensors Under Varying Humidity Conditions.* IEEE Transactions on NanoBioscience, 2014. **13**(1): p. 19-30.
61. Wang, X., et al., *Spintronic Memristor Temperature Sensor.* IEEE Electron Device Letters, 2010. **31**(1): p. 20-22.
62. Lu, W., *Going active.* Nature Materials, 2013. **12**(2): p. 93-94.
63. Zucker, R.S. and W.G. Regehr, *Short-term synaptic plasticity.* Annu Rev Physiol, 2002. **64**: p. 355-405.
64. Bliss, T.V. and G.L. Collingridge, *A synaptic model of memory: long-term potentiation in the hippocampus.* Nature, 1993. **361**(6407): p. 31-9.
65. Morris, R.G.M., *D.O. Hebb: The Organization of Behavior, Wiley: New York; 1949.* Brain Research Bulletin, 1999. **50**(5): p. 437.
66. Caporale, N. and Y. Dan, *Spike Timing–Dependent Plasticity: A Hebbian Learning Rule.* Annual Review of Neuroscience, 2008. **31**(1): p. 25-46.
67. Rachmuth, G., et al., *A biophysically-based neuromorphic model of spike rate- and timing-dependent plasticity.* Proceedings of the National Academy of Sciences, 2011. **108**(49): p. E1266.
68. Bienenstock, E.L., L.N. Cooper, and P.W. Munro, *Theory for the development of neuron selectivity: orientation specificity and binocular interaction in visual cortex.* The Journal of Neuroscience, 1982. **2**(1): p. 32.
69. Stathopoulos, S., et al., *Multibit memory operation of metal-oxide bi-layer memristors.* Scientific Reports, 2017. **7**(1): p. 17532.

70. Hossam, H., et al. *A New Read Circuit for Multi-Bit Memristor-Based Memories based on Time to Digital Sensing Circuit*. in *2018 IEEE 61st International Midwest Symposium on Circuits and Systems (MWSCAS)*. 2018.
71. Strukov, D.B. and R.S. Williams, *Exponential ionic drift: fast switching and low volatility of thin-film memristors.* Applied Physics A, 2009. **94**(3): p. 515-519.
72. Prodromakis, T., et al., *A Versatile Memristor Model With Nonlinear Dopant Kinetics.* IEEE Transactions on Electron Devices, 2011. **58**(9): p. 3099-3105.
73. Prodromakis, T., C. Toumazou, and L. Chua, *Two centuries of memristors.* Nature Materials, 2012. **11**: p. 478.
74. Béquin, P. and V. Tournat, *Electrical conduction and Joule effect in one-dimensional chains of metallic beads: hysteresis under cycling DC currents and influence of electromagnetic pulses.* Granular Matter, 2010. **12**(4): p. 375-385.
75. Di Ventra, M. and Y.V. Pershin, *On the physical properties of memristive, memcapacitive and meminductive systems.* Nanotechnology, 2013. **24**(25): p. 255201.
76. Ielmini, D. and A.L. Lacaita, *Phase change materials in non-volatile storage.* Materials Today, 2011. **14**(12): p. 600-607.
77. Caravelli, F. and J.P. Carbajal, *Memristors for the Curious Outsiders.* Technologies, 2018. **6**(4): p. 118.
78. Ovshinsky, S.R., *Reversible Electrical Switching Phenomena in Disordered Structures.* Physical Review Letters, 1968. **21**(20): p. 1450-1453.
79. Neale, R., D.L. Nelson, and G. Moore. *Non - Volatile and Reprogrammable, The Read Mostly Memory is Here*. 1970.
80. Buckley, W.D. and S.H. Holmberg, *Electrical characteristics and threshold switching in amorphous semiconductors.* Solid-State Electronics, 1975. **18**(2): p. 127-147.
81. Campbell, K.A., *Self-directed channel memristor for high temperature operation.* Microelectronics Journal, 2017. **59**: p. 10-14.
82. Sawa, A., *Resistive switching in transition metal oxides.* Materials Today, 2008. **11**(6): p. 28-36.
83. Hashem, N. and S. Das, *Switching-time analysis of binary-oxide memristors via a nonlinear model.* Applied Physics Letters, 2012. **100**(26): p. 262106.
84. Choi, B.J., et al., *Nitride memristors.* Applied Physics A, 2012. **109**(1): p. 1-4.

85. Li, Y., et al., *Ultrafast Synaptic Events in a Chalcogenide Memristor.* Scientific Reports, 2013. **3**(1): p. 1619.
86. Lai, C.-H., et al., *Effect of firing atmosphere and bottom electrode on resistive switching mode in TiO2 thin films.* Thin Solid Films, 2013. **529**: p. 430-434.
87. Waser, R., et al., *Redox-Based Resistive Switching Memories – Nanoionic Mechanisms, Prospects, and Challenges.* Advanced Materials, 2009. **21**(25-26): p. 2632-2663.
88. Valov, I., et al., *Electrochemical metallization memories—fundamentals, applications, prospects.* Nanotechnology, 2011. **22**(28): p. 289502.
89. Mohammad, B., et al., *State of the art of metal oxide memristor devices.* Nanotechnology Reviews, 2016. **5**(3): p. 311-329.
90. Chernov, A.A., D.R. Islamov, and A.A. Pik'nik, *Non-linear memristor switching model.* Journal of Physics: Conference Series, 2016. **754**(10): p. 102001.
91. Kim, C.J. and I.W. Chen, *Effect of top electrode on resistance switching of (Pr, Ca)MnO3 thin films.* Thin Solid Films, 2006. **515**(4): p. 2726-2729.
92. Yang, W.-Y. and S.-W. Rhee, *Effect of electrode material on the resistance switching of Cu2O film.* Applied Physics Letters, 2007. **91**(23): p. 232907.
93. Baikalov, A., et al., *Field-driven hysteretic and reversible resistive switch at the Ag–Pr0.7Ca0.3MnO3 interface.* Applied Physics Letters, 2003. **83**(5): p. 957-959.
94. Hang-Bing, L., et al., *Polarity-Free Resistive Switching Characteristics of Cu x O Films for Non-volatile Memory Applications.* Chinese Physics Letters, 2008. **25**(3): p. 1087-1090.
95. Singh, B. and B.R. Mehta, *Relationship between nature of metal-oxide contacts and resistive switching properties of copper oxide thin film based devices.* Thin Solid Films, 2014. **569**: p. 35-43.
96. Jo, S.H., et al. *Si Memristive devices applied to memory and neuromorphic circuits*. in *Proceedings of 2010 IEEE International Symposium on Circuits and Systems*. 2010.
97. Chang, Y.-C., et al., *Highly Uniform Resistive Switching Properties of Solution-Processed Silver-Embedded Gelatin Thin Film.* Small, 2018. **14**(13): p. 1703888.
98. Ridley, B.K., *Specific Negative Resistance in Solids.* Proceedings of the Physical Society, 1963. **82**(6): p. 954-966.

99. Futaki, H., *A New Type Semiconductor (Critical Temperature Resistor).* Japanese Journal of Applied Physics, 1965. **4**(1): p. 28-41.
100. Cope, R.G. and A.W. Penn, *High-speed solid-state thermal switches based on vanadium dioxide.* Journal of Physics D: Applied Physics, 1968. **1**(2): p. 161-168.
101. Berglund, C.N., *Thermal filaments in vanadium dioxide.* IEEE Transactions on Electron Devices, 1969. **16**(5): p. 432-437.
102. Pickett, M.D. and R. Stanley Williams, *Sub-100 fJ and sub-nanosecond thermally driven threshold switching in niobium oxide crosspoint nanodevices.* Nanotechnology, 2012. **23**(21): p. 215202.
103. Sun, J.Z., *Spin-current interaction with a monodomain magnetic body: A model study.* Physical Review B, 2000. **62**(1): p. 570-578.
104. Wang, X. and Y. Chen. *Spintronic memristor devices and application*. in *2010 Design, Automation & Test in Europe Conference & Exhibition (DATE 2010)*. 2010.
105. Lou, X., et al., *Demonstration of multilevel cell spin transfer switching in MgO magnetic tunnel junctions.* Applied Physics Letters, 2008. **93**(24): p. 242502.
106. Zhang, B., et al., *Redox gated polymer memristive processing memory unit.* Nat Commun, 2019. **10**(1): p. 736.
107. Wang, T.-Y., et al., *Flexible Electronic Synapses for Face Recognition Application with Multimodulated Conductance States.* ACS Applied Materials & Interfaces, 2018. **10**(43): p. 37345-37352.
108. van de Burgt, Y., et al., *A non-volatile organic electrochemical device as a low-voltage artificial synapse for neuromorphic computing.* Nature Materials, 2017. **16**(4): p. 414-418.
109. Gergel-Hackett, N., J. Tedesco, and C. Richter, *Memristors With Flexible Electronic Applications.* Proceedings of the IEEE, 2012. **100**: p. 1971-1978.
110. Chen, Y., et al., *Polymer memristor for information storage and neuromorphic applications.* Materials Horizons, 2014. **1**(5): p. 489-506.
111. Pender, L.F. and R.J. Fleming, *Memory switching in glow discharge polymerized thin films.* Journal of Applied Physics, 1975. **46**(8): p. 3426-3431.
112. Segui, Y., B. Ai, and H. Carchano, *Switching in polystyrene films: Transition from on to off state.* Journal of Applied Physics, 1976. **47**(1): p. 140-143.

113. Lee, B.-H., et al., *Direct Observation of a Carbon Filament in Water-Resistant Organic Memory.* ACS Nano, 2015. **9**(7): p. 7306-7313.
114. Gao, S., et al., *Reply to "Comment on 'Dynamic Processes of Resistive Switching in Metallic Filament-Based Organic Memory Devices'".* The Journal of Physical Chemistry C, 2013. **117**(22): p. 11881-11882.
115. Avizienis, A.V., et al., *Neuromorphic Atomic Switch Networks.* PLOS ONE, 2012. **7**(8): p. e42772.
116. Scharnhorst, K.S., et al., *Atomic switch networks as complex adaptive systems.* Japanese Journal of Applied Physics, 2018. **57**(3S2): p. 03ED02.
117. Caravelli, F., F.L. Traversa, and M. Di Ventra, *Complex dynamics of memristive circuits: Analytical results and universal slow relaxation.* Phys Rev E, 2017. **95**(2-1): p. 022140.
118. Kim, S.K., et al., *Conductive Graphitic Channel in Graphene Oxide-Based Memristive Devices.* Advanced Functional Materials, 2016. **26**(41): p. 7406-7414.
119. Zhu, X., J. Lee, and W.D. Lu, *Iodine Vacancy Redistribution in Organic–Inorganic Halide Perovskite Films and Resistive Switching Effects.* Advanced Materials, 2017. **29**(29): p. 1700527.
120. Son, D.I., et al., *Bistable Organic Memory Device with Gold Nanoparticles Embedded in a Conducting Poly(N-vinylcarbazole) Colloids Hybrid.* The Journal of Physical Chemistry C, 2011. **115**(5): p. 2341-2348.
121. Kim, W.T., et al., *Current bistability and carrier transport mechanisms of organic bistable devices based on hybrid Ag nanoparticle-polymethyl methacrylate polymer nanocomposites.* Applied Physics Letters, 2010. **96**(25): p. 253301.
122. Zhang, X., et al., *Black Phosphorus Quantum Dots.* Angewandte Chemie International Edition, 2015. **54**(12): p. 3653-3657.
123. Zhang, P., et al., *Facile Synthesis of Co9Se8 Quantum Dots as Charge Traps for Flexible Organic Resistive Switching Memory Device.* ACS Applied Materials & Interfaces, 2016. **8**(44): p. 30336-30343.
124. Sun, Y., et al., *Resistive switching memory devices based on electrical conductance tuning in poly(4-vinyl phenol)–oxadiazole composites.* Physical Chemistry Chemical Physics, 2015. **17**(44): p. 29978-29984.

125. Sun, Y., et al., *Bistable electrical switching and nonvolatile memory effect in mixed composite of oxadiazole acceptor and carbazole donor.* Organic Electronics, 2015. **25**: p. 283-288.
126. Ling, Q.-D., et al., *Nonvolatile Polymer Memory Device Based on Bistable Electrical Switching in a Thin Film of Poly(N-vinylcarbazole) with Covalently Bonded C60.* Langmuir, 2007. **23**(1): p. 312-319.
127. Pan, L., et al., *Role of oxadiazole moiety in different D–A polyazothines and related resistive switching properties.* Journal of Materials Chemistry C, 2013. **1**(30): p. 4556-4564.
128. Zhang, Q., et al., *Rational Design of Small Molecules to Implement Organic Quaternary Memory Devices.* Advanced Functional Materials, 2016. **26**(1): p. 146-154.
129. Xie, L.-H., et al., *An Effective Friedel−Crafts Postfunctionalization of Poly(N-vinylcarbazole) to Tune Carrier Transportation of Supramolecular Organic Semiconductors Based on π-Stacked Polymers for Nonvolatile Flash Memory Cell.* Journal of the American Chemical Society, 2008. **130**(7): p. 2120-2121.
130. Cho, B., et al., *Organic Resistive Memory Devices: Performance Enhancement, Integration, and Advanced Architectures.* Advanced Functional Materials, 2011. **21**(15): p. 2806-2829.
131. Möller, S., et al., *A polymer/semiconductor write-once read-many-times memory.* Nature, 2003. **426**(6963): p. 166-169.
132. Bhansali, U.S., et al., *Metal-Free, Single-Polymer Device Exhibits Resistive Memory Effect.* ACS Nano, 2013. **7**(12): p. 10518-10524.
133. Ha, H. and O. Kim, *Bipolar switching characteristics of nonvolatile memory devices based on poly(3,4-ethylenedioxythiophene):poly(styrenesulfonate) thin film.* Applied Physics Letters, 2008. **93**(3): p. 033309.
134. Jeong, H.Y., et al., *Bipolar resistive switching characteristics of poly(3,4-ethylene-dioxythiophene): Poly(styrenesulfonate) thin film.* Current Applied Physics, 2010. **10**(1, Supplement): p. e46-e49.
135. Chujo, Y., *Organic—inorganic hybrid materials.* Current Opinion in Solid State and Materials Science, 1996. **1**(6): p. 806-811.

136. Sanchez, C., et al., *Applications of hybrid organic–inorganic nanocomposites.* Journal of Materials Chemistry, 2005. **15**(35-36): p. 3559-3592.
137. Sanchez, C. and B. Lebeau, *Hybrid organic - inorganic materials with second-order optical nonlinearities synthesized via sol - gel chemistry.* Pure and Applied Optics: Journal of the European Optical Society Part A, 1996. **5**(5): p. 689-699.
138. Yoo, E.J., et al., *Resistive Switching Behavior in Organic–Inorganic Hybrid CH3NH3PbI3−xClx Perovskite for Resistive Random Access Memory Devices.* Advanced Materials, 2015. **27**(40): p. 6170-6175.
139. Baldi, G., et al., *Logic with memory: and gates made of organic and inorganic memristive devices.* Semiconductor Science and Technology, 2014. **29**(10): p. 104009.
140. Khan, M.U., et al., *Schottky diode based resistive switching device based on ZnO/PEDOT:PSS heterojunction to reduce sneak current problem.* Journal of Materials Science: Materials in Electronics, 2019. **30**(5): p. 4607-4617.
141. Khan, M.U., G. Hassan, and J. Bae, *Non-volatile resistive switching based on zirconium dioxide: poly (4-vinylphenol) nano-composite.* Applied Physics A, 2019. **125**(6): p. 378.
142. Kumatani, A., et al., *On Practical Charge Injection at the Metal/Organic Semiconductor Interface.* Scientific Reports, 2013. **3**(1): p. 1026.
143. Lee, J.H., et al., *Biocompatible and Biodegradable Neuromorphic Device Based on Hyaluronic Acid for Implantable Bioelectronics.* Advanced Functional Materials, 2021. **31**(50): p. 2107074.
144. Karthäuser, S., et al., *Resistive switching of rose bengal devices: A molecular effect?* Journal of Applied Physics, 2006. **100**(9): p. 094504.
145. Syed A. Moiz, I.A.K., Waheed A. Younis and Khasan S. Karimov, *Space Charge–Limited Current Model for Polymers.* Conducting Polymers, 2016.
146. Borghetti, J., et al., *'Memristive' switches enable 'stateful' logic operations via material implication.* Nature, 2010. **464**(7290): p. 873-876.
147. Gao, S., et al., *Improving Unipolar Resistive Switching Uniformity with Cone-Shaped Conducting Filaments and Its Logic-In-Memory Application.* ACS Applied Materials & Interfaces, 2018. **10**(7): p. 6453-6462.

148. Ye, L., et al., *Molecular Design toward Highly Efficient Photovoltaic Polymers Based on Two-Dimensional Conjugated Benzodithiophene.* Accounts of Chemical Research, 2014. **47**(5): p. 1595-1603.
149. Chakravarthi, N., et al., *The effect of with/without resonance-mediated interactions on the organic solar cell performance of new 2D π-conjugated polymers.* Polymer Chemistry, 2015. **6**(40): p. 7149-7159.
150. Bin, H., et al., *11.4% Efficiency non-fullerene polymer solar cells with trialkylsilyl substituted 2D-conjugated polymer as donor.* Nature Communications, 2016. **7**(1): p. 13651.
151. Wang, J., et al., *Enhancing Performance of Nonfullerene Acceptors via Side-Chain Conjugation Strategy.* Advanced Materials, 2017. **29**(35): p. 1702125.
152. Zhang, B., et al., *90% yield production of polymer nano-memristor for in-memory computing.* Nature Communications, 2021. **12**(1): p. 1984.
153. Goswami, S., et al., *Robust resistive memory devices using solution-processable metal-coordinated azo aromatics.* Nature Materials, 2017. **16**(12): p. 1216-1224.
154. Pan, L., et al., *Metal-Organic Framework Nanofilm for Mechanically Flexible Information Storage Applications.* Advanced Functional Materials, 2015. **25**(18): p. 2677-2685.
155. Zhu, J.X., et al., *Flexible, transferable and conformal egg albumen based resistive switching memory devices.* RSC Advances, 2017. **7**(51): p. 32114-32119.
156. Li, Y., et al., *Recent advances in organic-based materials for resistive memory applications.* InfoMat, 2020. **2**(6): p. 995-1033.
157. Sun, F., et al., *Flexible Artificial Sensory Systems Based on Neuromorphic Devices.* ACS Nano, 2021. **15**(3): p. 3875-3899.
158. Park, S.P., et al., *Analysis of the Bipolar Resistive Switching Behavior of a Biocompatible Glucose Film for Resistive Random Access Memory.* Adv Mater, 2018. **30**(26): p. e1800722.
159. Xu, J., et al., *Biodegradable Natural Pectin-Based Flexible Multilevel Resistive Switching Memory for Transient Electronics.* Small, 2019. **15**(4): p. 1803970.
160. Xu, Y., et al., *Memristive effect with non-zero-crossing current-voltage hysteresis behavior based on Ag doped Lophatherum gracile Brongn.* Current Applied Physics, 2020. **20**(4): p. 545-549.

161. Guo, B., et al., *A sustainable resistive switching memory device based on organic keratin extracted from hair.* RSC Advances, 2019. **9**(22): p. 12436-12440.
162. Jang, S.K., et al., *Harnessing Recombinant DnaJ Protein as Reversible Metal Chelator for a High-Performance Resistive Switching Device.* Chemistry of Materials, 2018. **30**(3): p. 781-788.
163. Lin, Q., et al., *Human hair keratin for physically transient resistive switching memory devices.* Journal of Materials Chemistry C, 2019. **7**(11): p. 3315-3321.
164. Wang, H., et al., *Sericin for Resistance Switching Device with Multilevel Nonvolatile Memory.* Advanced Materials, 2013. **25**(38): p. 5498-5503.
165. CHUA, L., V. SBITNEV, and H. KIM, *HODGKIN–HUXLEY AXON IS MADE OF MEMRISTORS.* International Journal of Bifurcation and Chaos, 2012. **22**(03): p. 1230011.
166. Kim, K., et al., *A carbon nanotube synapse with dynamic logic and learning.* Adv Mater, 2013. **25**(12): p. 1693-8.
167. Najem, J.S., et al., *Dynamical nonlinear memory capacitance in biomimetic membranes.* Nature Communications, 2019. **10**(1): p. 3239.
168. Basham, C., et al. *Memcapacitive Devices in Neuromorphic Circuits via Polymeric Biomimetic Membranes*. in *ASME 2019 Conference on Smart Materials, Adaptive Structures and Intelligent Systems*. 2019.
169. Balatti, S., et al., *Voltage-Controlled Cycling Endurance of HfOx-Based Resistive-Switching Memory.* IEEE Transactions on Electron Devices, 2015. **62**(10): p. 3365-3372.
170. Choi, J., et al., *Enhanced Endurance Organolead Halide Perovskite Resistive Switching Memories Operable under an Extremely Low Bending Radius.* ACS Applied Materials & Interfaces, 2017. **9**(36): p. 30764-30771.
171. Hamdioui, S., et al. *Memristor based computation-in-memory architecture for data-intensive applications*. in *2015 Design, Automation & Test in Europe Conference & Exhibition (DATE)*. 2015.
172. Xu, C., et al. *Design implications of memristor-based RRAM cross-point structures*. in *2011 Design, Automation & Test in Europe*. 2011.
173. Driscoll, T., et al., *Phase-transition driven memristive system.* Applied Physics Letters, 2009. **95**(4): p. 043503.

174. Liu, Q., et al., *Controllable Growth of Nanoscale Conductive Filaments in Solid-Electrolyte-Based ReRAM by Using a Metal Nanocrystal Covered Bottom Electrode.* ACS Nano, 2010. **4**(10): p. 6162-6168.
175. Chanthbouala, A., et al., *A ferroelectric memristor.* Nature Materials, 2012. **11**(10): p. 860-864.
176. Hai, L. and C. Yiran. *An overview of non-volatile memory technology and the implication for tools and architectures*. in *2009 Design, Automation & Test in Europe Conference & Exhibition*. 2009.
177. Xia, Q., et al., *Memristor−CMOS Hybrid Integrated Circuits for Reconfigurable Logic.* Nano Letters, 2009. **9**(10): p. 3640-3645.
178. Cong, J. and X. Bingjun. *mrFPGA: A novel FPGA architecture with memristor-based reconfiguration*. in *2011 IEEE/ACM International Symposium on Nanoscale Architectures*. 2011.
179. Lehtonen, E., J. Poikonen, and M. Laiho. *Implication logic synthesis methods for memristors*. in *2012 IEEE International Symposium on Circuits and Systems (ISCAS)*. 2012.
180. Vourkas, I. and G.C. Sirakoulis, *A Novel Design and Modeling Paradigm for Memristor-Based Crossbar Circuits.* IEEE Transactions on Nanotechnology, 2012. **11**(6): p. 1151-1159.
181. Shin, S., K. Kim, and S. Kang, *Memristor Applications for Programmable Analog ICs.* IEEE Transactions on Nanotechnology, 2011. **10**(2): p. 266-274.
182. MUTHUSWAMY, B., *IMPLEMENTING MEMRISTOR BASED CHAOTIC CIRCUITS.* International Journal of Bifurcation and Chaos, 2010. **20**(05): p. 1335-1350.
183. Kumar, S., J.P. Strachan, and R.S. Williams, *Chaotic dynamics in nanoscale NbO2 Mott memristors for analogue computing.* Nature, 2017. **548**(7667): p. 318-321.
184. Kumar, S., R.S. Williams, and Z. Wang, *Third-order nanocircuit elements for neuromorphic engineering.* Nature, 2020. **585**(7826): p. 518-523.
185. Joglekar, Y.N. and S.J. Wolf, *The elusive memristor: properties of basic electrical circuits.* European Journal of Physics, 2009. **30**(4): p. 661-675.

186. Afifi, A., A. Ayatollahi, and F. Raissi. *Implementation of biologically plausible spiking neural network models on the memristor crossbar-based CMOS/nano circuits*. in *2009 European Conference on Circuit Theory and Design*. 2009.
187. Kim, Y., et al., *A bioinspired flexible organic artificial afferent nerve.* Science, 2018. **360**(6392): p. 998.
188. Lee, Y., et al., *Stretchable organic optoelectronic sensorimotor synapse.* Science advances, 2018. **4**(11): p. eaat7387-eaat7387.
189. Wan, C., et al., *An Artificial Sensory Neuron with Tactile Perceptual Learning.* Advanced Materials, 2018. **30**(30): p. 1801291.
190. Zang, Y., et al., *A Dual-Organic-Transistor-Based Tactile-Perception System with Signal-Processing Functionality.* Advanced Materials, 2017. **29**(18): p. 1606088.
191. Merrikh-Bayat, F. and S.B. Shouraki, *Memristor-based circuits for performing basic arithmetic operations.* Procedia Computer Science, 2011. **3**: p. 128-132.
192. Merrikh-Bayat, F. and S.B. Shouraki, *Memristive Neuro-Fuzzy System.* IEEE Transactions on Cybernetics, 2013. **43**(1): p. 269-285.
193. Haas, J.S., C.M. Greenwald, and A.E. Pereda, *Activity-dependent plasticity of electrical synapses: increasing evidence for its presence and functional roles in the mammalian brain.* BMC cell biology, 2016. **17 Suppl 1**(Suppl 1): p. 14-14.
194. Haas, J.S., B. Zavala, and C.E. Landisman, *Activity-Dependent Long-Term Depression of Electrical Synapses.* Science, 2011. **334**(6054): p. 389.
195. Haas, J.S., *A new measure for the strength of electrical synapses.* Frontiers in cellular neuroscience, 2015. **9**: p. 378-378.
196. Pereda, Alberto E., *The Variable Strength of Electrical Synapses.* Neuron, 2016. **90**(5): p. 912-914.
197. Lin, W.-P., et al., *Polymer-Based Resistive Memory Materials and Devices.* Advanced Materials, 2014. **26**(4): p. 570-606.

CHAPTER II: Memristive plasticity in artificial electrical synapses via geometrically reconfigurable, gramicidin-doped biomembranes

Abstract

It is now known that mammalian brains leverage plasticity of both chemical and electrical synapses (ES) for collocating memory and processing. Unlike chemical synapses, ES join neurons via gap junction ion channels that permit fast, threshold-independent, and bidirectional ion transport. Like chemical synapses, ES exhibit activity-dependent plasticity, which modulates the ionic conductance between neurons and, thereby, enables adaptive synchronization of action potentials. Many types of adaptive computing devices that display discrete, threshold-dependent changes in conductance have been developed, yet far less effort has been devoted to emulating the continuously variable conductance and activity-dependent plasticity of ES. Here, we describe an artificial electrical synapse (AES) that exhibits voltage-dependent, analog changes in ionic conductance at biologically relevant voltages. AES plasticity is achieved at the nanoscale by linking dynamical geometrical changes of a host lipid bilayer to ion transport via gramicidin transmembrane ion channels. As a result, the AES uniquely mimics the composition, biophysical properties, bidirectional and threshold-independent ion transport and plasticity of ES. Through experiments and modeling, we classify our AES as a volatile memristor, where the voltage-controlled conductance is governed by reversible changes in membrane geometry and gramicidin channel density. Simulations show that AES plasticity can adaptively synchronize Hodgkin-Huxley neurons. Finally, by modulating the molecular constituents of the AES, we show that the amplitude, direction, and speed of conductance changes can be tuned. This work motivates the development and integration of ES-inspired computing devices for achieving more capable neuromorphic hardware.

Introduction

Two-terminal synaptic devices hold promise to store and process information at significantly lower energy cost than three-terminal devices[1-4]. By emulating threshold-dependent conductance changes and multi-timescale memory and plasticity found in their biological counterparts, artificial synapses could radically transform computing hardware by mimicking the way the brain learns, remembers, and processes information through activity-dependent plasticity [5]—originally believed to be present only in chemical synapses. Accordingly, research to develop synapse-inspired computing devices has produced material systems, including non-volatile memristors [6-

8] with hysteretic current-voltage relationships, that inherently mimic the discrete, threshold-dependent conductance switching used by chemical synapses.

In contrast, electrical synapses (ES) have long been thought to form fixed-conductance connections (modeled as fixed resistors) between neurons. However, it was recently reported that the magnitude of electrical coupling (i.e., proportional to synapse conductance) between neurons connected via electrical synapses can vary significantly through activity-dependent plasticity [9-11] to control the level of synchronization in neural networks. Similar to their chemical counterparts, ES exhibit multiple forms of plasticity (e.g., facilitation, depression) at timescales ranging from milliseconds to days [12]. For example, coupling between retinal photoreceptors can be very low in complete darkness or bright light and significantly elevated at moderate light intensities [13, 14]. This variation enhances the sensitivity of retinal circuits during transitioning between nighttime and daytime visual tasks.

ES are composed of gap junctions, aligned protein hemi-channels (e.g., connexins or innexins) contributed from adjacent cells [15, 16], that span the 2-4 nm gap between plasma membranes. These water-filled structures mechanically and electrically link neurons [17, 18] as illustrated in Figure 2.1A. Unlike the voltage-triggered release of neurotransmitters in chemical synapses, the pre-synaptic terminal of an electrical synapse does not have to cross a firing threshold to transmit an action potential [19]. Instead, ions diffuse passively through the always-open hemichannels to cells at lower potentials. The lack of a threshold enables quicker communication and sharing of action potentials. But, while always conductive, the conductance (i.e., coupling) of an electrical synapse is not static, but rather continuously variable. The coupling level between neurons is often measured as the ratio of voltages accumulated in both the pre- and postsynaptic neurons [20]. These dynamic variations in coupling levels instill modulation of both the temporal and spatial transmission of information exchange [21]. Mechanistically, electrical synapse plasticity can result from dynamic alterations of existing connexin conductance states [22-24], increases or decreases in number of connexin channels [25-27], and modification of passive and active membrane properties by synaptic inputs [28-31].

Undoubtedly, the superior cognitive ability of the brain stems from collective functionalities of networks of chemical and electrical synapses adapting and communicating together. However, brain-inspired materials and neuromorphic devices seeking to achieve signal processing, learning,

and memory capabilities of the brain have predominately focused on two- or three-terminal devices (e.g., memristors, transistors) with voltage-controlled, threshold-dependent changes in electrical/ionic conductance [2]. The vast majority of these systems exhibit sharp threshold-dependent switching [32, 33] between a small number of discrete conductance states [6, 33-38], thereby implicitly mimicking the functionalities of chemical synapses [39, 40]. On the other hand, the development of threshold-independent synaptic devices with activity-controlled, analog changes in conductance has received far less attention [41].

Here, we present an artificial electrical synapse (AES) constructed with a 5 nm-thick synthetic bio-membrane containing voltage-independent, pore-forming gramicidin peptides. Like biological ES, this assembly permits bidirectional ion transport via always-open channels and exhibits voltage-dependent memory resistance, with continuous conductance variations that occur across nominal ranges of 22-160 pS [16] and at biologically-relevant voltages. This contribution builds on our recent work [42], which demonstrated that insulating, lipid-only biomembranes formed between lipid-coated aqueous droplets in oil exhibit hysteretic, geometric reconfigurations stemming from voltage-driven modulation of membrane area and thickness. Introducing gramicidin peptides into the membrane creates always-conductive transmembrane ion channels similar to gap junctions—transforming the capacitive membrane into a memristive one that exhibits a pinched, hysteretic current-voltage relationship and displays short-term plasticity to successive voltage pulses. Experiments and modeling are performed to assess changes in membrane geometry and gramicidin channel densities in response to voltage and to explain the sources of resistance hysteresis and short-term plasticity. These allow us to show that the dynamic geometrical reconfigurations of the membrane dictate the rates of current-voltage hysteresis, even though the density of gramicidin channels also increases with applied voltage. Finally, we demonstrate through both experiments and modeling that the AES can be modularly configured to exhibit paired-pulse depression and that voltage-induced plasticity in conductance can synchronize the firing of Hodgkin-Huxley neurons.

Materials and methods

Materials. The aqueous droplets in each DIB-based AES consist of phospholipid vesicles, salt, and buffering agent in 99.99% pure deionized water. Sodium chloride (NaCl), 3-(N0morpholino) propanesulfonic acid (MOPS), sodium hydroxide (NaOH), agarose ($C_{12}H_{18}O_9$), *n*-hexadecane

(99% pure), *n*-decane (99%pure), ethanol, isopropyl alcohol was purchased from Sigma Aldrich. DPhPC, DOPC, and DOPhPC lipids are obtained from Avanti Polar Lipids, Inc and used without further purification. Lipid vesicles are prepared and stored at a concentration 2 mg/ml in aqueous buffer containing 500 mM NaCl, 10 mM MOPS at pH of 7.0 achieved via NaOH titration as described elsewhere [55]. Hydrogel (2% (w/v)) electrode coatings are prepared from agarose powder and the same buffer. A stock solution of gramicidin in ethanol (10 mg/mL) is diluted with the lipid vesicle solutions to yield the desired final concentration.

Methods for DIB formation. DIBs are formed between two, 300 nL aqueous droplets suspended agarose coated wire-type electrodes in an oil-filled reservoir as described elsewhere [71]. The oil reservoir and droplets are centered above a 4X objective lens on an Olympus IX50 inverted microscope. The positions of both electrodes are controlled by three-axis micromanipulators. A lipid bilayer forms spontaneously within a minute after bringing droplets into contact following a brief incubation period to ensure lipid monolayer assembly. Bottom-view images (Figure 2.1B) of DIB-based AES obtained using a QIClick-F-M-12-C (SN: Q31274) camera controlled by MicroManager software are used to estimate membrane area for computing specific capacitance and thickness. Based on the work by Taylor et al [55], a correction factor of 1.773 is used to account for membrane ellipticity due to sagging droplets.

Electrical Measurements. Current measurements are made using an Axopatch 200B patch clamp amplifier and Digidata 1440 data acquisition system (Molecular Devices). All recordings are made at room temperature with appropriate shielding using a well-grounded Faraday cage in place to minimize noise. Necessary input voltage waveforms are generated using Hewlett-Packard 3314A function generator and customized LabVIEW VI codes with NI four channel analogue output module (NI 9263). Outputs from these sources are input to the headstage of the Axopatch 200B through the external input to the amplifier. Confirmation of bilayer formation and measurements of nominal capacitance stems from the bilayer's current response to a 10 mV, 350 Hz triangular voltage waveform input as discussed earlier [55]. Sinusoidal cyclic voltammetry scans at various sweep rates are performed on the bilayer to generate the *I-V* relationships [72]. The pinched hysteretic loops presented in Figure 2.1 are obtained after filtering the residual capacitive current resulting from the lipid membrane as described elsewhere [73]. The short-term plasticity behavior is studied using rectangular voltage pulses at varying duty cycles.

Simulating the model. We numerically simulate the hysteretic responses and short-term plasticity of our AES and the variable synchronization of Hodgkin-Huxley neurons using the described model and measured parameters (e.g. Table 1) in MATLAB.

Results and discussions

A gramicidin-doped lipid membrane has similar structure and composition to biological ES. Inspired by the biomolecular memristor featuring voltage-activated alamethicin channels [43] and the capacitive, lipid-only biomolecular memcapacitor [42], the artificial electrical synapse (AES) studied herein represents a modular variation of those prior embodiments, one that is also based on a planar lipid bilayer membrane formed at the interface between two lipid-coated aqueous volumes in oil (also known as a droplet interface bilayer (DIB), see Experimental). Specifically, the ~5 nm-thick, insulating membrane is doped with gramicidin peptides that spontaneously insert [44, 45] in the absence of voltage into the membrane where monomers in each leaflet align end-to-end to form water-filled, conductive channels across the membrane. Illustrated in Figure 2.1B, this end-to-end alignment and the resulting ionic conductivity achieved with gramicidin channels closely mimic the structural configuration and voltage-independent transport properties of connexins in ES. Also, like gap-junctions in ES, this AES is always in a conductive (active) state.

Current-voltage relationships reveal memristive behavior. The hypothesis motivating this study is that the voltage-dependent geometric reconfigurations we observe in lipid-only membranes provides a lever for affecting the number of gramicidin channels in the membrane to instill activity-dependent plasticity found in ES. Therefore, to characterize these responses and reveal the effects of lipid and oil types, we measure the current, *I*, induced by a sinusoidal voltage, *V*, on gramicidin-doped membrane s constructed separately from two types of synthetic lipids (diphytanoyl phosphatidylcholine, DPhPC, and dioleoyl phosphatidylcholine, DOPC) that form stable lipid *I-V* responses for final gramicidin concentrations of 0.5 μM in each droplet are shown in Figure 2.1C-E, with the current normalized by the zero-volt membrane area to minimize effects of differing starting synapse areas. bilayers [46] and two different alkane oils (hexadecane, C16, and decane, C10) that result in varying sensitivities to voltage-drive changes in membrane area and thickness [42]. Representative

For all combinations, we measure pinched, hysteretic *I-V* loops at frequencies less than 50 mHz. Figure 2.1C shows that DOPC AES in C10 exhibit stronger nonlinearity and larger hysteresis when

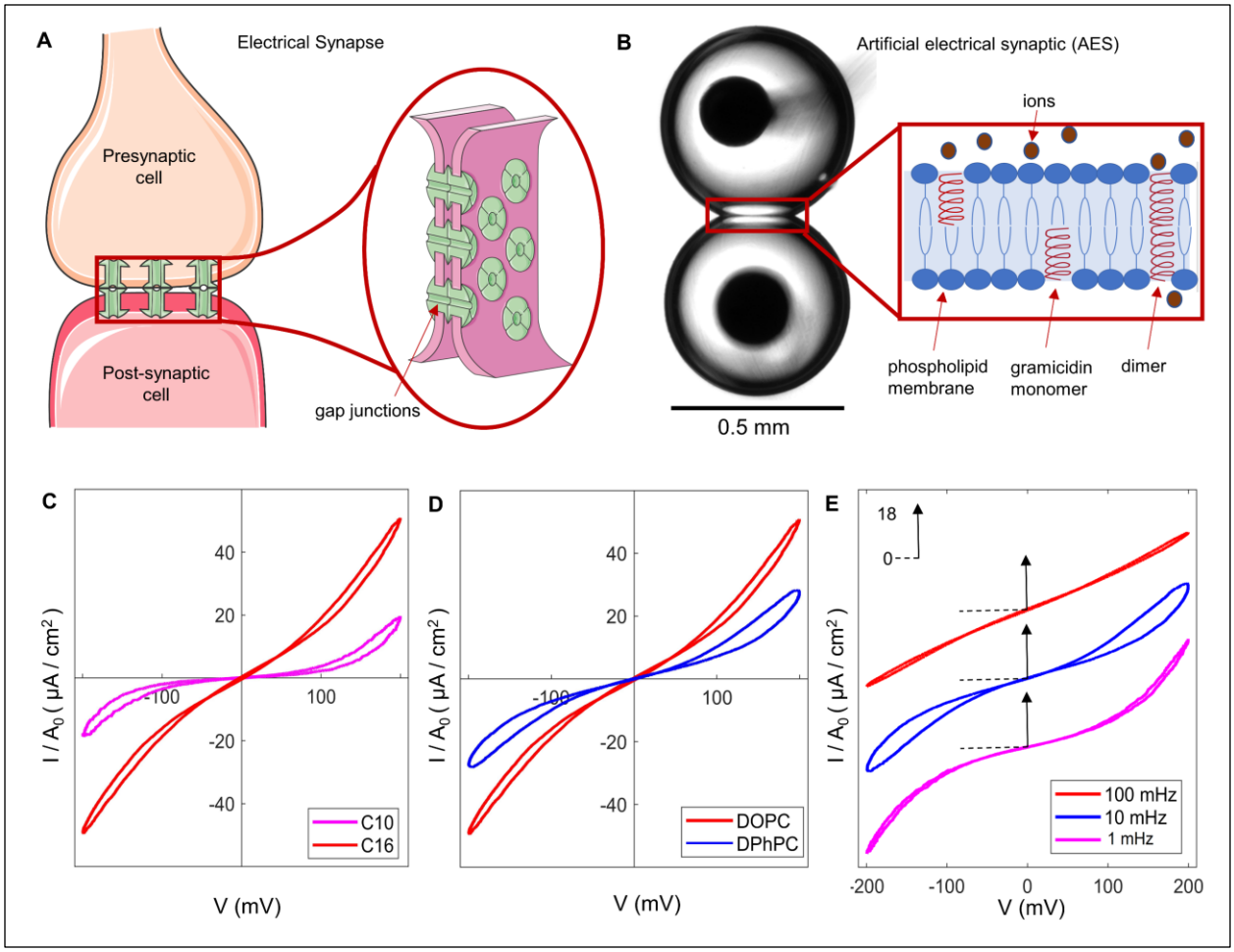


Figure 2.1. Two terminal AES exhibiting nonlinear memristive behavior. (A) Cartoon depicting ES gap junctions formed by connexin hemi-channels. (B) Biomolecular AES with gramicidin monomers dimerizing end-to-end to form channels for ion passage (inset) through the membrane. I-V relationships for: (C) DOPC AES assembled in two different oils: hexadecane (red) and decane (magenta); (D) AES formed in hexadecane from either DOPC or DPhPC lipids; and (E) DPhPC AES in hexadecane. All currents are normalized per zero-volt initial area, A_0. Applied bias consisted of a 200-mV bipolar sinusoidal voltage at 10 mHz, unless stated otherwise.

compared to hexadecane. Moreover, the instantaneous slopes of these data show that the DOPC AES in C10 exhibits relatively higher ohmic resistance (86 kΩ-cm^2) near 0 V (flatter) and lower resistance (12 kΩ-cm^2) near |200 mV| (steeper). In C16, both DOPC AES and DPhPC AES exhibit less variation in resistance versus voltage: 10 kΩ-cm^2 and 17 kΩ-cm^2 near 0 V, respectively, to 6.6 kΩ-cm^2 and 9 kΩ-cm^2 near 200 mV, respectively. In comparison, lipid-only membranes lacking gramicidin exhibit significantly higher resistances of 10-100 MΩ-cm^2 and do not exhibit *I-V* hysteresis at frequencies below 50 mHz (see Figure 2.7). Since the conductance of a gramicidin channel is relatively constant (5.8 pS) [47, 48], this suggests the number of gramicidin channels per unit area in DOPC AES in C10 is less than in a DOPC AES in C16.

Figure 2.1D compares the responses of AES formed from the two different lipids types (DPhPC and DOPC) in C16. Here, we see that a DOPC AES displays less *I-V* hysteresis and higher conductance, signifying a higher gramicidin channel density than in DPhPC. This difference is consistent with and can explained by prior research which demonstrated that gramicidin channels have higher affinity for [49] and greater stability (i.e., channel lifetime) [50] in DOPC membranes compared to DPhPC bilayers.

These measurements also reveal the frequency of the applied voltage sweep affects shape and hysteresis of the *I-V* relationship. The representative data in Figure 2.1E for a DPhPC AES in C16 show that the *I-V* response is most nonlinear at the lowest frequency (1 mHz) and the most linear at 100 mHz. These data also show that hysteresis is minimal at both the lowest and highest frequencies tested and significantly greater at the middle frequency of 10 mHz. While not shown, the same trend is observed for membrane-based AES constructed with DOPC or using decane. The disappearance of hysteresis at very low frequencies demonstrates that resistive hysteresis in the AES is volatile.

Moreover, unlike our prior study [43] using alamethicin-doped membranes that exhibited strong voltage-dependent increases in conductance and high nominal OFF resistances (>1 GΩ, when channels fully exited the membrane), these data show that gramicidin membranes are always conductive (≤ 86 kΩ), even at low voltages—just like ES. These trends remain across gramicidin concentrations (see Figure 2.8), which merely scales the number of channels in the interface, proportionally increasing the conductance of the membrane.

Chua established that the fingerprint of a memristor is a pinched hysteresis loop on an *I-V* plane at certain frequencies and initial conditions when subjected to a voltage or current signal producing a periodic response of similar frequency [3, 51-53]. Therefore, the results in Figure 2.1 prove that a gramicidin-doped AES is a volatile memristor, one in which the *I-V* shape, hysteresis, and frequency range of memristance can be tuned based on membrane composition and also the oil type surrounding the droplets. In the context to synaptic plasticity, the hysteresis implies that the conductance of the membrane depends on its prior history of excitation, not just the present stimulus. And unlike the pinched, hysteretic *I-V* responses measured previously using alamethicin-doped membranes that exhibited exponential increases in current only at voltages above an insertion threshold for the peptides, these AES do not require a specific threshold to become conductive. The modulations in AES resistance are also continuously variable, unlike most solid-state memristors that demonstrate discrete switching [54].

*Modelling gramicidin-doped membrane AES***.** As depicted in Figure 2.1C-E, gramicidin-doped membranes exhibit pinched and hysteretic current induced by a symmetric sinusoidal bias. Since the passage of ions is mediated by gramicidin dimers in the bilayer, these measurements indicate that nominal conductance of the membrane and thus the total number of dimers present depends on both voltage and time.

We know that the membrane elastically reconfigures in response to a nonzero membrane voltage [42, 55] . These reversible changes occur with time constants on the order of seconds and can result from formation of new membrane area due to electrowetting (EW) and a reduction in hydrophobic thickness caused by electrocompression (EC). While not explicitly linked, these geometrically changes are implicitly coupled by the fact that changes in membrane thickness modifies the effective forces driving both EW and EC [42]. The fact that our data show larger currents upon a decrease in voltage from some maximum value compared to an increase in magnitude of voltage from zero is consistent with the idea that a recent increase in membrane are driven by EW and a decrease in membrane thickness from EC could help to increase the total number of gramicidin dimers present in the interface. Another possibility is that the kinetics of gramicidin insertion, and thus the net number of channels present at equilibrium, are themselves functions of voltage (or membrane thickness) as is common in many other types of ion channels.

To properly identify and separate these mechanisms driving voltage-induced plasticity, we perform a series of experiments to quantify the dynamic changes in membrane geometry (area and thickness) and area-normalized channel density as a function of voltage. The dynamics and sensitivities of these variables are assessed by applying stepwise voltages. Membrane area is tracked via bottom view images of the AES, and membrane capacitance is determined from the amplitude of ac current induced by a superimposed ac voltage [42, 56].

Figure 2A shows a representative measurement of dynamic membrane area normalized to its zero-volt initial value, A_0, for a 200 mV, 10 mHz sinusoidal bias. The hysteresis observed here suggests that voltage-driven variations in channel density are not alone in causing the observed *I-V* hysteresis. Similar to the responses in Figure 2.1E, dynamical variations and hysteresis become very small at frequencies higher than 100 mHz (Figure 2.2A). And while hysteresis disappears at frequencies below 1 mHz (not shown), nonlinear quasi-static changes with respect to voltage become maximal at low frequencies [42].

Stepwise changes (0 to +200 mV) in voltage yield exponential rises in area (Figure 2.9), which we used to determine the characteristic time constant for EW, τ_{ew}, for the two lipids and oils (Table 1). These results indicate that EW-induced growth in membrane area is faster for DOPC lipids compared to DPhPC, and for C10 compared with C16. The former is likely the result of greater lipid acyl chain flexibility and mobility that enables faster oil exclusion and rearrangement upon bilayer formation [57], while the latter is the result of lower viscosity in C10 [42]. At equilibrium, bilayer area increases linearly with respect to the square of voltage (i.e. polarity does not matter) [55, 56, 58] , where the slope, α, denotes the EW coefficient. The data in Figure 2.2B and the average α values in Table 2.1 show that DOPC membranes in both C10 and C16 exhibit larger fractional changes in area with voltage compared to DPhPC membranes. Further, DOPC membranes formed with droplets in C16 exhibit a slightly higher area change than those formed with droplets submerged in C10. These differences are likely the result of DOPC membranes having higher monolayer and bilayer tensions and, thus, smaller zero-volt areas, which we show in Figure 2.10 results in larger fractional increases in bilayer area with voltage.

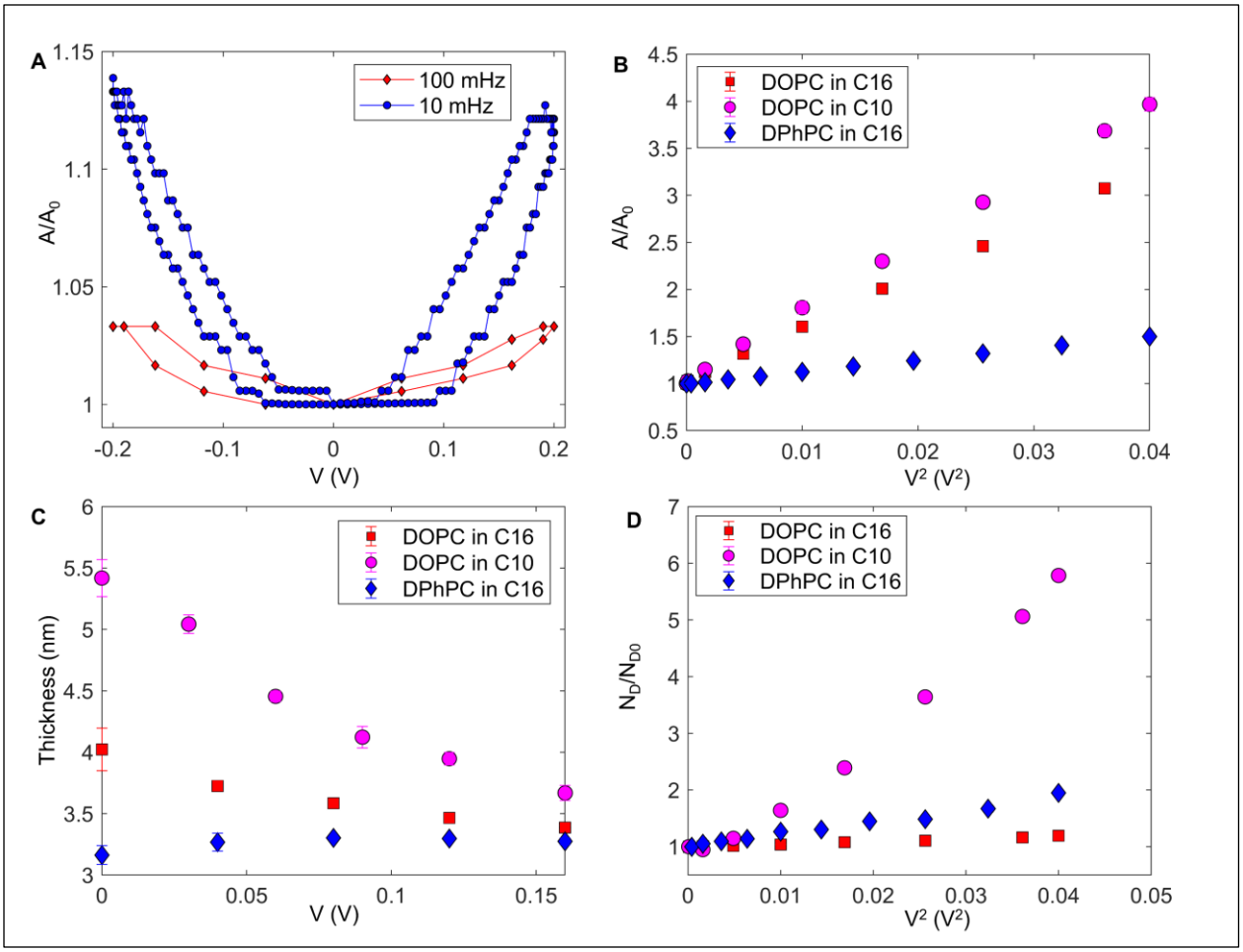


Figure 2.2. Characterization of the state variables at steady-state EW and EC conditions based of EW and EC time constants respectively. (A) Hysteretic geometric reconfiguration of the membrane interface when stimulated with a sinusoidal input bias voltage of 200 mV at different sweep rates, evaluated as mean of three (steady-state EW) cycles. (B) Response of the normalized area over initial area (at 0 mV) to step increase of bias voltage. (C) Relative thinning of the bio-membrane due to Electro-compression for different lipids in different oils in response to step increase in bias voltages. (D) Relative Channel density (normalized over 0 mV conditions) at the membrane interface for different lipid types in different oil environments.

Table 2.1: Summary of EW, EC, and gramicidin channel density dependencies on voltage.

Membrane/Oil	EW area growth		EC thinning	Channel Density ($\times 10^6$)
	τ_{ew} (s)	α (V^{-2})	τ_{ec} (s)	
DPhPC/C16	14.0 ± 0.3 (n=5)	12.4 ± 0.5 (n=4)	N/A	$N_d(V) = 220V^2 + 10$
DOPC/C16	5.9 ± 0.3 (n=5)	56.5 ± 0.5 (n=4)	40 ± 0.7 (n=3)	$N_d(V) = 220V^2 + 17$
DOPC/C10	1.8 ± 0.2 (n=3)	75.3 ± 0.2 (n=4)	22.3 ± 0.5 (n=3)	$N_d(V) = 300V^2 + 2$

We also assess changes in the hydrophobic thickness of these membrane AES by measuring the specific capacitance of the membrane versus bias using a method described elsewhere [56, 59]. Figure 2.2C shows that gramicidin-doped DPhPC membranes in C16 exhibit relatively constant membrane thickness versus voltage up to |160mV|, whereas gramicidin-decorated DOPC membranes in both C10 and C16 become significantly thinner (15% and 30%, respectively) at higher biases. In the absence of gramicidin, DOPC membranes are also relatively thicker at zero volts, which is attributed to greater oil retention in the hydrophobic region of the membrane upon bilayer formation compared with DPhPC as shown for lipid-only membranes in Figure 2.11. The larger initial thickness and steeper reduction in thickness with voltage for C10 is due to the fact that smaller molecule oils are retained in larger fractions in lipid bilayers [42, 60]. These trends, along with the fact that no significant change in thickness is recorded for DPhPC membranes containing <10% C16 by volume [42, 56], suggest that EC alters the thickness by compressive oil exclusion, not distortion or compression of the lipid molecules themselves [42]. While not shown, we have previously demonstrated that this mechanism for thickness reduction occurs on time scales of 5-25 s, slower than changes in area by EW [42].

The conducting unit in our system consists of a dimer (D) formed by two gramicidin monomers (M), aligned end-to-end across the thickness of the membrane [61-63]. Dimerization can be written as a reversible reaction given by,

$$M + M \rightleftharpoons D, \tag{1}$$

with separate forward and reverse reaction rate constants, k_R and k_D, respectively, that depend on membrane composition, temperature, ion concentration, etc. [44]. The accumulation of dimers (per unit area) in the system is thus given by:

$$\frac{dN_D}{dt} = k_R {N_M}^2 - k_D N_D. \tag{2}$$

Assuming the total concentration (mol/cm^2) of gramicidin in the interface is conserved ($N = N_M + 2N_D$), the population of gramicidin in each leaflet of the bilayer reaches an equilibrium of non-conducting (M) and conducting (D) units at fixed conditions.

Gramicidin channel formation does not require voltage, however prior research has established that k_R and k_D do vary with voltage. As a result, changing the voltage causes a transient reorganization of M and D to establish a new equilibrium in the system, where the time constant

of this transient depends on the nominal values of k_R and k_D. Specifically, the fraction of conductive channels in a membrane increases with decreasing membrane thickness [64]—signifying that k_R increases with voltage [44]. Because k_D also decreases with increasing voltage [44], the speed of dimer formation (dN_D/dt) also increases at higher applied biases and at high peptide concentrations. With C16 (i.e., constant thickness), and at the relatively high peptide concentrations used in our study, channels insert in the absence of voltage and reach equilibrium at all fixed voltage levels in less than 5 ms (Figure 2.12). This is considerably faster than the kinetics observed by Bamberg and Läuger, in which a peptide concentration of only 2 nM was used [44].

These trends, along with the thinning responses in Figure 2.2C, are consistent with the likelihood that an increase of the applied voltage in our system favors a higher density of channels in the membrane, and thus higher conductivity. To confirm and quantify this relationship, we measure the nominal current at equilibrium through our gramicidin doped membranes at multiple potentials. Dividing the current by the product of the applied potential, *V*, the unit conductance of one dimer, G_u, and the equilibrium area of the membrane at each voltage allows us to compute the channel density per unit area versus voltage (see Figure 2.2D and Figure 2.8). Here, we see that channel density increases linearly with respect to voltage squared and that a DOPC membrane in decane exhibits a larger fractional increase in channel density compared to either DOPC or DPhPC bilayers in C16. This finding is consistent with the fact that DOPC membranes in C10 retain more oil and, thus, exhibit greater fractional decreases in thickness with increasing voltage. The nominal data in Figure 2.8 also highlight the higher number of dimers in DOPC bilayers versus DPhPC and the higher number of channels in DOPC for C16 versus C10. The former is consistent with prior work [49, 50] which demonstrated a higher affinity of gramicidin with unsaturated DOPC lipids compared to DPhPC lipids, while the latter agrees with results by Hladky and Haydon which demonstrated that thinner membranes yield higher association rate constants and more dimers at equilibrium [47].

Based on these data, it is clear that both voltage-driven growth (fractional) in membrane area, A_m, and channel density, N_D, are the two states that influence the total nominal conductance, G, of the membrane as given by:

$$I = G(N_D, A_m)V. \tag{3}$$

Without a direct relationship between thickness and channel density, we perform linear regressions on the equilibrium channel density data provided in Figure 2.12 and use these steady-state empirical expressions to identify the initial channel densities at 0 mV, N_{D0}, and voltage dependences, m, as given by:

$$N_D(V) = N_{D0}(mV^2 + 1) \tag{4}$$

Because the channels exhibit nearly instantaneous responses to changes in voltage (and thickness) (Figure 2.12), the time constant for electrocompressive thinning ($O \sim s$), τ_{ec}, dictates the speed by which changes in channel density occur as a result of voltage-induced reductions in thickness. This allows us to write an empirical first order differential equation of the form:

$$\frac{dN_D}{dt} = \frac{1}{\tau_{ec}}(N_{D0}(mV^2 + 1) - N_D) \tag{5}$$

to describe the dynamic changes in N_D. For DPhPC bilayers in hexadecane which do not undergo EC, Equation 4 is used to define channel density at all points in time. Similarly, values of α and τ_{ew} (Table 1) are used as before [65] to describe the dynamic fractional area growth versus voltage, given by:

$$\frac{dA_m}{dt} = \frac{1}{\tau_{ew}}\left(\alpha v^2 - A_m(t)\right). \tag{6}$$

Given that the total number of channels in the membrane is the product of nominal membrane area, $A = A_0(1 + A_m)$ and N_D, and the unit conductance of each channel is G_u, the nominal conductance is written as

$$G(V,t) = G_u \times N_D(V,t) \times A_0(1 + A_m(V,t)) \tag{7}$$

where A_0 is the area of the interface at zero bias. Using Equations 4-7 and values in Table 1, we simulate dynamic changes in channel density and membrane area in response to a sinusoidal voltage and use these to compute the total current. Figure 2.3A shows the changes in N_D and A_m versus time for a DPhPC AES formed in C16 subjected to a 10 mHz, 200 mV sinusoidal voltage. Without significant changes in thickness, the voltage induced changes in channel densities occur nearly instantaneously, which causes the dynamic response to remain in phase with the applied voltage. EW-driven changes in membrane area occur more slowly (~14 s), resulting in a noticeable time lag behind the applied potential and causing a dc shift of ~+25%. At steady state, the amplitudes of normalized channel density and membrane area are 90% and ~20%, respectively.

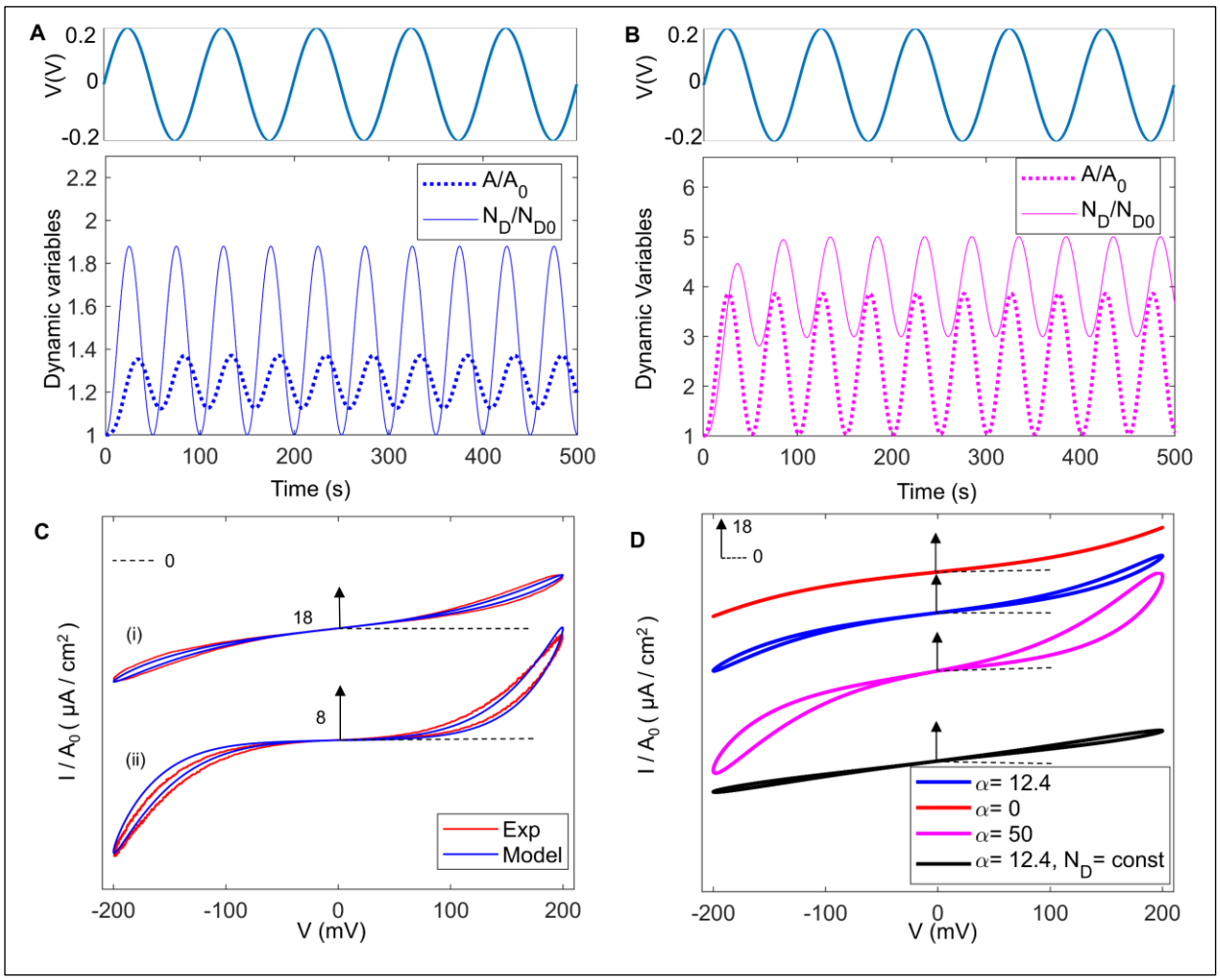


Figure 2.3. Simulated dynamic responses of AES. Membrane area and channel density using EW and EC parameters for a DPhPC membrane in C16 (A) and DOPC in C10 (B), respectively, in response to 200 mV, 10 mHz sinusoidal voltage (top). Simulated I-V relationships for: (C) (i) DPhPC AES in C16, and (ii) DOPC AES in C10; and (D) DPhPC AES in C16 at various electrowetting conditions with dynamic channel density. The black trace in (D) predicts the response of the device at a constant channel density. Vertical scales denoted using arrow length and value. All currents are normalized per zero-volt initial area, A_0. Applied bias consisted of a 200-mV bipolar sinusoidal voltage at 10 mHz, unless stated.

But for AES that undergo significant thinning with increased voltage (e.g., a DOPC AES in C10), changes in N_D are slower than those in A as seen in Figure 2.3B. Note that this occurs because the rate of thinning limits the speed of gramicidin insertion in the membrane. Figure 2.3C and Fig 2.14 show the simulated nominal current versus voltage and time, respectively, at steady state for the same sinusoidal voltage input. Here, we see the models accurately capture the nonlinear changes in synaptic conductance that affect the induced current.

In Figure 2.3D, we simulate the *I-V* response of a DPhPC AES in C16 at 10mV for varying α values to investigate the sources of nonlinearity and hysteresis. By setting α to zero (i.e., area is fixed), hysteresis vanishes and the nonlinear increase in current is explained by the instantaneous growth in channel density with voltage. Increasing α to a value of 50 amplifies both the total change in current and the hysteresis during a voltage. Further, keeping α at the measured value of 12.4 and setting N_D to be constant yields in a nearly linear *I-V* relationship with only a small amount of hysteresis. In contrast, the larger, slow increases in N_D for DOPC AES add additional *I-V* hysteresis and nonlinearity due to time-varying channel densities independent of the membrane area.

*Short-term facilitation and depression in AES***.** Activity-dependent short-term plasticity (STP) enables synapses to adjust their conductance strength in ways that either facilitate (strengthen) or depress (weaken) the activity of the post-synaptic neuron. The *I-V* hysteresis demonstrated in Figure 2.2 shows that at specific frequencies the AES exhibits a conductance that is dependent both on the present value and prior history of applied voltage. Because these hysteresis loops disappear at very low frequencies, the system can be classified as a volatile memristor for which the alterations in conductance return to an equilibrium level upon removal of the excitation. The prior section demonstrates that for gramicidin-doped bilayers with symmetric lipid compositions these alterations occur due to reversible increases in both area and channel density, processes that occur at characteristic time scales governed by the dynamics of EW and EC, respectively.

Plasticity of synaptic elements is commonly assessed by recording the responses to multiple, successive voltage excitations [66]. Therefore, we stimulate our AES with a train of positive, rectangular voltage pulses and study the dynamic current responses. As compared in Figure 2.4A, we consider gramicidin-doped AES membranes that have either symmetric and asymmetric lipid compositions—the latter, which we have previously shown can be used to

enable asymmetric EW responses with respect to 0 mV [42]. Specifically, we compare the behaviors of a symmetric DOPC bilayer in decane to an asymmetric membrane consisting of one DOPC leaflet and one leaflet containing a 1:1 molar mixture of DOPC and 1,2-di-O-phytanoyl-sn-glycero-phosphocholine (DOPhPC)—a combination that exhibits an intrinsic dipole potential difference of -85 mV. Unlike a symmetric membrane that exhibits zero intrinsic potential, the net potential across an asymmetric membrane is the sum of the applied voltage and the intrinsic potential [42]. This means that EW and EC are minimized when the applied potential is equal and opposite to the intrinsic potential, not at zero. Thus, the asymmetric membrane is larger in area and thinner at 0 mV than when +85 mV is applied. Here, we hypothesize that a voltage-dependent reduction in area and increase in thickness can be used to lessen the number of conductive channels in the membrane, thereby creating a depressive form of short-term plasticity.

Figure 2.4B shows the raw ohmic current measured across a symmetric gramicidin doped DOPC membrane in response to +150 mV, 50 ms ON pulses followed by 0 mV OFF periods. For the first 10 s when the OFF time is 1 ms (95.2% duty cycle, V_{RMS} = 95 mV), the peak current during ON times (normalized by the zero-voltage area) increases exponentially across many pulses with a time constant of 1.75 s. This type of facilitative short-term plasticity is consistent with the time for gramicidin channels/bilayer area to increase in response to a non-zero RMS voltage. With sufficient preceding rise in synaptic conductance, a change in the OFF time of the pulses to 50 ms (28.5% duty cycle, V_{RMS} = 29 mV) causes the membrane to gradually become less conductive as indicated by the reduction in ohmic current in Figure 2.4B after 10 s. This depressing response occurs as the area of the membrane drops, the thickness increases, and the channel density lowers a smaller positive RMS voltage. However, the fact that the steady-state peak current for 50 ms OFF times is still higher than the initial value prior to pulse train excitation means that if only this stimulus were provided instead, a symmetric membrane will not exhibit depressive STP without sufficient facilitative STP first occurring.

Yet, depression in electrical synapses is more common [10, 67], a trait that enables modulation of electrical coupling [67], regulates response to the sensory surround and arousal states [10]. Figure 2.4C shows the peak ohmic current versus time for an asymmetric DOPC: DOPC+DOPhPC membrane containing gramicidin at three different positive V_{RMS} levels

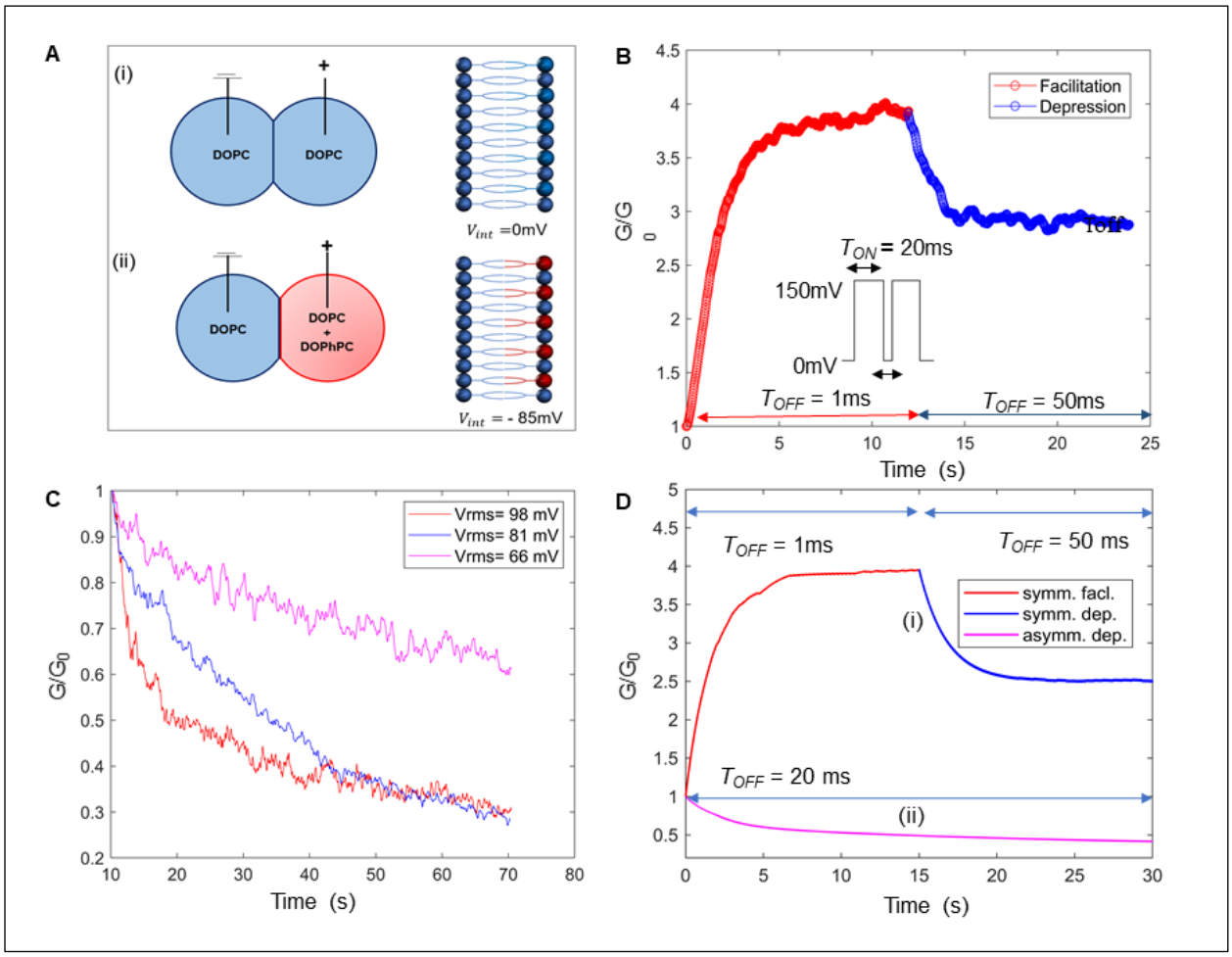


Figure 2.4. Short term plasticity in symmetric and asymmetric AES. (A) Cartoon depicting symmetric and asymmetric assembly of droplets and the interfacial membrane. (B) Accumulation and depression of current per unit area of the membrane (facilitation and depression) for varying T_{OFF} values. (C) Depression of conductance of the device even with increased stimuli (voltage input) because of reverse electrowetting stemming from dipole potential difference of asymmetric droplets. (D) Simulation of short-term facilitation and depression in symmetric (blue lines) and asymmetric AES (magenta line).

(varying duty cycle, equal amplitude). Representative *I-V* measurements for an asymmetric AES are provided in Figure 2.15. Here unlike the response in Figure 2.4B, we observe that current only decreases upon

application of a positive voltage. This occurs because the net membrane potential drops when voltage increases from 0 mV to +100 mV. The amount of decrease varies with the RMS value, which is consistent with the idea that the membrane becomes least conductive (see Figure 2.15) when the area is small, and the thickness is large which occurs at zero net potential. Quasi-static analysis (Figure 2.16) confirms that the interfacial area of an asymmetric AES responds to the transmembrane potential difference. However, we also observe the channel density to exhibit stronger increases with voltage at negative applied potentials, where the net membrane potential is larger, compared to positive stimuli. This effect is likely a combination of channel kinetics changing with the applied potential and the thickness of the membrane varying with respect to net membrane potential.

Figure 2.4D (i) and (ii) show simulated peak currents for symmetric and asymmetric AES subjected to unipolar square pulse inputs (150 mV, 20 ms ON, 0 mV, variable duration T_{OFF}). These trends bear close resemblance to the measured behaviors of symmetric and asymmetric AES devices as seen in Figure 2.4B-C. For the asymmetric system, the voltage dependent channel density equation (Equation 5) and electrowetting equation (Equation 6) are modified to accommodate a net bias input of $v = v_{appl} + v_{int}$.

AES enable variable synchronization of neurons. Electrical synapses synchronize the activities of many neurons [68, 69] by allowing fast, threshold-independent sharing of action potentials and ionic gradients. The AES presented in this paper share several traits in common with ES, including a variable conductance that occurs at biologically relevant levels of voltage and which spans nominal conductance ranges similar to ES. Therefore, to demonstrate that our voltage-dependent AES can synchronize neurons, we employ our model of AES conductance and simulate in MATLAB the responses of two Hodgkin-Huxley (H-H) neurons [70] connected by our adaptive AES (illustrated in Figure 2.5A). The variable resistances in the neurons represent the voltage-gated sodium and potassium channels in addition to leakage pathways. The neuron on the left is stimulated with a dc current density of 10 μA/cm^2, a level which is sufficient to elicit repeated oscillations. This injection charges neuron 1, whereby at a sufficient voltage the sodium channels

open in neuron 1, causing rapid depolarization of the cell. Then, at sufficiently positive voltage, potassium channels open, hyperpolarizing the cell and resetting the voltage. This nonlinear, oscillatory response creates an action potential with a spiking period of 15 ms. By connecting two neurons with a threshold-independent AES, some of the injected current can also enter neuron 2, where it can similarly charge and fire. The amount of current through the AES depends on its conductance, which in this application is modulated by the relative neuron voltages, V_1 and V_2. For these simulations, we use the parameters defined in Supplementary Table 1 for a gramicidin doped DOPC membrane in C10. The voltage-dependent membrane capacitance of the AES (C_m = 0.496 μF/cm^2) is also included in the calculation, and we assume the active areas of the neuron and synapse (zero-volt area) are equal to the DIB area (3.3 x 10^{-4} cm^2) observed in experiments.

Figure 2.5B shows the simulated voltages of both neurons versus time; Figures 5C-D show the computed nominal resistance of the AES and the spiking ratios (spike count of neuron 2 to that of neuron 1) and time lag between adjacent spikes, respectively. The simulation shows that only neuron 1 produces an action potential (Figure 2.5B (i)). The initial AES resistance (~80 MΩ) limits charging of neuron 2, resulting in only sub-threshold oscillations with amplitudes of 6-8% of V_1. This response shows that initially neuron 2 is completely desynchronized from action potentials from neuron 1.

However, over time the difference in neuron voltages (38 mV RMS) lowers the resistance of the AES to reduce to ~34 MΩ via bilayer area growth and increased channel density (Fig 2.17). Neuron 2 begins generating action potentials when the AES resistance falls below 74 MΩ. This voltage-dependent adaptation allows increasingly more current to enter neuron 2 and further increases the rate of action potential generation. Figure 2.5B (ii-iv) show this adaptation; here we see neuron 2 exhibiting action potentials with increasing frequency over time (total simulation time is 100 s to capture the full adaptation of the AES). The spiking ratio increases incrementally during this time, where after approximately 67 s, when the AES resistance drops below ~40 MΩ, every action potential by neuron 1 coincides with one from neuron 2. While synchronized in frequency at this point, action potentials from neuron 2 still lag by ~2 ms those from neuron 1. This time lag decreases non-monotonically during the AES adaptation; specifically, it appears to decrease exponentially in time for each period of constant spiking ratios. An electrical synapse mimic for synchronizing spiking neurons—e.g., for use in artificial neural networks—has real advantages

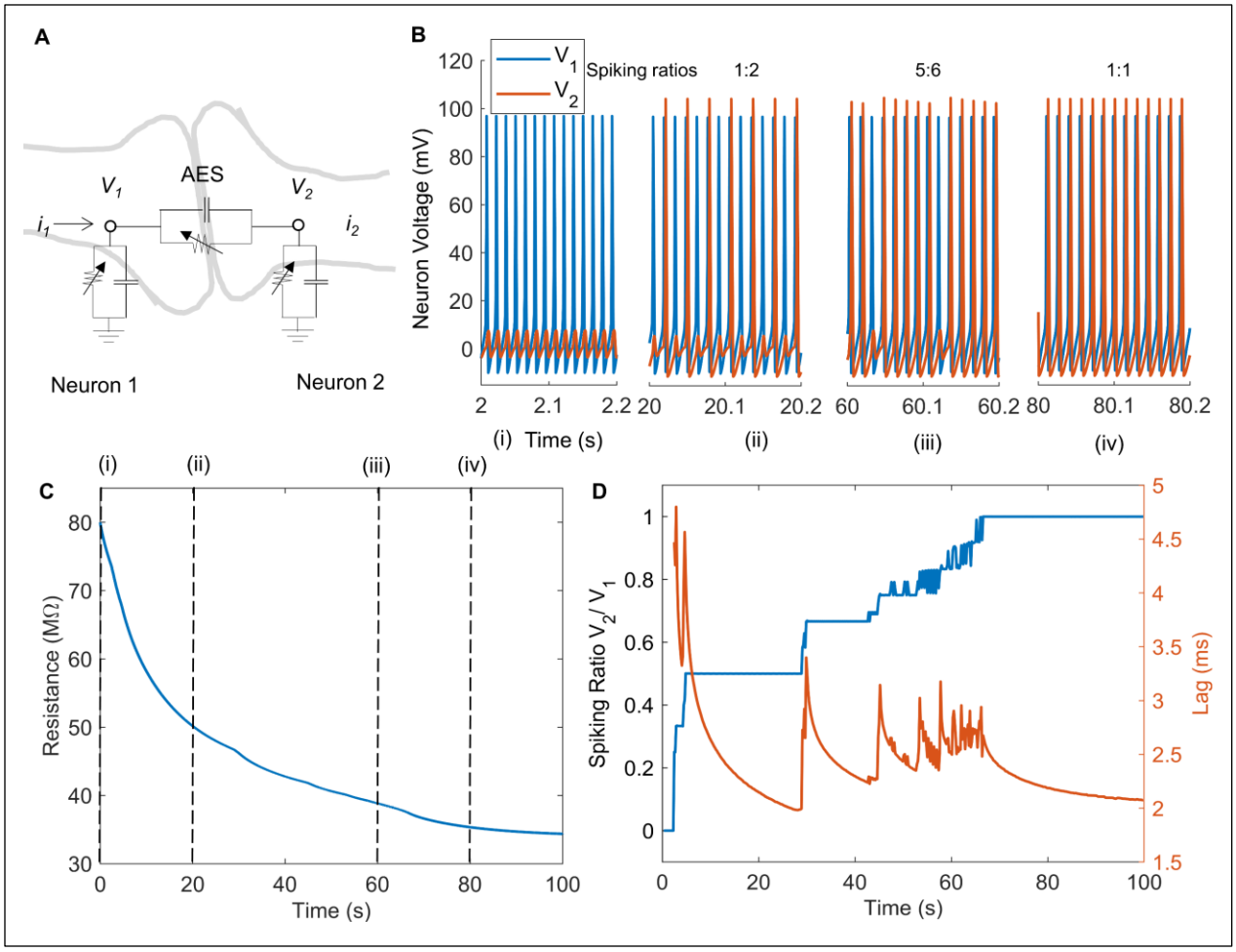


Figure 2.5. HH neuron synchronization through AES plasticity. (A) Illustration of two HH neurons joined by an AES. (B) Simulated neuron voltages versus time in response to a constant injected current into Neuron 1. (C) AES resistance versus time during adaption. (D) Neuron voltage spiking ratios and lag time between neuron spikes versus time.

compared to devices mimicking the one-direction, threshold dependent variable conductance of a chemical synapse. The bidirectional conductance of the AES means that if neuron 2 were stimulated with current instead, neuron 1 could become synchronized. Additionally, the lack of a voltage-threshold for ion channel formation allows ions to quickly pass through the AES to charge and fire neuron 2 with minimal lag. In contrast, a memristive synaptic mimic constructed using alamethicin [65] exhibits much slower channel insertion kinetics, which would prevent successful synchronization of the two neurons. The simulation shows how the voltage-dependent plasticity of an AES can be used to adaptively couple spiking neurons, and the conditions for the calculations require some tuning to demonstrate this

functionality. Specifically, initial channel density, N_{D0}, and the voltage dependency, m, of the synapse are set to 6.5 x 10^6 and 2 x 10^9, respectively, to ensure that the device exhibited an initial resistance of 80 MΩ and a large reduction in resistance at RMS voltages below 50 mV. In contrast, smaller values of N_{D0} and m (such as those in Table 1) result in a highly resistive junction that does not sufficiently reduce to cause firing in neuron 2. Nonetheless, the parameters used closely match experimentally obtained values on a symmetric DOPC membrane in C10 by mechanically reducing the membrane area after bilayer formation (see Supplementary Table S1 for measured values and Figure 2.10 for effect of membrane area on electrowetting sensitivity). In contrast, while an asymmetric AES displays short-term depression under a sufficiently large positive potential (see Figure 2.4C in the manuscript), the same device is unable to desynchronize H-H neurons because the average voltage across a highly conductive AES (required to synchronize neurons) is insufficient for appreciably changing AES. Figures 2.18 summarizes the response of an initially conductive AES placed between two Hodgkin-Huxley neurons.

In our simulation, the ratio of neuron area to synapse area is a parameter that strongly impacts the amount of nominal current flowing through the AES. This is based on the fact that Hodgkin-Huxley equations are normalized per area of the neuron membrane. Therefore, when the active area of the neuron is larger than that of the synapse, the synapse is considerably less conductive than the neurons. This change means that even less current passes through the AES, lowering the rate of firing of neuron 2. Less current through the AES also causes the V_{RMS} difference between the neurons to shrink to 27 mV, which subsequently results in a smaller voltage-induced plasticity. Furthermore, higher neuron conductance means even larger reductions in AES resistance from the

same initial value (80 MΩ) are needed to fully synchronize the two neurons. For example, increasing the area ratio to just 10 raises the final synapse resistance to 50 MΩ, a value that now only results in sub-threshold voltage oscillations in neuron 2. This demonstrates that effectively matching the impedances of the neurons and the adjoining synapse is important for making use of voltage-activity plasticity in hardware-based neural circuits.

Conclusion

We present a threshold-independent, artificial electrical synapse that exhibits volatile memristance and which mimics the composition, structure, and transport properties of an electrical synapse found in the mammalian brain. Our unique, two-terminal AES consists of a lipid bilayer membrane doped with gramicidin peptides that form conductive ion channels through the lipid bilayer. Like connexins in ES, these channels feature an end-to-end connection across both leaflets of the membrane and do not require a threshold-voltage to conduct ions. The current-voltage relationships of gramicidin-based AES exhibit pinched hysteresis at excitation frequencies between 10-100 mHz. Experiments reveal that the volatile memristive device is affected by two voltage-dependent state variables: the gramicidin channel concentration per unit area and membrane area, the product of which dictate the total number of channels in the AES and, thus the conductance of the device. In addition, the current-voltage relationships show that combinations of peptide concentration, oil composition, and lipid type and arrangement modulate the conductivity, nonlinearity, and hysteresis of the AES. Using a mathematical model of AES developed from empirical expressions for both state variables, we also show that the voltage-induced plasticity in an AES can dynamically synchronize the firing of two HH neurons, illustrating one of the key uses of ES in neural networks.

Like the brain, ES functionality in neural networks may also enable greater cognitive power in neuromorphic circuits. Our AES devices, unlike most neuromorphic devices, mimic the continuously variable conduction, bidirectional ion transport, and activity-dependent plasticity of ES. These results also highlight that a biomolecular approach is one that enables uniquely modular transport properties and tunable plasticity that can be achieved at biologically relevant voltages.

The contents of this chapter have been published in Nanoscale journal published by the Royal Society of Chemistry in 2019,
DOI: 10.1039/c9nr07288h. To be cited as : Nanoscale, 2019, 11, 18640

References

1. Chua, L.O., *Nonlinear circuit foundations for nanodevices. I. The four-element torus.* Proceedings of the IEEE, 2003. **91**(11): p. 1830-1859.
2. Chua, L., *Memristor-The missing circuit element.* IEEE Transactions on Circuit Theory, 1971. **18**(5): p. 507-519.
3. Ventra, M.D., Y.V. Pershin, and L.O. Chua, *Circuit Elements With Memory: Memristors, Memcapacitors, and Meminductors.* Proceedings of the IEEE, 2009. **97**(10): p. 1717-1724.
4. ZhenYu, Y., et al., *What are Memristor, Memcapacitor, and Meminductor?* IEEE Transactions on Circuits and Systems II: Express Briefs, 2015. **62**(4): p. 402-406.
5. Colicos, M.A., *Activity-Dependent Synaptic Plasticity*, in *Encyclopedia of Neuroscience*, M.D. Binder, N. Hirokawa, and U. Windhorst, Editors. 2009, Springer Berlin Heidelberg: Berlin, Heidelberg. p. 50-52.
6. Strukov, D.B., et al., *The missing memristor found.* Nature, 2008. **453**(7191): p. 80-3.
7. Prodromakis, T., C. Toumazou, and L. Chua, *Two centuries of memristors.* Nature Materials, 2012. **11**: p. 478.
8. Li, Y., et al., *Review of memristor devices in neuromorphic computing: materials sciences and device challenges.* Journal of Physics D: Applied Physics, 2018. **51**(50): p. 503002.
9. Haas, J.S., C.M. Greenwald, and A.E. Pereda, *Activity-dependent plasticity of electrical synapses: increasing evidence for its presence and functional roles in the mammalian brain.* BMC cell biology, 2016. **17 Suppl 1**(Suppl 1): p. 14-14.
10. Haas, J.S., B. Zavala, and C.E. Landisman, *Activity-Dependent Long-Term Depression of Electrical Synapses.* Science, 2011. **334**(6054): p. 389.
11. Haas, J.S., *A new measure for the strength of electrical synapses.* Frontiers in cellular neuroscience, 2015. **9**: p. 378-378.
12. Pereda, Alberto E., *The Variable Strength of Electrical Synapses.* Neuron, 2016. **90**(5): p. 912-914.
13. Bloomfield, S.A., D. Xin, and T. Osborne, *Light-induced modulation of coupling between AII amacrine cells in the rabbit retina.* Visual Neuroscience, 1997. **14**(3): p. 565-576.
14. Bloomfield, S.A., D. Xin, and S.E. Persky, *A comparison of receptive field and tracer coupling size of horizontal cells in the rabbit retina.* Visual Neuroscience, 1995. **12**(5): p. 985-999.

15. Connors, B.W. and M.A. Long, *ELECTRICAL SYNAPSES IN THE MAMMALIAN BRAIN.* Annual Review of Neuroscience, 2004. **27**(1): p. 393-418.
16. Bennett, M.V.L., *Gap junctions as electrical synapses.* Journal of Neurocytology, 1997. **26**(6): p. 349-366.
17. Tawfik, V.L. and P. Flood, *Electrical Synapses: High-speed Communication in the Maintenance of Neuropathic Pain.* Anesthesiology: The Journal of the American Society of Anesthesiologists, 2016. **124**(1): p. 13-15.
18. Purves D, A.G., Fitzpatrick D, et al., , *Neuroscience.* 2nd Edition ed. Electrical Synapse. 2001, Sunderland (MA): Sinauer Associates.
19. Rela, L. and L. Szczupak, *Gap junctions.* Molecular Neurobiology, 2004. **30**(3): p. 341-357.
20. Pereda, A.E., et al., *Gap junction-mediated electrical transmission: Regulatory mechanisms and plasticity.* Biochimica et Biophysica Acta (BBA) - Biomembranes, 2013. **1828**(1): p. 134-146.
21. Debanne, D. and M. Russier, *How do electrical synapses regulate their strength?* The Journal of physiology, 2017. **595**(13): p. 4121-4122.
22. Curti, S. and J. O'Brien, *Characteristics and plasticity of electrical synaptic transmission.* BMC Cell Biology, 2016. **17**(1): p. 13.
23. L. Harris, A., *Emerging issues of connexin channels: biophysics fills the gap.* Quarterly Reviews of Biophysics, 2001. **34(**3): p. 325-472.
24. Bukauskas, F.F. and V.K. Verselis, *Gap junction channel gating.* Biochimica et Biophysica Acta (BBA) - Biomembranes, 2004. **1662**(1): p. 42-60.
25. Rozental, R., et al., *Temporal expression of neuronal connexins during hippocampal ontogeny.* Brain Research Reviews, 2000. **32**(1): p. 57-71.
26. Belousov, A.B. and J.D. Fontes, *Neuronal gap junctions: making and breaking connections during development and injury.* Trends in Neurosciences, 2013. **36**(4): p. 227-236.
27. Samoilova, M., et al., *Epileptiform activity in hippocampal slice cultures exposed chronically to bicuculline: increased gap junctional function and expression.* Journal of Neurochemistry, 2003. **86**(3): p. 687-699.

28. Spira, M.E. and M.V.L. Bennett, *Synaptic control of electronic coupling between neurons.* Brain Research, 1972. **37**(2): p. 294-300.
29. Carew, T.J. and E.R. Kandel, *Two functional effects of decreased conductance EPSP's: synaptic augmentation and increased electrotonic coupling.* Science, 1976. **192**(4235): p. 150.
30. Lefler, Y., Y. Yarom, and Marylka Y. Uusisaari, *Cerebellar Inhibitory Input to the Inferior Olive Decreases Electrical Coupling and Blocks Subthreshold Oscillations.* Neuron, 2014. **81**(6): p. 1389-1400.
31. Jaslove, S.W. and P.R. Brink, *Electrotonic Coupling in the Nervous System*, in *Cell-to-Cell Communication*, W.C. De Mello, Editor. 1987, Springer US: Boston, MA. p. 103-147.
32. Chiolerio, A., et al., *Coupling Resistive Switching Devices with Neurons: State of the Art and Perspectives.* Frontiers in neuroscience, 2017. **11**: p. 70-70.
33. Yang, J.J., et al., *Memristive switching mechanism for metal/oxide/metal nanodevices.* Nature Nanotechnology, 2008. **3**: p. 429.
34. Waser, R. and M. Aono, *Nanoionics-based resistive switching memories.* Nature Materials, 2007. **6**: p. 833.
35. Jo, S.H. and W. Lu, *CMOS Compatible Nanoscale Nonvolatile Resistance Switching Memory.* Nano Letters, 2008. **8**(2): p. 392-397.
36. Jo, S.H., K.-H. Kim, and W. Lu, *Programmable Resistance Switching in Nanoscale Two-Terminal Devices.* Nano Letters, 2009. **9**(1): p. 496-500.
37. Syu, Y.-E., et al., *Atomic-level quantized reaction of HfOx memristor.* Applied Physics Letters, 2013. **102**(17): p. 172903.
38. Lv, Z., et al., *From biomaterial-based data storage to bio-inspired artificial synapse.* Materials Today, 2018. **21**(5): p. 537-552.
39. Duan, N., et al., *Gate Modulation of Excitatory and Inhibitory Synaptic Plasticity in a Low-Temperature Polysilicon Thin Film Synaptic Transistor.* ACS Applied Electronic Materials, 2019. **1**(1): p. 132-140.
40. Südhof T.C., S.K., *Neurotransmitter Release*, in *Pharmacology of Neurotransmitter Release. Handbook of Experimental Pharmacology*. 2008, Springer: Berlin, Heidelberg.
41. Berco, D., et al., *Nanoscale Conductive Filament with Alternating Rectification as an Artificial Synapse Building Block.* ACS Nano, 2018. **12**(6): p. 5946-5955.

42. Najem, J.S., et al., *Dynamical nonlinear memory capacitance in biomimetic membranes.* Nature Communications, 2019. **10**(1): p. 3239.
43. Najem, J.S., et al., *Memristive Ion Channel-Doped Biomembranes as Synaptic Mimics.* ACS Nano, 2018. **12**(5): p. 4702-4711.
44. Bamberg, E. and P. Läuger, *Channel formation kinetics of gramicidin A in lipid bilayer membranes.* The Journal of Membrane Biology, 1973. **11**(1): p. 177-194.
45. Clement, N.R. and J.M. Gould, *Kinetics for the development of gramicidin-induced ion permeability in unilamellar phospholipid vesicles.* Biochemistry, 1981. **20**(6): p. 1544-1548.
46. Johnson, M.E., et al., *A synthetic lecithin containing branched-chain fatty acids: Physical properties and membrane studies.* Biochimica et Biophysica Acta (BBA) - Biomembranes, 1973. **291**(3): p. 587-591.
47. Hladky, S.B. and D.A. Haydon, *Ion transfer across lipid membranes in the presence of gramicidin A: I. Studies of the unit conductance channel.* Biochimica et Biophysica Acta (BBA) - Biomembranes, 1972. **274**(2): p. 294-312.
48. Andersen, O.S., *Ion movement through gramicidin A channels. Single-channel measurements at very high potentials.* Biophysical journal, 1983. **41**(2): p. 119-133.
49. Muller, J.M., G. van Ginkel, and E.E. van Faassen, *Effect of Lipid Molecular Structure and Gramicidin A on the Core of Lipid Vesicle Bilayers. A Time-Resolved Fluorescence Depolarization Study.* Biochemistry, 1996. **35**(2): p. 488-497.
50. Camaleño-Delgado, J.-M., X.K. Zhao, and J.H. Fendler, *Intrinsic gramicidin fluorescence lifetimes in bilayer lipid membranes and in vesicles.* Canadian Journal of Chemistry, 1990. **68**(6): p. 888-896.
51. Chua, L.O. and K. Sung Mo, *Memristive devices and systems.* Proceedings of the IEEE, 1976. **64**(2): p. 209-223.
52. Kim, H., M. Pd. Sah, and S. Adhikari, *Pinched Hysteresis Loops is the Fingerprint of Memristive Devices*. 2012.
53. Chua, L., *Resistance switching memories are memristors.* Applied Physics A, 2011. **102**(4): p. 765-783.

54. Flood Sung, Y.Y., Li Zhang, Tao Xiang, Philip H.S. Torr, Timothy M. Hospedales *Learning to Compare: Relation Network for Few-Shot Learning.* IEEE/CVF Conference on computer vision and pattern recognition, 2018: p. 1199-1208.
55. Taylor, G.J., et al., *Direct in situ measurement of specific capacitance, monolayer tension, and bilayer tension in a droplet interface bilayer.* Soft Matter, 2015. **11**(38): p. 7592-7605.
56. Gross, L.C.M., et al., *Determining Membrane Capacitance by Dynamic Control of Droplet Interface Bilayer Area.* Langmuir, 2011. **27**(23): p. 14335-14342.
57. Venkatesan, G.A., et al., *Adsorption Kinetics Dictate Monolayer Self-Assembly for Both Lipid-In and Lipid-Out Approaches to Droplet Interface Bilayer Formation.* Langmuir, 2015. **31**(47): p. 12883-12893.
58. White, S.H. and T.E. Thompson, *Capacitance, area, and thickness variations in thin lipid films.* Biochimica et Biophysica Acta (BBA) - Biomembranes, 1973. **323**(1): p. 7-22.
59. White, S.H., *Formation of "solvent-free" black lipid bilayer membranes from glyceryl monooleate dispersed in squalene.* Biophysical journal, 1978. **23**(3): p. 337-347.
60. McIntosh, T.J., S.A. Simon, and R.C. MacDonald, *The organization of n-alkanes in lipid bilayers.* Biochimica et Biophysica Acta (BBA) - Biomembranes, 1980. **597**(3): p. 445-463.
61. Bamberg, E., H.J. Apell, and H. Alpes, *Structure of the gramicidin A channel: discrimination between the piL,D and the beta helix by electrical measurements with lipid bilayer membranes.* Proceedings of the National Academy of Sciences of the United States of America, 1977. **74**(6): p. 2402-2406.
62. Urry, D.W., *The gramicidin A transmembrane channel: a proposed pi(L,D) helix.* Proceedings of the National Academy of Sciences of the United States of America, 1971. **68**(3): p. 672-676.
63. Jones, T.L., et al., *Gramicidin channels are internally gated.* Biophysical journal, 2010. **98**(8): p. 1486-1493.
64. Bamberg, E. and R. Benz, *Voltage-induced thickness changes of lipid bilayer membranes and the effect of an electric field on gramicidin A channel formation.* Biochimica et Biophysica Acta (BBA) - Biomembranes, 1976. **426**(3): p. 570-580.
65. Joseph S. Najem, G.J.T., Charles P. Collier and Stephen A. Sarles., *Memristive Ion Channel-Doped Biomembranes as Synaptic Mimics.* ACS Appl Mater Interfaces, 2018.

66. Stevens, C.F. and Y. Wang, *Facilitation and depression at single central synapses.* Neuron, 1995. **14**(4): p. 795-802.
67. Landisman, C.E. and B.W. Connors, *Long-Term Modulation of Electrical Synapses in the Mammalian Thalamus.* Science, 2005. **310**(5755): p. 1809.
68. Magee, J.C. and D. Johnston, *A Synaptically Controlled, Associative Signal for Hebbian Plasticity in Hippocampal Neurons.* Science, 1997. **275**(5297): p. 209.
69. Morris, R.G.M., *D.O. Hebb: The Organization of Behavior, Wiley: New York; 1949.* Brain Research Bulletin, 1999. **50**(5): p. 437.
70. Hodgkin, A.L. and A.F. Huxley, *Currents carried by sodium and potassium ions through the membrane of the giant axon of Loligo.* The Journal of physiology, 1952. **116**(4): p. 449-472.
71. Taylor, G.J. and S.A. Sarles, *Heating-enabled formation of droplet interface bilayers using Escherichia coli total lipid extract.* Langmuir, 2014. **31**(1): p. 325-337.
72. Au - Najem, J.S., et al., *Assembly and Characterization of Biomolecular Memristors Consisting of Ion Channel-doped Lipid Membranes.* JoVE, 2019(145): p. e58998.
73. Okazaki, T., et al., *Ion channels of alamethicin dimer N-terminally linked by disulfide bond.* Biophysical journal, 2003. **85**(1): p. 267-273.

Appendix

Derivation of state equations for an artificial electrical synapse

The nominal current through our artificial electrical synapse (AES) is given by:

$$I = G(\mathbf{x})V \qquad \text{S1}$$

where G is the non-linear conductance and **x** represents multiple, voltage-dependent state variables [1]. The dynamic equations defining the voltage-dependence of the state variables is given by:

$$\frac{d\mathbf{x}}{dt} = f(\mathbf{x}; V). \qquad \text{S2}$$

The nonlinear and hysteretic plots of *I*-*V* in Figures 1 C-E display the voltage-dependent conductance of a memristive AES. Since ions cross the membrane through gramicidin dimers and not via the insulating membrane, the nominal conductance is determined by the total number of gramicidin channels present in the interface. Our experiments further reveal that the number of gramicidin channels per unit area, N_D, and the fractional increase in area, A_m, are the two, independent, voltage-controlled state variables in an AES. Therefore, equation S1 is rewritten as:

$$I = G(N_D, A_m)V. \qquad \text{S3}$$

Voltage dependent dynamic change in membrane area

The area of a droplet interface bilayer (DIB) increases dynamically in response to an increase in net transmembrane voltage due to electrowetting (EW), which reduces the net interfacial tension of the membrane [2-5]. This relaxation increase changes the contact angle between droplets and, through conservation of droplet volumes, leads to a larger contact (i.e., bilayer) area. The steady state fractional increase in bilayer area at constant thickness, A_m, is given by:

$$A_m(V) = \frac{A(V) - A_0}{A_0} = \alpha V^2 \qquad \text{S4}$$

where A_0 and α are the bilayer area at zero volts and voltage sensitivity constant, respectively[4].

Based on observations that changes in area display first-order exponential time responses, we express dynamic fractional changes in area as:

$$\frac{dA_m}{dt} = \frac{1}{\tau_{ew}}\left(\alpha V^2 - A_m(t)\right) \quad \text{S7}$$

where τ_{ew} is the characteristic time constant for electrowetting.

Nominal conductance, G

With the empirical expressions for voltage-dependent channel density (equations 4 and 5) and the fractional change in area upon electrowetting (equation S7), we write the total conductance term of equation S3 as:

$$G(V,t) = G_u N_D(V) A_0\left(1 + A_m(V,t)\right) \quad \text{S5}$$

where G_u is the unit conductance single gramicidin channel (5.8 pS).

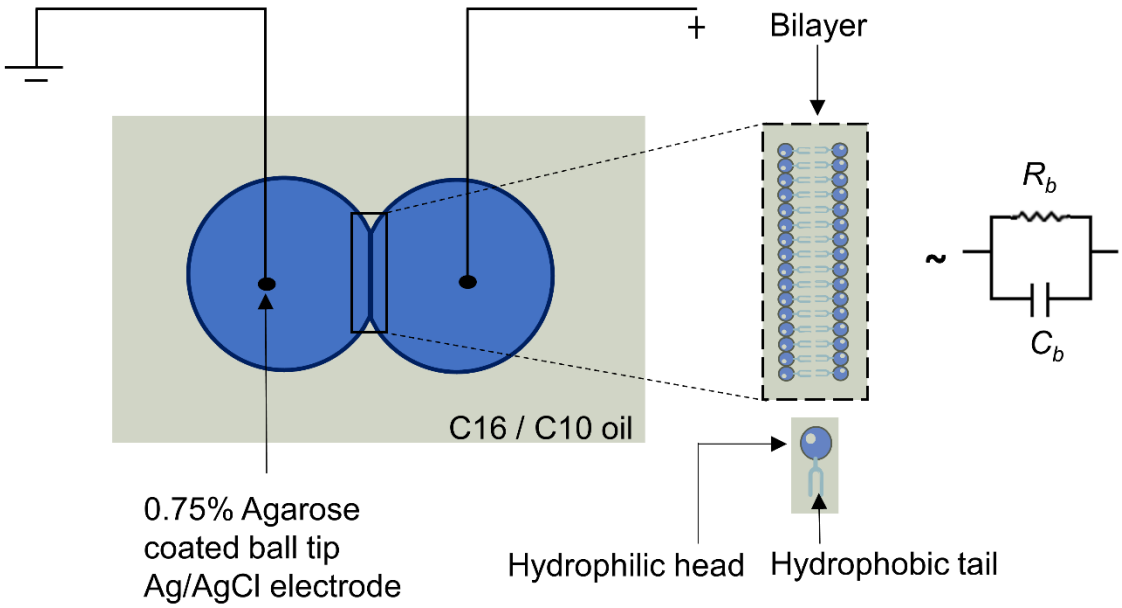


Figure 2.6. Experimental setup used to assemble and characterize droplet-interface bilayer-based artificial electrical synapse. Two lipid-encased aqueous droplets in oil are brought in contact to form a planar lipid bilayer. Ag/AgCl electrodes inserted into the droplets enable application of voltage and measurement of ionic current via a patch clamp amplifier. The ball-shaped electrode tips are coated with hydrophilic agarose gel to aid adhesion to the hanging droplets. A 3-axis micromanipulator supporting each electrode/droplet provides accurate droplet positioning and manipulation for the study. The lipid bilayer devoid of any peptides can be modelled as a parallel resistor-capacitor circuit with typical values of 10 GΩ and 0.63 μF/cm^2, respectively for the nominal resistance and specific capacitance [4].

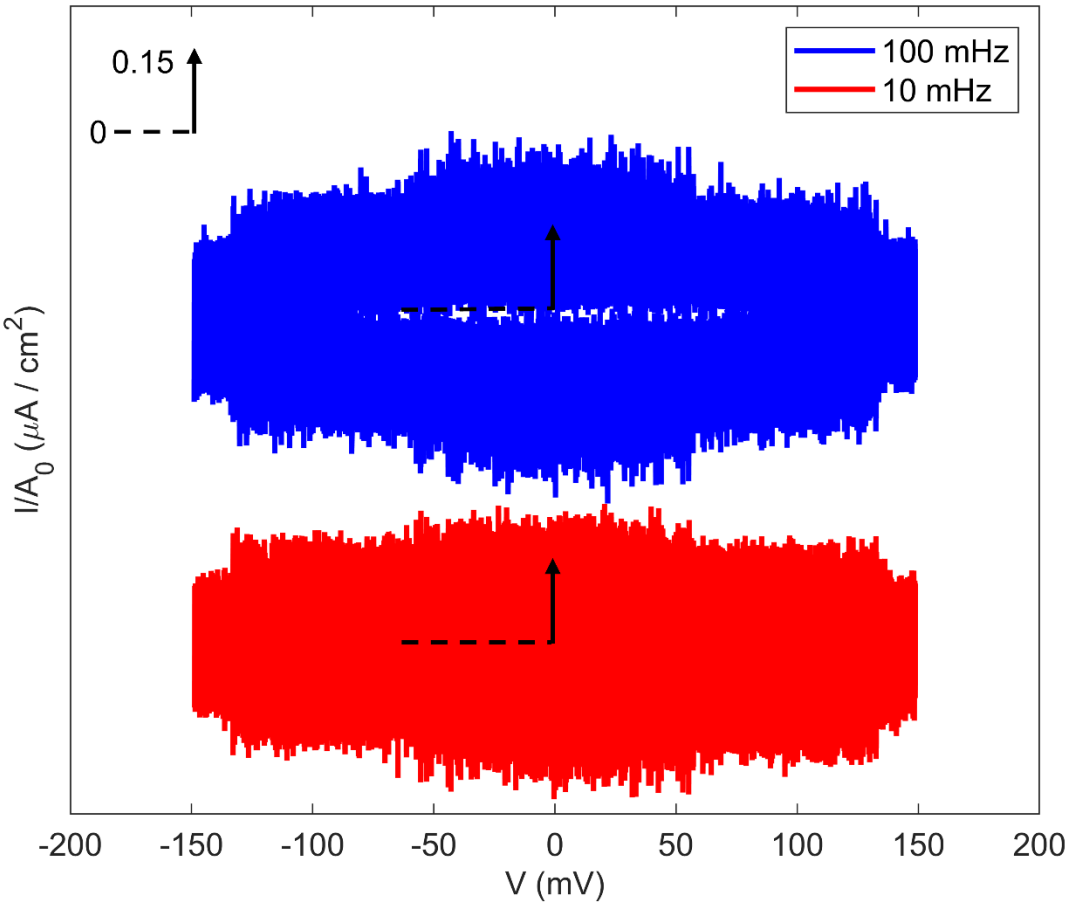


Figure 2.7. *I-V* relationship of an insulating DOPC membrane in hexadecane oil (C16) in response to a 200 mV sinusoidal bias voltage. In absence of any ion conducting gramicidin channels, the elliptical current response stems from frequency-dependent capacitive current.

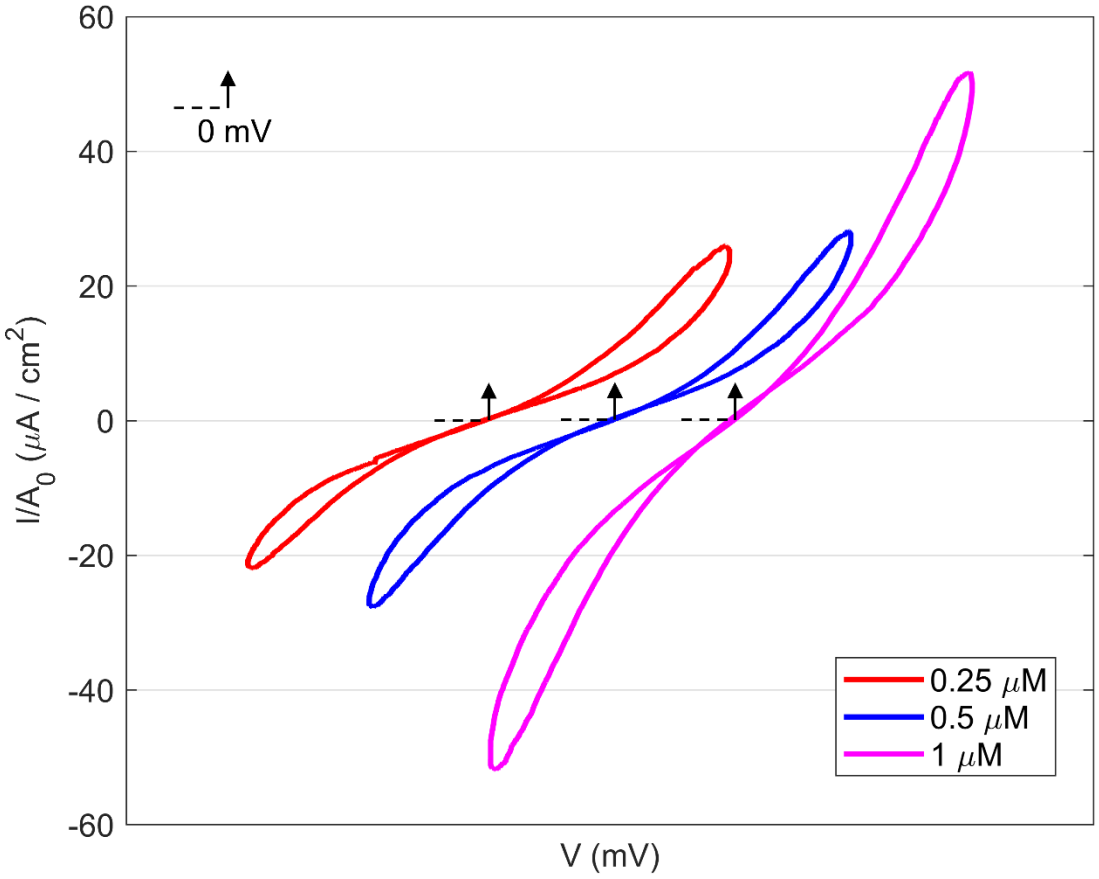


Figure 2.8. *I-V* relationship of AES at varying gramicidin concentrations when excited with 200 mV sinusoidal bias voltage at 10 mHz frequency. The 0 mV pinching points are shifted here for discrete pictorial representation. The data show that increased number of gramicidin pores leads to higher currents due to higher numbers of ions traversing the membrane in the same voltage range.

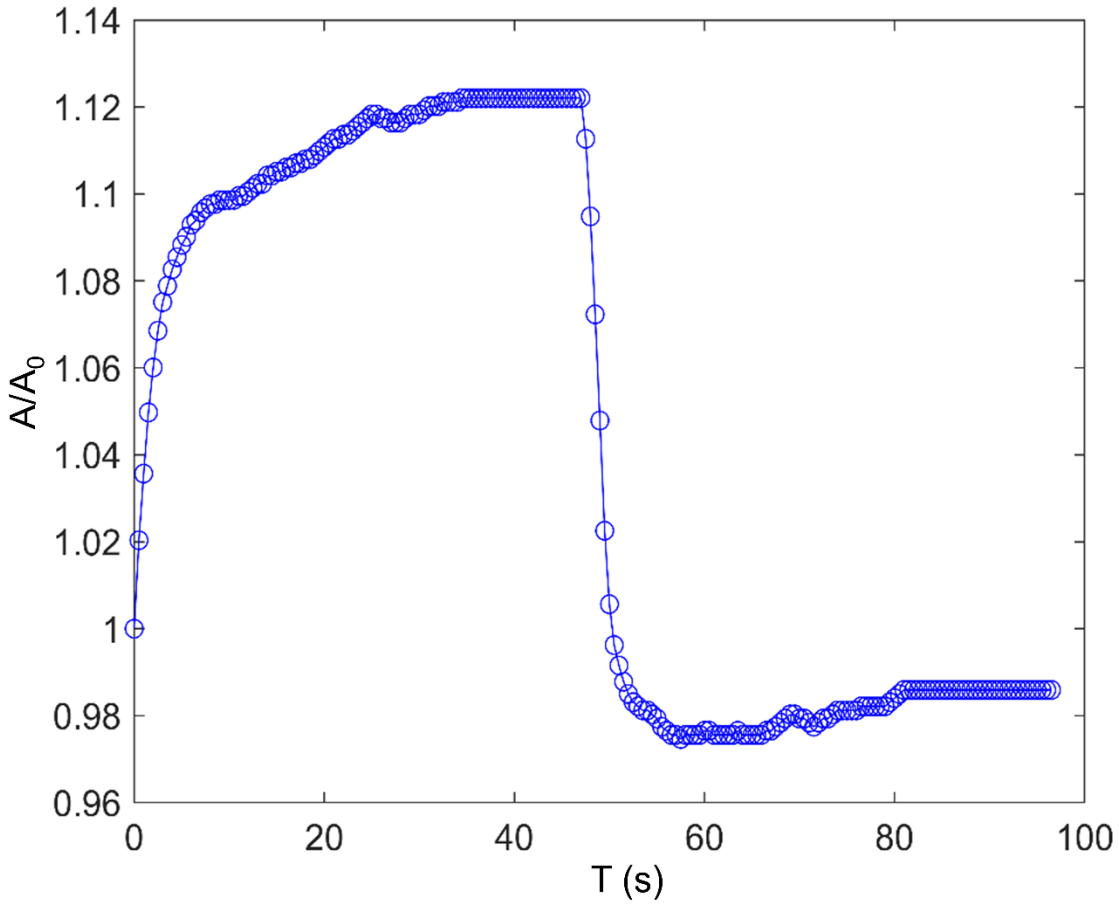


Figure 2.9. Bilayer area growth and decay. The bilayer is allowed to form at 0 mV applied bias. Once the bilayer reaches an equilibrium area, a step voltage of +200 mV is applied for 60 s and then removed. The growth and decay in bilayer area are assessed via image analysis of the connected droplets. For each lipid/oil combination, we report the average time constant from the two dynamic processes.

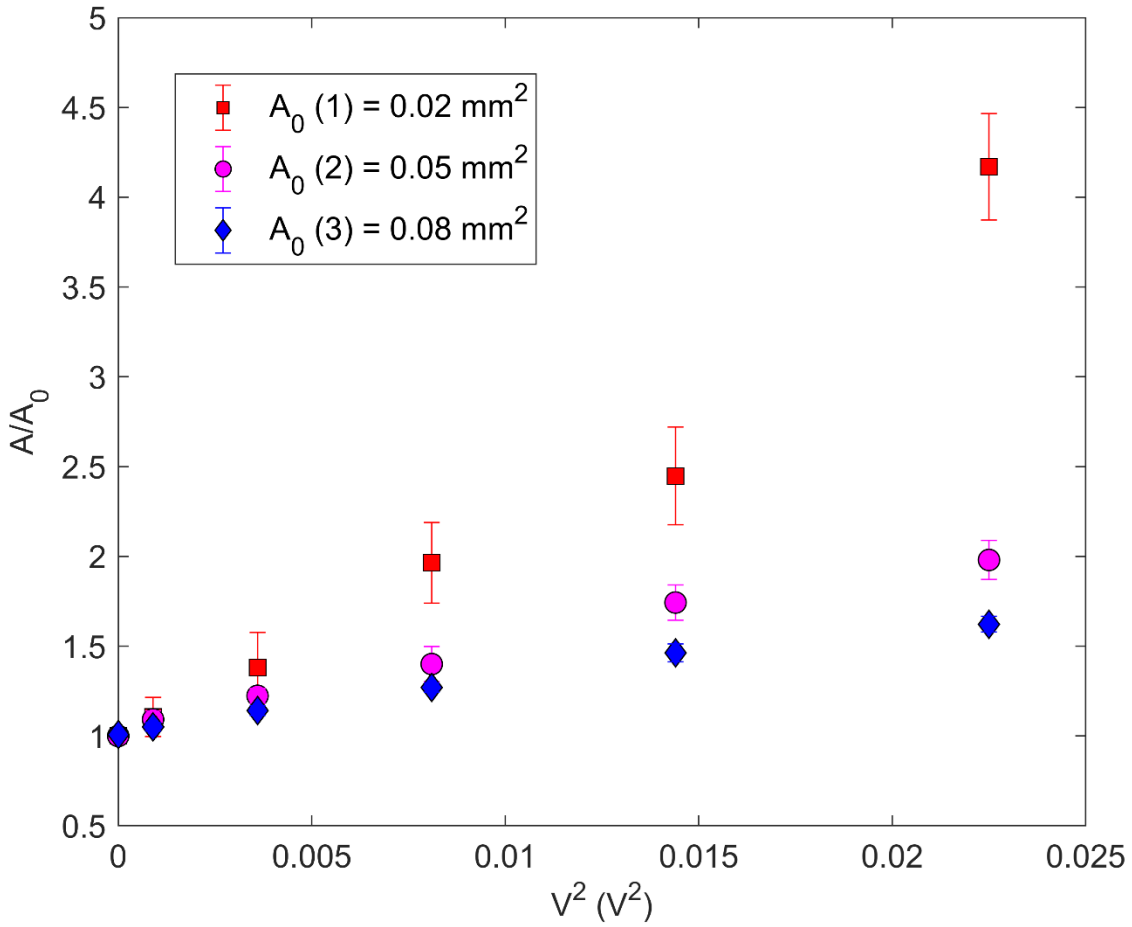


Figure 2.10. Steady-state normalized area of a DOPC bilayer in C16, for different starting areas prescribed through electrode/droplet positioning in response to discrete voltage steps. Each bilayer that forms can have a different nominal area depending on droplet volumes and positioning on electrodes. Therefore, all data reported in the manuscript represent those obtained from bilayers of equal zero-volt areas (either 7.0 x 10^{-4} cm^2 for C16 or 3.3 x 10^{-4} cm^2 for C10). To reach this target, the droplets were either brought closer or separated as needed. The data provided here show that when droplets are separated slightly to reduce the nominal area of the bilayer, the membrane exhibits a stronger normalized electrowetting sensitivity.

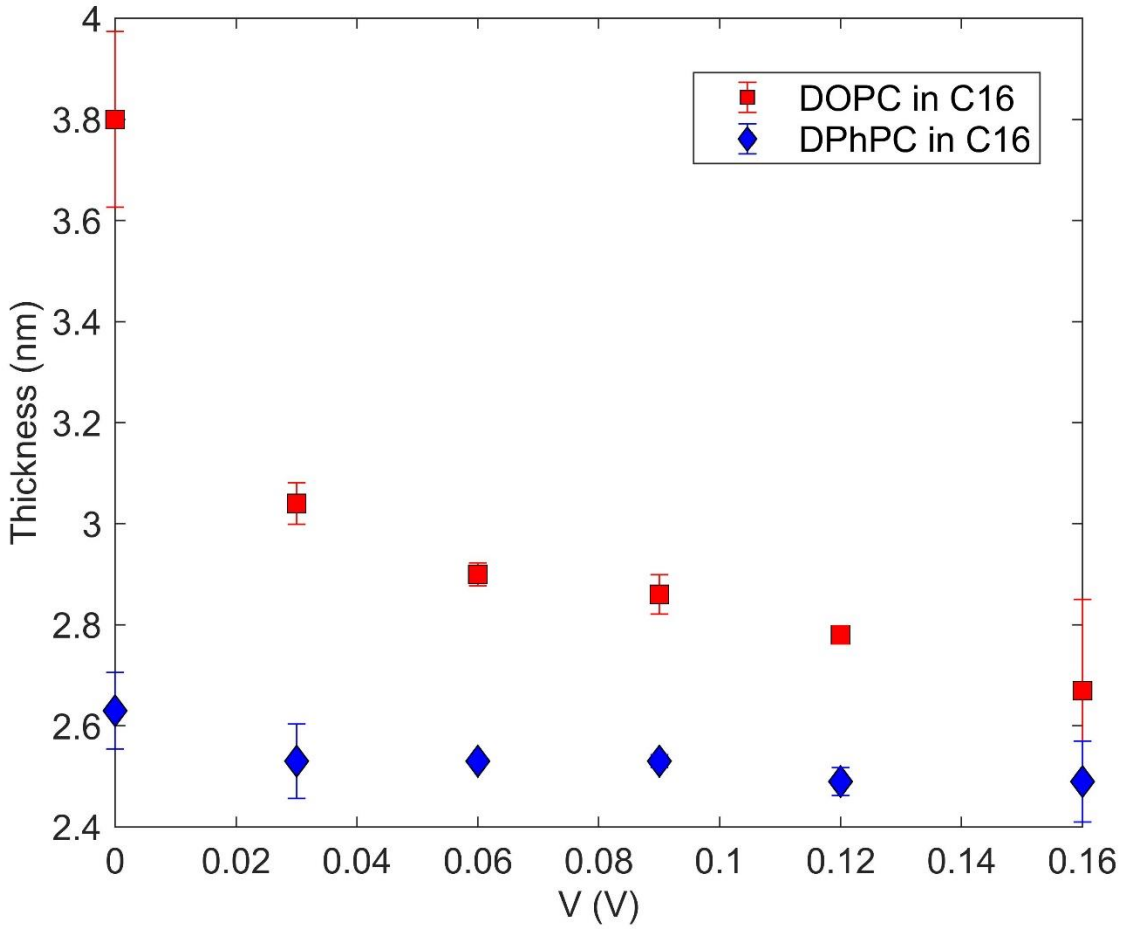


Figure 2.11. Steady-state dielectric thickness versus applied voltage for a DOPC and DPhPC lipid membrane without gramicidin peptides in it. It reflects the thinning of a DOPC from an initially thicker (electrocompression) state in response to increase in bias voltage. Whereas a DPhPC membrane does not undergo significant thinning.

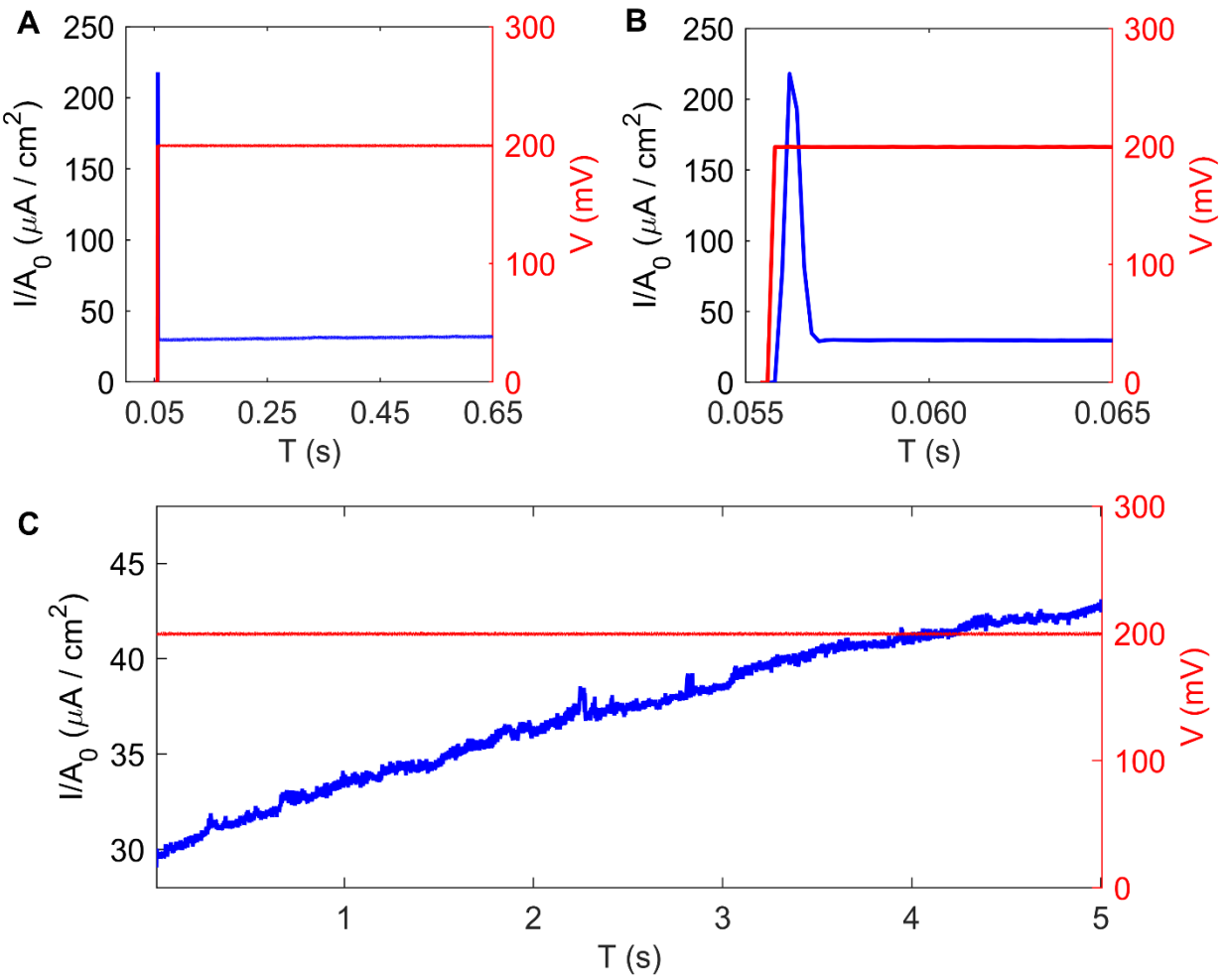


Figure 2.12. Transient current measurements following step-wise changes in applied voltage on a gramicidin-doped DOPC AES formed in C16. (B) is an enlarged representation of (A). The data in (C) show the slower, long-term changes in current that occur at the same time constant of electrowetting, indicating a rise in the number of channels due to an increase in membrane area. Importantly and unlike the work by Bamberg, et al [6, 7] which showed exponential current rises in the first second after a voltage increase, which they used to quantify the kinetics of gramicidin insertion, the data in (A-B) shows that current is flat immediately following the brief capacitive spike. This difference is attributed to much higher concentration of gramicidin used and indicates that the kinetics of channel rearrangement with voltage are nearly instantaneous, which means that hysteretic changes in current are rate-limited by geometrical changes to the bilayer and not due to voltage-dependent channel kinetics.

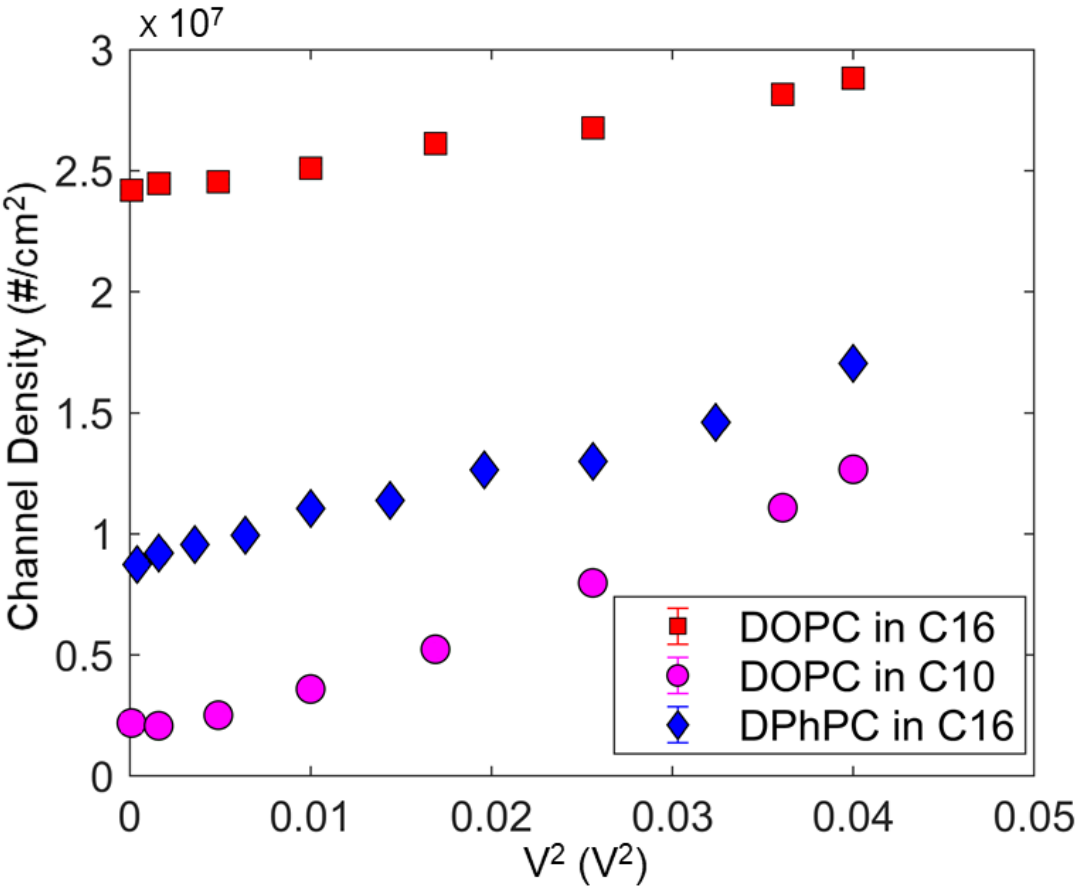


Figure 2.13. Nominal channel density versus voltage for different lipids in both oils (C16 and C10). DOPC in C10 exhibits a lower concentration of channels at 0 mV and a steeper rise with increasing voltage compared to DOPC in C16 or DPhPC in C16. This is due to the fact that DOPC in C10 is thicker at 0 mV (which limits channel insertion) and thins considerably with increasing voltage.

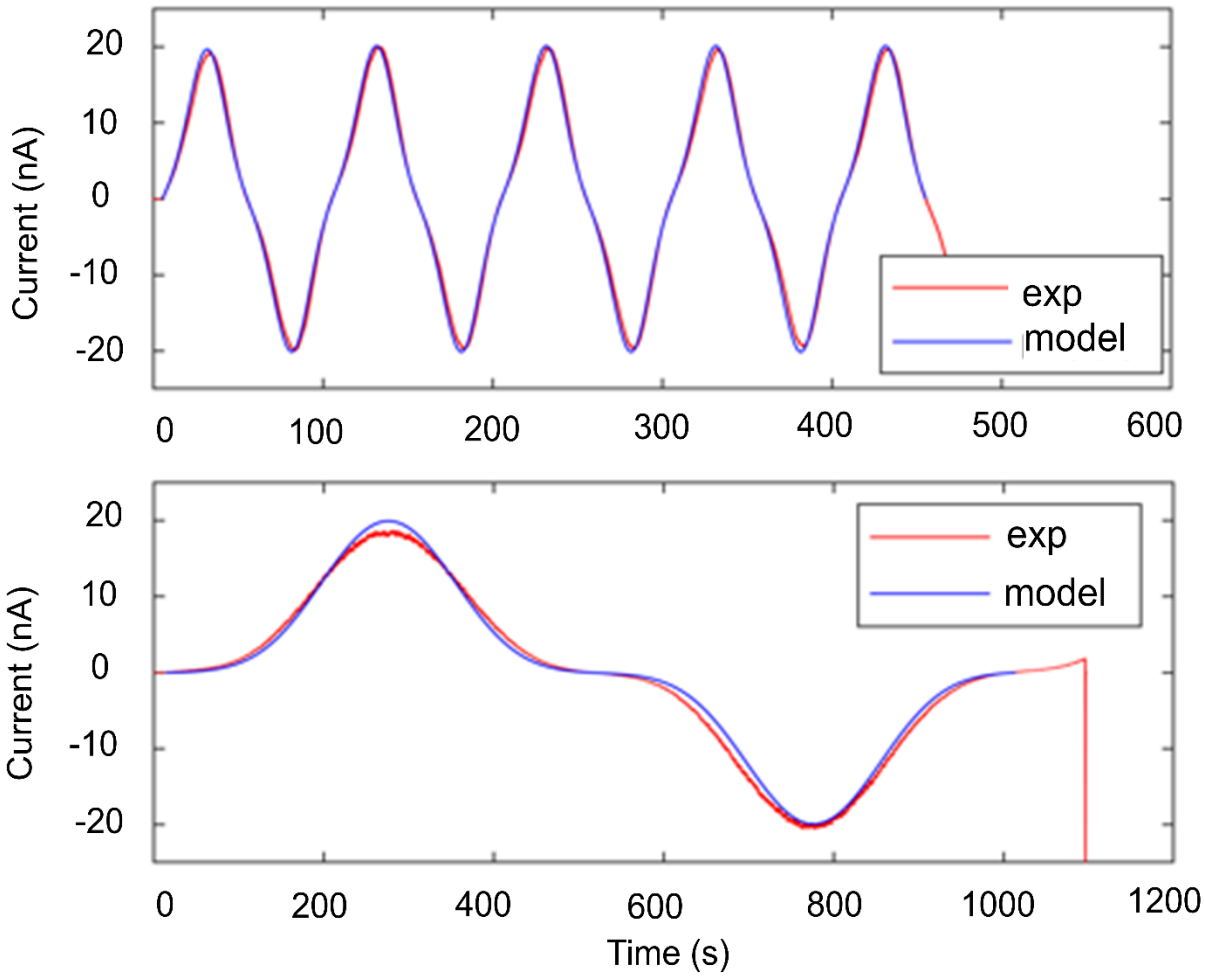


Figure 2.14. Comparison of experimental data (red) and simulated (blue) dynamic current (in blue) for a DPhPC AES in C16 in response to a 0.01Hz, 200mV bias (top) and a DOPC AES in C10 subjected to a 0.001Hz, 200 mV bias (bottom).

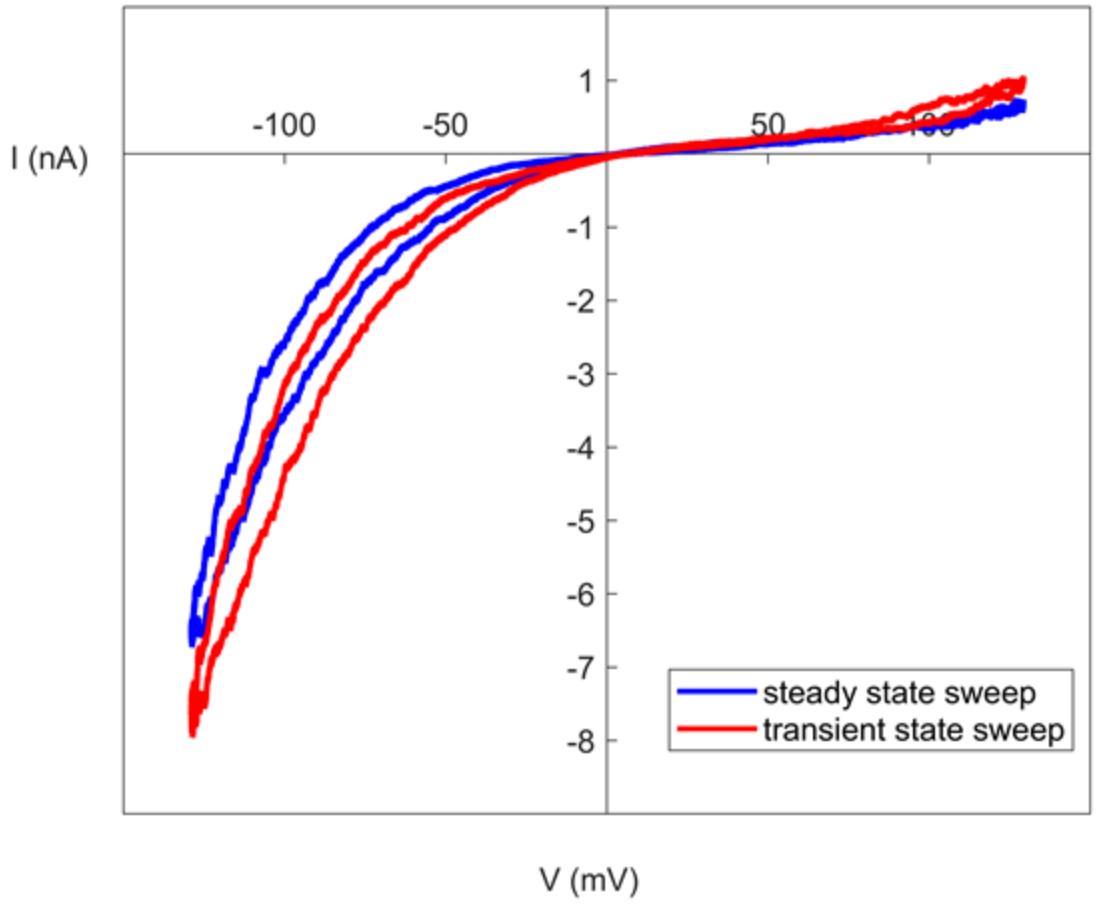


Figure 2.15. *I-V* response of an asymmetric AES consisting of one DOPC leaflet and one leaflet containing a 1:1 molar mixture of DOPC and 1,2-di-O-phytanoyl-sn-glycero-phosphocholine (DOPhPC) and formed in C10 environment to 100 mHz sinusoidal voltage. The red trace depicts the first cycle of the *I-V* sweep, where the device starts from an elevated membrane area (compared to A_0, the area at zero membrane potential) stemming from the non-zero net transmembrane potential difference that exists when 0 mV is applied. The blue trace represents the current response after it has reached steady state conditions of electrowetting (EW) and electrocompression (EC).

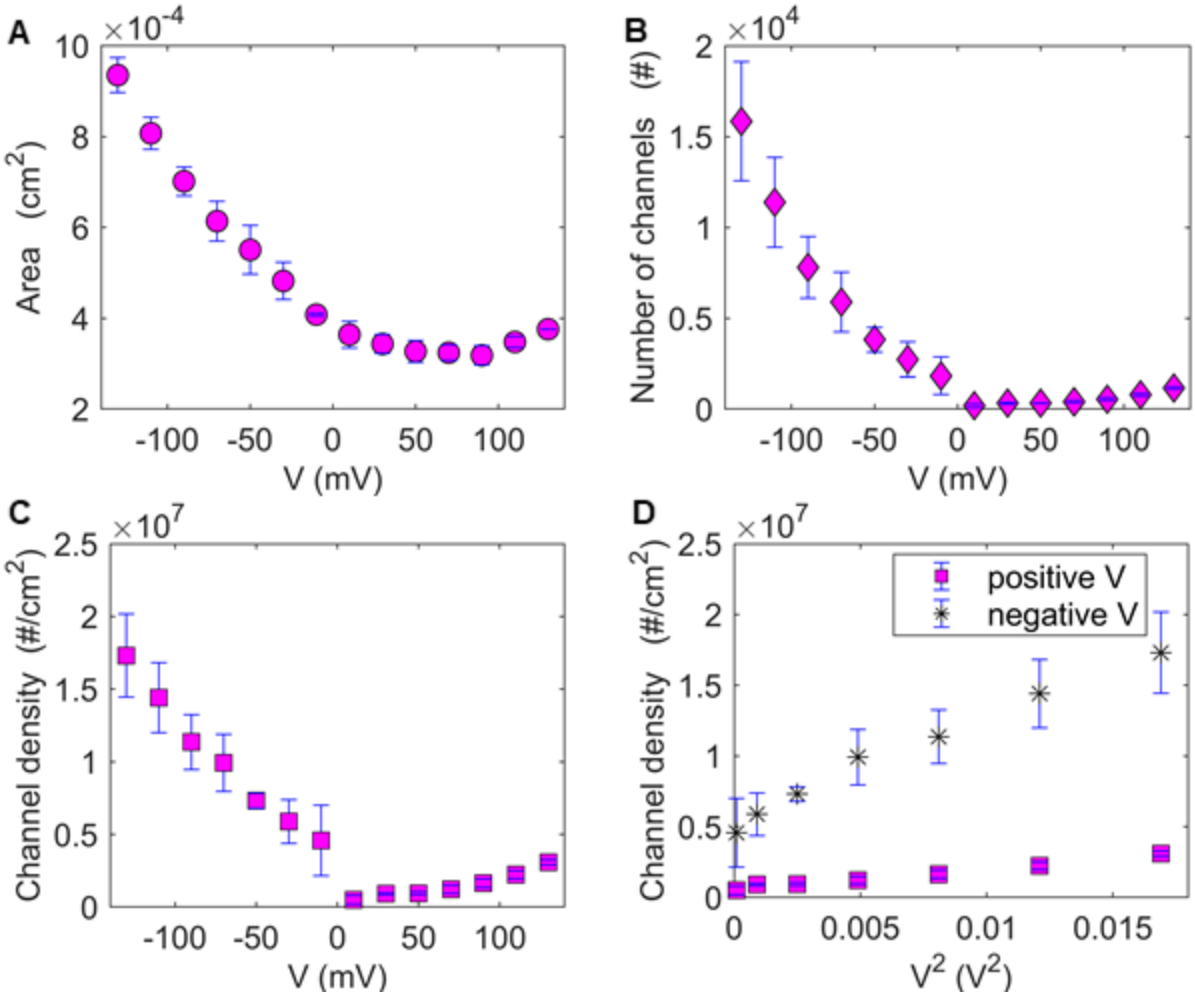


Figure 2.16. Experimental characterization of voltage-dependent state variables for an asymmetric AES. (A) Quasi-static membrane area versus applied voltage reveals a parabolic relationship with a minimum that occurs when the applied voltage is equal and opposite to the intrinsic membrane potential ($v_{int} \approx -85$ mV). The drop in the membrane area with applied positive voltages results from a compensation of net transmembrane potential ($v = v_{appl} + v_{int}$), whereas the steep increase in the area with negative voltages stems from the increase in the total net potential across the membrane. (B) Quasi-static total number of gramicidin channels versus voltage. (C) & (D) displays the rise in channel density which is fueled by an increase in number of channels with voltage and a decrease in membrane area. The slope is steeper for negative voltages because electro compression is playing a crucial role along with electrowetting to help the channels populate the membrane.

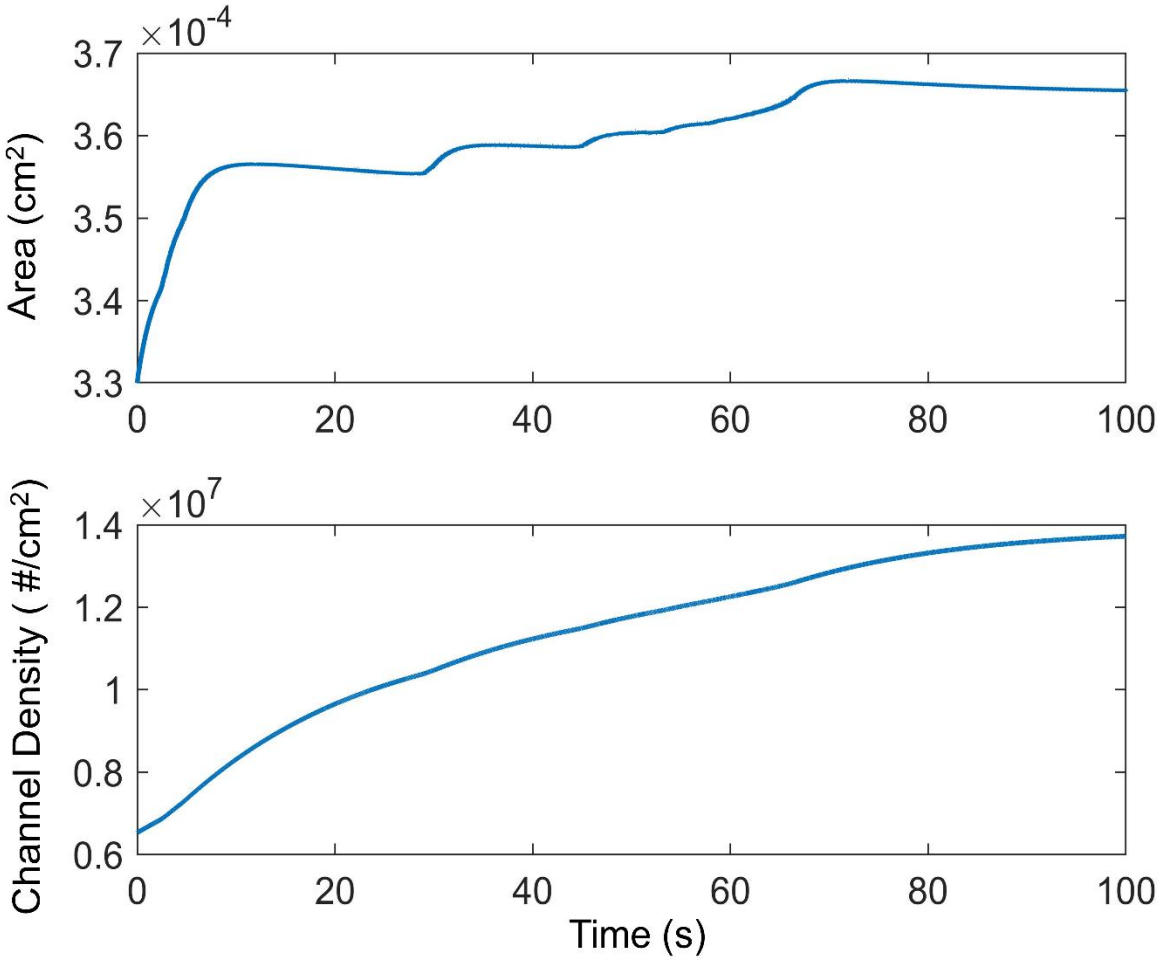


Figure 2.17. Simulated bilayer area (top) and channel density (bottom) versus time for the AES during constant current injection of 10 μA/cm^2 into neuron 1.

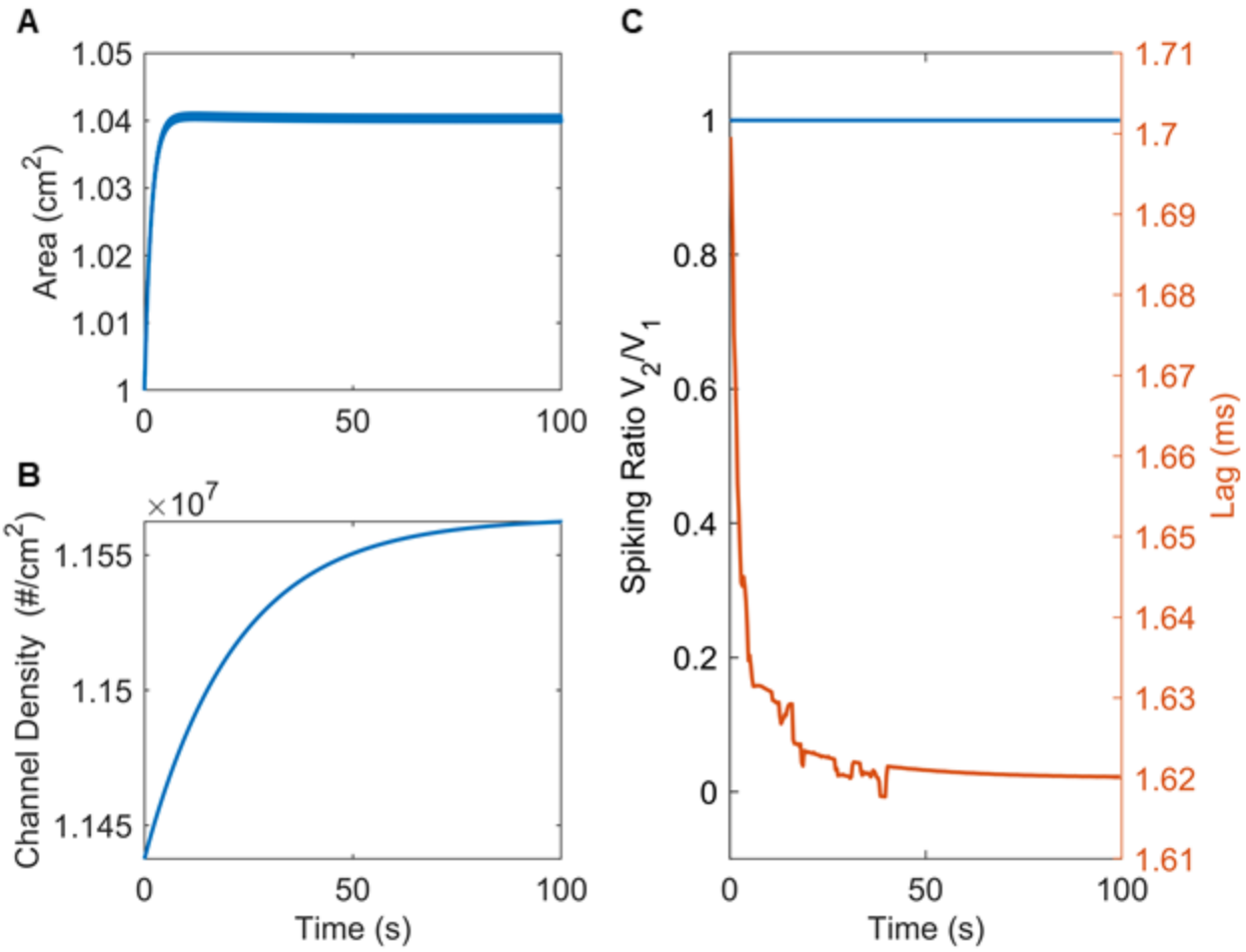


Figure 2.18. Simulation of asymmetric AES interfacing two fully synchronized Hodgkin-Huxley neurons. **(**A, B) Changes in membrane area and channel density versus time (over 100 s). (C) Neuron voltage spiking ratios and lag time versus time. This simulation included a constant current injection of 10 µA/cm^2 into neuron 1 and assumed an initial AES resistance of 30 MΩ, a value low enough to synchronize the action potentials of both neurons. The channel density voltage-dependency was empirically modeled using a linear fit of the quasi-static channel density versus squared voltage data for positive applied potentials (Figure 2.16D); the fitting results are provided in Supplementary Table S1.

Table 2.2. EW, EC, and gramicidin channel density dependencies on voltage obtained when the membrane area was reduced through mechanical droplet manipulation.

Membrane/Oil	EW area growth		EC thinning	Channel Density ($\times 10^6$)
	τ_{ew} (s)	α (V^{-2})	τ_{ec} (s)	
DOPC/C10	1.8 $\pm$ 0.2 (n=3)	75.3$\pm$0.2 (n=4)	22.3$\pm$0.3 (n=3)	$N_d(V) = 2000V^2 + 10$
DOPC/C10	1.8 $\pm$ 0.2 (n=3)	75.3$\pm$0.2 (n=4)	22.3$\pm$0.3 (n=3)	$N_d(V) = 10000V^2 + 40$
DOPC: DOPC+DOPhPC/C10	1.8 $\pm$ 0.2 (n=3)	69.9$\pm$0.2 (n=4)	22.3$\pm$0.3 (n=3)	$N_d(V) = 100V^2 + 4.5$

References

1. Strukov, D.B., et al., *The missing memristor found.* Nature, 2008. **453**(7191): p. 80-3.
2. White, S.H. and T.E. Thompson, *Capacitance, area, and thickness variations in thin lipid films.* Biochimica et Biophysica Acta (BBA) - Biomembranes, 1973. **323**(1): p. 7-22.
3. White, S.H. and W. Chang, *Voltage dependence of the capacitance and area of black lipid membranes.* Biophysical journal, 1981. **36**(2): p. 449-453.
4. Taylor, G.J., et al., *Direct in situ measurement of specific capacitance, monolayer tension, and bilayer tension in a droplet interface bilayer.* Soft Matter, 2015. **11**(38): p. 7592-7605.
5. Najem, J.S., et al., *Dynamical nonlinear memory capacitance in biomimetic membranes.* Nature Communications, 2019. **10**(1): p. 3239.
6. Bamberg, E. and P. Läuger, *Channel formation kinetics of gramicidin A in lipid bilayer membranes.* The Journal of Membrane Biology, 1973. **11**(1): p. 177-194.
7. Gross, L.C.M., et al., *Determining Membrane Capacitance by Dynamic Control of Droplet Interface Bilayer Area.* Langmuir, 2011. **27**(23): p. 14335-14342.

CHAPTER III. Comprehensive assessment of homogeneous hybrid droplet interface bilayers assembled from binary mixtures of DPhPC phospholipids and PB-*b*-PEO di-block copolymers

Abstract

Hybrid membranes built from phospholipids and amphiphilic block copolymers seek to capitalize on the benefits of both constituents for constructing biomimetic interfaces with improved performance. However, hybrid membranes have not been formed or studied using the droplet interface bilayer (DIB) method, an approach that offers advantages for revealing nanoscale changes in membrane structure and mechanics and offers a path toward assembling higher-order tissues. We report on *hybrid* droplet interface bilayers (hDIBs) formed in hexadecane from binary mixtures of synthetic diphytanoyl phosphatidylcholine (DPhPC) lipids and low molecular weight 1,2 polybutadiene-b-polyethylene oxide (PBPEO) amphiphilic block copolymers and use electrophysiology measurements and imaging to comprehensively assess the effects of PBPEO in the membrane. This work reveals that hDIBs containing up to 15 mol% PBPEO in DPhPC are not phase-separated into lipid-rich and polymer-rich domains, remain highly resistive to ion transport, and are stable—including under applied voltage. Moreover, they exhibit hydrophobic thicknesses similar to DPhPC-only bilayers, but also have significantly lower values of membrane tension. These characteristics coincide with reduced energy of adhesion between droplets and the formation of alamethicin ion channels at significantly lower threshold voltages, demonstrating that even moderate amounts of amphiphilic block copolymers in a lipid bilayer provide a route for tuning the physical properties of a biomimetic membrane.

Introduction

The many active and passive functions performed by cellular membranes motivate the need for effective materials and methods to obtain biomimetic model membranes with similar capabilities. For example, biomimetic membranes in the form of spherical vesicles and planar bilayers are needed for researching biophysical mechanisms related to selective transport, ion channel gating, and stimuli-responsive transmembrane signaling. They are also key to developing functional materials that offer either similar capabilities to membranes or controlled interactions with cellular interfaces. Such technologies hold significant promise for applications such as biosensing[1], nanoparticle-assisted drug-delivery[2, 3], DNA sequencing[4], artificial tissue development[5], and desalination and bio-separations[6-8].

Biomimetic membranes are usually assembled from either phospholipids (PL)[9, 10] or amphiphilic block copolymers (BCP)[11-14] (e.g., diblock or triblock architectures with

alternating hydrophilic and hydrophobic blocks) organized into a bilayer. Amphiphilic BCPs are most frequently constructed from poly(2-methyl oxazoline) (PMOXA) or poly(ethylene oxide) (PEO) hydrophilic groups, linked to poly(butadiene) (PB), poly(dimethyl siloxane) (PDMS), or poly(isoprene) (PI) hydrophobic blocks[15, 16]. While synthetic or naturally derived PL closely resemble lipid compositions in cells and yield membranes with similar dimensions and physical properties, their use *ex vivo* is often curtailed by chemical degradation, higher permeability ~~to water~~, and limited mechanical strength (e.g., bending rigidity, lysis strain) [17-20]. In contrast, while many BCP-based membranes hold advantages in these same metrics, using BCP in place of PL can result in artificially large hydrophobic thicknesses [21, 22] and reduced lateral fluidity[17], which limit the ability to host transmembrane biomolecules for selective signaling and transport.

Alternatively, hybrid membranes combine BCP and PL, seeking to leverage the most favorable properties of each constituent in the resulting biomimetic membrane. This approach has been taken by several groups, many of which used PB-*b*-PEO BCPs in combination with phosphatidylcholine (PC) lipids [17, 21, 23-35]. The results from these studies demonstrate that hybrid PL-BCP membranes in the form of vesicles or planar bilayers can exhibit properties superior to PL-only or BCP-only models[28]. Depending on the types of PL and BCP used and their relative fractions in the membrane, hybrid membranes can exist as homogeneous mixtures or as laterally phase-separated PL and BCP domains. Thus, the local environment (e.g. hydrophobic thickness, lateral fluidity, chemical functionality) of a hybrid membrane can be tailored to recognize membrane-active species [25] and host integral membrane proteins including OmpF [32, 36] and potassium channels [35], whilst also improving the global characteristics (e.g., permeability, stability, dehydration resistance) [17, 27, 28, 37]. However, the benefits of hybrid membranes may not materialize until methods to assemble and comprehensively assess them move beyond closed vesicles and fragile planar bilayers.

The droplet interface bilayer (DIB) technique permits assembling a fluid bilayer membrane between two surfactant-coated water droplets immersed in oil [38-40]. Compared to planar membranes painted across apertures or resting on solid surfaces, a DIB membrane (or *DIB*) offers key advantages: a simpler formation that demands less user skill, greater longevity due to removed interactions with a substrate, independent aqueous volumes needed to perform electrophysiology and establish leaflet asymmetry and direct control over bilayer area. These plusses translate into

greater control for use in a wide variety of experimental studies. Hence DIBs have been used by microbiologists, chemists, and physicists to explore *in situ* a variety of basic biophysical questions and processes[41-44] as well as by engineers to develop biomimetic sensors[45, 46], energy conversion devices[47, 48], and even brain-inspired computing elements[49-52]. Moreover, because an adhesive droplet-based approach is inherently modular, the DIB technique translates well to microfluidic environments for high throughput analyses[53-55] and it permits connecting many droplets together to construct 3D tissue-like synthetic materials[56-58]. In the latter, droplet networks enabled by bilayer-stabilized adhesive droplets result in a compartmentalized soft material that closely mimics the hierarchy of living cells and tissues achieved via membrane barriers. This approach at synthetic tissues establishes the potential to obtain emergent functional properties within biological membrane-inspired—and perhaps biocompatible materials—that sense, actuate, learn, and remember.

DIBs are typically formed from either synthetic PL or natural lipid extracts. Far less research has been reported on assembling DIBs from non-PL surfactants, such as BCPs, despite a potential payoff of improved biomimetic membranes. We previously examined the dynamics of DIB formation using ABA-type block copolymers, which exhibited voltage-triggered reversible adhesion[59, 60]. This behavior resulted from the hair-pin arrangements of the surfactants at the oil-water interface. Depending on the oil, these bilayer interfaces exhibited hydrophobic thicknesses of 10-20 nm, far too thick for supporting transmembrane species (e.g., proteins, ion channels) needed to selectively regulate transport between compartments. This work reiterated the importance of molecular-scale interactions between the solvent and the hydrophobic portion of the BCP molecule in determining whether bilayer formation (via oil exclusion from between droplets) is energetically favorable[59]. Alternatively, our attempts to assemble DIBs from similar types of diblock BCP (e.g., PMOXA-*b*-PDMS, PDMS-*b*-PEO, MW >= 2kDa) have thus far failed to yield stable polymeric DIBs.

Motivated by the potential advantages of hybrid membranes and the opportunity to investigate them using electrophysiology and the DIB technique, we report on *hybrid DIBs* (hDIBs) assembled in hexadecane from symmetric binary mixtures of DPhPC phospholipids and PBPEO diblock copolymers, components that individually yield membranes with low permeabilities to small molecules, ions, and water [37, 42]. The diblock selected for this study is a carboxylic acid

terminated 1,2 poly(butadiene)-co-poly(ethylene oxide) copolymer (PBPEO from here on). We chose a low molecular weight (short-chain) variant ($PB_{12}PEO_8$-COOH, MW ~ 1000 g/mol) because it results in sufficiently thin polymer bilayer membranes capable of hosting both biological OmpF membrane proteins [61, 62] and artificial transmembrane channels [63]. The objectives of the study are to use a combination of simultaneous electrical measurements and imaging to comprehensively characterize the effects of PBPEO concentration on the equilibrium physical properties (e.g., electrical resistance, thickness, stability under voltage, membrane tension, and adhesion energy), the distribution of PBPEO within the bilayer, and the insertion of voltage-activated ion channels in DPhPC:PBPEO hDIBs. This approach shows how electrical measurements of hDIBs can reveal greater understanding of the effects of BCPS in hybrid membranes.

Materials & Methods

Materials. The aqueous droplets used to construct DIBs consisted of phospholipid vesicles, salt, and buffering agent in 99.99% pure deionized water. Potassium chloride (KCl), 3-(*N*-morpholino) propanesulfonic acid (MOPS), sodium hydroxide (NaOH), agarose ($C_{12}H_{18}O_9$), sucrose, *n*-hexadecane (99% pure), ethanol, and isopropyl alcohol were purchased from Sigma Aldrich. DPhPC lipids (>99% purity) were obtained from Avanti Polar Lipids, Inc and used without further purification. The diblock material used in this work is a carboxylic acid terminated 1,2 polybutadiene-block-polyethylene oxide (PB_{12}-*b*-PEO_8-COOH, MW ~ 1000 g/mol, PDI = 1.18) synthesized via anionic polymerization as described elsewhere [61].

Large unilamellar vesicles (LUVs) preparation. To prepare a solution of hybrid LUVs, PBPEO was first solvated in chloroform at a concentration of 10 mg/mL and then mixed with DPhPC lipids dissolved in chloroform at the desired lipid:polymer molar ratio. The chloroform was then evaporated first using a gentle nitrogen stream and then under vacuum for 3 h. Once the solvent fully evaporated, the lipid:polymer film was then rehydrated with 500 mM KCl 10 mM MOPS buffer to a final lipid concentration of 2 mg/ml (see Table S1 in the supplementary information (SI) for total amphiphile concentrations of mixed vesicle solutions). The hydrated suspension was subjected to 5 freeze-then-thaw cycles with passive cooling and heating at -20 °C and ~20 °C, respectively, to create a solution of multilamellar vesicles. Large unilamellar vesicles were formed

by extrusion, using 11 passes through a 100 nm-pore polycarbonate membrane (Whatman) in an Avanti Mini Extruder. Extruded LUV solutions were stored at 4 °C until further use.

DIB formation. DIBs were formed at room temperature (22 °C) between two, 300 nL aqueous droplets of LUV solution suspended on agarose-coated wire-type electrodes in an oil-filled reservoir as described elsewhere [64]. The oil reservoir and droplets were centered above a 4X objective lens on an inverted microscope. The positions of both electrodes were controlled by manual, three-axis micromanipulators. A lipid bilayer was formed by bringing droplets into contact following a brief incubation period to ensure lipid monolayer assembly. To aid in holding droplets, electrodes were lowered in the oil such that the bottom of the droplets gently rest on the substrate. Bottom-view images (Figure 3.1A) of connected droplets were obtained using a QIClick-F-M-12-C (SN: Q31274) camera controlled by Micromanager software. Side view images of connected droplets (Figure 3.5 in the appendix) were obtained using an IDS-UI-3360CP-M_GL R2 camera controlled by IDS suite software. Images from both views were used to estimate membrane area for computing specific capacitance and thickness as described elsewhere [65].

Giant unilamellar vesicles (GUVs) formation and confocal imaging. Giant unilamellar vesicles (GUVs) were formed via gel-assisted swelling. PBPEO and lipids dissolved in chloroform are mixed at various PL:BCP molar ratios: 100:0, 90:10, 80:20, and 50:50. Nile Red hydrophobic dye was added to all mixtures at a final concentration of 0.1 mol%. A petri dish was plasma cleaned for 1 min and then spin-coated with a warm 1 wt/vol% agarose solution, which was left to dry at room temperature. Small droplets of lipid/BCP mixture were deposited onto the agarose coated petri dish that was then placed under a gentle stream of nitrogen for a few min and then in a desiccator for one h to evaporate the chloroform. The GUV growth buffer containing 400 mM sucrose in water was added and left for 30 min for swelling to proceed and form GUVs. For harvesting the GUVs, the narrow end of a 100 µl pipette tip was cut to create a larger opening and avoid damaging GUVs. Confocal fluorescence imaging was performed at room temperature using a Nikon Eclipse Ti2-E confocal microscope equipped with a 60X oil immersion objective and a 561 nm laser line.

Electrophysiology. Bilayer current measurements were made using an Axopatch 200B patch clamp amplifier and Digidata 1440A data acquisition system (Molecular Devices). All recordings were made at room temperature with appropriate shielding using a well-grounded Faraday cage in place

to minimize noise. Voltage waveforms were generated using either a Hewlett-Packard 3314A function generator or a National Instruments Compact DAQ with a NI 9263 analog output module controlled by a custom LabVIEW script. Voltages from these sources were sent to the headstage of the Axopatch 200B via the external input to the amplifier. Current measurements were lowpass filtered at 1 kHz on the Axopatch 200B and then sampled at 20 kHz. All data were processed using Matlab.

Monolayer formation and interfacial tension measurement. Pendant drop tensiometry was performed on a Dataphysics OCA 15EC to assess monolayer formation at the oil-water interface, including measuring equilibrium tension. A Teflon-coated blunt tip needle with a 0.72mm inner diameter was used for dispensing 1μL volumes of the aqueous phase into a quartz cuvette filled with hexadecane. Images of the hanging droplets were collected once per second, and interfacial tension was calculated using Laplace-Young fitting in DataPhysics SCA20 software. Experiments were performed at room temperature.

Results and Discussion

hDIB formation and electrical characterization

In addition to DPhPC-only DIBs that are well characterized [66-68], hDIBs with symmetric leaflet compositions were assembled in hexadecane oil with 300 nL droplets of LUV solution consisting of binary mixtures of DPhPC phospholipids and PBPEO diblock copolymers. The chemical structures for these amphiphiles are compared in Figure 3.6 in the appendix, and Table 1 in the SI shows that these solutions spontaneously reduce the interfacial tension from a value of ~45-50 mN/m for the neat oil-water interface within a few minutes, indicating the adsorption of amphiphiles and formation of well-packed monolayers [69]. At PBPEO fractions up to 15 mol%, which produced equilibrium monolayer tensions below 1 mN/m at the oil-water interface, we observed spontaneous bilayer formation between contacting droplets in hexadecane; i.e., no applied voltage was needed to induce bilayer thinning as previously observed with triblock BCPs[59]. However, unlike lipid-only DIBs that exhibit bilayer thinning within ~1 min, hDIBS often required more than 10 min for thinning to initiate after droplet contact. This delayed response is especially prominent at PBPEO molar ratios above 10 mol% in the LUVs. Interfacial thinning (and removal of excess oil) results in visual changes to the shared interface between droplets, as well as an increase in the amplitude of capacitive current induced by an AC voltage applied

between the two supporting electrodes. In hexadecane, the area, A, (and thus the contact angle, θ) of the interface reaches an equilibrium state within 60 s. Figure 3.1A compares bottom-view images of a DPhPC-only DIB and an hDIB formed with 15 mol% PBPEO in the LUVs, both taken at their equilibrium zero-volt configurations. Compared to the DPhPC only case, the addition of PBPEO resulted in a smaller equilibrium bilayer area and lower contact angle (see Figure 3.3a). Finally, though, the proportion of PBPEO in the droplet interface may differ from that found in the LUVs, we denote hDIB compositions from here on using the molar ratio of polymers to lipids in LUVs, as is common in describing DIBs from mixtures of species[70, 71].

At PBPEO molar fractions greater than 15 mol%, contacting droplets routinely coalesced (i.e., no stable membrane was formed) either before or shortly after thinning began. This same result was observed for 100% PBPEO LUV solutions, which is consistent with the finding that polymer-only monolayers display higher values of equilibrium monolayer tension (>5 mN/m, Table S1) at the hexadecane water interface, indicating a lower packing density is obtained with only PBPEO amphiphiles. Lower monolayer tensions correspond to higher packing density, a requirement for stabilizing a bilayer between droplets [69]. Alternatively, we found that incorporating PBPEO into the oil phase instead resulted in an average equilibrium tension of only ~0.5 mN/m (Table S1). Yet, while putting DPhPC lipids in hexadecane is a viable route to forming a DIB, droplets submerged in PBPEO-hexadecane did not connect to form a thinned bilayer, even under the application of voltage. Therefore, ensuing measurements focus solely on hDIBs formed with aqueous LUV solutions at PBPEO molar ratios from 0-15 mol%.

To approximate how PL and BCP distribute in an hDIB, we assembled and imaged giant unilamellar vesicles (GUVs) from mixtures of the two species and added 0.1 mol% Nile Red, a lipophilic fluorescent dye. As control cases, DPhPC vesicles were found to be uniformly fluorescent (Figure 3.1B), while PBPEO- only GUVs exhibited no fluorescence, despite being visible in brightfield with phase contrast (Figure 3.7). For the latter, the dye precipitated into irregular clumps in the viewing chamber. However, mixtures of lipids and PBPEO were observed to be fluorescent, either uniformly or locally depending on the lipid type. Vesicles appeared uniformly fluorescent at the tested molar ratios of 5%, 10%, 20%, 50%, and 80% PBPEO (Figure 3.1B, and Figures S4-S6) when PBPEO was combined with DPhPC, and we did not find evidence of GUVs visible in brightfield but not in fluorescence mode, which would have occurred if there

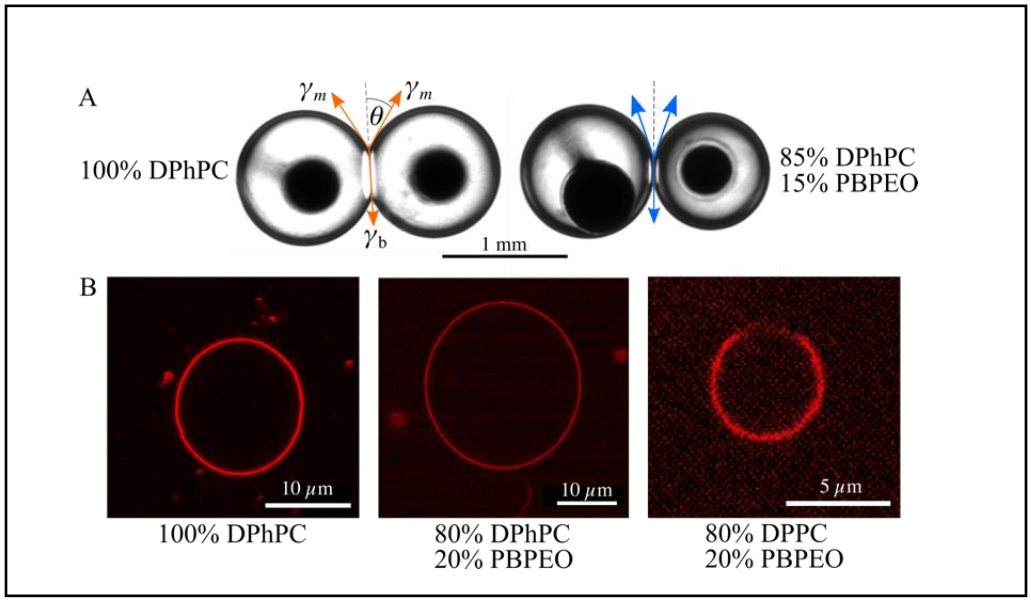


Figure 3.1: Hybrid DIBs and GUVs. (A) bottom-view images of a DPhPC DIB (left) to an hDIB with 15 mol% PBPEO (right). (B) Confocal images near the equators of lipid-only and hybrid lipid-polymer GUVs containing 0.1 mol% Nile Red. % denotes molar fractions.

were PBPEO-only vesicles present. This was true even at a PBPEO concentration of 80 mol % (Figure 3.8), where PBPEO outnumber DPhPC 4:1. The observation that fluorescence intensity is noticeably lower for GUVs with 80 mol% versus 20 mol% PBPEO (Figure 3.10) shows that more PBPEO leads to less Nile Red in the vesicle and a weaker fluorescent signal. In contrast, we observed locally non-fluorescent regions in GUVs comprised of 20 mol% PBPEO and 80 mol% DPPC (Figure 3.1B), suggesting co-existing lipid-rich (fluorescent) and polymer-rich (non-fluorescent) regions in these membranes. Phase separation was routinely observed in many (n>10) separate DPPC:PBPEO GUVs (Figure 3.11), which we qualitatively confirmed by viewing multiple vertical slices on separate GUVs. Phase separation in hybrid vesicles is common, especially when a high melting point lipid such as DPPC is used [26, 35, 36].

Therefore, in combination with our finding that mixtures of DPhPC and PBPEO (even at high copolymer:lipid ratios) do not produce visible non-fluorescent GUVs, we conclude that PBPEO is present in the GUVs and that DPhPC and PBPEO are evenly mixed. Thus, we expect DIBs formed from mixed vesicles to consist of similar lipid:polymer ratios and remain homogeneously mixed. Mixing of these constituents makes sense given that DPhPC is in a liquid crystalline fluid phase at room temperature[72] and the low molecular weight of the PBPEO polymer chosen for this work is expected to minimize the difference in hydrophobic thickness that can drive phase separation. These conditions are consistent with those from Gettel et al, who observed that a low molecular weight PIPEO diblock copolymer forms well-mixed hybrid bilayers when combined with fluid-phase POPC lipids [28].

To evaluate the equivalent electrical parameters and assess structural differences in DPhPC-based hDIBs, we applied a 10 mV, 10Hz triangular voltage waveform between connected droplets and measured the induced square-wave current using a patch-clamp amplifier. As discussed elsewhere [67], the square wave current response can be analyzed to extract nominal values of bilayer resistance, *R*, and capacitance, *C*. A DC voltage can also be superimposed onto the AC signal to evaluate these quantities at nonzero average transmembrane potentials. Bottom view images of the connected droplets are intermittently obtained during electrical measurements to assess A and θ versus membrane composition and applied voltage. Figure 3.2A and Table 1 present average values of specific membrane resistance, R_m, (where $R_m = R \times A$) measured at 0 and 200 mV DC for varying percentages of PBPEO. Across all compositions, we observe values of specific

resistance on the order of 1-25 MΩ cm^2, which indicates that both lipid-only and hybrid.interfaces create an effective ionic seal between the two droplets. Increasing the transmembrane potential to 200mV significantly reduces the values of specific resistance (possibly due to electroporation aided by voltage-induced thinning or electrowetting-driven reductions in membrane tension); however, all values remain above 1 MΩ cm^2, and there is no clear trend that increasing amounts of PBPEO lowers the specific resistance under applied voltage.

Similarly, Figure 3.2B and Table 1 compare the average values of specific capacitance, C_m ($C_m = \delta C/\delta A$), measured for hDIBs with various percentages of PBPEO. Specific capacitance is determined as described elsewhere [67]. These data reveal that hDIBs containing up to 10 mol% PBPEO exhibit values of C_m similar to DPhPC-only DIBs at 0 mV DC (C_m = 0.64 μF/cm^2 [67]). Since C_m represents the ratio of dielectric permittivity, ϵ, to hydrophobic thickness, t, matching values of C_m and similar hydrophobic region dielectric constants (2.2 for DPhPC [67] vs. 2.5 for PB [73]) imply that hDIBs formed with 10 mol% or less PBPEO have similar hydrophobic thicknesses at 0 mV (Table 1). However, at 15 mol% PBPEO, the value of C_m measured at 0 mV DC decreases to ~0.55 μF/cm^2, which corresponds to a 3-4Å increase in hydrophobic thickness. Additionally, measurements of C_m at 200 mV DC are used to gauge changes in thickness due to voltage-induced oil exclusion or bilayer compression [51, 68]. All membrane types show higher values of C_m at 200 mV DC compared to their respective values at 0 mV DC, and the largest increase is observed for 15 mol% PBPEO, where C_m increases to an average value of ~0.62 μF/cm^2. This higher sensitivity to voltage correlates to the larger initial (zero-volt) thickness, and it suggests that a greater amount of oil-exclusion or membrane compression can occur when approximately 1 in 7 molecules in the membrane is PBPEO. Unfortunately, we failed to form bilayers with a PBPEO composition higher than 15 mol%. Therefore, it remains unknown how much thicker a PBPEO-only bilayer would be or how much its thickness decreases when a DC voltage is applied.

Equilibrium energetics of hDIBs

As observed in the image of 15 mol% PBPEO hDIB in Figure 3.1A, the presence of PBPEO in the interface results in adhered droplets with smaller values of contact area and contact angle at 0 mV than are observed for a DPhPC-only DIB. Figure 3A confirms this trend, showing that the average

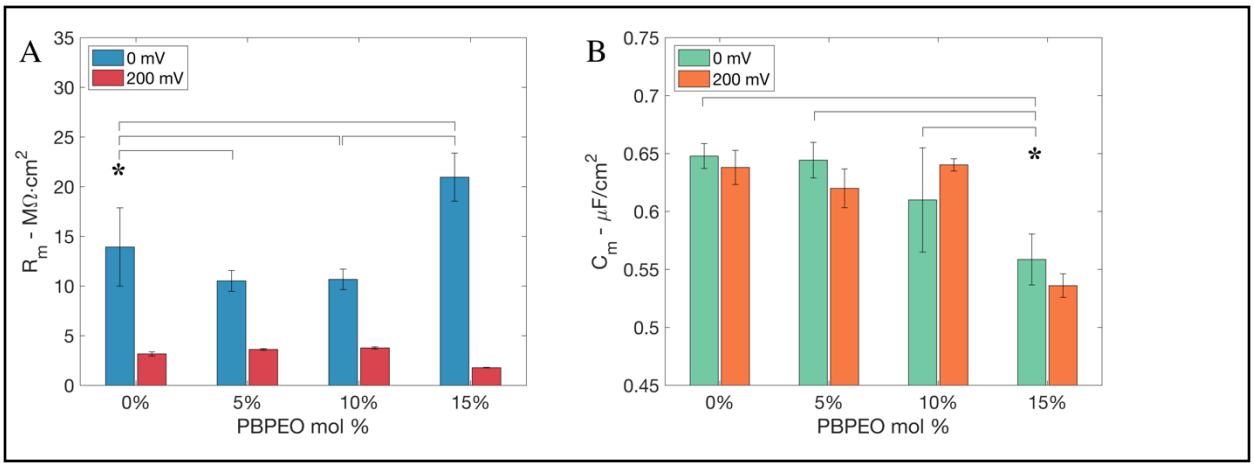


Figure 3.2. Electrical properties of hDIBs. (A) Membrane resistance measured at 0 mV (blue, n = 7) and 200 mV (red, n = 5). (B) Specific capacitance at 0 mV (green) and 200 mV (orange). Error bars represent one standard deviation; **denotes significant differences, where p < 0.05.*

contact angle at 0 mV, θ_0, decreases linearly from 34° at 0% PBPEO to ~24° at 15 mol% PBPEO. This reduction in contact reflects a lower gain in free energy through spontaneous adhesion [74]. To quantify how much the PBPEO alters the tensions of the monolayers, γ_m, and bilayer, γ_b, and the resulting adhesive energy describing the connected droplet pair, we employed an established technique [67] to first determine equilibrium values of γ_m. This is achieved by measuring changes in θ caused by applied voltage.

Due to electrowetting, an applied voltage charges the capacitive interface and lowers the apparent bilayer tension, γ_b [67]. This relaxation in bilayer tension leads to concomitant increases in contact area and angle needed to satisfy the three-force balance (Figure 3.1A) and conserve the fixed droplet volumes. Figure 3b

shows these changes in contact angle due to electrowetting, quantified as the change in the cosine of θ versus the square of the applied DC voltage for each membrane type. These data exhibit linear relationships, where the slope for a given series is governed by the ratio $C_m/4\gamma_m$. Therefore, performing a linear regression on each data series resulted in values of slope for each membrane composition that were used with their corresponding value of C_m (Table 3.1) to determine average values of γ_m [30]. Figure 3C and Table 3.1 show that γ_m decreases from 0.95 mN/m for a DPhPC-only DIB to ~0.56 mN/m for a DIB containing 15 mol% PBPEO. These differences in γ_m show that PBPEO molecules present in the membrane reduce interactions between oil and water molecules at the droplet surfaces. This could stem from hydrophobic PB blocks increasing the lateral packing density of amphiphiles in the monolayers or hydrophilic PEO blocks adopting mushroom like conformations that shield the hydrophobic lipid tails from water. Spectroscopy techniques such as vibrational sum frequency generation [75, 76] could be used to reveal PBPEO's specific mechanisms of action. The zero-volt tension of the bilayer γ_b was then computed

$$\gamma_b = 2\gamma_m \cos\theta_0. \qquad (1)$$

Values reported in Table 1 show that PBPEO in the interface lowers the γ_b by an amount proportional to the molar percentage of PBPEO. Thus, these measurements reveal that an hDIB formed by DPhPC and PBPEO has a similar hydrophobic thickness but a reduced lateral tension, a relationship that may affect the interactions of membrane-active species, such as transmembrane channels or engineered particles. Finally, the free energy of formation, ΔF, was calculated using:

Table 3.1. Summary of measured hDIB physical parameters at 0 mV.*

PBPEO mol%	Specific Resistance, R_m [MΩ·cm^2]	Specific Capacitance, C_m [μF/cm^2]	Hydrophobic thickness†, t [Å]	Contact Angle, θ_0 [°]	Monolayer Tension, γ_m [N/m]	Bilayer Tension, γ_b [N/m]	Free Energy of Formation, ΔF [mJ/m^2]
0	13.9 ± 3.92	0.65 ± 0.01	30.00 ± 0.04	33.5 ± 0.33	0.95 ± 0.10	1.58 ± 0.10	0.31 ± 0.03
5	10.5 ± 1.04	0.64 ± 0.02	30.46 ± 0.06	30.7 ± 0.27	0.90 ± 0.06	1.56 ± 0.05	0.25 ± 0.02
10	10.7 ± 1.03	0.62 ± 0.04	31.34 ± 0.21	26.8 ± 2.14	0.70 ± 0.09	1.31 ± 0.08	0.15 ± 0.04
15	21.0 ± 2.40	0.56 ± 0.47	34.81 ± 0.13	25.1 ± 1.60	0.53 ± 0.09	0.96 ± 0.08	0.09 ± 0.01

*average values and standard deviations computed from $n \geq 5$ independent measurements.

†computed from values of C_m using a value of 2.2 for the dielectric constant.

$$\Delta F = 2\gamma_m - \gamma_b \qquad (2)$$

This quantity reflects the reduction in free energy of the system gained by replacing the opposing monolayer-coated regions of the droplets with a shared bilayer interface. Alternatively, it can be interpreted as the energy per unit area (mN/m = mJ/m^2) required to separate the attached droplets. The specific value of ΔF is strongly dependent on both the choice of surfactant and oil [59, 74]. Here, the ΔF data in Figure 3.3D and Table 1 show that increasing the % of PBPEO reduces the free energy of formation from ~0.3 mJ/m^2 for 0% PBPEO to ~0.1 mJ/m^2 at 15 mol% PBPEO (a 66% reduction). Despite lower values of γ_m corresponding to bilayers containing PBPEO (a factor itself that can reduce ΔF), this trend suggests that DPhPC:PBPEO monolayers favor interactions with hexadecane molecules over those with an opposing monolayer of DPhPC:PBPEO. This trend is revealed in the data as well; the free energy gained during bilayer formation is a larger percentage of the monolayer tension when PBPEO is absent ($\Delta F/\gamma_m \sim 33\%$ for 0% PBPEO) versus when it is present ($\Delta F/\gamma_m \sim 17\%$ for 15 mol% PBPEO). More-favorable surfactant-oil interactions can also lead to a greater amount of oil retained in the membrane after thinning, a result that is consistent with the reduction in C_m (and the increase in t) observed for hDIBs containing 15 mol% PBPEO.

Ion channel formation and hDIB stability under applied voltage

The prior sections examined changes in membrane structure and energetics when PBPEO is present in both leaflets of the bilayer. Because the addition of PBPEO to DPhPC DIBs results in an increase in average hydrophobic thicknesses of less than 20 mol%, homogeneous mixing of the two components, and reduced membrane tension, we hypothesized these conditions may affect the voltage-driven insertion and ion channel formation of alamethicin (alm) peptides. To test this hypothesis, we performed cyclic voltammetry (CV) measurements on hDIBs of varying PBPEO% with 0.5 µg/ml alm added to both droplets.

Representative measurements of bilayer area-normalized ion currents versus applied voltage (120 mV amplitude, 10 mHz sinusoidal waveform) are shown in Figure 3.4A. The low current densities at voltages below 80mV correspond to alm residing in a surface-bound state on the membrane [77, 78]. At higher applied voltages, however, alm peptides are driven into the membrane, where they oligomerize and form conductive channels with neighboring monomers. This change of conformation by many alm peptides leads to an exponential increase in the measured ion current

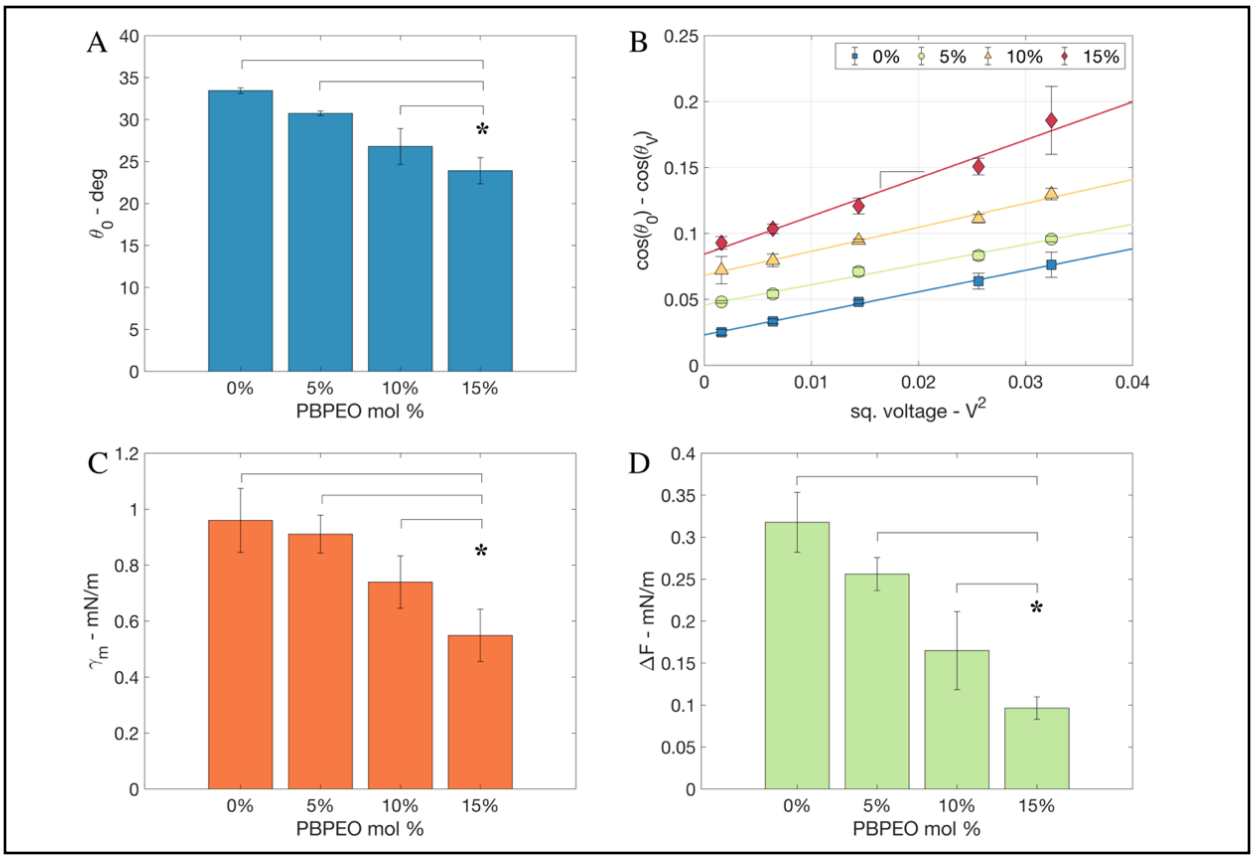


Figure 3.3. Energetics of hDIBs. (A) Contact angles measured at 0 mV. (B) The change in the cosine of the contact angle versus the square of the applied voltage for different PBPEO mol% in DPhPC. Data have been offset vertically for clarity of presentation. (C) In situ monolayer tensions calculated from the slopes obtained in (B). (D) Free energy of formation at 0 mV determined from monolayer tensions in (C) and contact angles in (A). A minimum of n=5 measurements were made of each quantity; error bars represent one standard deviation.

[49, 79], as is observed in Figure 3.3A at voltages near and above 100mV. The voltage threshold, V_{th}, is a thermodynamic parameter dependent on peptide concentration, temperature, and membrane fluidity, tension, and thickness [70, 80, 81]. V_{th} can be quantified and compared across measurements by locating the voltage at which the conductance of the bilayer increases above an arbitrary level. Herein, we select 100 μS/cm^2 as the threshold specific conductance for the membrane (shown as a dashed line) [82].It is visually apparent from 3.4 that an increased percentage of PBPEO leads to a lower intersection voltage between the measured current density and the threshold conductance (100 μS/cm^2). Specifically, V_{th} for 15 mol% PBPEO is 92 mV, versus 111 mV for 0 mol% PBPEO. This difference means that alm inserts and oligomerizes in an hDIB more easily (i.e., at lower voltage) than in a DPhPC-bilayer; i.e. there is a lower barrier to insertion and oligomerization. One reason for the drop in V_{th} is that macromolecular crowding (caused by the hydrated PEO groups) enhances peptide association on the membrane [83]—an increase in peptide concentration corresponds to an apparent reduction threshold voltage. Also, it may be that PEO groups extending past the lipid head groups blanket nearby regions of the membrane, which causes alm to adsorb in higher concentrations in remaining unshielded areas. A third possibility is that PBPEO interspersed in the membrane increases the fluidity of the bilayer by disrupting DPhPC tail order Nonetheless, this trend is interesting because it shows that the PEO hydrophilic groups, which extend past the phosphate head groups of the lipids into the bulk aqueous phase, do not inhibit membrane association/binding necessary for alm insertion. Thus, these measurements on alm show proof of concept that BCPs can be used to tune membrane properties in ways that could assist the interactions of other membrane-active species.

We observed a second change caused by PBPEO in alm-doped hDIBs. Figure 3.4B presents bar graphs of the average rupture potential of DIBs with (0.5 μM) and without alamethicin versus the percentage of PBPEO. Membrane rupture occurs when an electric field creates and drives unstable growth in voltage-induced pores (or defects) through the membrane [84]. The rupture potential for each composition was recorded when the two droplets coalesced under a slowly increasing DC voltage. Without PBPEO, the average rupture potential of a DPhPC DIB with and without alm is statistically similar (~250mV). However, as PBPEO% increases, the average rupture potential decreases steadily in the absence of alm (~200 mV for 15 mol% PBPEO). The energy required to

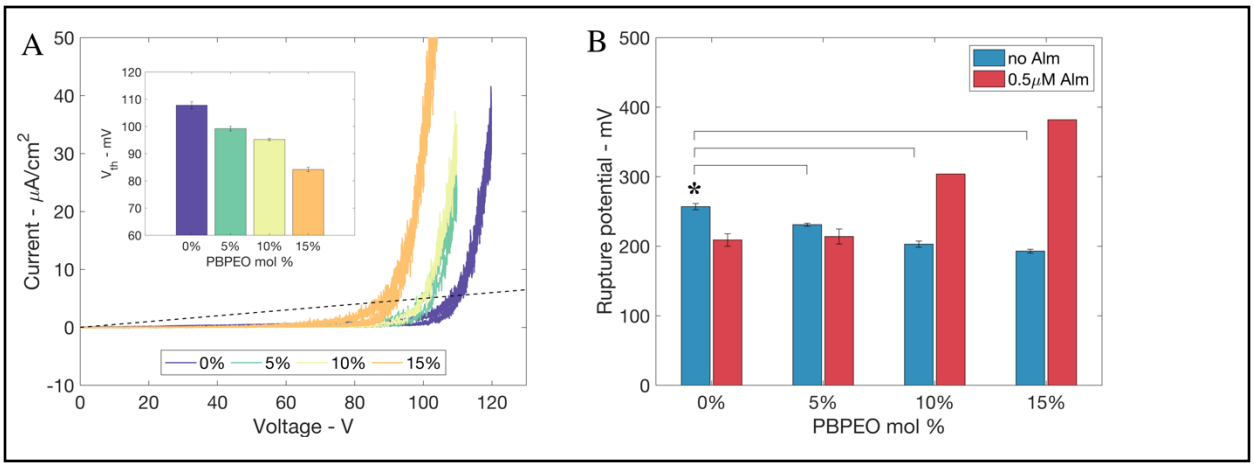


Figure 3.4. Behavior of alm in hDIBs. (A) Current-voltage curves of hDIBs with 0.5 μM alamethicin added to both droplets. Each current response is normalized by the initial membrane area at zero volts. The black line represents the specific conductance threshold (100 μS/cm^2) used to determine the voltage threshold for alamethicin insertion. Inset: Voltage threshold versus PBPEO mol% (n=5). (B) Bar graphs of the average rupture potential (n=5) measured with (0.5 μM) and without alamethicin versus PBPEO mol%. Error bars represent one standard deviation.

increase the size of a voltage-induced pore in the bilayer, and thus drive it to an unstable state that causes rupture, is proportional to membrane tension [84]. Therefore, the reduced rupture potentials of hDIBS correlate to the PBPEO-induced reductions in bilayer tension reported in Table 1. This relationship shows that the presence of PBPEO in the membrane, and its corresponding disordering effect on DPhPC tails, fails to equally penalize electroporation, which results in a lower rupture voltage. However, this relationship also suggests that the maximum rupture potential of a hDIB could be increased by understanding and controlling the lateral organization of lipids and diblocks in a bilayer. For example, some combinations of hybrid membrane constituents enhance molecular packing, as seen when cholesterol is added to bilayers constructed from low-melting point lipids [85].

In contrast, the rupture potential *increases* steadily when alm peptides are present. No error bars are provided for the 10 mol% and 15 mol% conditions because membranes were still intact despite the measured current exceeding the limits of measurement equipment; the reported rupture potential values for these conditions are therefore lower limits. However, the fact that rupture occurred at potentials well above 300 mV for these higher fractions of PBPEO strongly demonstrates the opposite trend. While the cause of this result is not fully understood, it appears to indicate a collective stabilizing effect caused by PBPEO and alm in the membrane. Differences in bilayer tensions, including under high voltages, may be a reason. Unfortunately, our method for extracting monolayer tension via changes in contact angle versus voltage is not well suited to assessing the tensions in alm-doped membranes due to the difficulty in measuring C_m at voltages where ion channels are open, and the conductance of the membrane is high. Moreover, due to the fact that membranes containing PBPEO exhibit lower threshold voltages for alm insertion, which leads to larger currents at a particular voltage, the resistance to rupture may be helped by more open ion channels in the bilayer. Nonetheless, this result adds to the possibility that doping lipid membranes with amphiphilic di-block copolymers can be used to augment the properties of a membrane while retaining a sufficiently biomimetic structure and function.

Conclusion

Herein, we examined the effects of adding a low molecular weight di-block copolymer amphiphile into lipid bilayers assembled between aqueous droplets in oil. We found that DPhPC DIBs doped with 0-15 mol% PBPEO form homogeneously mixed hybrid bilayers. These hybrid membranes

demonstrated similar (within 0 to +20 %) average hydrophobic thickness to lipid-only DIBs, are leak-free to ion transport, and are stable under applied potentials, which enabled a comprehensive assessment of the effects of added PBPEO on the physical properties of the interfacial bilayer. Our data show that increasing the fraction of PBPEO lowers both the monolayer and bilayer tensions by nearly 50% compared to DPhPC DIBs in hexadecane. Also, the energy of adhesion fell by 66% for 15 mol% PBPEO, which explains the reduced contact areas between droplets. It was also observed that an increased percentage of PBPEO in hDIBs reduces the voltage threshold for alamethicin channel formation and raises the rupture potential of membranes containing alm.

These results show proof of concept that BCPs can be used to selectively preserve and modulate the properties of hybrid membranes in ways that favor the interactions of other membrane-active species, yet also make them stable at higher voltages. These improvements, when combined with targeted studies of membrane permeability, could lead to further tunability of biomimetic membranes, such as enabling the development of bioelectronic devices for sensing, signal processing, and selective transport via ion-channels. Finally, this work also motivates research to better understand conditions and polymer architectures that allow for polymer-only DIBs with similar thickness to lipid membranes but significantly greater mechanical durability and resistance to chemical degradation.

Author Contributions

Subhadeep Koner: Conceptualization, Investigation, Formal Analysis, Writing – Original Draft. **Joseph Tawfik:** Investigation. **Farzin Mashali:** Conceptualization, Investigation. **Kristen Kennison:** Investigation. **Fred Heberle:** Formal Analysis, Writing – Review & Editing. **Yu-Ming Tu:** Investigation. **Manish Kumar:** Resources. **S. A. Sarles:** Conceptualization, Formal Analysis, Visualization, Writing – Review & Editing

The contents of this chapter are under review with the journal BBA Biomembranes.

References

1. Zhang, Y., et al., *Supported Lipid Bilayer Assembly on PEDOT:PSS Films and Transistors.* Advanced Functional Materials, 2016. **26**(40): p. 7304-7313.
2. Jewell, C.M., et al., *Oligonucleotide Delivery by Cell-Penetrating "Striped" Nanoparticles.* Angewandte Chemie International Edition, 2011. **50**(51): p. 12312-12315.
3. Verma, A., et al., *Surface-structure-regulated cell-membrane penetration by monolayer-protected nanoparticles.* Nat Mater, 2008. **7**(7): p. 588-595.
4. Astier, Y., O. Braha, and H. Bayley, *Toward Single Molecule DNA Sequencing: Direct Identification of Ribonucleoside and Deoxyribonucleoside 5'-Monophosphates by Using an Engineered Protein Nanopore Equipped with a Molecular Adapter.* Journal of the American Chemical Society, 2006. **128**(5): p. 1705-1710.
5. Bayley, H., I. Cazimoglu, and C.E.G. Hoskin, *Synthetic tissues.* Emerging Topics in Life Sciences, 2019. **3**(5): p. 615-622.
6. Song, W., et al., *Artificial water channels enable fast and selective water permeation through water-wire networks.* Nature Nanotechnology, 2020. **15**(1): p. 73-79.
7. Kumar, M., et al., *Highly permeable polymeric membranes based on the incorporation of the functional water channel protein Aquaporin Z.* Proceedings of the National Academy of Sciences, 2007. **104**(52): p. 20719-20724.
8. Tang, C.Y., et al., *Desalination by biomimetic aquaporin membranes: Review of status and prospects.* Desalination, 2013. **308**(0): p. 34-40.
9. Ottova, A.L. and H. Ti Tien, *Self-assembled bilayer lipid membranes: from mimicking biomembranes to practical applications.* Bioelectrochemistry and Bioenergetics, 1997. **42**(2): p. 141-152.
10. Cremer, P.S. and S.G. Boxer, *Formation and Spreading of Lipid Bilayers on Planar Glass Supports.* The Journal of Physical Chemistry B, 1999. **103**(13): p. 2554-2559.
11. Nardin, C., M. Winterhalter, and W. Meier, *Giant Free-Standing ABA Triblock Copolymer Membranes.* Langmuir, 2000. **16**(20): p. 7708-7712.
12. Discher, D.E. and A. Eisenberg, *Polymer Vesicles.* Science, 2002. **297**(5583): p. 967-973.
13. Wong, D., T.-J. Jeon, and J. Schmidt, *Single molecule measurements of channel proteins incorporated into biomimetic polymer membranes.* Nanotechnology, 2006. **17**(15): p. 3710.

14. Belegrinou, S., et al., *Biomimetic supported membranes from amphiphilic block copolymers.* Soft Matter, 2010. **6**(1): p. 179-186.
15. Krywko-Cendrowska, A., et al., *Recent Advances in Hybrid Biomimetic Polymer-Based Films: from Assembly to Applications.* Polymers, 2020. **12**(5).
16. Go, Y.K. and C. Leal, *Polymer–Lipid Hybrid Materials.* Chemical Reviews, 2021. **121**(22): p. 13996-14030.
17. Ruysschaert, T., et al., *Hybrid Nanocapsules: Interactions of ABA Block Copolymers with Liposomes.* Journal of the American Chemical Society, 2005. **127**(17): p. 6242-6247.
18. Kowal, J., et al., *Planar Biomimetic Membranes Based on Amphiphilic Block Copolymers.* ACS Macro Letters, 2014. **3**(1): p. 59-63.
19. Gonzalez-Perez, A., et al., *Biomimetic triblock copolymer membranes: from aqueous solutions to solid supports.* Soft Matter, 2011. **7**(3): p. 1129-1138.
20. Wang, H.L., et al., *Mechanically robust and highly permeable AquaporinZ biomimetic membranes.* Journal of Membrane Science, 2013. **434**: p. 130-136.
21. Winzen, S., et al., *Submicron hybrid vesicles consisting of polymer–lipid and polymer–cholesterol blends.* Soft Matter, 2013. **9**(25): p. 5883-5890.
22. Garni, M., et al., *Biopores/membrane proteins in synthetic polymer membranes.* Biochimica et Biophysica Acta (BBA) - Biomembranes, 2017. **1859**(4): p. 619-638.
23. Cheng, Z. and A. Tsourkas, *Paramagnetic Porous Polymersomes.* Langmuir, 2008. **24**(15): p. 8169-8173.
24. Kita-Tokarczyk, K., et al., *Monolayer Interactions between Lipids and Amphiphilic Block Copolymers.* Langmuir, 2009. **25**(17): p. 9847-9856.
25. Nam, J., P.A. Beales, and T.K. Vanderlick, *Giant Phospholipid/Block Copolymer Hybrid Vesicles: Mixing Behavior and Domain Formation.* Langmuir, 2011. **27**(1): p. 1-6.
26. Schulz, M., et al., *Hybrid lipid/polymer giant unilamellar vesicles: effects of incorporated biocompatible PIB–PEO block copolymers on vesicle properties.* Soft Matter, 2011. **7**(18): p. 8100-8110.
27. Lim, S.K., et al., *Hybrid, nanoscale phospholipid/block copolymer vesicles.* Polymers, 2013. **5**(3): p. 1102-1114.

28. Gettel, D.L., et al., *Mixing, Diffusion, and Percolation in Binary Supported Membranes Containing Mixtures of Lipids and Amphiphilic Block Copolymers.* Journal of the American Chemical Society, 2014. **136**(29): p. 10186-10189.
29. Balestri, A., et al., *Organized Hybrid Molecular Films from Natural Phospholipids and Synthetic Block Copolymers: A Physicochemical Investigation.* Langmuir, 2020. **36**(37): p. 10941-10951.
30. Kang, J.Y., et al., *Enhancing membrane modulus of giant unilamellar lipid vesicles by lateral co-assembly of amphiphilic triblock copolymers.* Journal of colloid and interface science, 2020. **561**: p. 318-326.
31. Hamada, N., S. Gakhar, and M.L. Longo, *Hybrid lipid/block copolymer vesicles display broad phase coexistence region.* Biochimica et Biophysica Acta (BBA)-Biomembranes, 2021. **1863**(4): p. 183552.
32. Bieligmeyer, M., et al., *Reconstitution of the membrane protein OmpF into biomimetic block copolymer–phospholipid hybrid membranes.* Beilstein journal of nanotechnology, 2016. **7**(1): p. 881-892.
33. Meuse, C.W., et al., *Hybrid Bilayer Membranes in Air and Water: Infrared Spectroscopy and Neutron Reflectivity Studies.* Biophysical Journal, 1998. **74**(3): p. 1388-1398.
34. Dao, T.P.T., et al., *Phase Separation and Nanodomain Formation in Hybrid Polymer/Lipid Vesicles.* ACS Macro Letters, 2015. **4**(2): p. 182-186.
35. Kowal, J., et al., *Hybrid Polymer–Lipid Films as Platforms for Directed Membrane Protein Insertion.* Langmuir, 2015. **31**(17): p. 4868-4877.
36. Thoma, J., et al., *Membrane protein distribution in composite polymer–lipid thin films.* Chemical Communications, 2012. **48**(70): p. 8811-8813.
37. Ruiz-Pérez, L., et al., *Separating Extreme pH Gradients Using Amphiphilic Copolymer Membranes.* ChemPhysChem, 2018. **19**(16): p. 1987-1989.
38. Bayley, H., et al., *Droplet interface bilayers.* Molecular BioSystems, 2008. **4**(12): p. 1191-1208.
39. Hwang, W.L., et al., *Asymmetric Droplet Interface Bilayers.* J. Am. Chem. Soc., 2008. **130**(18): p. 5878-5879.
40. Holden, M.A., D. Needham, and H. Bayley, *Functional Bionetworks from Nanoliter Water Droplets.* J. Am. Chem. Soc., 2007. **129**(27): p. 8650-8655.

41. Mruetusatorn, P., et al., *Control of Membrane Permeability in Air-Stable Droplet Interface Bilayers.* Langmuir, 2015. **31**(14): p. 4224-4231.
42. Milianta, P.J., et al., *Water Permeability across Symmetric and Asymmetric Droplet Interface Bilayers: Interaction of Cholesterol Sulfate with DPhPC.* Langmuir, 2015. **31**(44): p. 12187-12196.
43. Michalak, Z., et al., *Effect of Monoglyceride Structure and Cholesterol Content on Water Permeability of the Droplet Bilayer.* Langmuir, 2013. **29**(51): p. 15919-15925.
44. Michalak, Z., et al., *Tunable crystallization via osmosis-driven transport across a droplet interface bilayer.* CrystEngComm, 2012. **14**(23): p. 7865-7868.
45. Sarles, S.A., J.D.W. Madden, and D.J. Leo, *Hair cell inspired mechanotransduction with a gel-supported, artificial lipid membrane.* Soft Matter, 2011. **7**(10): p. 4644-4653.
46. Tamaddoni, N. and S.A. Sarles, *Toward cell-inspired materials that feel: measurements and modeling of mechanotransduction in droplet-based, multi-membrane arrays.* Bioinspiration & Biomimetics, 2016. **11**(3): p. 036008.
47. Xu, J. and D.A. Lavan, *Designing artificial cells to harness the biological ion concentration gradient.* Nat Nano, 2008. **3**(11): p. 666-670.
48. Restrepo Schild, V., et al., *Light-Patterned Current Generation in a Droplet Bilayer Array.* Scientific Reports, 2017. **7**: p. 46585.
49. Najem, J.S., et al., *Memristive Ion Channel-Doped Biomembranes as Synaptic Mimics.* ACS Nano, 2018. **12**(5): p. 4702-4711.
50. Koner, S., et al., *Memristive plasticity in artificial electrical synapses via geometrically reconfigurable, gramicidin-doped biomembranes.* Nanoscale, 2019. **11**(40): p. 18640-18652.
51. Najem, J.S., et al., *Dynamical nonlinear memory capacitance in biomimetic membranes.* Nature Communications, 2019. **10**(1): p. 3239.
52. Maraj, J.J., et al., *Short-Term Facilitation-Then-Depression Enables Adaptive Processing of Sensory Inputs by Ion Channels in Biomolecular Synapses.* ACS Applied Electronic Materials, 2021.
53. Taylor, G.J., et al., *Electrophysiological interrogation of asymmetric droplet interface bilayers reveals surface-bound alamethicin induces lipid flip-flop.* Biomicrofluidics, 2018. **accepted**(in print).

54. Nguyen, M.-A., et al., *Hydrodynamic trapping for rapid assembly and in situ electrical characterization of droplet interface bilayer arrays.* Lab on a chip, 2016. **16**(18): p. 3576-3588.
55. Schimel, T.M., et al., *Pressure-driven generation of complex microfluidic droplet networks.* Microfluidics and Nanofluidics, 2021. **25**(9): p. 78.
56. Villar, G., A.D. Graham, and H. Bayley, *A Tissue-Like Printed Material.* Science, 2013. **340**(6128): p. 48-52.
57. Challita, E.J., et al., *Encapsulating Networks of Droplet Interface Bilayers in a Thermoreversible Organogel.* Scientific Reports, 2018. **8**: p. 6494.
58. Booth, M.J., I. Cazimoglu, and H. Bayley, *Controlled deprotection and release of a small molecule from a compartmented synthetic tissue module.* Communications Chemistry, 2019. **2**(1): p. 142.
59. Tamaddoni, N., et al., *Reversible, voltage-activated formation of biomimetic membranes between triblock copolymer-coated aqueous droplets in good solvents.* Soft Matter, 2016. **12**: p. 5096 - 5109.
60. Basham, C., et al. *Memcapacitive Devices in Neuromorphic Circuits via Polymeric Biomimetic Membranes*. in *ASME 2019 Conference on Smart Materials, Adaptive Structures and Intelligent Systems*. 2019.
61. Klara, S.S., et al., *Magnetically Directed Two-Dimensional Crystallization of OmpF Membrane Proteins in Block Copolymers.* Journal of the American Chemical Society, 2016. **138**(1): p. 28-31.
62. Kumar, M., et al., *High-density reconstitution of functional water channels into vesicular and planar block copolymer membranes.* Journal of the American Chemical Society, 2012. **134**(45): p. 18631-18637.
63. Shen, Y.-x., et al., *Achieving high permeability and enhanced selectivity for Angstrom-scale separations using artificial water channel membranes.* Nature Communications, 2018. **9**(1): p. 2294.
64. Taylor, G.J. and S.A. Sarles, *Heating-enabled formation of droplet interface bilayers using Escherichia coli total lipid extract.* Langmuir, 2014. **31**(1): p. 325-337.

65. El-Beyrouthy, J., et al., *A new approach for investigating the response of lipid membranes to electrocompression by coupling droplet mechanics and membrane biophysics.* Journal of The Royal Society Interface, 2019. **16**(161): p. 20190652.
66. Venkatesan, G.A. and S.A. Sarles, *Droplet immobilization within a polymeric organogel improves lipid bilayer durability and portability.* Lab on a Chip, 2016. **16**: p. 2116 - 2125.
67. Taylor, G.J., et al., *Direct in situ measurement of specific capacitance, monolayer tension, and bilayer tension in a droplet interface bilayer.* Soft Matter, 2015. **11**(38): p. 7592-7605.
68. Gross, L.C.M., et al., *Determining Membrane Capacitance by Dynamic Control of Droplet Interface Bilayer Area.* Langmuir, 2011. **27**(23): p. 14335-14342.
69. Venkatesan, G.A., et al., *Adsorption Kinetics Dictate Monolayer Self-Assembly for Both Lipid-In and Lipid-Out Approaches to Droplet Interface Bilayer Formation.* Langmuir, 2015. **31**(47): p. 12883-12893.
70. Taylor, G.J. and S.A. Sarles, *Heating-Enabled Formation of Droplet Interface Bilayers Using Escherichia coli Total Lipid Extract.* Langmuir, 2015. **31**(1): p. 325-337.
71. Korner, J.L. and K.S. Elvira, *The role of temperature in the formation of human–mimetic artificial cell membranes using droplet interface bilayers (DIBs).* Soft Matter, 2021. **17**(39): p. 8891-8901.
72. Kara, S., et al., *Diphytanoyl lipids as model systems for studying membrane-active peptides.* Biochimica et Biophysica Acta (BBA) - Biomembranes, 2017. **1859**(10): p. 1828-1837.
73. Pegoraro, M. and K. Mitoraj, *Dielectric properties of trans-1,4 polybutadiene.* Die Makromolekulare Chemie, 1963. **61**(1): p. 132-138.
74. Poulin, P. and J. Bibette, *Adhesion of Water Droplets in Organic Solvent.* Langmuir, 1998. **14**(22): p. 6341-6343.
75. Basham, C.M., et al., *Nanoparticle-Induced Disorder at Complex Liquid–Liquid Interfaces: Effects of Curvature and Compositional Synergy on Functional Surfaces.* ACS Nano, 2021. **15**(9): p. 14285-14294.
76. Chowdhury, A.U., et al., *Insight into the Mechanisms Driving the Self-Assembly of Functional Interfaces: Moving from Lipids to Charged Amphiphilic Oligomers.* Journal of the American Chemical Society, 2020. **142**(1): p. 290-299.

77. Hall, J.E., et al., *Alamethicin. A rich model for channel behavior*. Biophysical Journal, 1984. **45**(1): p. 233-247.
78. Vodyanoy, I., J.E. Hall, and T.M. Balasubramanian, *Alamethicin-induced current-voltage curve asymmetry in lipid bilayers.* Biophys. J., 1983. **42**(1): p. 71-82.
79. Okazaki, T., et al., *Ion Channels of Alamethicin Dimer N-Terminally Linked by Disulfide Bond.* Biophys. J., 2003. **85**(1): p. 267-273.
80. Vodyanoy, I., J.E. Hall, and T.M. Balasubramanian, *Alamethicin-induced current-voltage curve asymmetry in lipid bilayers.* Biophysical Journal, 1983. **42**(1): p. 71-82.
81. Stankowski, S., U.D. Schwarz, and G. Schwarz, *Voltage-dependent pore activity of the peptide alamethicin correlated with incorporation in the membrane: salt and cholesterol effects.* Biochimica et Biophysica Acta (BBA) - Biomembranes, 1988. **941**(1): p. 11-18.
82. Taylor, G., et al., *Electrophysiological interrogation of asymmetric droplet interface bilayers reveals surface-bound alamethicin induces lipid flip-flop.* Biochimica et Biophysica Acta (BBA) - Biomembranes, 2019. **1861**(1): p. 335-343.
83. McClintic, W.T., et al., *Macromolecular Crowding Affects Voltage-Dependent Alamethicin Pore Formation in Lipid Bilayer Membranes.* The Journal of Physical Chemistry B, 2020. **124**(25): p. 5095-5102.
84. Freeman, S.A., M.A. Wang, and J.C. Weaver, *Theory of electroporation of planar bilayer membranes: predictions of the aqueous area, change in capacitance, and pore-pore separation.* Biophysical Journal, 1994. **67**(1): p. 42-56.
85. Karal, M.A.S., et al., *Influence of cholesterol on electroporation in lipid membranes of giant vesicles.* European Biophysics Journal, 2020. **49**(5): p. 361-370.

Appendix



Figure 3.5: Side view images of connected droplets suspended in hexadecane oil.

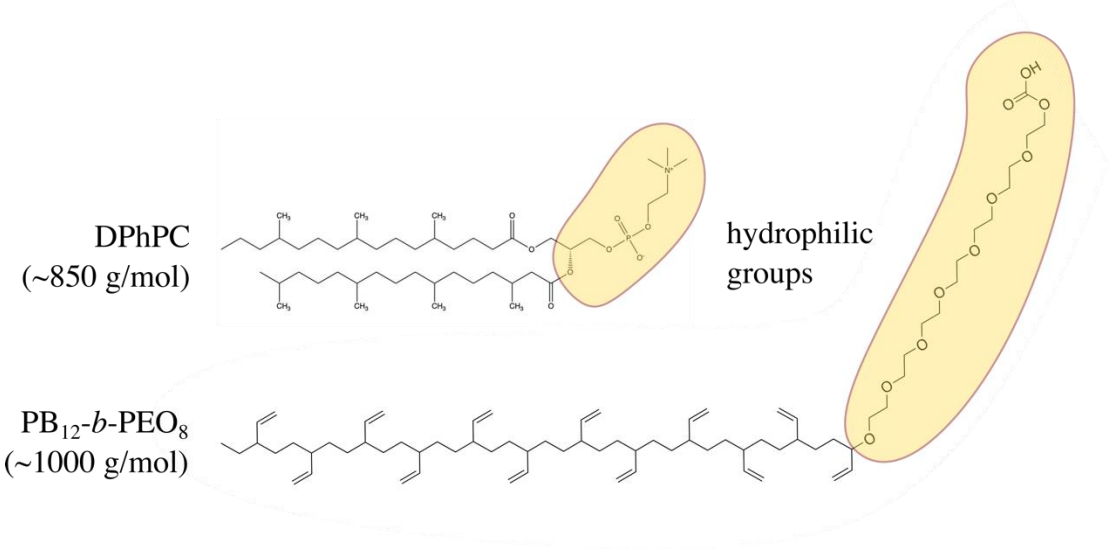
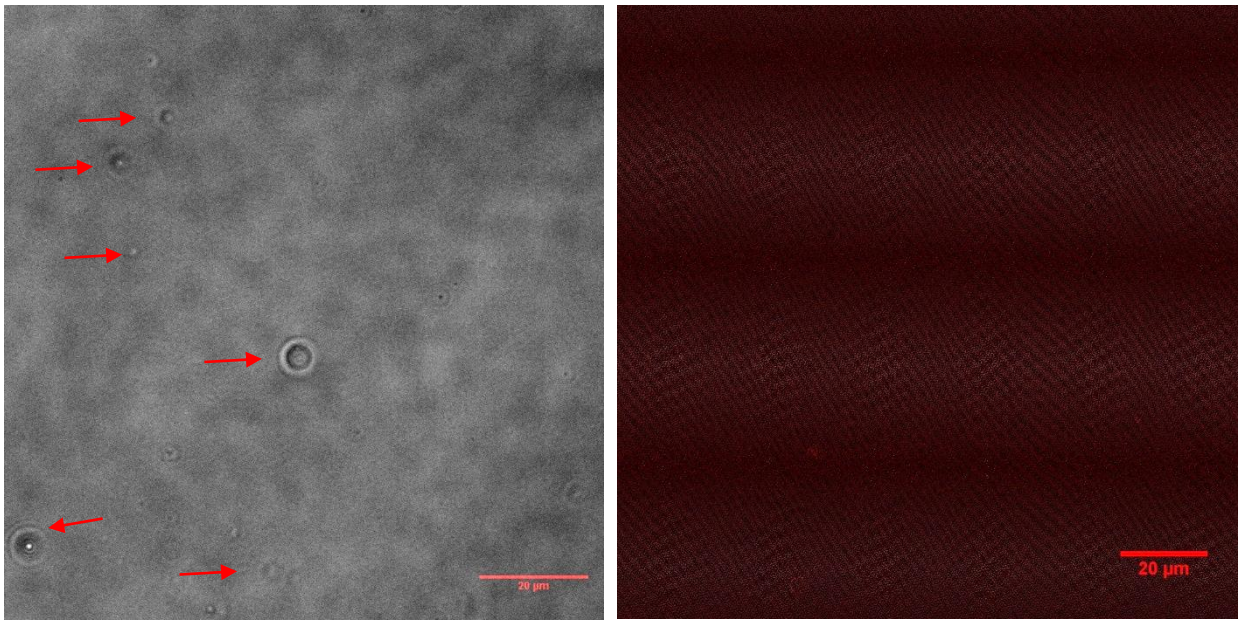
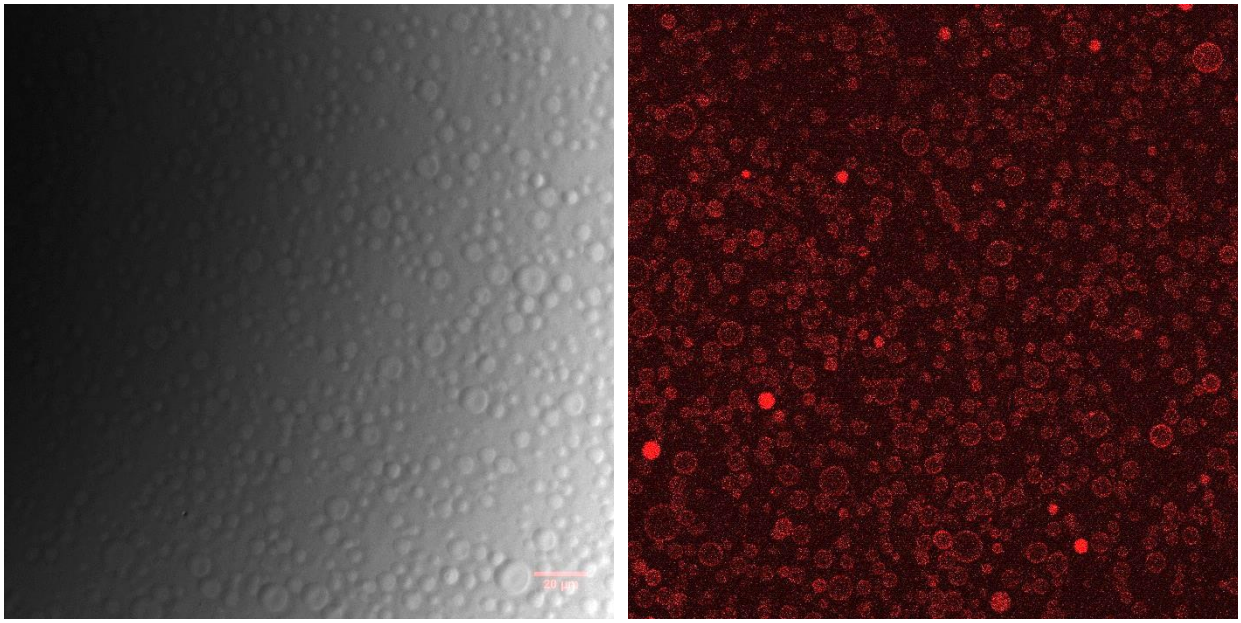


Figure 3.6. Chemical structures of DPhPC phospholipids and PBPEO diblock copolymers, with hydrophilic portions, highlighted.



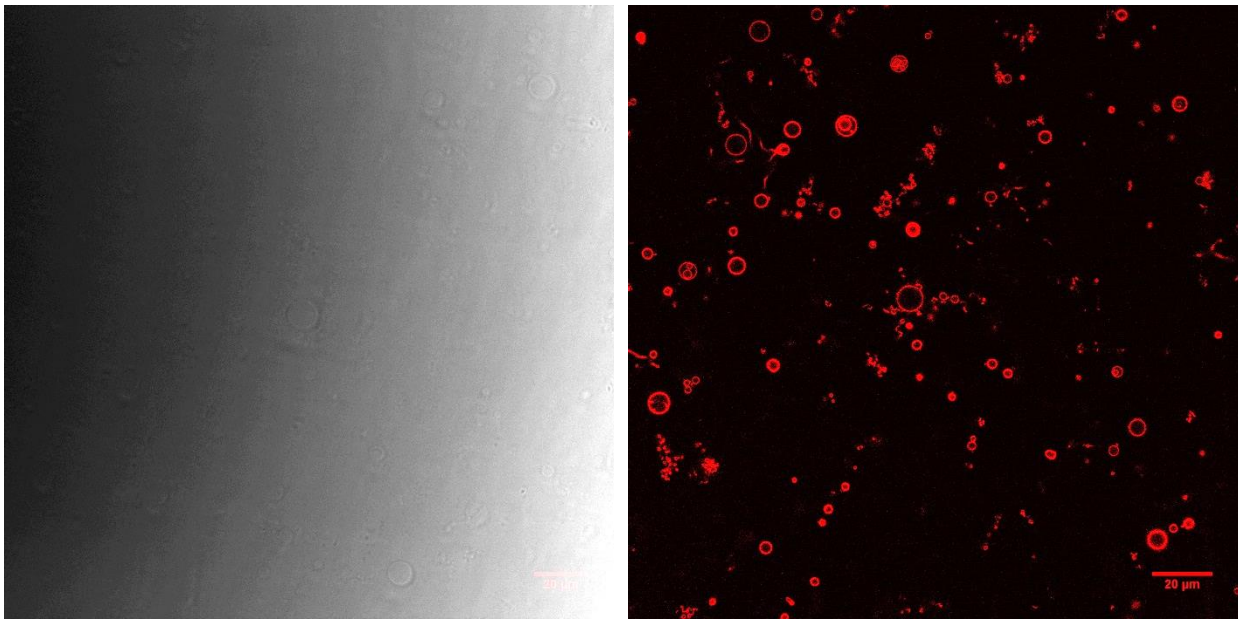
A B

Figure 3.7. Brightfield with phase contrast (A) and fluorescence (B) images of PBPEO-only GUVs.



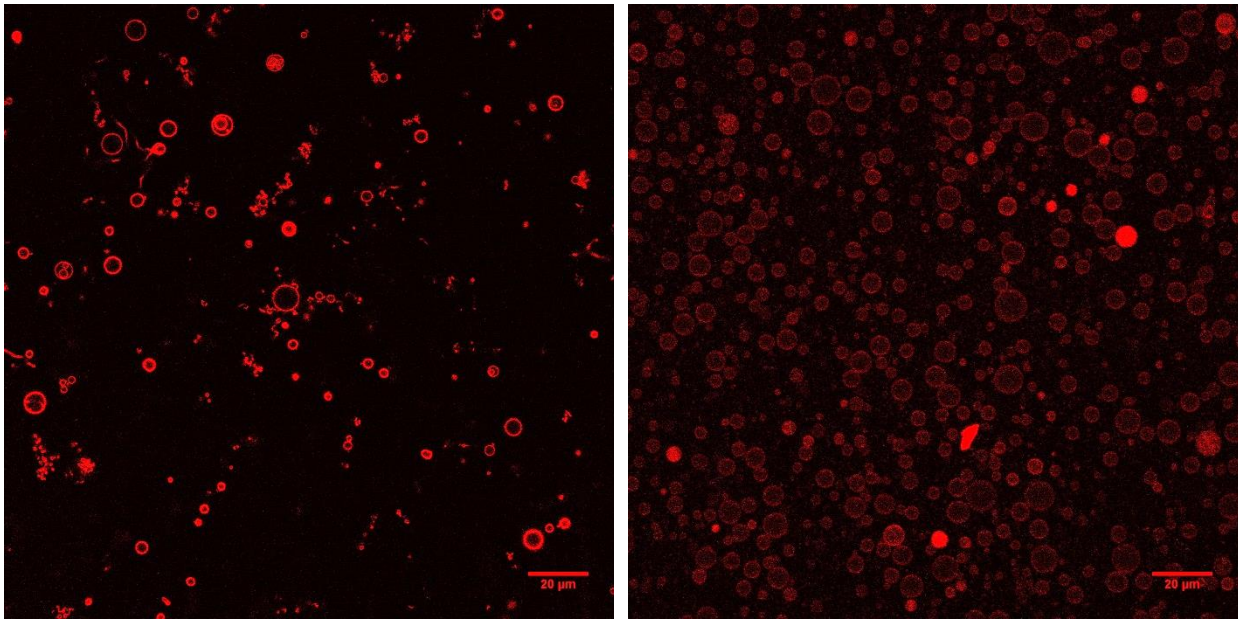
A B

Figure 3.8. Brightfield with phase contrast (A) and fluorescence (B) images of GUVs containing 20 mol% DPhPC and 80 mol% PBPEO plus 0.1 mol% Nile Red.



A B

Figure 3.9. Brightfield with phase contrast (A) and fluorescence (B) images of GUVs containing 80 mol% DPhPC and 20 mol% PBPEO plus 0.1 mol% Nile Red.



A B

Figure 3.10. Confocal fluorescence images of GUVs containing 80 mol% DPhPC and 20 mol % PBPEO (A) versus those with 80 mol% DPhPC and 20 mol % PBPEO (B).

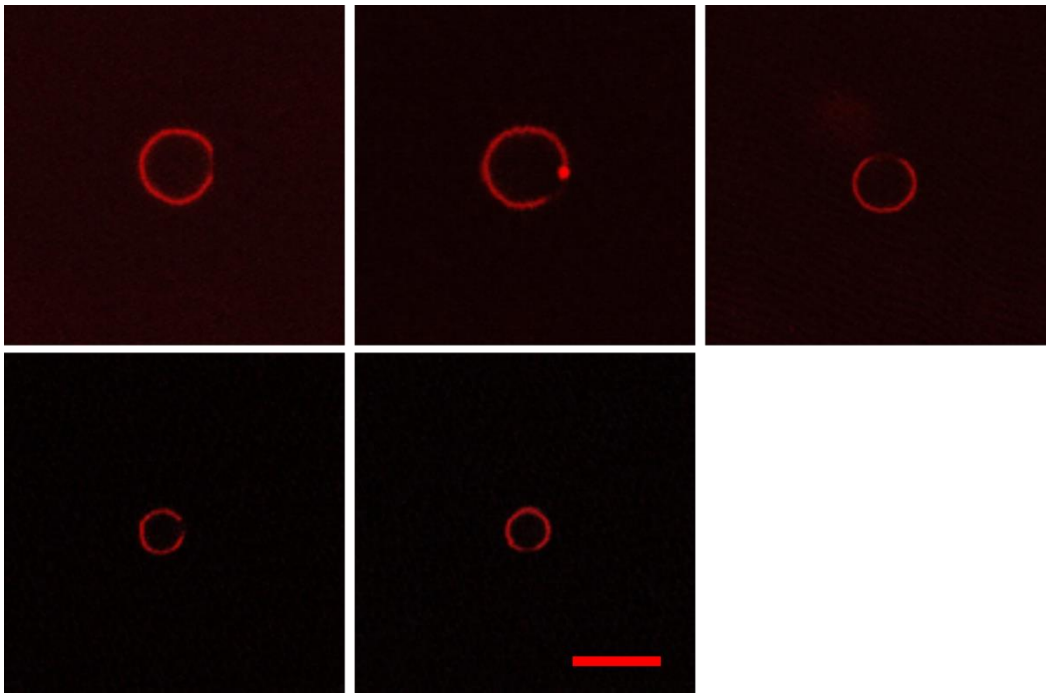


Figure 3.11. Representative confocal slices of unique hGUVs formed with 80 mol% DPPC, 20 mol% PBPEO, plus 0.1 mol% NR, showing phase separation. The non-fluorescent regions of the perimeters are polymer-rich regions. Scale bar: 5 *µm.*

Table 3.3. Equilibrium interfacial tension (IFT) values obtained on DPhPC and PBPEO monolayers.

% PBPEO	Amphiphile phase	Final Conc. (mg/ml)	Equilibrium IFT (mN/m)*	Time to Steady State (min)
0% (100% DPhPC)	aqueous	2.00	1.02	4.0
5%	aqueous	2.12	0.95	8.0
10%	aqueous	2.24	0.68	12
15%	aqueous	2.36	0.55	20
100%	aqueous	3.00	9.8	8.3
		5.00	7.0	6.7
		8.00	6.3	9.2
100%	oil	0.50	0.48	0.5

* average of $n \geq 4$ measurements

CHAPTER IV. Neuromorphic metamaterials for mechanosensing and perceptual associative learning.

Preface to the chapter IV

This chapter is a realization of combined effort of multiple people from two research groups at University of Tennessee and Purdue University.

The bistable meta-sheet with strain sensors used in this project was designed and manufactured by my colleagues at Purdue University. Polymeric thin film memristors were integrated via other traditional electronic components to create a smart system capable of classification of spatial information originating from any tactile activity on the bi-stable meta-sheet. The usage of memristors as components for both processing and memory reflects the advantage of these devices and highlights the importance of these devices in building novel systems capable of autonomous learning.

My efforts were towards delivering feedback on strain sensor development via electrical characterization the same, design and fabrication of memristors, integration of memristors with other transducers (guided and helped by my colleague at UTK), and analyzing output of the network.

Abstract

Physical systems exhibiting neuromechanical functions promise to enable structures with directly encoded autonomy and intelligence. We report on a class of neuromorphic metamaterials embodying bioinspired mechanosensing, memory, and learning functionalities obtained by leveraging mechanical instabilities and flexible memristive materials. Our prototype system comprises a multistable metamaterial whose bistable units filter, amplify, and transduce external mechanical inputs over large areas into simple electrical signals using piezoresistivity. We record these mechanically transduced signals using non-volatile flexible memristors that remember sequences of mechanical inputs, providing a means to store spatially distributed mechanical signals in measurable material states. The accumulated memristance changes resulting from the sequential mechanical inputs allow us to physically encode a Hopfield network into our neuromorphic metamaterials. This physical network learns a series of external spatially distributed input patterns. Crucially, the learned patterns input into our neuromorphic metamaterials can be retrieved from the final accumulated state of our memristors. Therefore, our system exhibits the ability to learn without supervised training and retain spatially distributed inputs with minimal external overhead. Our system's embodied mechanosensing, memory, and learning capabilities establish an avenue for synthetic neuromorphic metamaterials enabling the learning of touch-like sensations covering large areas for robotics, autonomous systems, wearables, and morphing structures.

Introduction

The nervous systems of animals comprise networks of distributed sensory, memory, and control elements that enable perception, reaction and adaptation in response to varied external stimuli. The coevolution of the nervous system and body morphology is thought to reduce the complexity of sensed signals due to morphological computing and short neuronal connections. This results in a form of neuromechanical control that requires few inputs to fulfil complex functions[1, 2]. Some organisms, such as comb jellies (phylum Ctenophora[3]), perform complex tasks even without a central nervous system. This capability stems from coevolved neuromechanical systems that exploit morphological and sensory couplings to create autonomic responses,[2] which constitute one of the simplest forms of learned behavior. Typical autonomic behaviors include reflexes[4], preflexes, and central pattern generators,[5] all of which leverage fast, decentralized sense-compute-actuate control loops.[1] At the most basic level, this is achieved through the synergy of

morphology, sensing, computation, and actuation systems that perceive stimuli,[6] filter noise,[7] and store valuable information in the physical state of the systems. Achieving similar capabilities in synthetic systems is important for realizing the next generation of autonomic, multifunctional, power-efficient materials, devices, and systems. Single artificial neuromechanical functions encoded into material systems have been demonstrated, including sensing,[8, 9] filtering and thresholding,[10, 11] and different forms of mechanically-encoded memory [12, 13].

Learned autonomic biological responses are thought to be created when groups of neurons reinforce synaptic connections, resulting in simultaneous firing.[14, 15] Inspired by synapses and neurons, neuromorphic computing has emerged as a field leveraging history-dependent responses and electrical tunability of materials and devices to approximate brain-inspired computation.[16] Many neuromorphic systems exploit memory resistive, or memristive, materials to achieve the characteristics of synaptic plasticity, memory storage, and even threshold-gated neural spiking. Thus, memristors offer a low-power, analog route for highly parallelized computation.[17] Recently, neuromorphic materials have been integrated with sensory systems to encode and process external inputs that enable the formation of memory and learning.[18] In a seminal work, afferent nervous functions have been mimicked via neuromorphic circuits to convert information from mechanical inputs into motor functions, thereby completing a synthetic reflex arc.[19] Artificial neuromechanical perception has also been demonstrated in flexible substrates embedding synaptic transistors[20] and Nafion-based memristors[21] capable of durably encoding spatiotemporal tactile excitations into signals amenable for *ex-situ* classification using supervised learning. Spatiotemporal, long-term memory formation and retention has also been shown using a 3x3 array of CNT/PDMS piezoresistive sensors and Pt/HfO_2/TiN memristors.[22]

Online learning (implying adaptation as data is sensed) is a crucial function of neuromechanical systems that has so far been much less explored in mechanically reconfigurable, neuromorphic material systems. Thus, synthetic material systems enabling integrated mechanosensing, memory, and autonomic learning capabilities remain rare. Realizing synthetic systems that embody natural neuromechanical systems' functions promises to enable structures with advanced functionalities such as autonomy and intelligence. We report on a class of neuromorphic metamaterials embodying bioinspired mechanosensing, memory, and learning functionalities achieved by leveraging local mechanical instabilities and soft memristive materials. Our prototype consists of

a multistable metamaterial whose mechanosensing units filter, amplify, and transduce into simple electrical signals external mechanical inputs applied over large areas (c.a. 10^2 cm^2) using threshold-dependent structural bistability and embedded piezoresistive sensors (Figure 4.1). We encode the transduced signals using non-volatile flexible memristors, thus providing a means to store spatially distributed mechanical signals in analog material states. Notably, the additive nature of the accumulated memristance changes allows us to physically encode into our neuromorphic metamaterials a Hopfield network[23, 24] that learns a series of applied spatially distributed mechanical inputs. This is achieved with memristor arrays connected to capture pair-wise interactions between different mechanosensing units yielding the Hopfield network's connectivity matrix. Crucially, the learned, mechanically applied patterns can be retrieved from the final electrical resistance states of the memristors. Therefore, our system displays the ability to learn online, retaining spatially distributed inputs exceeding a critical threshold with minimal external overhead.

The combined mechanosensing and thresholding behavior of our neuromorphic metamaterial is reminiscent of event cameras[25, 26] in which pixels asynchronously record events when light intensity exceeds a specified threshold, offering power-efficient and low-latency visual perception. In such systems, pixel triggering events are timestamped and recorded in silicon-implemented memory components. Our metamaterial provides a tactile analog to an event camera where recording occurs when the mechanical input exceeds a threshold value; however, it is augmented with the capacity to sequentially encode these input events as memories in the form of accumulated final memristance states. In the sense that the Hopfield network is continuously updated as tactile events exceed a threshold, our neuromorphic metamaterial offers a new route for realizing engineering systems with online learning through tactile perception for applications in robotics, autonomous systems, wearables, and morphing structures.

Materials and Methods

Unit cell and metasheet fabrication– The unit cells are 3D printed using fused deposition modeling (FDM) on a Raise3D Pro2 printer using the settings in Table S1. We use Ninjatek Cheetah TPU filament (E = 26 MPa)[27] for the dome and base and BlackMagic3D PLA + graphene composite filament (E = 3767 MPa) for the sensor.[28, 29] Due to the PLA + graphene material being two orders of magnitude stiffer than the TPU, the sensors are embedded in the TPU base to avoid

delamination. A connection point is left exposed at each end. To address the high contact resistance,[30, 31] we paint each connection point with a thin layer of highly conductive carbon paint[32] before attaching copper wire, using another layer of conductive paint. After drying, we apply a dot of hot glue on each connection to secure the wire in place. Metasheets are manufactured following the same procedure, with one continuous 3D print.

Unit cell resistance measurements– The resistances of the dome sensors are measured using a voltage divider circuit with a 2 kΩ shunt resistor. The voltage drop over the sensor is measured using a National Instruments USB-6251 data acquisition system and a simple National Instruments Labview multimeter program. The DC power supply (Keysight E36313A) applies 2 V to the circuit.

Mechanical tests– Inversion force and thresholding tests are performed on an Instron 3345 Universal Testing Machine with

Bluehill software. Test domes are printed with a 2 mm diameter hole in the center, where an M2 screw is attached with a nut and washer. The other end of the screw attaches to a machined aluminum block, which is held by the Instron machine grips. The dome sample to be tested sits on a 3D printed base with a 20 mm x 20 mm square hole centered under the dome to allow for free inversion (Figure 4.18). The sensor is hooked up to the same voltage divider circuit as used for other resistance measurements. Resistance data is gathered for 10 seconds before the Instron test begins in order to capture the initial state of the sensor. For each test, the head of the machine moves down at a rate of 20 mm/min. Once inversion is detected via a drop in the reaction force, the test stops, and the machine returns the dome to the starting position. The sensor data is collected until the total test time reaches 2 minutes. The dome is then reset manually and the test rerun. Each specimen tested first undergoes 10 full inversion tests. Then, the threshold behavior is tested following the same settings as for the inversion force, but with the end of test triggered by a maximum applied load. This maximum load is incrementally increased each test until the inversion force threshold is reached.

Finite element analysis– The unit cells are modeled in Abaqus using linear elastic material properties and S4R shell elements. To capture the bistable behavior, geometric nonlinear analysis is used. The unit cell is initially modeled in the stress-free ground state. Snap-through is triggered using an enforced displacement applied to the center node of the dome while the edges are pinned.

These boundary conditions are then released while the center node is fixed to show the free inverted state of the unit cell.

Fabrication of memristors– ITO glass slides (10-15 Ω/sq) were cleaned with (in the following order) soap-water, de-ionized water, ethanol, acetone, propanol via sonification for 15 minutes each and dried using ultra-pure Nitrogen. The conductive face of clean ITO slide was oxidized in an oxygen plasma chamber using a PE 50 XL Benchtop low-pressure plasma system for 1 minute to increase the hydrophilicity of the surface, which encourages wetting of PEDOT:PSS solution resulting in uniform distribution. 3 wt % PEDOT:PSS solution bought from Sigma-Aldrich was spin-coated on to a clean ITO glass slide at 3000 rpm for 40 seconds. It was then dried at 120 ˚C for 20 minutes and vacuum annealed for more than 24 hours. This results in a thin film (~ 60 nm thickness) measured using a F20 device from Filmetrics. Portions of the ITO were covered with insulating tape, which when removed post-fabrication recovered a naked ITO surface to be used as a bottom electrode as seen in Figure 4.12b.

Characterization of memristors– Electrical characterization of the fabricated devices was done using a SP 200 Potentiostat from Biologic. Spring-loaded copper contacts were used as the top electrode as shown in Figure 4.12b. Bipolar sinusoidal voltage waveforms of 5 V and 100 mHz were used for the current-voltage (i-v) characterization of the devices.

Programming of pulsatile input– A function generator (Hewlett–Packard 3314A) was used to generate unipolar square voltage pulses as supply V(t) and V_{ref} to the circuit. Multiple Op-Amps were used to build the amplifier circuit as shown in Figure 4.14. A DC power source (BK precision Triple Output DC power source 1762) was used to tune $V_{in}(t)$ for reading and writing pulses. An Arduino (DUE R3) was used to record the response signals across the memristor, i.e V_m.

Results and discussions

Mechanosensing– The mechanosensing unit cell is comprised of a bistable, compliant dome with a piezoresistive sensor embedded in the flat membrane surrounding the dome. This membrane may connect multiple dome unit cells to form a metasheet. The geometry of the unit cell is defined by the dome height, h; thickness, t; and radius, r_d; as well as the base width, w, and piezoresistive sensor dimensions (Figure 4.5).[33] Each dome-shaped unit is geometrically bistable with two stable states: the stress-free, as-printed *ground* state and the *inverted* state (Figure 4.2a). The state

of the dome determines the deflection and strain in the surrounding base membrane (Figure 4.2b). The bistability of the dome consequently means the sensor at the base also exhibits two stable configurations with corresponding resistance levels. Thus, the electrical resistance of the piezoresistive sensor, *R*, and the structural behavior of the dome are intrinsically linked.

We demonstrate this mechanoelectrical coupling over multiple inversion cycles using 3D printed unit cells composed of TPU with conductive PLA sensors (Figure 4.2c). The initial cycles differ from the steady-state largely due to the strain softening behavior of the TPU substrate, which is most significant in the first inversion cycles (Figure 4.6).[34] This effect is compounded by permanent damage induced by strain in the stiffer and more brittle conductive PLA sensor.[35] Thus, repeatedly strained sensors show higher ground state resistance than the as-printed resistance.[30, 34-36] This baseline drift can be reduced by inverting the domes several times before use. After this initial phase, the unit cell has two distinct, repeatable resistance levels (Figure 4.2c), with the lower resistance level, $R_\epsilon = R_g$, indicating the ground state and the higher resistance level, $R_\epsilon = R_i$, indicating the inverted state. The difference in resistance between the two states is on the order of several hundred Ohms. The short transient spikes in between steady-state values are due to the high strains experienced during dome snap-through between states, which cause the sensors to briefly lose conductivity.[11, 30]

Filtering and Thresholding– Filtering is a critical function of neuromechanical systems that allows them to consolidate external stimuli to those which which meet a particular threshold. In our neuromorphic metasheet, switching between the stable states of the dome is a threshold-dependent process: a minimum force, F_{th}, is required to trigger snap-through of the dome from the ground state to the inverted state. The force and energy required for snap-through are proportional to the material properties and geometry as follows, where *E* is the elastic modulus and *v* is the Poisson's ratio:[33, 38]

$$F_{th} \sim \textit{Inversion energy} \sim \frac{Et^3}{1-\nu^2}\left(\frac{4h^2}{r_d^2}\right) \quad (1)$$

Forces below the inversion threshold, $F < F_{th}$, do not cause the dome to snap-through to the inverted state. Therefore, when a sub-threshold force is removed, the deflected dome returns to the ground stable state, and the sensor reverts to its ground state resistance, R_g. Consequently, no

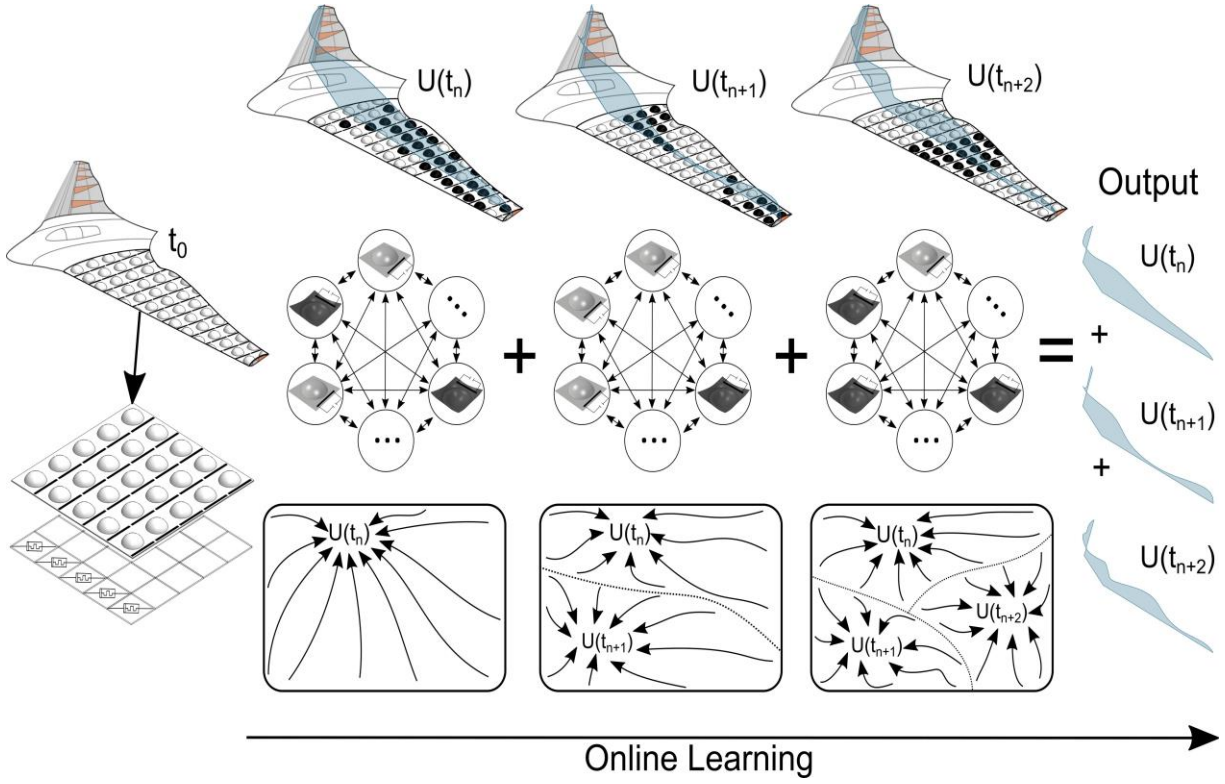


Figure 4.1. Neuromorphic metamaterial composed of mechanosensing unit cells with inherent filtering, transduction, mechanoelectric signal amplification, and memory capabilities. The units' transduction drives non-volatile memristors that display cumulative memristance variation when excited above a voltage threshold mediated by the dome state-dependent piezoresistive sensor. These characteristics allow for realizing physical Hopfield networks capable of encoding several spatiotemporal patterns as attractors of the network's interaction matrix, the synaptic weights of which are stored as the final (current) states of the memristors. The physical Hopfield networks enabled by our neuromorphic metamaterials are trained online by continuously changing distributed mechanical inputs (such as pressures over wings). This allows for realizing substrates exhibiting event camera-like tactile perception[37] with online learning and reduced external memory as several patterns can be retrieved from the memristors' final states.

memory is written into the structure. However, forces at or above this threshold, $F \geq F_{th}$, trigger snap-through to the inverted stable state, and memory of the force application event is encoded in the structure. The strains associated with the inverted state cause the sensor to remain at R_i (Figure 4.7). This filtering capability is schematically illustrated in Figure 4.2d.To demonstrate tunable thresholding capabilities in our metasheet design, we compare unit cells with domes of two different thicknesses: 0.8 mm and 0.9 mm (Figure 4.2e). All other parameters are preserved for both domes (h = 7 mm, r_d = 8 mm). Using a tensile testing machine, we apply point loads to the top of each dome (Figure 4.8). When the load is limited to 16 N, $F < F_{th}$ for both domes, so neither dome inverts, and the applied load is filtered out: the sensors return to their original ground state resistance values once the load is removed. When the load is increased to 18 N, the inversion threshold is met for the t = 0.8 mm dome, and the final resistance of the sensor shifts to its inverted state value, thereby demonstrating memory of the event. For the thicker t = 0.9 mm dome, 18 N $< F_{th}$, so the load is again filtered out. By increasing the applied load to 22 N, the inversion threshold is met for the t = 0.9 mm dome, and this is remembered by the change in the sensor resistance. This comparison illustrates the geometry-dependent thresholding that enables filtering of insufficient mechanical signals. The same threshold force tunability can also be achieved by varying the dome height (Figure 4.9).

Nonlinear Signal Amplification– The second key function of mechanosensing units is the amplification of input signals for easier detection. Switching the states of the bistable domes amplifies the local mechanical strain in the metasheet, a nonlinear response that produces large changes in sensor resistance in response to dome inversion. This amplification is critical for writing memory to the linked memristors; at least a 10% change in sensor resistance is preferred. To quantify this amplification of local mechanical strain, we conducted finite element analyses (FEA) to examine the stresses and strains in the membrane surrounding the dome, where the sensors are located. These simulations reveal that the stresses and strains in the membrane are inversely proportional to the radial distance from the center of the dome, r (Figure 4.2b, Figure 4.5b). This relationship between r and the radial and tangential stresses, σ_r and σ_θ, follow the below analytical expressions, where D_2, D_3, and D_4 are constants:[39]

$$\sigma_r = D_2(1/r^2) + D_3 + D_4 \log(r) \quad (2)$$

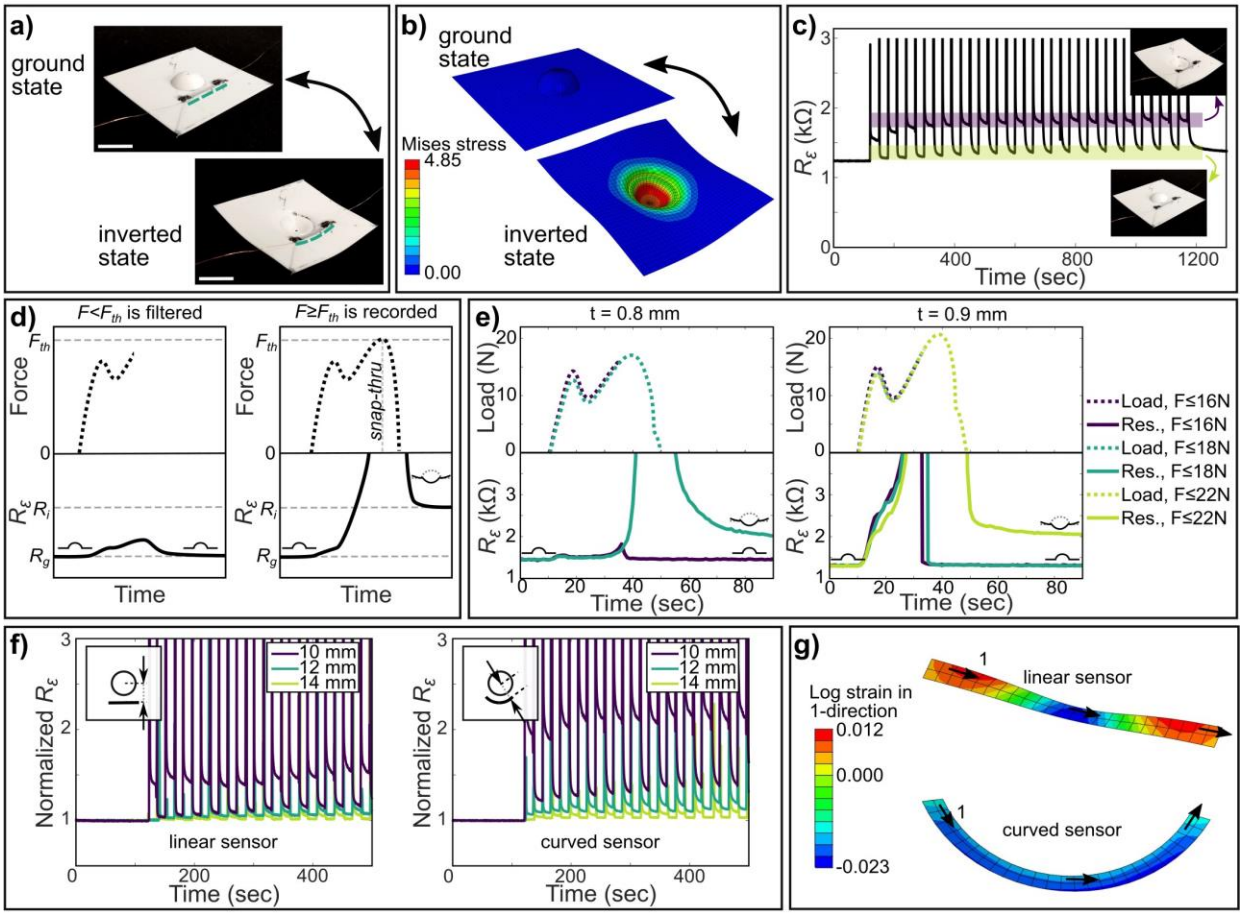


Figure 4.2. a) The bistable unit cell in its ground and inverted states. The sensor is flat in the ground state and curves out-of-plane in the inverted state. Scale bars are 16 mm, the diameter of the dome. b) FEA stress plots of the unit cell dome without an embedded sensor. c) The resistance of the sensor, R, over 18 inversion cycles with 30 second intervals between snap-through events. After the initial increase in resistance, the unit cell displays two distinct, consistent levels of resistance corresponding to the stable states. The dome has dimensions h = 7 mm, t = 0.8 mm, and r_d = 8 mm. d) The bistability thresholding functionality is schematically illustrated. Forces below the threshold, $F < F_{th}$, do not induce snap-through and are filtered out: the sensor's initial and final resistances correspond to the ground state, R_g. Forces at or above the threshold, $F \geq F_{th}$ cause the dome to undergo snap-through to the inverted state, and the event is recorded via the sensor's final resistance corresponding to the inverted state, R_i. e) The filtering tunability is experimentally demonstrated by the changing snap-through load for unit cells of two different thicknesses, t = 0.8 mm and t = 0.9 mm (h = 7 mm, r_d = 8 mm). f) Linear and curved sensors at distances of 10, 12, and 14 mm from the center of the dome (h = 7 mm, t = 0.8 mm, r_d = 8 mm)

are compared to demonstrate changing nonlinear signal amplification. g) Isolated FEA strain plots for the linear and curved sensors at 10 mm from the center of the dome in the inverted state.

$$\sigma_\theta = -D_2(1/r^2) + D_3 + D_4(1 + \log(r)) \quad (3)$$

Therefore, changing the location of the piezoresistive sensor relative to the dome changes the effective amplification factor of the mechanosensing unit, which govens the magnitude of the change in sensor resistance in response to dome inversion. We experimentally demonstrate this first with a basic linear sensor, measuring 24 mm x 1.75 mm x 0.3 mm. Using a dome radius of 8 mm, we print unit cells with sensors placed at 14, 12, and 10 mm from the dome center (Figure 4.2f). To compare the changes in sensor resistance and remove the variations due to 3D printing, we normalize the resistance values using each sensor's as-printed resistance. At a distance of 14 mm, there is little discernible change in the sensor's resistance value when the dome is inverted. At 12 mm, the observed spikes indicate snap-through, but the sensor lacks two distinct resistance levels. At 10 mm, the sensor exhibits both the snap-through spikes and distinguishable ground and inverted state resistance levels. By placing the sensor closer to the dome, we increase the strain in the sensor in the inverted state and therefore its corresponding change in electrical resistance.

The amplification can be further increased by changing the geometry of the sensor. To target the region of high strain close to the dome perimeter, we print and test sensors with the same dimensions but following circular arcs with varying radii from the center of the dome. At r = 14 mm and r = 12 mm, the spikes indicating snap-through are clearly displayed. Unlike a linear sensor at a distance of 12 mm, the curved sensor displays two distinct levels of resistance, differing in value by 10-15%. At 10 mm away, the difference between the two resistance levels is 90% of the initial resistance, compared to only a 40% difference for the linear sensor. This increase in signal amplification may be explained by inspecting the longitudinal (1-direction) strain in each type of sensor with FEA (Figure 4.2g). We are most interested in the 1-direction strain because the conductivity is highly directionally dependent due to the internal alignment of conductive microparticles in the direction of extrusion.[40] The linear sensor shows bands of very low strains, which should not significantly contribute to a change in resistance. Furthermore, the presence of both tensile and compressive strains in the linear sensor causes resistance fluctuations that result in partial signal cancellation. In contrast, the curved sensor shows a uniform compressive strain, with no regions of strain below 1%. This uniform strain means the effects of dome inversion are more strongly displayed throughout the sensor, resulting in increased signal amplification. For simplification purposes and to avoid the increased damage that occurs with more highly strained

curved sensors (Figure 4.10), we use metasheets with linear sensors to connect to memristors. Curved sensors could be made more practical by using a less brittle conductive filament; this is left to future work.

Spatiotemporal Memory– The mechanosensing functionality of our metasheets can be used to encode the transduced distributed mechanical inputs into memories. When mechanical inputs cause certain domes to invert, the events' occurrence and spatial pattern are recorded by the metasheet's deflection. The pattern formed in the metasheet indicates the sites experiencing a force exceeding a programmed threshold, $F \geq F_{th}$. To catalogue sequentially applied patterns, we couple the dome strain sensors to non-volatile memory resistors, resulting in an auxiliary memory layer. Specifically, this layer consists of voltage-dependent polymeric memristors based on flexible polymer films and off-the-shelf components and aims to electrically remember dome inversion events transduced by the mechanosensing units. Figure 4.3a illustrates the scheme we used to convert discrete (and even repeated) changes in dome sensor resistance, R, into multi-bit memristive states, M (Ω). Other integration schemes are also feasible, such as for a 1:1 dome-memristor pair (Figure 4.3a) or scaled in parallel across larger $m \times n$ arrays.

Because the dome sensors are passive devices and the memristors are voltage-activated, a fixed amplitude voltage waveform, $V(t)$, is supplied to induce a current through the sensor and a proportional voltage drop across a resistor in series with the sensor. A rectangular voltage waveform (where $V_{min} = 0$ and $V_{max} > 0$) is chosen to reduce the DC power consumption and enable incremental programming of the memristor during times when the dome is inverted (i.e. the applied force is $\geq F_{th}$, and thus the sensor resistance is high:$R_\epsilon = R_i$). To enable this signal to program a voltage-controlled memristor, we implemented a fixed gain amplification circuit that outputs a voltage proportional to $\Delta R_\epsilon$and fed this through a switch regulator with a 5 V switching threshold (See Figure 4.11 for details). The switch regulator ensures that the voltage transmitted to the memristor, $V_{in}(t)$, has a consistent amplitude, even when successive dome inversions affect the total change in R. In this way, $V_{in}(t)$ represents the convolution of $V(t)$ and the time when the dome is inverted (i.e.,$R_\epsilon = R_i$): the resulting response yields $V_{in}(t)$ equal to 0 V
when the dome is not inverted and a peak voltage value of 5 V when the dome is inverted. Voltage signal $V_{in}(t)$ is then applied to the memristor and a resistor wired in series (see appendix section A.6 for details on how R_s was selected), which enables the divided voltage across the memristor, $V_m(t)$, to be sampled as a measurable state of electrical memory for the corresponding dome. Table

1 shows the scheme's logic, illustrating that changes in memristance ($|\Delta M| > 0$) can only occur when the dome is inverted and $V_m(t)$ (which is also proportional to $V(t)$) is sufficiently high to induce a change in M.

The polymeric memristors used herein consist of a PEDOT:PSS thin film (~ 60 nm thick) sandwiched between indium tin oxide(ITO) and copper (Cu) electrodes (effective electrode diameter ~ 1.8 mm; see Figure 4.13 for device architecture). PEDOT:PSS forms a strong, flexible polymer matrix[41, 42] that enables mixed ionic-electronic transport, and it has been used to create organic memristive devices interfaced with reactive and noble metal electrodes displaying high OFF/ON ratios.[43, 44] Furthermore, the fact that PEDOT:PSS films can be fabricated through simple, low-temperature processing to make functional memristors makes it a promising memristor material candidate for enabling a conformal memory layer in mechanosensitive neuromorphic metasheets.

Representative voltage-controlled current measurements obtained on six distinct PEDOT:PSS memristors are shown in Figure 4.3b. The arrows denote the direction of the measured current path in response to one cycle of a 100 mHz sinusoidal voltage. The significant hysteresis in these $i - v$ curves indicates that the devices can reversibly switch between a high resistive state (HRS ~ 15.2 kΩ) and a low resistance state (LRS ~ 1.31 kΩ) in response to varying the applied voltage. The counterclockwise direction of current flow at positive voltages and the clockwise direction of current flow at negative voltages shows that these memristors exhibit a non-volatile memristance.[45, 46] Specifically, when the applied voltage on the Cu electrode relative to the grounded ITO electrode increases above +3 V (V_{th}) (See S10 Figure for measurement technique details), the devices switch (i.e., SET) from the HRS to the LRS as reflected in the sharp increase in current. Only when the probe voltage is lowered below -4 V do the devices RESET to the HRS. This means that programmed states of resistance can be stored in the sample even when the voltage to the device is removed (or set to zero). While the precise mechanism of voltage-activated resistive switching in these devices is still under investigation, these simple, low-cost, potentially conformal devices yield consistent performance across dozens of batches (Figure 4.14) and suitable cycle-to-cycle stability (Figure 4.15).

The 1:1 dome-memristor pair operation scheme described above and shown in Figure 4.3a seeks to incrementally reduce from HRS the memristance of a specific memory device in response to

Table 4.1. Dome inversion and memristance logic.

Applied force	Dome state	Sensor resistance, R	Input voltage	Memristor voltage	$\lvert\Delta M\rvert$
$< F_{th}$	Ground	Low (R_g)	$V_{in}(t) = 0$	$V_m(t) = 0$	0
$\geq F_{th}$	Inverted	High (R_i)	$V_{in}(t) \propto V(t)$	$V_m(t) \propto V_{in}(t)$	> 0

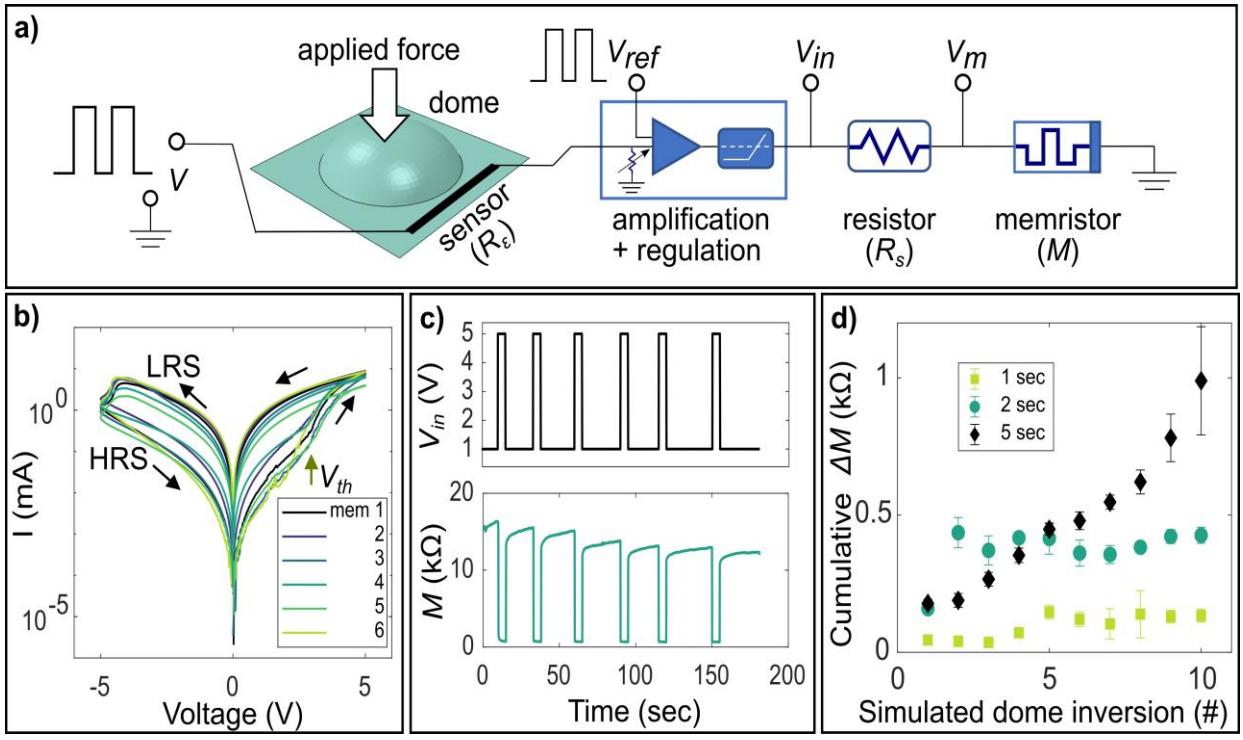


Figure 4.3. Integration scheme for transducing dome inversions into electrical memories. a) Schematic layout of 1:1 dome-memristor pair connection to incrementally program the memristor in response to changes in dome state. b) Current-voltage relationship for ITO/PEDOT:PSS/Cu memristors shows non-volatile memristance. c) Incremental reductions in memristance (from HRS) induced by 6 subsequent dome inversions corresponding to when the input voltage is 5 V, following the scheme in a). d) Cumulative reduction in memristance with each simulated dome inversion event across different pulse widths.

discrete dome inversions. Based on the $i - v$ behaviors in Figure 4.3, we tested the ability to incrementally program the memristors using a series of 5 V rectangular pulses. Each pulse lasts 5 sec and occurs once every 15 sec, an intentional choice that corresponds closely to the 100 mHz sweep frequency used for $i - v$ measurements (Figure 4.16). A low-amplitude voltage (1 V < V_{th}) is used to *read* the new resistance state of the memristor between pulses. Figure 4.3c shows the incremental reductions in $M(t)$ induced by successive 5 V pulses, i.e., it is partially switched from HRS to LRS with each pulse. Adjusting the pulse width and tuning the pulse amplitude relative to the SET voltage can be used to design the memristance variation per event and extend the number of programmable resistance states that each memristor can access. By varying the amplitude of $V_{in}(t)$ from the switch regulator, we observed that a 4 V amplitude of V_m results in a steady cumulative change in resistance across subsequent pulses (Figure 4.17). For V_m values below 3.5 V, we observe smaller total changes and greater variability per subsequent pulse. This information allowed us to determine the necessary amplitude of $V_{in}(t)$ supplied by the switch regulator. We also explored the duration of the writing pulses to determine a suitable pulse width. We compared the cumulative reductions in a memristor's resistance for three different pulse widths(T_{on}), revealing that for 1 and 2 second pulses, the cumulative changes in the resistance are small and unsteady (Figure 4.3d). This is because the pulse is too brief to drive adequate memristance changes. In contrast, using 5 sec pulses yielded consistent, monotonic changes in device resistance, validating the 1:1 dome-memristor operational scheme. While this writing pulse is long compared to other memristors, we expect they could respond significantly faster by reducing the thickness and electrode dimensions and unveiling the mechanisms of switching. For comparison, PEDOT:PSS-based organic electrochemical transistors can exhibit voltage-driven conductance changes in less than one millisecond [47].

Spatially distributed input learning: physical Hopfield networks– The combined mechanosensing and history recording capabilities of our metamaterial allow us to implement a physical learning system based on Hopfield networks[23] and the Hebbian learning rule.[48, 49] Hopfield networks consist of interconnected neurons and synapses that learn a series of input patterns stored as minima (i.e., attractors) in their energy landscapes. These patterns can be retrieved following the associative memory paradigm.[48] Hopfield networks achieve this by utilizing a fully connected network architecture that strengthens the synaptic connection between activated artificial neurons. Specifically, patterns ascribed to neuron states, such as images represented by

pixels, are stored in the network's interaction matrix (**J**) (Appendix section A.12 for details), which form different attractors in the networks' energy landscape (Figure 4.19).[49] We leverage the cumulative resistance changes in our memristors, triggered by dome inversions, to capture the interactions between dome units, thus updating the synaptic weights J_{ij} and storing the spatial patterns sequentially input into our metamaterial.

The physical Hopfield network consists of a $m \times n$ dome metasheet array (Figure 4.4a), with each unit cell (dome + sensor) acting as an individual artificial neuron[1] and the interconnecting memristors acting as synapses. Each unit can adopt two possible states: (+1) ground state and (-1) inverted state (Figure 4.2a). The interactions between unit cells can be captured by connecting different dome pairs to an XOR gate, as illustrated for a 2 × 2 ($n = m = 2$) array in Figure 4.4a. This writes a resistance change for every "on" and "off" neuron pair interaction (Figure 4.20). The number of memristors was reduced by considering the convergence properties of the networks ($J_{ii} \leq 0$ and $J_{ij} = J_{ji}$), which reduces the number of needed interactions to the upper triangular positions of the $mn \times mn$ interaction matrix labeled asU_i $(i = 1, 2, \ldots, M = \frac{m \times n}{2}(m \times n - 1)$; see Figure 4.4a). By using this scheme, the Hopfield network can be trained directly by physical inputs with different external patterns as they occur (i.e., the network is trained online).

A 3-stage measurement scheme was implemented to capture the interactions between dome units by using the cumulative memristor response (Figure 4.4b). In stage 1, an initialization pulse (INIT) of 4.3 V for 20 sec was used to pre-set each memristor to a value that changes linearly in response to subsequent voltage pulses (described in Figure 4.18). Stage 2 involves a calibration procedure consisting of a series of four 4.3 V, 5 sec writing pulses (simulating dome inversion events) preceded and followed by 1.5 V, 10 sec reading pulses. The voltage across the memristor (V_m) is measured correspondingly, which directly reflects the resistance state of the memristor. The first read pulse reflects the initial HRS of the memristor (V_0^{iC}), and the second read pulse reflects the resistance state of the memristor after the four calibration writing pulses (V_f^{iC}). The difference between the two read pulses accounts for the net change $\Delta V^i = (V_0^{iC} - V_f^{iC})/4$ due to four simulated dome inversions. In stage 3, the memristor network is subjected to a series of training pulses generated by actual dome inversion events (physically induced), which are also preceded and

[1] The term artificial neuron refers to a unit in Hopfield networks jargon; however, the terminology does not imply biomimetic neural functionality.

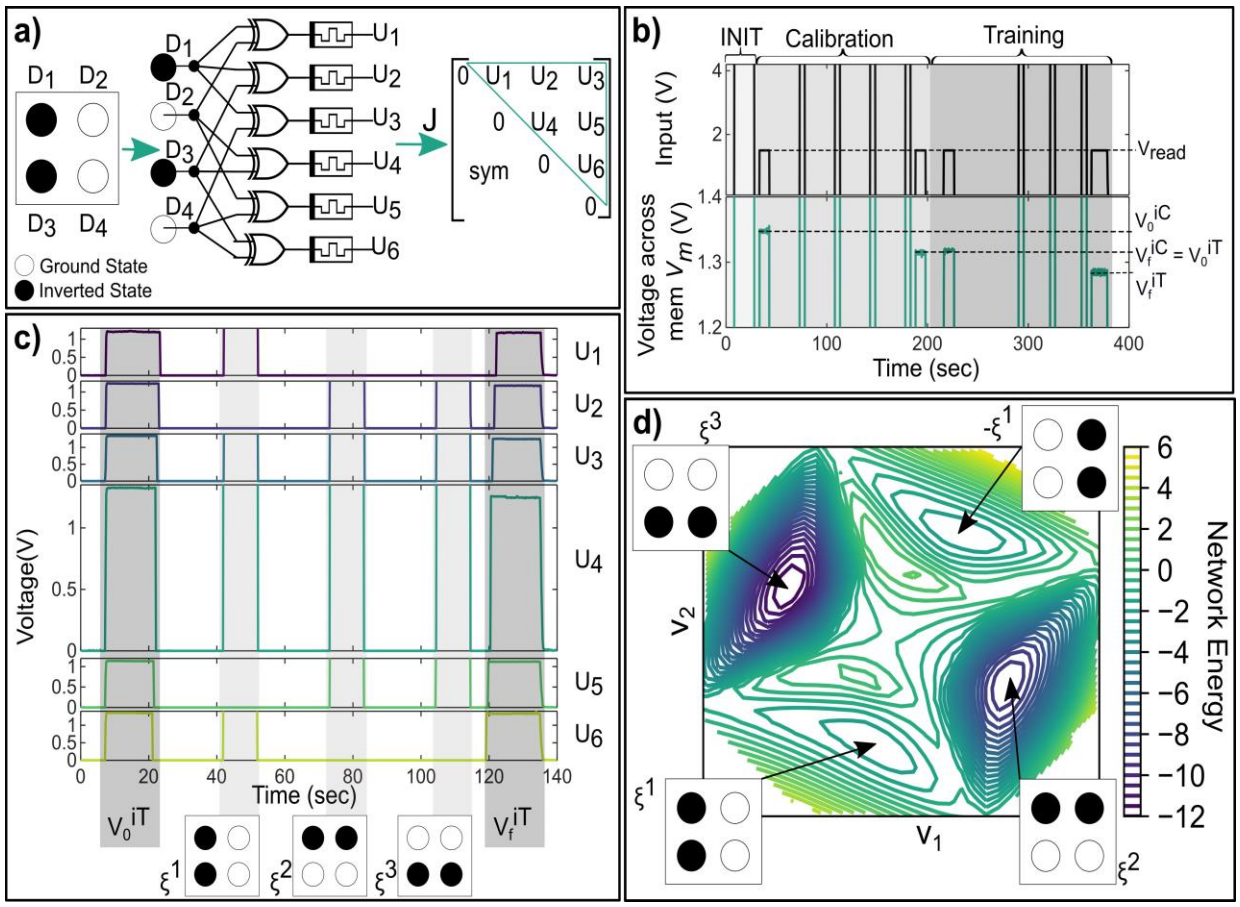


Figure 4.4. Physical Hopfield network implementation and test for different input patterns. a) Schematic of physical Hopfield network and connection between memristors to capture the interactions between mechanosensor units. b) 3-stage scheme designed to capture the interaction between mechanosensors with memristor response. c) Voltage across six different memristors, input patterns (light gray), and initial and final voltage reads (dark gray). The $y-$axis of U_4 is extended to show the difference between voltage reads. d) The Hopfield network energy landscape projected into the (V_1,V_2) plane by dimensionality reduction shows the input patterns as energy minima/attractors. Input patterns $\in R^4$ are visualized using the directions with the two largest variances (V_1,$V_2 \in R^2$).

followed by reading pulses. The measured difference in V_m read between the third (V_0^{iT}) and final (V_f^{iT}) read events reflects the net change in V_m^T (resistance) due to pair-wise interactions between dome inversion events. The entries to the interaction matrix are calculated as $U_i = \text{round}\left(\frac{V_0^{iT} - V_f^{iT}}{\Delta V^i}\right)$. By performing this procedure across the six memristors in parallel, we can automatically store and update interaction values between units (Figure 4.4c), generate the interaction matrix between dome units, and learn the input patterns using the physical Hopfield network.

We demonstrate the Hopfield network's online learning capability with a 2 × 2 metasheet array ($n = m = 2$, with unit cell dimensions w = 30 mm, h = 7 mm, t = 0.8 mm, r_d = 8 mm; see Figure 4.4). The array was trained by applying a sequence of patterns using physical dome inversions (see Movie S1). The resulting inter-unit firing is captured by constructing the interaction matrix from the memristor voltages read before and after the patterns are input (Figure 4.4c dark gray shaded region). As the Hopfield network's interaction matrix stores several patterns additively in the final values of the weights (see SI section A.12), only the differences between initial and final memristance measurements are necessary to retrieve the stored collection weights of the trained network. Once the interactions are stored, the network's weights are set, and the unique patterns are retrieved offline by presenting corrupted images to the network and performing an energy minimization process with asynchronous neuron update (see SI/appendx section A.12).

The training performance was evaluated by examining the Hopfield network's energy landscape to determine whether the physically input patterns were successfully stored as energy minima (Figure 4.4d). To achieve this, we utilized a dimensionality reduction technique[50] that uses random data generated based on the trained interaction matrix and the energy function to visualize the network's attractors using the two largest variance directions (V_1 and V_2). This procedure reveals four different attractors within the landscape (Figure 4.4d), each corresponding to the input patterns (ξ^i) and their reflections ($-\xi^i$). This behavior is expected as the Hopfield network's energy function is quadratic, yielding equal values for ξ^i and $-\xi^i$. This leads to the system learning both configurations (i.e., ξ^i and $-\xi^i$) since both are energy minima. Moreover, it is worth mentioning that ξ^2 and ξ^3 are the reflections of one another. This implies that during the training process the network learns this pattern twice, resulting in deeper energy wells (see Figure 4.4d). The obtained results indicate that the training procedure captured all interactions between dome units, and the metasheet's memory layer successfully remembers the input patterns. Classification accuracy of

the physical training is evaluated by presenting 3000 different corrupted patterns (Figure 4.19) to the network and then determining the number of correct identifications (i.e., implying no errors with respect to the stored patterns during training). A 91% overall accuracy is found with the pattern sequence shown in Figure 4.4c (see appendix section A.14), which has a 5% difference from the offline trained Hopfield network (Table S3). These results show that one of the learned patterns during the physical training is retrieved with no error 91% of the time a pattern is tested. The energy minimization process entailing the weights' updating when several corrupted patterns are presented to our physically trained network is shown in Movie S2.

Conclusion

We introduce a new class of flexible metamaterials which demonstrate spatiotemporal mechanosensing and neuromorphic functionalities. Our prototype leverages the structural bi-stability of dome-shaped units to filter, amplify, and transduce external mechanical signals into electrical states that are used to induce non-volatile (permanent) changes in memristance. The proposed architecture allows for producing neuromorphic properties in metamaterials that can cover large areas (102 cm2), in contrast to many examples of neuron-inspired sensing and perceptual systems. We use the spatial organization of our dome units and the cumulative changes in memristance of our metamaterial to realize a physical Hopfield network capable of learning a series of mechanical input patterns online. Specifically, we leverage the bistability-based filtering and amplification of our dome units to generate threshold-dependent changes in sensor resistance that can themselves be used to program a corresponding memristor state. We use the memristance value to populate associated interaction matrix weights, thus capturing the firing of units following a well-known Hebbian rule. Crucially, the cumulative resistance changes of our metamaterial's memristors allow for retrieving all the stored patterns from their final states. As a result, our metamaterial encodes several input patterns without the need to store temporal information. In this sense, our metamaterial exhibits analogous behavior to threshold-dependent event cameras augmented with a type of memory that encodes the captured episodes directly into the physical network's weights. We envision this unique capability as providing a route to continuously learning new spatiotemporal mechanical inputs which can be compared to known patterns of interest that may trigger specific control actions. For example, known pressure patterns associated with dangerous aerodynamic conditions could be presented to the current

state of the physical Hopfield network connectivity matrix (see equation S.6). Reaching an energy minimum would indicate that such a pattern has been learned (see Figure 4.1), indicating with minimal computational cost that a control action is needed. Thus, our mechanosensitive neuromorphic metamaterials reduce the need for costly online data storage, transmission, and processing of spatiotemporal inputs in situations where tactile pattern identification is of interest, including for robotics, autonomous systems, wearables, and morphing wings.

Author Contributions

All authors designed the research. KSR, HM, and JPU developed the initial sensor design. KSR developed the metasheet manufacturing method and conducted mechanosensor unit characterization. KSR and JCO conducted FE simulations of the mechanosensors. SK, YY, and SAS conducted memristor material development, characterization, and electrical activation. JCO, KSR, and AFA developed the Hopfield network concept and JCO conducted the simulations. SK, JCO, and KSR developed the physical implementation of the Hopfield network, and SK conducted the experiments. All authors contributed to the writing and revision of the manuscript and supplementary materials at different stages, and AFA and SAS provided guidance throughout the research.

The contents of this chapter are currently under review with the journal Science Advances.

References

1. Laschi, C. and B. Mazzolai, *Lessons from animals and plants: The symbiosis of morphological computation and soft robotics.* IEEE Robotics and Automation Magazine, 2016. **23**: p. 107-114.
2. Sangbae, K., L. Cecilia, and T. Barry, *Soft robotics: a bioinspired evolution in robotics.* Trends in Biotechnology, 2013. **31**: p. 287-294.
3. Moroz, L.L., *Convergent evolution of neural systems in ctenophores.* Journal of Experimental Biology, 2015. **218**(4): p. 598-611.
4. Proctor, J. and P. Holmes, *Reflexes and preflexes: on the role of sensory feedback on rhythmic patterns in insect locomotion.* Biol Cybern, 2010. **102**(6): p. 513-31.
5. Futakata, Y. and T. Iwasaki, *Entrainment to Natural Oscillations via Uncoupled Central Pattern Generators.* IEEE Transactions on Automatic Control, 2011. **56**(5): p. 1075-1089.
6. Fratzl, P. and F.G. Barth, *Biomaterial systems for mechanosensing and actuation.* Nature, 2009. **462**(7272): p. 442-448.
7. McConney, M.E., et al., *Viscoelastic nanoscale properties of cuticle contribute to the high-pass properties of spider vibration receptor (Cupiennius salei Keys).* Journal of The Royal Society Interface, 2007. **4**(17): p. 1135-1143.
8. Jung, Y.H., et al., *Bioinspired Electronics for Artificial Sensory Systems.* Advanced Materials, 2019. **31**(34): p. 1803637.
9. Wang, Q., et al., *Engineered Mechanosensors Inspired by Biological Mechanosensilla.* Advanced Materials Technologies, 2021. **6**(11): p. 2100352.
10. Park, J., et al., *Fingertip skin–inspired microstructured ferroelectric skins discriminate static/dynamic pressure and temperature stimuli.* Science Advances, 2015. **1**(9): p. e1500661.
11. *Filtered Mechanosensing Using Snapping Composites with Embedded Mechano-Electrical Transduction.* ACS Nano, 2019. **13**(4): p. 4752--4760.
12. Nathan, C.K., et al., *Memory formation in matter.* Reviews of Modern Physics, 2019. **91**: p. 35002.
13. Chen, T., M. Pauly, and P.M. Reis, *A reprogrammable mechanical metamaterial with stable memory.* Nature, 2021. **589**(7842): p. 386-390.

14. Jain, A.K., M. Jianchang, and K.M. Mohiuddin, *Artificial neural networks: a tutorial.* Computer, 1996. **29**(3): p. 31-44.
15. Fields, R.D., *The Brain Learns in Unexpected Ways.*, in *Scientific American*. 2020.
16. Xia, Q. and J.J. Yang, *Memristive crossbar arrays for brain-inspired computing.* Nature Materials, 2019. **18**(4): p. 309-323.
17. Tang, J., et al., *Bridging Biological and Artificial Neural Networks with Emerging Neuromorphic Devices: Fundamentals, Progress, and Challenges.* Advanced Materials, 2019. **31**(49): p. 1902761.
18. Hea Lim, P., et al., *Flexible Neuromorphic Electronics for Computing, Soft Robotics, and Neuroprosthetics.* Advanced Materials, 2020. **32**.
19. Kim, Y., et al., *A bioinspired flexible organic artificial afferent nerve.* Science, 2018. **360**(6392): p. 998-1003.
20. Changjin, W., et al., *An Artificial Sensory Neuron with Tactile Perceptual Learning.* Advanced Materials, 2018. **30**.
21. Chen, Z., et al., *Bioinspired Artificial Sensory Nerve Based on Nafion Memristor*. Advanced Functional Materials, 2019. **29**.
22. Qing, X., et al., *A Multifunctional Biomimetic Flexible Sensor Based Novel Artificial Tactile Neuron with Perceptual Memory.* Advanced Materials Interfaces, 2021. **8**.
23. Hopfield, J.J., *Neural networks and physical systems with emergent collective computational abilities.* Proceedings of the National Academy of Sciences, 1982. **79**(8): p. 2554-2558.
24. Hopfield, J.J. and D.W. Tank, *"Neural" computation of decisions in optimization problems.* Biological Cybernetics, 1985. **52**(3): p. 141-152.
25. Lichtsteiner, P., C. Posch, and T. Delbruck, *A 128X128 120dB 30mW asynchronous vision sensor that responds to relative intensity change.* Digest of Technical Papers - IEEE International Solid-State Circuits Conference, 2006.
26. Guillermo, G., et al., *Event-Based Vision: A Survey.* IEEE transactions on pattern analysis and machine intelligence, 2022. **44**: p. 154-180.
27. NinjaTek, *NinjaTek Cheetah Technical Specifications*.
28. *Conductive Graphene Filament - Material Safety Data Sheet*. 2015.

29. Mansour, M., K. Tsongas, and D. Tzetzis, *Measurement of the mechanical and dynamic properties of 3D printed polylactic acid reinforced with graphene.* Polymer-Plastics Technology and Materials, 2019. **58**(11): p. 1234--1244.
30. Schouten, M., et al., *A Review of Extrusion-Based 3D Printing for the Fabrication of Electro-and Biomechanical Sensors.* IEEE Sensors Journal, 2020(AUGUST): p. 1--12.
31. Cao, C., et al., *Methodology for the additive manufacture of embedded conductive paths connecting microelectromechanical sensors using conductive and flexible filaments with extrusion devices.* Rapid Prototyping Journal, 2020. **26**(2): p. 349--359.
32. Pelco, *Electrodag 502, 30g*.
33. Faber, J.A., et al., *Dome-Patterned Metamaterial Sheets.* Advanced Science, 2020. **7**(22): p. 2001955.
34. Christ, J.F., et al., *3D printed highly elastic strain sensors of multiwalled carbon nanotube/thermoplastic polyurethane nanocomposites.* Materials \& Design, 2017. **131**: p. 394--401.
35. Sau, K.P., T.K. Chaki, and D. Khastgir, *The effect of compressive strain and stress on conductivity.* Rubber chemistry and technology, 2000. **73**(2): p. 310--324.
36. Liu, H., et al., *Electrically conductive strain sensing polyurethane nanocomposites with synergistic carbon nanotubes and graphene bifillers.* Nanoscale, 2016. **8**(26): p. 12977--12989.
37. Tasbolat, T., et al., *Robotics: Science and Systems ssss Corvalis, Oregon Event-Driven Visual-Tactile Sensing and Learning for Robots.*
38. Seffen, K.A. and S. Vidoli, *Eversion of bistable shells under magnetic actuation: a model of nonlinear shapes.* Smart Materials and Structures, 2016. **25**(6): p. 065010.
39. Udani, J.P. and A.F. Arrieta, *Taming Geometric Frustration by Leveraging Structural Elasticity.* SSRN Electronic Journal, 2022.
40. Santo, J., P.K. Penumakala, and R.B. Adusumalli, *Mechanical and electrical properties of three-dimensional printed polylactic acid–graphene–ca \textless scp \textgreater rbon \textless /scp \textgreater nanofiber composites.* Polymer Composites, 2021. **42**(7): p. 3231--3242.

41. Vosgueritchian, M., D.J. Lipomi, and Z. Bao, *Highly Conductive and Transparent PEDOT:PSS Films with a Fluorosurfactant for Stretchable and Flexible Transparent Electrodes.* Advanced Functional Materials, 2012. **22**(2): p. 421-428.
42. Fan, X., et al., *Transfer-Printed PEDOT:PSS Electrodes Using Mild Acids for High Conductivity and Improved Stability with Application to Flexible Organic Solar Cells.* ACS Applied Materials \& Interfaces, 2016. **8**(22): p. 14029-14036.
43. Möller, S., et al., *A polymer/semiconductor write-once read-many-times memory.* Nature, 2003. **426**(6963): p. 166-169.
44. Ha, H. and O. Kim, *Bipolar switching characteristics of nonvolatile memory devices based on poly(3,4-ethylenedioxythiophene):poly(styrenesulfonate) thin film.* Applied Physics Letters, 2008. **93**(3): p. 033309.
45. Michael, H., *Found: the missing circuit element.* Nature, 2008.
46. Leon, C., *Memristor -- The Missing Circuit Element.* Ieee Trans. On Circuit Theory, 1971. **18**: p. 507--519.
47. Khodagholy, D., et al., *High speed and high density organic electrochemical transistor arrays.* Applied Physics Letters, 2011. **99**(16): p. 163304.
48. Feldman, J. and R. Raul, *Neural Networks : A Systematic Introduction*. 1996: Springer Berlin Heidelberg.
49. John, H., K. Anders, and G.P. Richard, *Introduction to the theory of neural computation*. Introduction to the Theory of Neural Computation. 2018.
50. Xin, K. and L. Chunhe, *A Dimension Reduction Approach for Energy Landscape: Identifying Intermediate States in Metabolism-EMT Network.* Advanced Science, 2021. **8**: p. 2003133.
51. Barahona, F., *On the computational complexity of ising spin glass models.* Journal of Physics A: Mathematical and General, 1982. **15**: p. 3241-3253.

Appendix

A.1 Mechanosensing Unit Cell

The key dimensions of the dome unit cell are shown in Figure 4.5. Print settings are listed in Table S1.

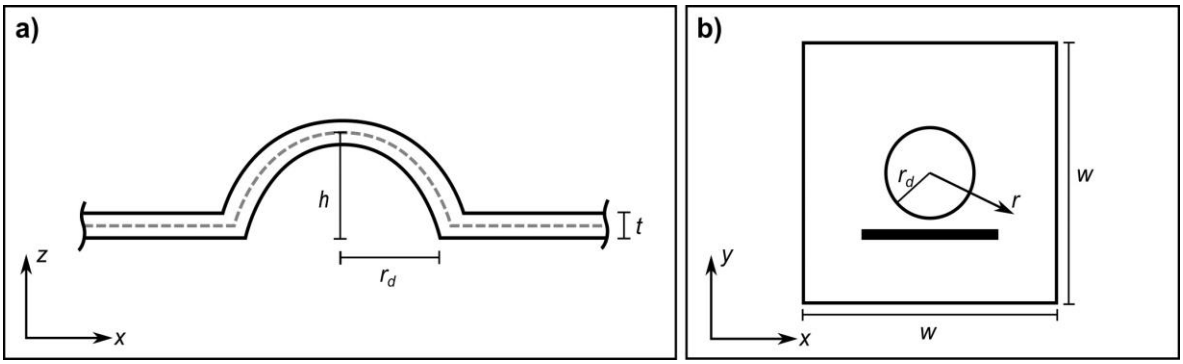


Figure 4.5 a) Cross-section of the dome showing the height, h; thickness, t; and radius, r_d b) The dome is in the center of a w × w unit cell; r is the distance from the center of the dome.

Table 4.2: Mechanosensor print settings

TPU	
Nozzle Diameter	0.40 mm
Layer Height	0.10 mm
Extruder Temperature	$230^{\circ}C$
PLA + graphene	
Nozzle Diameter	0.40 mm
Layer Height	0.10 mm
Extruder Temperature	$200^{\circ}C$
Print Bed	
Bed Temperature	$50^{\circ}C$
Bed Material	Glass

A.2 Dome Behavior

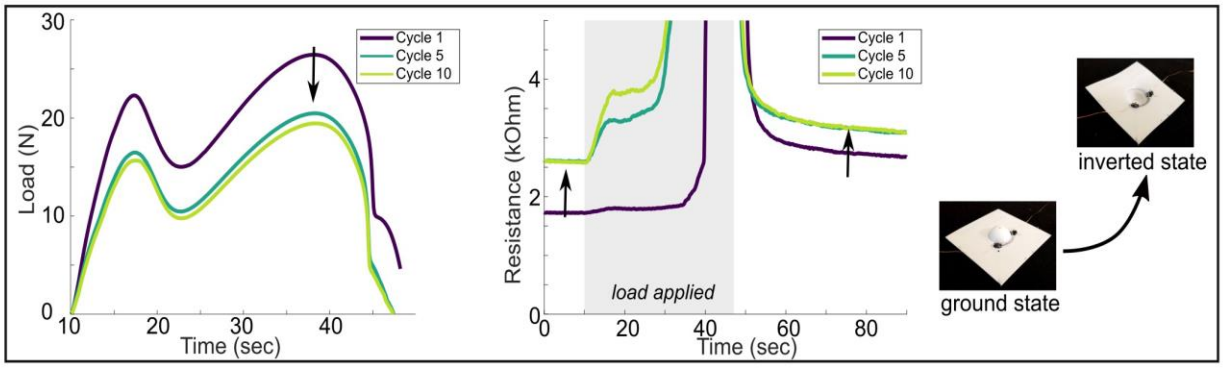


Figure 4.6. Typical of viscoelastic structures, the first loading cycle is always noticeably different than subsequent cycles. This stress-softening is reflected in the resistance values of the sensor. As shown in Figure 4.2c, the first loading cycle generally shows different behavior from subsequent cylces for a mechanosensing unit cell. This is due to the stress-softening behavior, as shown in Figure 4.6.[31] The ground and inverted state resistances are steady over time, showing the mechanosensor retains information about whether or not an inversion has occurred (Figure 4.7).

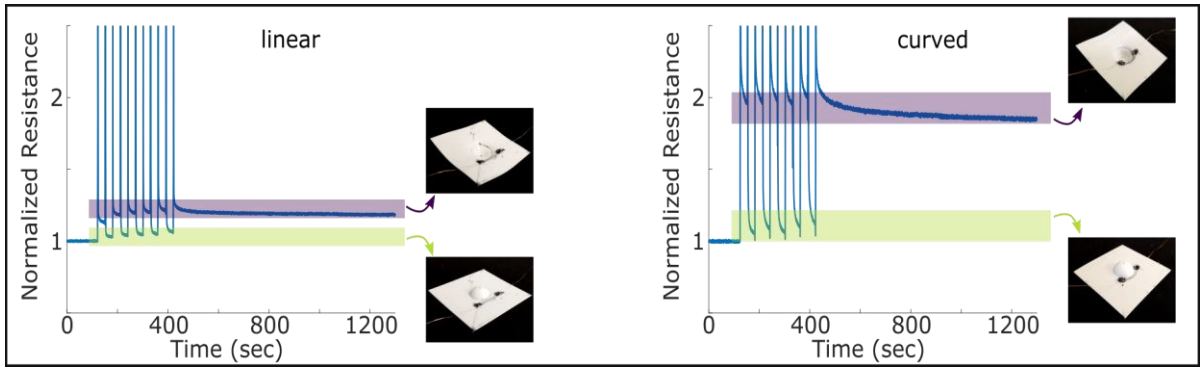


Figure 4.7. The resistance of the inverted state is maintained over time.

A.3 Instron Tests

The Instron test setup used to demonstrate the thresholding capability is shown in S4. The threshold load for filtering may be determined by changing the geometric parameters of thickness (Figure 4.2d,e) and height (Figure 4.9).

A.4 Curved Sensors

While curved sensors offer significantly higher signal amplification, there are several practical drawbacks. Because they follow a region of higher stress and strain, they are more prone to cracking (Figure 4.10) and failures at the connection points. While the damaged sensors may still function, the damage alters the ground state resistance. The curved shape also makes them more sensitive to the hysteresis and viscoelastic effects of the TPU base; this can be seen in changing slopes of the resistance after snap-through and the gradual increase in the ground state resistance over cycling. Furthermore, the conductivity of printed conductive filament is highly dependent on the internal alignment of the conductive microparticles.[40] The effects of printing along a curve rather than in a straight line on this alignment are not fully understood.

A.5 Circuit diagram for signal amplification

The model of Op-Amp is LM741, which is the most used model. OpAmp1 is used as a voltage follower circuit, which can also be considered as a buffer amplifier. Here, the op-amp does not amplify the input signal, and the gain is 1. Therefore, the output voltage is same as the input voltage. Because the voltage follower circuit has a very high input impedance, it can provide a stable voltage output, which follows the input voltage. In this circuit design, the input voltage is decided by V_{in1} and the resistance ratio between R_{ref} and resistance of the dome (R_ϵ). Originally, the R_{ref} is adjusted to equal to dome resistance. Therefore, the output voltage is half the input voltage ($V_{in11} = 0.5V_{in1}$). Whereas OpAmp2 is a typical differential amplifier circuit. The V_{out} is defined as:

$$V_{out} = \left(\frac{R_1 + R_4}{R_5 + R_6}\right)\left(\frac{R_4}{R_1}\right)V_{in2} - \frac{R_4}{R_3}V_{in11} \tag{S.4}$$

When $R_1 = R_3 = 100\Omega$ and $R_2 = R_4 = 2000\Omega$. The equation can be simplified as:

$$V_{out} = \frac{R_2}{R_1}\left(V_{in11} - V_{in2}\right) \tag{S.5}$$

From the equation, it can be seen that the OpAmp2 circuits are amplifying the difference between V_{in11} and V_{in2}. In our design,

V_{in2} is set to 1 V and V_{in11} is $\frac{1}{2}V_{in1}$, which is 1 V as well. Therefore, originally, there is no voltage output from op-amp circuits. By inverting the dome, the resistance of the dome changes, which leads to a change in resistance ratio between R_ϵ and R_{ref}. This event will change the V_{in11} because of the characteristic's voltage follower circuits. Therefore, a voltage difference will be created between V_{in11} and V_{in2}. This voltage difference will be picked up and amplified by the OpAmp2 circuits.

A.6 Scheme for selection of resistor in series with memristor

We use a resistor in series with the memristor to read the voltage across the memristor V_m by using an Arduino circuit. Therefore, a careful choice of a resistor in series is required for ensuring i) majority of the voltage amplitude ($> V_{th}$) from the pulse is felt across the memristor for effective drop in resistance, ii) resolution of change in V_m is adequately above any noise level. A 500 Ω and 2000 Ω resistor was tested in series with the memristors. Initially, a pulse of 4.3 V was applied for 20 seconds to the resistor-memristor duo to drive the first big non-linear change in the memristor and set the memristor in the more linearly increasing conductive region. This was followed by cycles of a read pulse (1.5 V, 10 seconds) and five write pulses (4.3V, 5 seconds). Figure 4.12 compares the voltage drops across the memristor (V_m) using the read pulses, which are proportional to the current resistive state of the memristors. It's observed when the 500 Ω resistor is connected in series, upon subsequent voltage pulses, there is a significant drop in read voltage compared to the 2000 Ω. These distinguishable drop in V_m above noise level represent change in memristance (M).

A.7 Device architecture and electrical characterization

Figure 4.13a displays the device architecture for a Cu/PEDOT:PSS/ITO device. The film is sandwiched between a copper top electrode and ITO glass bottom electrode to form a vertically stacked device. For electrical characterization of the device, voltage

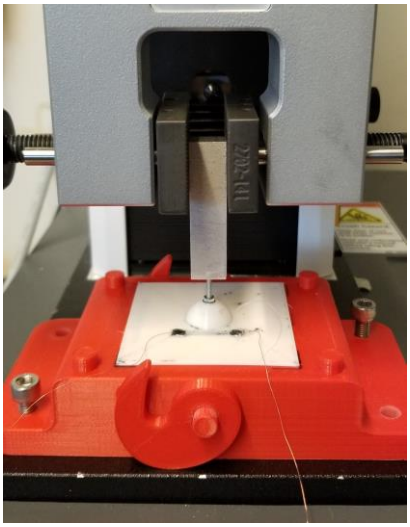


Figure 4.8. Instron testing setup for measuring snap-through load of domes.

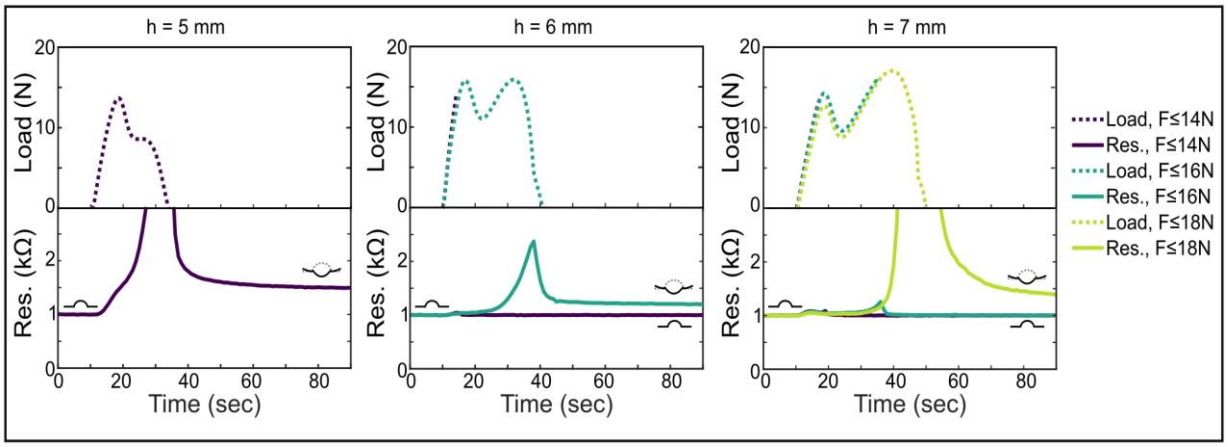


Figure 4.9. The filtering tunability is demonstrated by the changing snap-through load for three different heights for domes of thickness 0.8 mm. Loads below this threshold load are not recorded by the sensor.

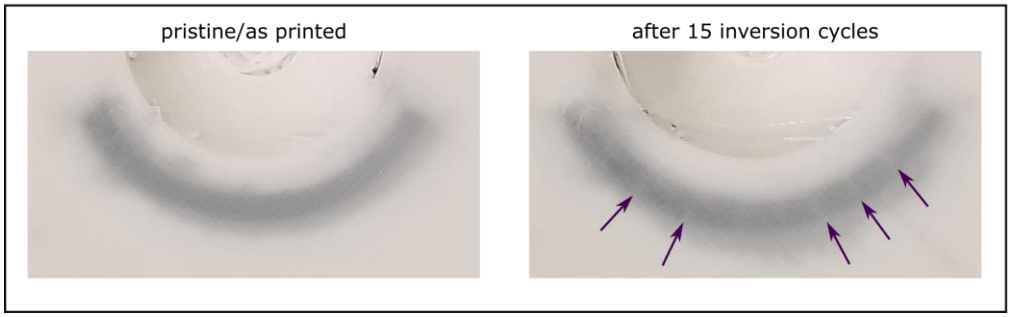


Figure 4.10. Curved sensors are more prone to cracking after repeated inversion cycles due to the higher strains. A pristine/as printed sensor (left) is compared with a sensor after 15 inversion cycles (right). Arrows indicate visible crack locations

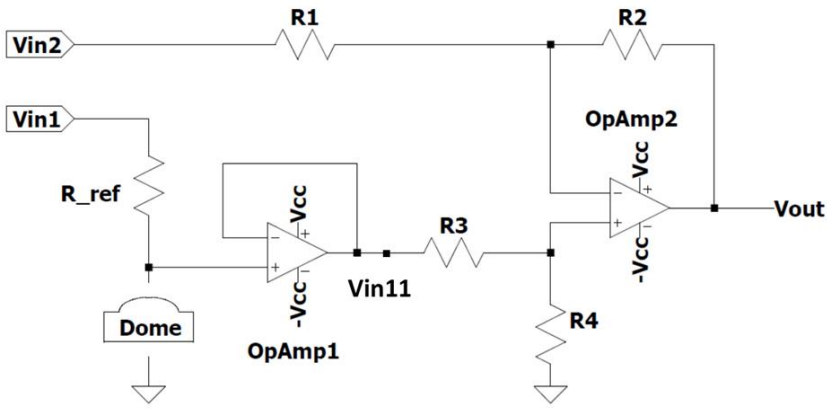


Figure 4.11. Circuit diagram for amplification of input signal.

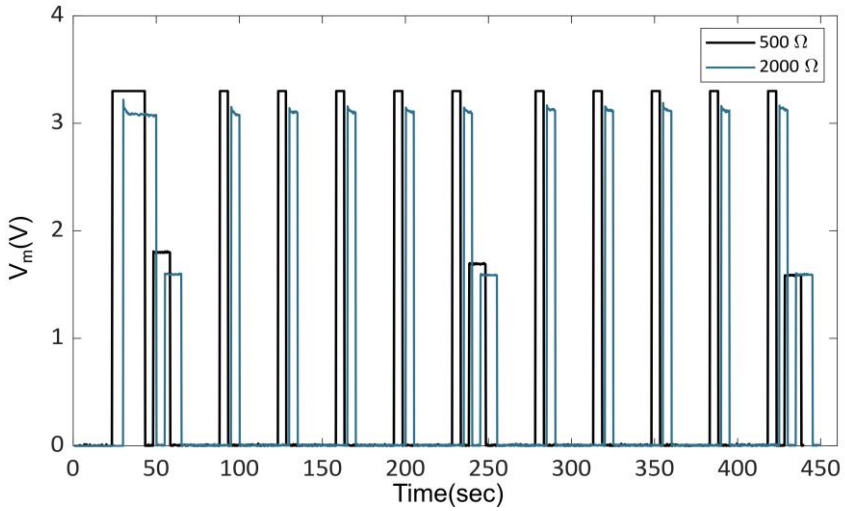


Figure 4.12. Selection of a resistor in series to achieve distinguishable change in V_m (~ resistance of memristor).

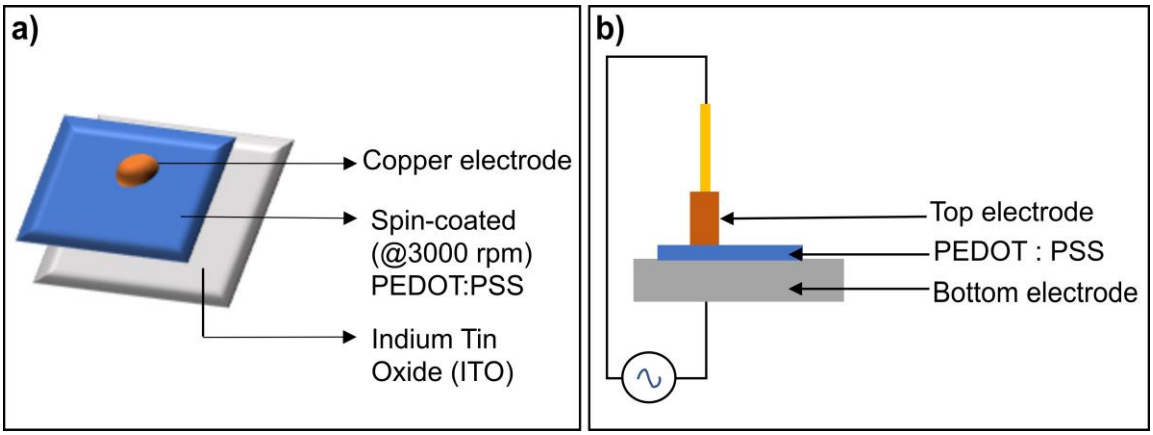


Figure 4.13. (a) Schematic describing polymeric thin-film device architecture. (b) and set-up for electrical characterization. Voltage is directed to the top electrode via a function generator (enabling the supply of different voltage waveforms). Current is measured via the bottom electrode.

A.8 Scheme for estimation of V_{th}, HRS and LRS

Current-voltage (i-v) characterization of the Cu/PEDOT:PSS/ITO devices reveal non-volatile hysteretic behavior with distinct switching regimes as seen in Figure 4.3b. Calculations were done using Matlab software to reveal the voltage threshold (V_{th}) of switching of resistance states of the devices as well as the estimated values of high resistance state (HRS) and low resistance state (LRS) of the devices. A conductance line of 0.033 mS was established as shown by the horizontal black dotted trace. A red dotted trace was made to fit the slope of the i-v response as the device switches to a lower resistive state. The voltage corresponding to the intersection of the red and black dotted trace highlights the voltage threshold of switching given by the blue dotted trace. Also, to estimate the nominal values of HRS and LRS, we measured the slopes of the i-v response corresponding to the two regions as given by the brown and green trace respectively. The table displays the calculated voltage thresholds, HRS, and LRS values of 12 devices. The standard deviation reveals variability across devices within a batch which reflects device-to-device reproducibility. This highlights an important challenge in using memristive analog devices: no two devices are exactly the same.

A.9 Repeatability of i-v behavior across cycles of periodic input

Measurements were performed across multiple voltage sweeps to assess cycle-to-cycle variations in setting and resetting the resistive states of the devices. The former displayed more variability than the latter. Also, the slope of the i-v when the device is in the conductive domain decreases from cycle-to-cycle.

A.10 Scheme for selection of required V_m

To achieve a change in resistance of a memristor, the voltage across the memristor (V_m) needs to be above the V_{th} of switching for the device. Figure 4.17 displays the cumulative conductive response of six memristive devices to a series of pulses for various pulse amplitudes and fixed pulse width (Ton) of 5 seconds and Toff ~30 seconds. The selected pulse amplitudes demonstrate the response of the memristor at V_{th} (3 V), slightly beyond V_{th} (3.5 V), and considerably beyond V_{th} (4 V). For 3 V, we notice there is a drop in the cumulative resistance of the memristors. We also observe for pulse amplitude of 3.5 V, initially, the cumulative drop in resistance is relatively steady with respect to that of 3 V but there is significant variability or the direction of change varies significantly after several pulses. These inconsistencies motivated the usage of pulses with

higher amplitude ~4V, where we observe a steady cumulative decrease in resistance across 20 pulses. This comparison shows that applying a voltage well above the switching threshold improves the consistency of incremental changes in the memristive state.

A.11 Response of device to step input and pulsatile input

Response of a Cu/PEDOT:PSS/PSS device to a step voltage input of 4 V for 50 seconds revealed a significant shift in conductance from a low conductive state (HRS) to a very conductive state (LRS). The low conductive state recorded for this device was 0.8 mS which equals to 1.25 kΩ, roughly around the same values for LRS recorded from i-v measurements as shown in Figure 4.18. Similarly, the response of the device to consecutive pulses of amplitude 4 V and width 5 seconds revealed a cumulative increment in conductance of the device. We also observed a region of non-linear increase in conductance followed by a more linear increment in conductance indicated by the dotted green trace in Figure 4.18b. Therefore, a step voltage for 20 seconds can enable to shift the device conductance to a linearly incrementing domain.

A.12 Associative Memory and Hopfield networks

Associative memory problems mainly focus on storing/learning a set of patterns ($\xi_i^{\mu} \in \mathbb{R}^{m \times n}$) such that when presented with new patterns (ζ_i), the system responds by retrieving the closest pattern/memory[49] (Fig S15a).

Hopfield networks are a type of associative memory network which can store different memories as attractors or fixed points in their energy landscape that can then be retrieved using asynchronous neuron update and energy minimization of the network. The network is trained by computing the outer product between the patterns intended to be learned ($J_{ij} = \xi_i \xi_j$), strengthening the synapse/interaction between neurons which are both "on" (+1) or "off" (-1) and storing all the pattern information within the interaction matrix (J_{ij}). This same procedure can be applied to learn multiple patterns by adding the interaction matrix of each pattern as $J_{ij} = J^{(1)} + J^{(2)} + J^{(3)} + .. + J^{(p)}$. [12] It can be observed that the training of these types of networks is just based on the strength of the interaction between neurons and a sum of the interactions matrix; hence, a physical system that can capture the additive neuron interaction over time can train the Hopfield network and store the desired patterns. The Hopfield network mathematical model is based on the neuron state, either

firing (+1) or not (-1). The state of the pattern can be calculated using the dynamics of the network,[49] as follows:

$$\xi_i^{\mu} := \operatorname{sgn}\left(J_{ij}\xi_j^{\mu}\right) \tag{S.6}$$

Where stored patterns are labelled by $\mu = 1,2,...,p$, while the units/neurons are represented by $i = 1,2,....,M$, sgn(x) is the sign function, $J_{ij} \in \mathrm{R}^{mn\times mn}$ is the interaction matrix between the neurons. Memories can be retrieved from the network using two different methods:

- Asynchronous updating: The state of a random neuron of the input pattern ζ_i is changed (-1 to +1) independently until an energy minimum is achieved within the state ζ_i.
- Synchronous updating: All neurons are updated simultaneously by multiplying the interaction matrix (J_{ij}) and the initial pattern ($J_{ij}\zeta_j$). This process is repeated until the input pattern is the same as the stored memory ($\xi_i = \zeta_i$).

The energy of the network is calculated using a simplified version of the Ising model[49, 51] :

$$E = -\frac{1}{2}\sum J_{ij}\zeta_i\zeta_j \tag{S.7}$$

One can see that asynchronous updating is more suitable for any application. It does not require knowing the outcome of the network or the stored patterns, just the minimization of the network's total energy.

A.13 Calculated interaction matrix using memristor data

To capture the interaction between dome units/neurons for the Hopfield network, an XOR gate connected to two different units was utilized. By doing this, the resistance of the memristor was reduced every time two units were not in the same state (see Figure 4.20 and Movie 4.1). This guarantees that the values within the interaction matrix J are weakened when both neurons are activated at the same time, as expected from the Hopfield network training.

The number of times two units interact with each other (U_i in Figure 4.4) can be calculated for every memristor by taking the resistance drop. However, to reduce the noise within the memristor response and considering that $R \propto V$, this difference was calculated using voltage drop as shown in Figure 4.4b:

U_i = roundround(S.8) $\left(\frac{R_0^T - R_f^T}{\Delta R}\right) =$ $\left(\frac{V_0^T - V_f^T}{\Delta V}\right)^{!}$

Where U_i is the interaction at the i memristor, R_0^T is the initial resistance, R_f^T is the resistance value after the dome inversion events and ΔR is the average resistance change for every memristor. Experimental tests were performed by inverting the domes with the patterns shown in Figure 4.4c, but alternating the order within the patterns. U_i results for four different experimental tests can be observed in Table S2.

U_i values are arranged on the upper triangular positions of a $mn \times mn$ matrix. For a 2×2 dome array, we can write the interaction matrix as:

$$J^M = \begin{bmatrix} 0 & U_1 & U_2 & U_3 \\ U_1 & 0 & U_4 & U_5 \\ U_2 & U_4 & 0 & U_6 \\ U_3 & U_5 & U_6 & 0 \end{bmatrix} \quad \text{(S.9)}$$

As memristors can only strengthen the interaction between units with opposite states, a linear transformation was stabilized to consider the weakening of units with the same state. The linear transformation for $m = n = 2$ can be written as

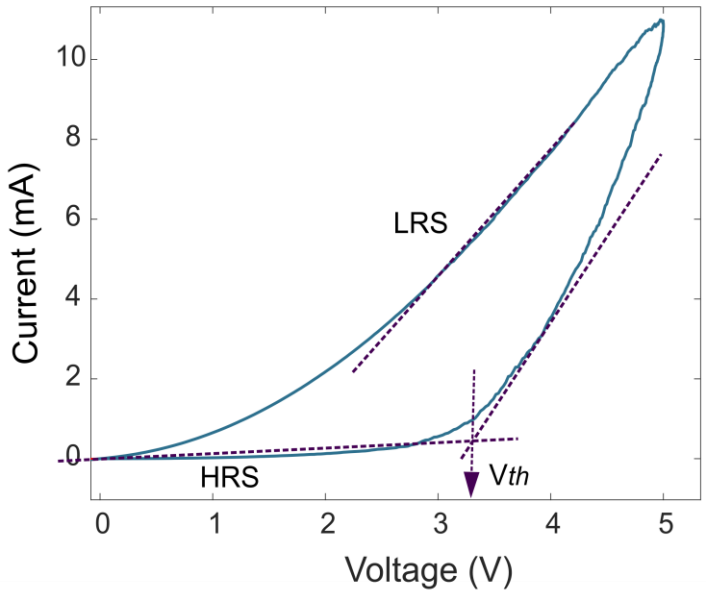
$$\mathbf{J} = -2\mathbf{J^M} + ||\mathbf{J^M}||_{\max}\mathbf{I} \quad \text{(S.10)}$$

Where J is the Hopfield network interaction matrix, J^M is the interaction matrix obtained from the memristor data, $\max(J^M)$ is the maximum value within the matrix, and I is a $mn \times mn$ identity matrix.

A.14 Physical Hopfield network statistics

The physical Hopfield network and the interaction matrix performance were evaluated using the network's accuracy. This was calculated by training the physical Hopfield network with the memristors and running the energy minimization problem with 3000 corrupted patterns (see Movie S2).

A maximum of 20 iterations and four asynchronous updates are utilized to find the stored patterns. The corrupted patterns were variations of the original ones, but with an added normally distributed noise between -1 and +1. Accuracy was calculated by counting the number of retrieved patterns that exactly match the ones on which the network was trained. Results for the network performance for every experimental test can be observed in Table S3.



Sl. no	V_{th} (V)	HRS (kΩ)	LRS (kΩ)
1	2.9	13.7	0.89
2	3.4	12.89	1.0
3	3.2	14.90	1.2
4	3.0	13.0	0.9
5	3.0	13.26	1.2
6	3.1	15.7	1.7
7	2.9	16.2	1.2
8	3.1	17.7	1.44
9	3.1	17.5	2.3
10	3.1	15.55	1.12
11	3.1	16.8	1.07
12	3.2	17.8	1.8
Avg	3.09	15.42	1.31
Std	0.13	1.77	0.4

Figure 4.14. Technique for calculating V_{th}, HRS ,and LRS of PEDOT:PSS devices and the corresponding nominal values of 12 devices.

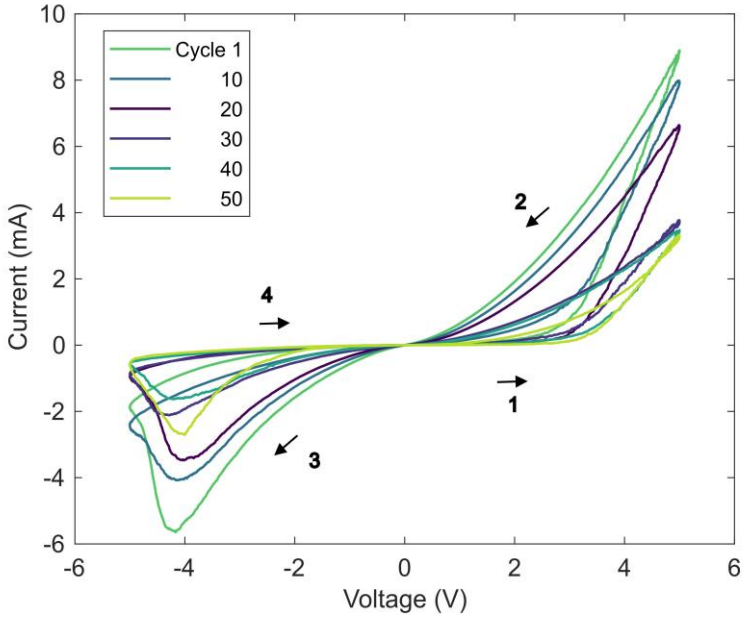


Figure 4.15. Cycle to cycle behavior of Cu / PEDOT:PSS / ITO device studied here.

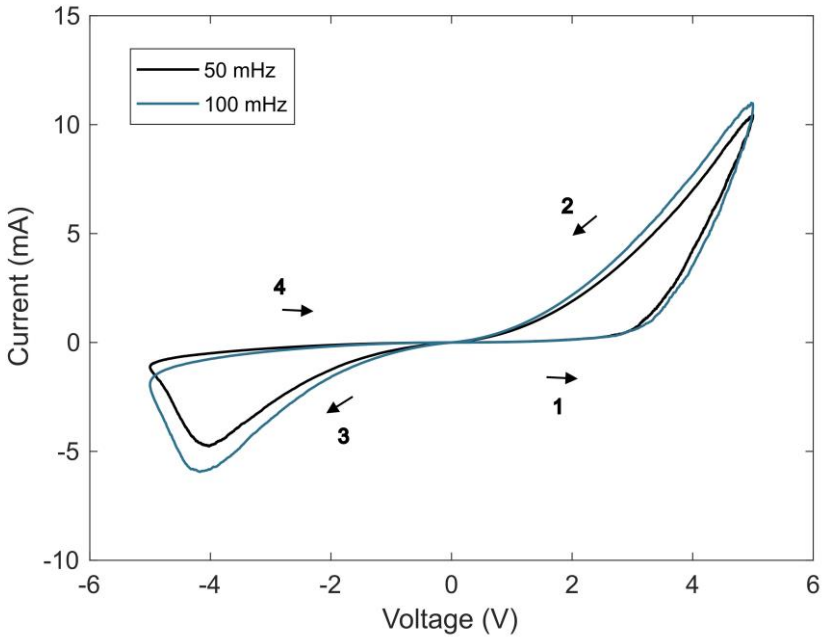


Figure 4.16. Response of PEDOT:PSS device to 50 mHz and 100 mHz sinusoidal voltage waveforms. When the Cu/PEDOT:PSS/ITO device is stimulated with 100 mHz and 50 mHz sinusoidal voltage stimuli, minimal change in the i-v properties of the device was noticed.

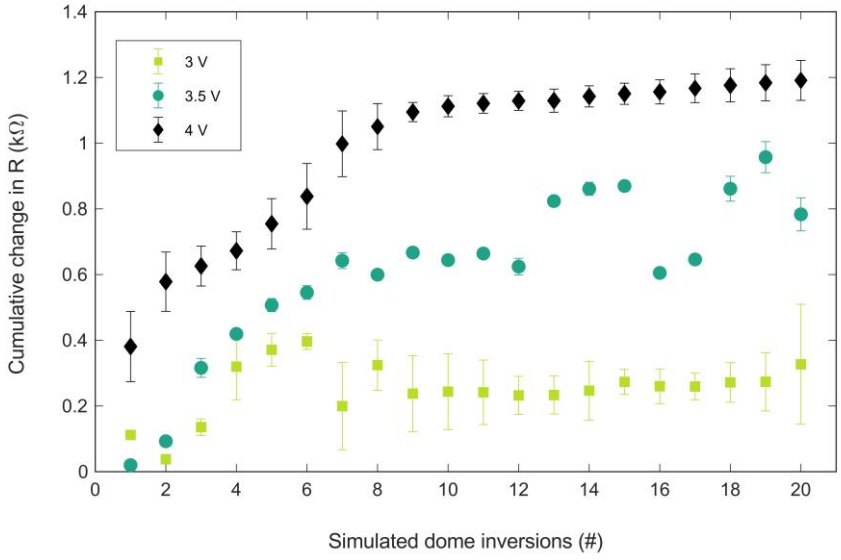


Figure 4.17. Cumulative change in resistance of six memristors from a higher resistive state (HRS) to a lower resistive state (LRS) across different voltages of 3,3.5 and 4V for a fixed pulse width of 5 seconds.

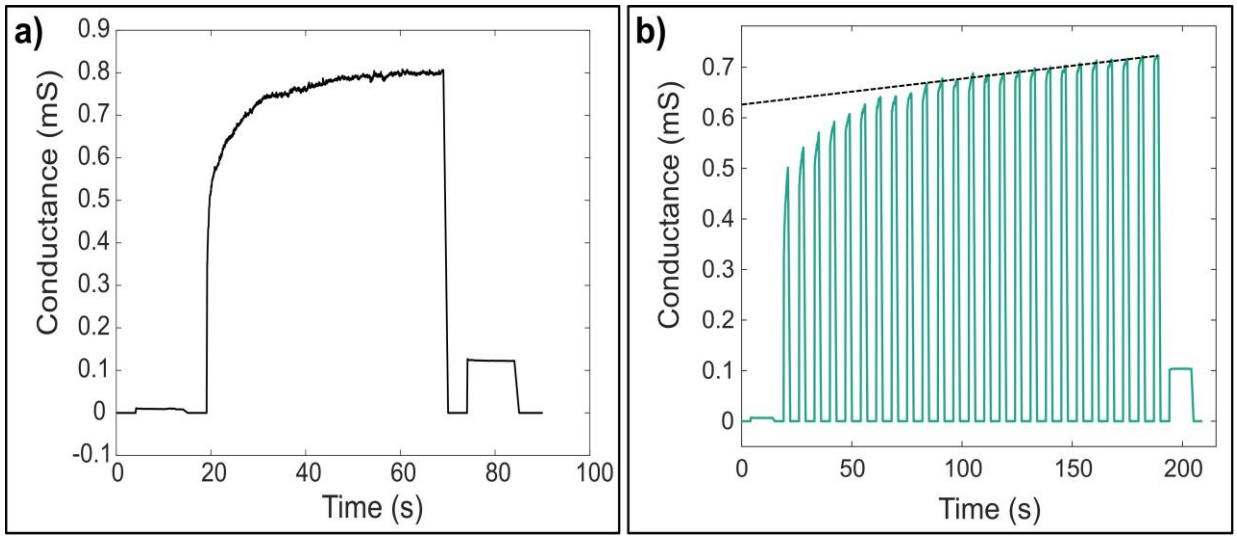


Figure 4.18. Response of a Cu/PEDOT:PSS/PSS device to (a) step voltage input (b) pulsatile voltage input.

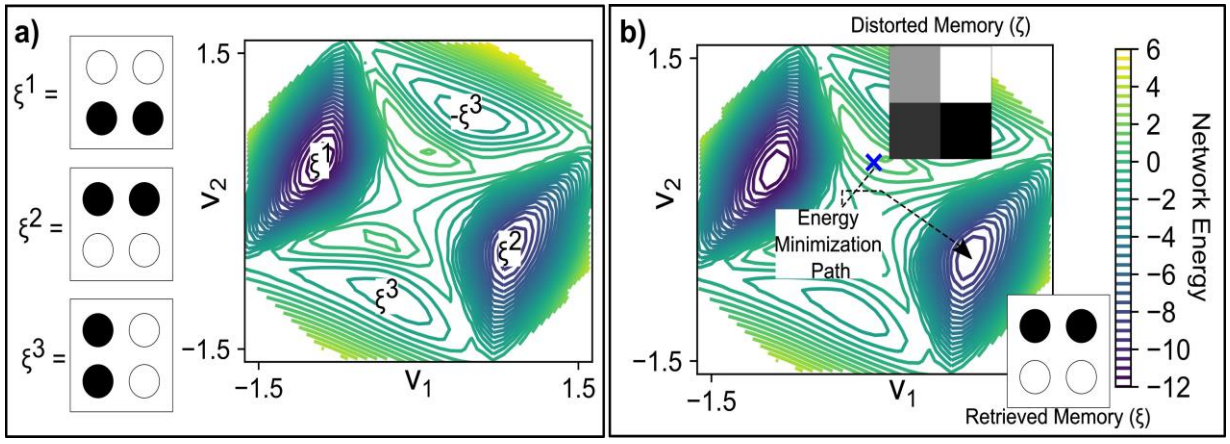


Figure 4.19. a) Associative memory energy landscape and stored memories b) Energy minimization path. Initial distorted pattern ζ to retrieved memory ξ

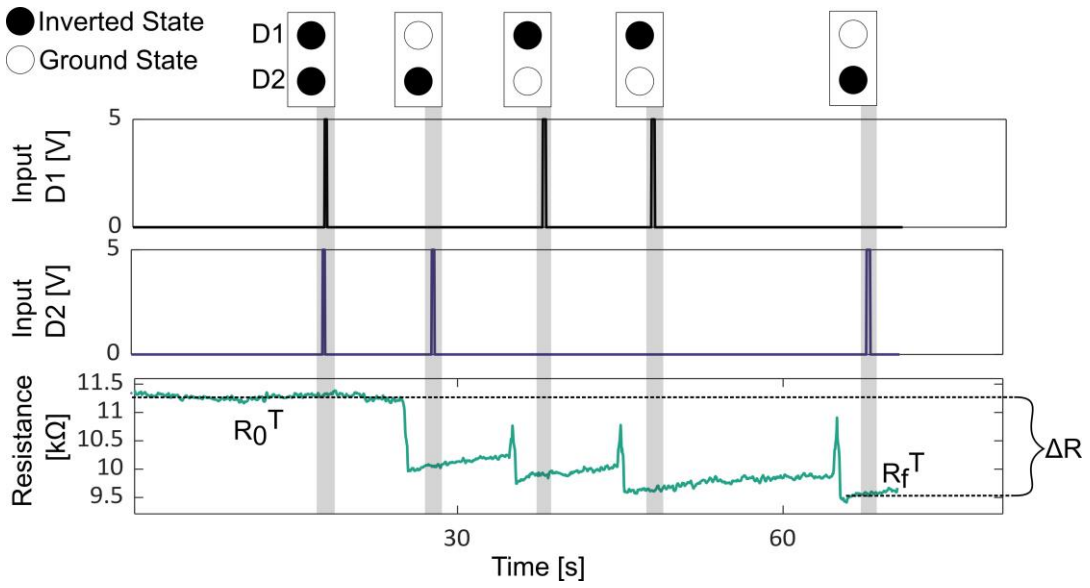


Figure 4.20. Interaction of pairwise domes displaying non-volatile writing of memristance only for dissimilar dome states.

Table S2: U_i experimental test values obtained from memristor data. Comparison with expected U vector.

Expected *U*	Test 1 *U*	Test 2 *U*	Test 3 *U*	Test 4 *U*
1	1	1	1	1
2	2	4	2	2
3	3	3	3	3
3	3	3	3	3
2	0	1	1	1
1	1	0	1	0

Table S3: Hopfield network accuracy. Expected results with regular training and results with experimental tests.

Expected Accuracy	Test 1	Test 2	Test 3	Test 4
97.43%	95.8%	81.5%	96.93%	89.86%

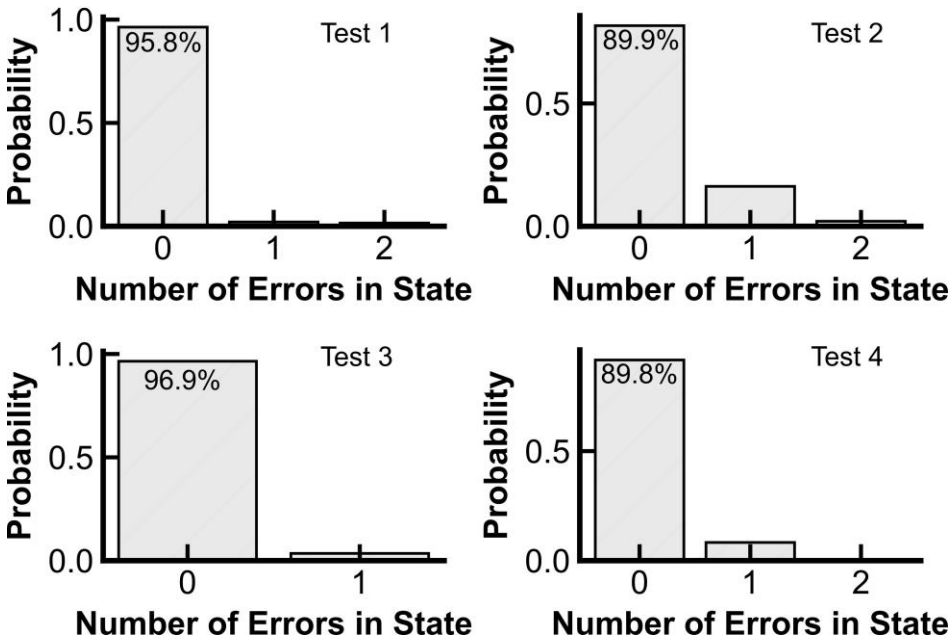


Figure 4.21. Probability of occurrence of errors in final retrieved memories from physical Hopfield network. To further explore the network accuracy, we determine the probability of errors by counting the number of state errors in the retrieve patterns and the number of times the error was present.

CHAPTER V. Understanding the influence of electrode material on the bipolar resistive switching mechanism of a Cu/PEDOT:PSS memristor.

Abstract

PEDOT:PSS polymer has been used as a sandwiched thin film between metal-metal or metal-inorganic oxides to display resistive switching (RS) characteristics. Various conduction mechanisms have been proposed till-date co-related to the RS mechanism. However, the specific physical mechanism(s) for RS, and the ensuing changes in the materials, remains unknown for Cu/PEDOT:PSS device. Here, we reveal the voltage driven changes in the device material composition that contribute to the RS mechanism via elemental analysis of the device material composition before and after RS. These findings will motivate engineering of material combinations and materials processing techniques for required applications and maximize reproducibility of the devices respectively.

Introduction

Organic two terminal resistive switching (RS) devices are commonly built by sandwiching an insulative organic layer/organic electrolyte between two metal electrodes [1]. These metal electrodes can be chemically inert or active (react with other materials to form different compounds). These devices have gained interest from researchers because of their potential applications in integrated flexible neuromorphic circuits [2, 3] due to a high level of scalability [4], flexibility, ultra-low-cost electronics [5] such as neuromorphic skins [6]. An understanding of the RS mechanism of these devices is therefore very crucial for designing the device architecture to maximize device performance and repeatability.

Depending on the composition and active nature of the electrode, switching between high and low resistive states of these devices has primarily been described through the formation and dissolution of electrochemically metalized (ECM) conducting metal filaments [7, 8]. First, these devices require a high voltage for conductive filament (CF) formation and growth through the insulative region as well as considerably high working voltage [9]. Second, they also need a thick insulative layer to avoid leakage currents [9, 10]. Together they become highly energy invasive [9].

Organic RS devices have been built to work at lower voltages than ECM cells, just by replacing the insulative polymeric layer with a semiconductive polymeric thin film [11]. PEDOT:PSS (p-type) is a semiconductive material [12] which has been widely used. PSS is used as an dopant or counterion for better dispersion of PEDOT in the solvent [13]. PEDOT:PSS is an attractive

material due to its adaptable RS characteristics in ITO/PEDOT:PSS/Au devices [11], unipolar resistive switching in Au/PEDOT:PSS/Au devices [14], and bipolar resistive switching (URS) in ITO/PEDOT:PSS/Al [15] and Al/PEDOT:PSS/Al devices [16]. ITO/PEDOT:PSS/Au devices [11] revealed write once read many time (WORM) type device which was limited by non-repeatable RS and hysteretic current-voltage (*i-v*) behavior. Various charge transport mechanisms have been proposed for these two terminal PEDOT:PSS devices, like voltage-driven redox reaction of the polymer [11, 14, 15], and space charges induced by interface reaction between the top active metal electrode and bulk PEDOT:PSS thin films [16, 17]. But scientific gaps prevail in revealing the switching mechanism and understanding the contributions of electrode material, exploration of newer electrode materials, electrode-polymer interface, and the bulk towards the voltage threshold for switching, and the current-voltage (i-v) hysteresis.

Here, our research objective was to understand the RS in Cu/PEDOT:PSS/ITO devices. We also studied the charge transport mechanisms of the device and the role of all the materials in the device. We built vertical sandwiched devices with PEDOT:PSS as the semiconductive material and Cu (biased first) and ITO as the ground electrode. *I-V* characterization of the devices revealed Cu in contact with PEDOT:PSS as the necessary condition for bipolar RS and *i-v* hysteresis of the device. Also, copper is cheap, readily available, has low internal resistance (resistivity ~ 7×10^{-6} Ω-m), and exhibits efficient hole injection with good contact between electrodes and polymer [18]. Through mathematical analysis of the current-voltage traces, we revealed the dominant charge transport mechanism of the device. But the transformation in the active material contributing to RS between HRS to LRS and vice-versa could not be revealed. Therefore, we studied lateral devices with symmetric (Cu-Cu) and asymmetric (Cu-Au). The results suggest dominant influence of the material composition at the Cu/PEDOT:PSS interface towards the RS.

Materials and Methods

Fabrication of vertical device: Glass slides/silicon wafers were cleaned with (in the following order) soap-water, de-ionized water, ethanol, acetone, propanol via sonification for 15 minutes each and dried using ultra-pure Nitrogen. The clean substrates were oxidized in an oxygen plasma chamber using a PE 50 XL Benchtop low pressure plasma system for 1 minute to increase hydrophilicity of the surface, which encourages wetting of PEDOT:PSS solution resulting in uniform distribution. 3 wt % PEDOT:PSS solution bought from Sigma-Aldrich was spin-coated

on to the substrates at 3000 rpm for 40 seconds. It was then dried at 120 ◦ C for 20 minutes and vacuum annealed for more than 24 hours. This results in a thin film (∼ 50 nm thickness).

Electrical characterization of devices: Electrical characterization of the fabricated devices were done using a SP 200 Potentiostat from Biologic. For vertical devices, spring loaded copper(Cu) and gold(Au) contacts were used as the top and ground electrodes respectively. Bipolar sinusoidal voltage waveforms of 5 V and 100 mHz were used for i-v characterization of the devices. For lateral devices, tungsten micro probes purchased from Microprobes, were mounted on a semiconductor probing station were used for current-voltage measurements. Bipolar sinusoidal voltage waveforms of 5 V and 100 mHz were used for *i-v* characterization of the devices.

I-V mathematical analysis: Current-voltage responses obtained were plotted on a double logarithm (base 10) scale. The slope of the traces was measured by fitting the data for different voltage regimes using a power log fitting routine for a R^2 value of 0.99. The slopes indicate the possible charge transport mechanism through the device as shown elsewhere [19].

X-ray Photoelectron Spectroscopy (XPS): XPS measurements were done using an Advanced photoelectron spectrometer at Institute for Advanced Materials and Manufacturing at UTK.

Results and discussion

Cu plays crucial role in the resistive switching: For the inorganic-organic Cu/PEDOT:PSS device it is crucial to determine the role of the materials of the device towards the *i-v* response. Response of Cu/PEDOT:PSS/ITO were compared to responses of Au/PEDOT:PSS/ITO, Cu/ITO (no PEDOT:PSS), and Cu/PEDOT:PSS/Au devices as shown in Figure 5.1 to determine materials which are crucial for the hysteretic *i-v* behavior observed in a Cu/PEDOT:PSS/ITO device.

Figure 5.1A displays response of a device with Au electrodes atop PEDOT:PSS/ITO. It reveals a similar *i-v* response to when Cu electrodes are put on bare ITO (no PEDOT:PSS film). The linear, non-hysteretic large current traces without any resistive switching characteristics are indicative of very low Ohmic resistance at the contact. Cu electrodes on ITO (~15 Ω cm^2) should form a short-circuit and the response in Figure 5.1A is reflective of that. A very similar response from Au/PEDOT:PSS/ITO device indicates a highly conductive path from Au through PEDOT:PSS to ITO through the thickness of PEDOT:PSS thin film. While the conduction pathway for this device

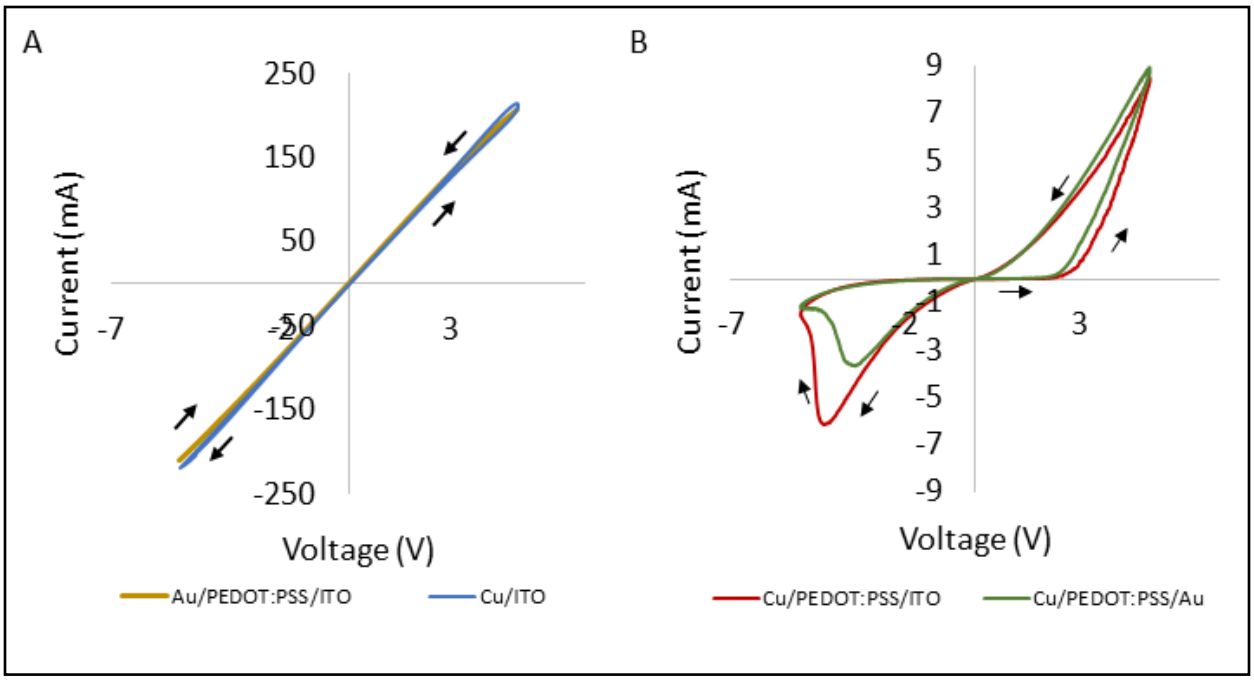


Figure 5.1. Responses of vertically stacked (sandwiched) devices with and without PEDOT:PSS for different electrode combinations.

has not been exclusively investigated here, highly conductive linear response has been earlier associated with filament formation and short-circuit [20]. Figure 5.1B displays change in the *i-v* behavior of the devices when we replace Au electrodes with Cu atop a PEDOT:PSS/ITO combination. A non-linear, non-volatile, hysteretic current response is observed with clear bipolar resistive switching beyond voltage thresholds. These attributes establish Cu/PEDOT:PSS/ITO device is a memristor. Response Cu/PEDOT:PSS/ITO in comparison to Au/PEDOT:PSS/ITO and Cu/ITO clearly indicates the combination of Cu metal electrode and PEDOT:PSS plays a crucial role in the memristive response of the device. However, advanced measurements of Cu/PEDOT:PSS/Au displayed very similar *i-v* response to that of Cu/PEDOT:PSS/ITO device. This indicates dominant contribution of the Cu/PEDOT:PSS combination towards the RS mechanism and hysteresis and negligible contribution of ITO for the same. Equivalent electrical circuitry of an electrode/PEDOT:PSS/electrode device can be written as

$$R_{eff} = R_{electrode} + R_{int} + R_{bulk} + R_{int} + R_{electrode} \quad (1)$$

where, $R_{electrode}$ = internal resistance of electrode material Au or Cu, R_{int}= impedance of the electrode-PEDOT:PSS interface, and R_{bulk}= impedance of PEDOT:PSS.

For an Au/PEDOT:PSS/ITO device, $R_{electrode=Au}$ (internal resistivity ~ $2.4*10^{-8}$ Ω-m) is very low (cite) and R_{ITO} can be considered very low. $R_{int_Au} + R_{bulk} + R_{int_ITO}$ can be considered to have maximum impedance in the circuit, which accounts to 0.023 kΩ. Similarly, for a Cu/PEDOT:PSS/ITO device, $R_{int_Cu} + R_{bulk} + R_{int_ITO}$ can be considered to have maximum impedance, which amounts to 190 kΩ. As $R_{int_ITO} \leq 0.023$ kΩ, therefore, simplified version of equation 1 indicates $R_{int_Cu} + R_{bulk}$ must be the region of maximum impedance ~ 190 kΩ.

Eliminating involvement of PEDOT:PSS bulk in the RS of the device: For electrode/polymer/ electrode devices, if the bulk of the polymer stretching across the inter-electrode distance contributes towards the total impedance of the device, the total amount of current, voltage threshold of switching, and high and low resistance values of the device should be affected with change in the inter-electrode gap (*g*) (PEDOT:PSS bulk) of the device. Multiple different co-planar devices were formed with different inter-electrode gaps for Cu-Cu and Au-Au electrodes. Symmetrical electrode combinations were chosen for easier and quicker fabrication as it was

concluded that the Cu-PEDOT:PSS was the crucial in these devices, and Au/PEDOT:PSS can form control/comparable cases. If $R_{bulk} \gg R_{int}$ and for identical resistive area, with increased resistive length (inter-electrode gap 'g'), the impedance ($R = (\rho * g)/A$) of the device should vary proportionately. Figure 5.1A and table 1 reflects decrease in conductivity of the device with increase of PEDOT:PSS bulk (because of increase in 'g').

For a Cu/PEDOT:PSS/Cu device current voltage measurements were also done across *g*= 5,10,50,100 µm with electrode width configurations (*w*) of 20 µm as shown in Figure 5.2B. *GxWx* reads as inter-electrode gap and width of the electrodes respectively. It is observed that with symmetric Cu electrodes, the response of the device changes from non-volatile in Cu/PEDOT:PSS/ITO or Au to a volatile response as shown by arrows in Figure 5.2B.

It is also observed that, with change in gap distance (*g*), the conductivity of the device does not vary proportionately at similar voltages. The values in Table 1 also reflect no proportionate change in resistance of the HRS values for devices with 10-fold to 20-fold increase in the bulk PEDOT:PSS. This contrasts with the *i-v* response of Au/PEDOT:PSS/Au devices. Although the internal resistance of Cu (R_{Cu}) is very low (resistivity ~ 7 x 10^{-6} Ω-m), R_{int} must be comparable or higher than R_{bulk}. But, as the total impedance (R_{eff}) does not vary with increase in the 'g' (bulk) R_{bulk} must not be changing or $R_{int_Cu} \gg R_{bulk}$, where major voltage drop happens across R_{int_Cu} . HRS listed in table 1 for Cu/PEDOT:PSS/Cu device displaying much higher nominal values comparable to Au/PEDOT:PSS/Au device (precisely of the bulk) also suggests $R_{int_Cu} \gg R_{bulk}$. Also, the observed voltage threshold for resistive switching does not vary for Cu based devices (Figure 4.2B). Therefore, we can say i) conductive path spanning through the bulk of PEDOT:PSS connecting two electrodes is unlikely and ii) Cu/PEDOT:PSS interface dominantly contributes towards the RS and hysteretic *i-v* behavior in Cu/PEDOT:PSS devices.

Charge transport mechanism: With Cu/PEDOT:PSS/Au and Cu/PEDOT:PSS/ITO devices yielding similar *i-v* response, we analyzed the response of a Cu/PEDOT:PSS/Au device. Mathematical techniques as described in the methods section were used to determine the conduction mechanism of the device in both polarities as shown in Figure 5.3 A & B respectively. In the increasing positive voltage sweep, the HRS has two different slope regions as shown in Figure 5.3A. Initially, current is linearly proportional (slope ~ 1.09) to voltage (< 0.4V) signifying

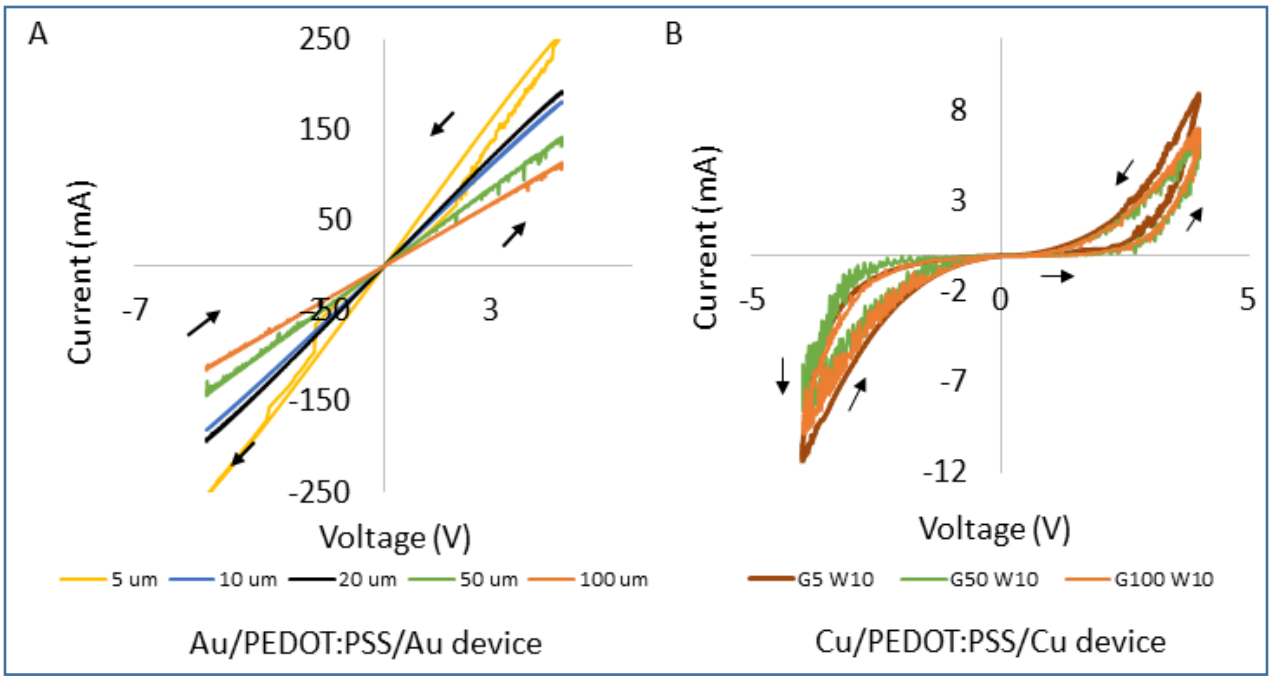


Figure 5.2. Response from Cu/PEDOT:PSS/Cu and Au/PEDOT:PSS/Au electrode combinations.

Table 5.1. Resistance values of Cu/PEDOT:PSS/Cu and Au/PEDOT:PSS/Au devices. These represent average values across n=5 devices.

Gap (μm)	Cu/PEDOT:PSS/Cu (HRS)	Au/PEDOT:PSS/Au (kΩ)
5	4.11 ± 0.33	0.019 ± 0.013
10	-	0.027 ± 0.007
20	-	0.026 ± 0.010
50	3.99 ± 0.13	0.036 ± 0.011
100	4.07 ± 0.20	0.044 ± 0.020

Ohmic conduction [17] stemming from thermally excited free electrons as discussed elsewhere[16]. At moderate voltages (slope ~ 1.77), the space charge limited current (SCLC) starts dominating due to traps in the material as discussed elsewhere[17]. Plotting the *i-v* data in the HRS region on a $\ln I \ \ vs \sqrt{V}$ plane reveals a perfect linear fit which is indicative of Schottky emission current as shown in Figure 5.6 in the Appendix. At higher voltages the current transitions into Child's Law region (slope ~ 7.87) where $I \alpha V^n$ [21]. This is the region of RS and transition from HRS to LRS. The rapid rise in current indicates overcoming of the possible Schottky barrier and free pathway for the charge carriers. With saturated SCLC [17], the slope can decrease (slope ~ 3.77) displaying a less abrupt increase in current which can be correlated to the traps being filled/saturated [16]. During the decreasing positive scan, the current again follows a trap-free SCLC regime (slope ~1.57) and a Ohmic conduction (slope ~ 1.2) region as seen in Figure 5.3A. Though the slopes of current traces in the HRS, transition and LRS region indicate the charge transport/conduction processes of the device, they fail to reveal any change in the material properties of the device resulting in RS and hysteretic response.

In the increasing negative voltage scan, the current continues to display Ohmic conduction (slope ~ 1.12) and un-trapped SCLC behaviors (slope ~ 1.73). These slopes are in similar ranges for current slopes corresponding to the decreasing positive voltage region indicating similar conduction processes underway. At higher negative voltages (> 4V), the high value of negative slope (-11.88) signifies change in the conduction process, and this corresponds to the resetting of the device. Thereafter, we see Child's law region of conduction (slope ~3.77) with accelerated drop in current and Ohmic conduction (slope ~ 1.09) of very low current which indicates a reversible change in the material occurred to induce a barrier to the flow of charge carriers.

Resistive switching mechanism and hysteresis: From Figure 5.1 & 2 we have strong evidence that ITO or Au contact has negligible contribution towards the observed *i-v* behavior of the device and Cu/PEDOT:PSS interface plays a dominant role. The possible charge transport mediums for holes in a Cu/PEDOT:PSS/Au device will be from i) Cu metal to PEDOT:PSS to Au ii) Cu metal to an interlayer of copper oxide to PEDOT:PSS to Au because reactive metals like Cu can oxidize to its transition metal oxide states easily under favorable conditions or electrode deposition processes [16]. Therefore, formation of Cu_2O or CuO or a combination of both is likely at the interface of Cu/PEDOT:PSS. This can then make the composition of electrode-polymer interface to be Cu/Cu-

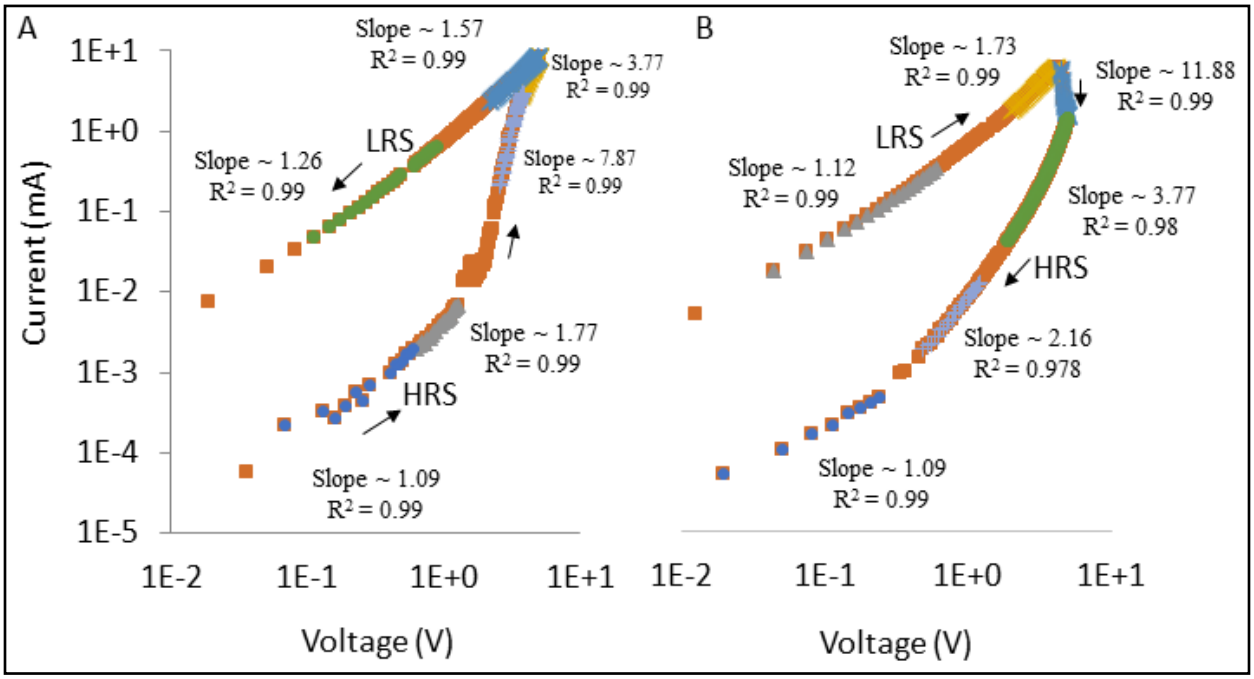


Figure 5.3. Slopes of current versus voltage traces at (A) positive and (B) negative polarities indicate different charge transport mechanisms of the device in the different voltage regions.

oxides/PEDOT:PSS. The HRS region for Cu/PEDOT:PSS displays there is a barrier to charge flow. The *i-v* behavior here can possibly be explained based on the Schottky contact model as shown in Figure 5.4 because of the Schottky diode like *i-v* traces as seen in Figure 5.4B & 5.2B.

Both Cu_2O and CuO are known to be *p*-type semiconductors [26, 27] with band gap of 2.1 and 1.2 eV respectively. The difference in work function for the metal-semiconductor combination contributes to the Schottky barrier. Here, as the work function of the metal (Cu ~ 5.1 eV) is lower than the work function of the p-type semiconductor (CuO ~ 5.32 eV), therefore there is no barrier to the flow of holes under positive bias. But the heterojunction at the CuO (5.32 eV)/PEDOT:PSS (5 eV) creates a barrier for the holes which results in a region of low current or the HRS as shown by the blue trace in Figure 5.4. With sufficient energy supply via voltage, this barrier is crossed at the voltage threshold (Vth ~ 3V for these devices), transport of holes can happen unhindered to the semiconductive PEDOT:PSS region (which effectively acts as an electrode [28]) as seen from accelerated growth in current for voltages 3- 5 V as shown by the green trace in Figure 5.4B. This results in RS from HRS to LRS and the Schottky diode like behavior also seen elsewhere [22]. If Cu_2O is the oxide at the inter-layer, then a Schottky energy barrier is created at the Cu (5.1 eV)/ Cu_2O(4.84 eV) interface, which can also result in a HRS region. At sufficient positive voltages, the oxidized state of Cu as present in copper oxides get reduced significantly (cite) which will lower the work function of the overall oxide region. This results in reduced energy barrier for hole movement and thus higher current for decelerating voltages (5 V to 3V). We observe a non-linear, mild Schottky diode like *i-v* response (also seen with Cu_2O/Cu interface elsewhere [22]), in contrast to a linear filamentary response when the sweeping voltages drop, which further indicates modification of the Schottky barrier height. This results in the hysteretic current loop we observe in the positive polarity.

With reversal in polarity holes move towards the Cu metal electrodes. Negative polarity now favors oxidation of the previously reduced Cu and the doping of the oxide interface changes and the material becomes more resistive. Negative polarity regions (0 to -4V) in Figure 5.4B again displays a mild Schottky diode like *i-v* response and it is evident that de-doping induced modification of Schottky barrier height requires a sufficient negative voltage (V_{reset} ~ 4V). With increased de-doping of the oxide layer, the resistance to flow of holes increases from the

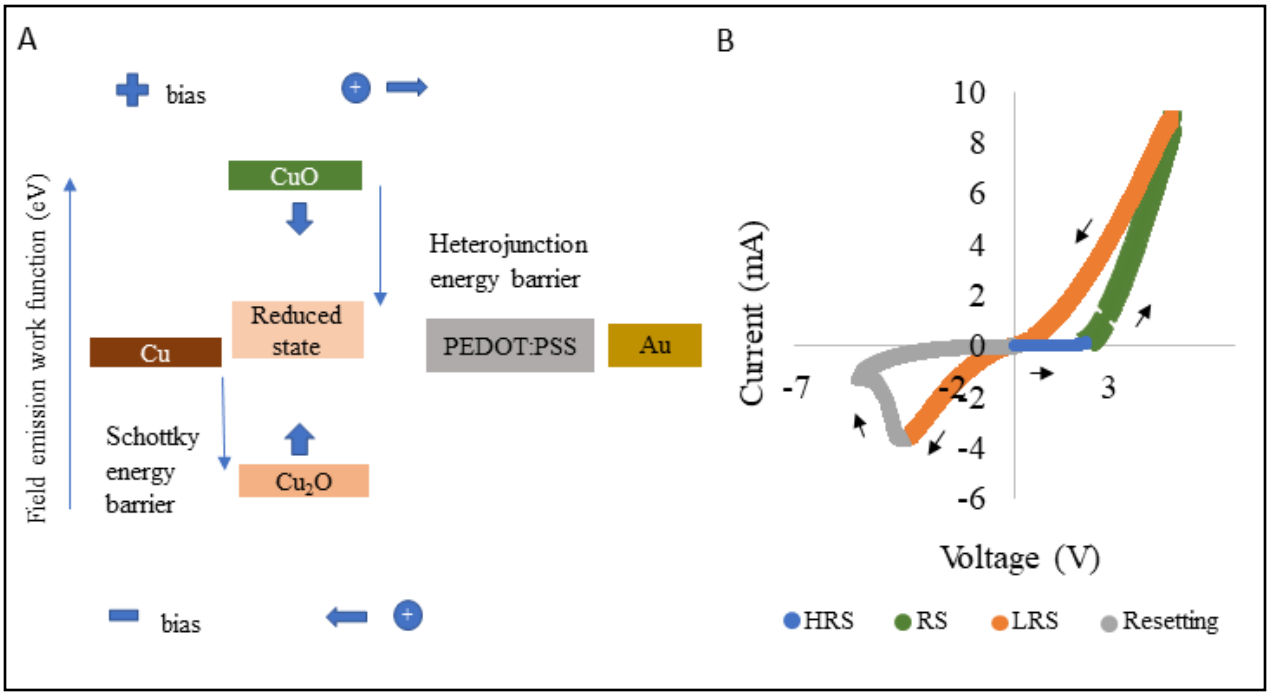


Figure 5.4. Schematic displaying the modulation in energy barrier to hole movement giving rise to bipolar resistive switching in Cu/PEDOT:PSS/Au device.

Table 5.2. Field emission work function of metals, metal-oxides, and polymer [22-25].

Material	**Work function (eV)**
Cu	5.1
ITO	4.68
Au	5.2
CuO	5.32
Cu_2O	4.84
PEDOT:PSS	5.0

PEDOT:PSS layer back to the CuO or Cu_2O to Cu and the device returns to the HRS. This explains the resetting mechanism and the hysteretic current we observe in the negative polarity. Identification and then recording of changes in the doping of the oxide at Cu/PEDOT:PSS interface can be ascertained via X-ray photoelectron spectroscopy (XPS) measurements prior to and post voltage excited RS. XPS analysis can confirm existence of the type of transitional metal oxide at the interfacial region. Basic TEM diffraction analysis or XPS of the oxide interlayer pre and post unipolar *i-v* sweeps can reflect changes in the oxide composition. These findings can confirm the RS mechanism suggested here, thereby explain the hysteretic *i-v* response of Cu/PEDOT:PSS devices.

Conclusion

A Cu/PEDOT:PSS/ITO or Au device was fabricated and characterized via electrical measurement, and electron microscopy and elemental analysis of its material composition. We revealed that Cu metal electrode on PEDOT:PSS thin film is a necessary combination for RS and non-volatile *i-v* response. Also, only asymmetric electrode combinations can produce bipolar RS, else we get a volatile device with symmetric RS in both polarities. We also revealed that the Cu/PEDOT:PSS interface is crucial for the RS. For a newly built device, there is rapid oxidization of the copper electrode. With positive bias, holes encounter a Schottky energy barrier at the Cu/Cu oxide interface or a heterojunction energy barrier at the copper oxide polymer interface. With voltage across eclipsing a threshold, the holes can cross the energy barrier and accelerated growth in current is observed. The supplied voltage also causes reduction of the copper oxide contributing to drop in the Schottky energy barrier height and switching the device to a different resistance state. With sufficient negative bias, oxidation of copper undertakes and the Schottky barrier height is regained contributing to a higher resistive state. Via XPS analysis and TEM imaging of the Cu/PEDOT:PSS interface we aim to reveal the changes in the material composition at the Cu/PEDOT:PSS interface that contribute to the RS of the device thus supporting the proposed mechanism.

References

1. Yang, Y., et al., *Electrical Switching and Bistability in Organic/Polymeric Thin Films and Memory Devices.* Advanced Functional Materials, 2006. **16**(8): p. 1001-1014.
2. Liu, G., et al., *Organic Biomimicking Memristor for Information Storage and Processing Applications.* Advanced Electronic Materials, 2016. **2**(2): p. 1500298.
3. van de Burgt, Y., et al., *Organic electronics for neuromorphic computing.* Nature Electronics, 2018. **1**(7): p. 386-397.
4. Kotova, M., et al., *Impact of scaling to the resistive switching effect in organic polymer – based structures.* Organic Photonics and Photovoltaics, 2016. **4**.
5. Forrest, S.R., *The path to ubiquitous and low-cost organic electronic appliances on plastic.* Nature, 2004. **428**(6986): p. 911-918.
6. Katherine S. Riley, S.K., Juan C. Osorio, Yongchao Yu, Harith Morgan, Janav P. Udani, Stephen A. Sarles, Andres F. Arrieta *Neuromorphic metamaterials for mechanosensing and perceptual associative learning*. 2022.
7. Zhao, X., et al., *Sp2 clustering-induced improvement of resistive switching uniformity in Cu/amorphous carbon/Pt electrochemical metallization memory.* Journal of Materials Chemistry C, 2017. **5**(22): p. 5420-5425.
8. Valov, I., et al., *Electrochemical metallization memories—fundamentals, applications, prospects.* Nanotechnology, 2011. **22**(28): p. 289502.
9. Lee, S.-H., et al., *Organic Flexible Memristor with Reduced Operating Voltage and High Stability by Interfacial Control of Conductive Filament Growth.* physica status solidi (RRL) – Rapid Research Letters, 2019. **13**(6): p. 1900044.
10. Mangalam, J., et al., *Resistive switching in polymethyl methacrylate thin films.* Organic Electronics, 2016. **29**: p. 33-38.
11. Möller, S., et al., *A polymer/semiconductor write-once read-many-times memory.* Nature, 2003. **426**(6963): p. 166-169.
12. Lee, Y.J., et al., *Flexible p-type PEDOT:PSS/a-Si:H hybrid thin film solar cells with boron-doped interlayer.* Solar Energy, 2018. **163**: p. 398-404.
13. Ouyang, J., *"Secondary doping" methods to significantly enhance the conductivity of PEDOT:PSS for its application as transparent electrode of optoelectronic devices.* Displays, 2013. **34**(5): p. 423-436.

14. Liu, X., et al., *Organic nonpolar nonvolatile resistive switching in poly(3,4-ethylene-dioxythiophene): Polystyrenesulfonate thin film.* Organic Electronics, 2009. **10**(6): p. 1191-1194.
15. Ha, H. and O. Kim, *Bipolar switching characteristics of nonvolatile memory devices based on poly(3,4-ethylenedioxythiophene):poly(styrenesulfonate) thin film.* Applied Physics Letters, 2008. **93**(3): p. 033309.
16. Jeong, H.Y., et al., *Bipolar resistive switching characteristics of poly(3,4-ethylene-dioxythiophene): Poly(styrenesulfonate) thin film.* Current Applied Physics, 2010. **10**(1, Supplement): p. e46-e49.
17. Rutledge, S.A. and A.S. Helmy, *Carrier mobility enhancement in poly(3,4-ethylenedioxythiophene)-poly(styrenesulfonate) having undergone rapid thermal annealing.* Journal of Applied Physics, 2013. **114**(13): p. 133708.
18. Di, C.-a., et al., *High-Performance Organic Field-Effect Transistors with Low-Cost Copper Electrodes.* Advanced Materials, 2008. **20**(7): p. 1286-1290.
19. Syed A. Moiz, I.A.K., Waheed A. Younis and Khasan S. Karimov, *Space Charge–Limited Current Model for Polymers.* Conducting Polymers, 2016.
20. Karthäuser, S., et al., *Resistive switching of rose bengal devices: A molecular effect?* Journal of Applied Physics, 2006. **100**(9): p. 094504.
21. Khan, M.U., et al., *Schottky diode based resistive switching device based on ZnO/PEDOT:PSS heterojunction to reduce sneak current problem.* Journal of Materials Science: Materials in Electronics, 2019. **30**(5): p. 4607-4617.
22. Singh, B. and B.R. Mehta, *Relationship between nature of metal-oxide contacts and resistive switching properties of copper oxide thin film based devices.* Thin Solid Films, 2014. **569**: p. 35-43.
23. Nehate, S.D., et al., *Work Function Extraction of Indium Tin Oxide Films from MOSFET Devices.* ECS Journal of Solid State Science and Technology, 2018. **7**(3): p. P87-P90.
24. Yang, W.-Y. and S.-W. Rhee, *Effect of electrode material on the resistance switching of Cu2O film.* Applied Physics Letters, 2007. **91**(23): p. 232907.
25. Xing, Y.-J., et al., *Increased work function in PEDOT:PSS film under ultraviolet irradiation.* Chinese Physics B, 2014. **23**(3): p. 038504.

26. Raebiger, H., S. Lany, and A. Zunger, *Origins of the p-type nature and cation deficiency in ${\mathrm{Cu}}_{2}\mathrm{O}$ and related materials.* Physical Review B, 2007. **76**(4): p. 045209.
27. Balamurugan, B. and B.R. Mehta, *Optical and structural properties of nanocrystalline copper oxide thin films prepared by activated reactive evaporation.* Thin Solid Films, 2001. **396**(1): p. 90-96.
28. Sanyoto, B., et al., *Solution processable PEDOT:PSS based hybrid electrodes for organic field effect transistors.* Organic Electronics, 2016. **37**: p. 352-357.

Appendix

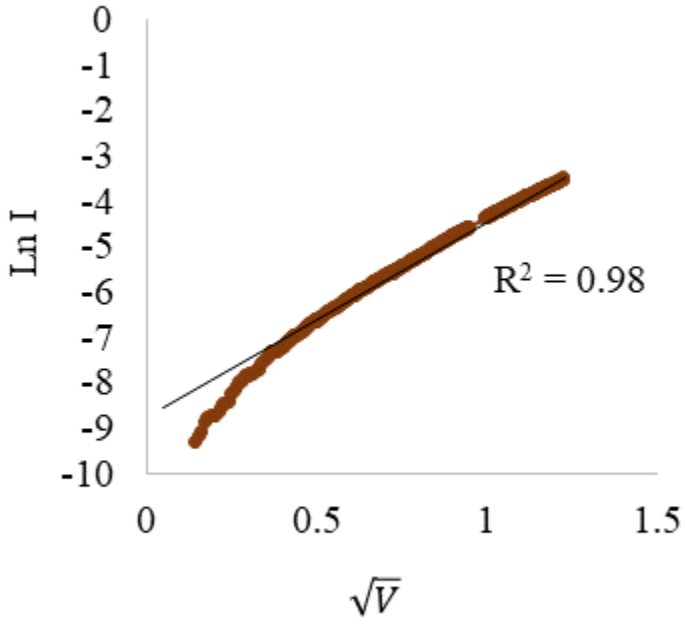


Figure 5.5. Schottky emission detected from fitting of current response in the HRS region in positive polarity.

CHAPTER VI. Conclusion

In the current times, where data and time are of prime importance, there is an ever-growing need for electronic devices amongst consumers which come with faster processing of huge amounts of data, have denser memories and are also not power invasive. As modern-day electronics still use traditional electronic components like transistors which are hindered by the Von Neumann bottleneck [1, 2], efforts have been made to build tinier transistors and increase their density in the network all aimed to increase processing capacity and speed. This has pushed researchers towards a physics-based limit of making atomistical small transistors. This is where the biological brain inspires modern day research to develop newer electronic devices. The brain consumes very less power and can yet process diverse types and large number of data simultaneously. The brain has dense network of neurons and it leverages adaptable interconnections of neurons (which are strengthened or weakened depending on past activity) for information processing and memory.

Synapses form this interconnection and can adaptively process signals as well as store processed data. Therefore, devices which can mimic the history dependent change in connection strength of synapses via alteration in the physical properties of its materials based on previous excitations can revolutionize conventional computing techniques. Memristors [3] have emerged as potential solutions to the Von Neumann bottleneck problem. Very recently Modor Intelligence market research reported that memristors are popular in the wearable electronics industry whose demand is expected to grow from 593 million units in 2018 to 1105 million units by 2022 [4]. They also stated that increasing demand for higher graphics systems with better processing speeds is expected to increase the adoption rate of memristors during the forecast period. Since 2008, huge amount of effort has been invested to build different types of memristors using different types of materials. But with increasing demands of memristive systems in diverse applications, exploration of newer materials is required.

In this dissertation, I demonstrate the different potentialities of using alternate material compositions for construction of memristors and memristive systems. I briefly review the literature about memristors encompassing its properties, functionalities, mathematic model, and its applications. I also discuss different types of memristors based on diverse kind materials used to build the devices. Three general types studied in the first chapter are solid state (phase change, oxides, spintronic), organic (polymeric) and biomaterial based memristors. The potential applications, advantages, limitations, and consequences of those limitations from using each one

has been presented too. The solid state memristor has been widely used in comparison to others in different research works from non-volatile memory, artificial synapse, and in networks for supervised/unsupervised learning mechanisms. The organic memristor bears potential applications in the flexible electronics and biomedical devices industry. Biomolecular memristors built from biomaterials closely resemble the composition of biological synapses and capable of geometric reconfigurability alike the morphological growth seen in synapses. While solid state memristors are compatible with current CMOS architecture and fabrication techniques, they are limited in shelf life and device tunability. Organic memristor better them in tunability, flexibility, and easier fabrication, they are limited by poor reproducibility. Biomolecular devices though provide lower working voltages and closer similarity to bio-synapses, they are limited by their chemical degradation in shorter span of time.

Although all types of memristors had varied mechanism of functioning and advantages, they had one thing in common amongst them, i.e. they all loosely mimicked the threshold dependent change in conductance strength of a chemical synapse. This is because the threshold dependent functioning of the chemical synapse is believed to inspire filtering of signals above a threshold, eliminate noise in signals, better decision making via history dependent plasticity. But brain neurons also employ electrical synaptic connections for communications. Traditionally thought to be mere conductive wire like connections because they do not display threshold dependent behavior, recent research highlighted importance of plasticity of electrical synapses in neuron communication, like synchronizing of neuron firing. Therefore, as shown in chapter 2, I constructed an artificial electrical synaptic (AES) device using a biomolecular lipid membrane via droplet interface bilayer technique and doped with gramicidin peptides. These peptides created always-conductive transmembrane ion channels similar to gap junctions—transforming the otherwise capacitive membrane into a memristive one that exhibits a pinched, hysteretic current-voltage relationship and displays short-term plasticity to successive voltage pulses [5]. I also demonstrated through both experiments and modeling that the AES can be modularly configured to exhibit paired-pulse depression and that voltage-induced plasticity in conductance can synchronize the firing of Hodgkin-Huxley neurons. Therefore, this work addressed a major research gap in the construction and characterization of artificial synaptic devices that emulate the synaptic plasticity and functionality of electrical synapses. In parallel, due to the recent introduction of biomaterials as components of memristor building, there continues to be

opportunities to advance our learning about the methods to build, characterize, use, and improve these devices. While methods to better characterize these biomolecular devices was advanced, improvement of these devices like making them more robust and durable remained to be explored.

In chapter 3, I studied the effect of amphiphilic block co-polymers as lipid substitutes or in hybrid environment with lipids on biomolecular membranes to investigate ways to make thin, durable, and robust biomolecular membrane.. I doped lipid membranes with low molecular weight $PB_{12}PEO_8$-COOH (polybutadiene-co-polyethylene oxide, M_w=1000 g/mol) di-block species to study the effect on the membrane thickness, geometric sensitivity of membrane to applied voltages, durability of the bilayer, and its response to ion channel forming species. Through experiments and analysis of results I showed proof of concept that BCPs can be used to selectively preserve and modulate the properties of hybrid membranes in ways that favor the interactions of other membrane-active species, yet also make them stable at higher voltages. The findings should encourage future research to employ hybrid membranes in construction of memristive devices working at lower voltage thresholds and stable to higher voltage inputs. Hence, I contributed to the understanding of the electrical and structural effects of BCPs in lipid bilayers.

Chapter 4 investigated the construction, characterization and integration of polymeric thin film memristors with strain sensors on a bistable meta-sheet for unsupervised classification of spatial information received from tactile sensing. With inversion of a dome on the bistable dome meta-sheet, we (me and team) recorded the mechanically transduced signals using non-volatile flexible memristors that remember sequences of mechanical inputs, providing a means to store spatially-distributed mechanical signals in measurable material states. The accumulated memristance changes resulting from the sequential mechanical inputs allowed us to physically encode a Hopfield network into our neuromorphic metamaterials. The physical network learns a series of external spatially distributed input patterns. Crucially, the learned patterns input into our neuromorphic metamaterials can be retrieved from the final accumulated state of our memristors. Therefore, our system exhibits the ability to learn without supervised training and retain spatially distributed inputs with minimal external overhead [6]. Hence, we could reveal understanding on how tactile information received can be processed and memorized leading to learning. These capabilities set the stage for an era of smart sensing and memory (via memristors) applications

with emerging systems (reconfigurable sheet) that interact with the world for autonomous classification of tactile information.

Although we could reproduce the electrical behavior of Cu/PEDOT:PSS/ITO memristors used for integration with other transducers as described in chapter 4, its resistive switching mechanism was yet to be revealed at the time. In chapter 5, I investigated the mechanism for resistive switching and hysteresis and demonstrated that these devices exhibit a Schottky barrier at the Cu/PEDOT:PSS interface that undergoes a change in response to applied voltage, which enables either volatile or non-volatile hysteresis depending on symmetric or asymmetric electrode material composition. Unpublished results indicate the Cu/PEDOT:PSS interface as the dominant contributor to the resistive switching (RS) and hysteretic memory of the device. Through experiments with varied electrode materials and dimensions, I revealed the Cu/PEDOT:PSS interface as the dominant contributor to the RS. With advanced elemental analysis via XPS and TEM imaging of the Cu/PEDOT:PSS interface pre and post electrical excitation, I aim to reveal changes in the material composition which modulates the Schottky barrier height between metal electrode and semiconductive material resulting in the RS of the device. Findings will deliver an understanding of the physics via which organic/ organic-inorganic devices display RS in general, which has been a long-standing research gap as discussed in chapter 1 due to concrete evidence usually filled with proposed mechanisms.

Therefore, chapter 1 reviews memristor properties and lays down the upside and limitation of different types of memristors, prevalent research gaps, proposed research plans to execute specific research objective in my effort to address some of those gaps. It also highlights the contributions of the subsequent chapters that follow. Chapters 2-5 highlights the fabrication, characterization, different types of memristors, their potential applications, and description of the memristive mechanisms. Prototype of embedded intelligent material system using memristors was also displayed with physical integration techniques and learning mechanisms achieved.

Thus, this dissertation addressed some of the research gaps discussed in Chapter 1 via fulfillment of the research objectives laid down in Chapter 1. The findings in Chapter 2 and 3 motivates future research on biomolecular devices using different types of membranes and ion-channels as it successfully demonstrated uniquely modular transport properties and tunable plasticity that can be achieved at biologically relevant voltages. Chapter 4 demonstrates unique capability of our

prototype which provides a route to continuously learning new spatiotemporal mechanical inputs which can be compared to known patterns of interest that may trigger specific control actions. The findings demonstrated here opens avenues for: i) integrating printed memristors on the bistable dome sheets; ii)scaling up from a 2x2 array to a much larger configuration; and iii) training of robotic systems to recognize shapes of objects etc. Better understanding of the working mechanism of the memristors used here motivates engineering to tune the material combinations for 3-D printing of memristors on flexible materials such a dome sheets used here.

In conclusion, this work answers the gaps stated earlier in Chapter 1 and provides direction for research to i) to develop fully biomolecular circuit with signal processing and propagation. Based on work demonstrated here, it can be envisioned to build biomolecular neuristors which can generate neuron like firing of signals. These neuristors can then be connected via a biomolecular synaptic mimic for signal processing and propagation, ii) to interface biomolecular memristors to with biological components like tissues/cells in-vivo which can then find applications in medical devices iii) understand how to fabricate and densely integrate Cu/PEDOT:PSS memristors on flexible materials which act as contact surfaces to build autonomous systems capable of learning and decision making.

References

1. Backus, J., *Can programming be liberated from the von Neumann style? a functional style and its algebra of programs*, in *ACM Turing award lectures*. 2007, Association for Computing Machinery. p. 1977.
2. McKee, S.A., *Reflections on the memory wall*, in *Proceedings of the 1st conference on Computing frontiers*. 2004, Association for Computing Machinery: Ischia, Italy. p. 162.
3. Strukov, D.B., et al., *The missing memristor found.* Nature, 2008. **453**(7191): p. 80-3.
4. *GLOBAL MEMRISTORS MARKET - GROWTH, TRENDS, COVID-19 IMPACT, AND FORECASTS (2022 - 2027)*. 2022, Modor Intelligence.
5. Koner, S., et al., *Memristive plasticity in artificial electrical synapses via geometrically reconfigurable, gramicidin-doped biomembranes.* Nanoscale, 2019. **11**(40): p. 18640-18652.
6. Katherine S. Riley, S.K., Juan C. Osorio, Yongchao Yu, Harith Morgan, Janav P. Udani, Stephen A. Sarles, Andres F. Arrieta *Neuromorphic metamaterials for mechanosensing and perceptual associative learning*. 2022.

VITA

Originally from India, Subhadeep Koner pursued higher education in Georgia (Masters) and Tennessee (Ph.D.). After high school in India, he attended Jalpaiguri Government Engineering College in India and received a Bachelor of Technology degree in Mechanical Engineering. Soon after graduating with his undergraduate degree, he knew he wanted to attend graduate school. He chose to attend the Georgia Southern University, Statesboro to pursue a master's degree in mechanical engineering. He then chose to pursue Doctor of Philosophy degree in Mechanical Engineering at university of Tennessee, Knoxville. His research interest includes studying novel materials, materials processing techniques for building electronic devices capable of brain like adaptive signal processing and memory. After graduation, he will continue to do research and aims to significantly contribute to science. He is incredibly grateful for all the support from his wife, family, and friends as he begins his new career